Universidad de Santiago de Compostela


# Superparamagnetic nanoparticles for cell tracking and magnetic vectorization in ischemic stroke

Nanopartículas superparamagnéticas para seguimiento celular y vectorización magnética en el ictus isquémico

**PhD Thesis**

Tesis doctoral

**Bárbara Argibay González**

**2014**

El **Prof. Dr. José Castillo Sánchez**, Catedrático y Director del Departamento de Medicina de la Universidad de Santiago de Compostela, Jefe del departamento de Neurología del Hospital Clínico Universitario de Santiago de Compostela y Director Científico del Instituto de Investigación Sanitaria de Santiago de Compostela (IDIS), el **Dr. Francisco Campos Pérez**, Investigador Miguel Servet y colaborador docente del Departamento de Medicina de la Universidad de Santiago de Compostela y el **Dr. Pablo Taboada Antelo**, Profesor Titular del Departamento de Física de la Materia Condensada de la Universidad de Santiago de Compostela,

CERTIFICAN:

Que el presente trabajo titulado "**Nanopartículas superparamagnéticas para seguimiento celular y vectorización magnética en el ictus isquémico**" ha sido realizado bajo su dirección, por la licenciada en física **Dña. Bárbara Argibay González**, y se encuentra en condiciones de ser presentado y defendido como Tesis Doctoral ante el tribunal correspondiente en la Universidad de Santiago de Compostela.

Santiago de Compostela, Diciembre de 2014

Prof. José Castillo Dr. Francisco Campos Dr. Pablo Taboada

Dña. Bárbara Argibay

**Prof. Dr. José Castillo Sánchez**, Professor of Neurology and Director of the Department of Medicine of the University of Santiago de Compostela, Chief of Neurology Department of the University Clinical Hospital of Santiago de Compostela and Scientific Director of Health Research Institute of Santiago de Compostela (IDIS), **Dr. Francisco Campos Pérez** (PhD and Miguel Servet researcher) and **Dr. Pablo Taboada Antelo**, Associate Professor of Condensed Matter Department of Physics of the University of Santiago de Compostela,

CERTIFY:

That the present research study entitled "**Superparamagnetic nanoparticles for cell tracking and magnetic vectorization in ischemic stroke**" has been carried out under their supervision by **Bárbara Argibay González,** graduated in physics, and the document fulfill all requisites for its defense under the corresponding committee proposed by the University of Santiago de Compostela.

Santiago de Compostela, December 2014

Prof. José Castillo Dr. Francisco Campos Dr. Pablo Taboada

Dña. Bárbara Argibay

# Abbreviations

**ACA**: Anterior Cerebral Artery

**ADC**: Apparent Diffusion Coefficients

**ATP**: Adenosine Tri-Phosphate

**BA**: Basilar Artery

**BBB**: Blood Brain Barrier

**BM-MSCs**: Bone Marrow Derived Cells

**C17.2**: Multi-potent neural progenitor cell line C17.2

**CBF**: Cerebral Blood Flow

**CCA**: Common Carotid Artery

**CFSE**: Carboxyfluorescein Succinimidyl Ester

**CNS**: Cerebral Nervous System

**Con-CC**: Contralateral Common Carotid Artery

**CT**: X-ray Computed Tomography

**DLS**: Dynamic Light Scattering

**D-MNPs**: Dextran-coated Superparamagnetic Nanoparticles

**DW**: Distilled Water

**DWI**: Diffusion Weighted Imaging

**EAATs**: Excitatory Amino-Acid Transporters

**ECA**: External Carotid Artery

**EGF**: Epidermal Growth Factor

**EPO**: Erythropoietin

**ESCs**: Embryonic Stem cells

**FOV**: Field of View

**FTIR**: Fourier Transformed Infra Red

**GOT**: Glutamate-Oxaloacetate Transaminase

**HUCBCs**: Human Umbilical Cord Blood Cells

**i.a.**: Intra-arterial

**i.v.**: Intravenous

**ICA**: Internal Carotid Artery

**ICP-OES or ICP**: Inductive Coupled Plasma Optical Emission Spectroscopy

**IL-6**: Interleukin-6

**Ip-CC**: Ipsilateral Common Carotid Artery

**Ip-EC**: Ipsilateral External Carotid Artery

**iPSCs**: Induced Pluripotent Stem Cells

**LDH**: Lactate Dehydrogenase Assay

**MCA**: Middle Cerebral Artery

**MGE**: Multi Gradient Echo

**MMPs**: Matrix Metalloproteinases

**MNPS**: Magnetic Nanoparticles

**MRA**: Magnetic Resonance Angiography

**MRI**: Magnetic Resonance Imaging

**MSCs**: Mesenchymal Stem Cells

**MSME**: Multi Slice Multi Echo

**NePi**: Neuropil

**nNOS**: neuronal Nitric Oxide Sintase

**NSCs**: Neural Stem Cells

**OA**: Oleic Acid

**PBS**: Phosphate Buffered Saline

**PCA**: Posterior Cerebral Artery

**PCoA**: Posterior Communicating Artery

**PEO**: Poly(ethylene oxide)

**PFA**: Paraformaldehyde

**PLL**: Poly-L-Lysine

**P-MNPs**: Pluronic F127-coated Superparamagnetic Nanoparticles

**PPA**: Pterygopalatin Artery

**PPO**: Poly(Prolpylene oxide)

**PWI**: Perfusion Weighted Imaging

**Rb**: Red Blood Cell

**RF**: Radio Frequency Pulse

**rt-PA**: recombinant tissue Plasminogen Activator

**SPIONs**: Superparamagnetic Iron Oxide Nanoparticles

**SZV**: Subventricular zone

**TA**: Transfection Agents

**TE**: Echo Time

**TEM**: Transmission Electron Microscopy

**TGA**: Thermal Gravimetric Analysis

**TIA**: Transient Ischemic Attack

**TLDF**: Transcranial Laser Doppler Flow

**tMCAO**: transient Middle Cerebral Artery Occlusion

**TMNPs**: Tetronic 908-coated Superparamagnetic Nanoparticles

**TR**: Repetition Time

**VEGF**: Vascular Endothelial Growth Factor

**VSM**: Vibrating Sample Magnetometer

**WHO**: World Health Organization

**XRD**: X-ray Diffraction

# Index

# Section I

USC
UNIVERSIDADE
DE SANTIAGO
DE COMPOSTELA

# 1. Introduction

## 1.1. Stroke

Stroke is a cerebrovascular disease, consequence of the alteration of normal cerebral blood flow, which results in a transient or permanent deficit of the function of one or more parts of the brain. This alteration of normal cerebral blood flow induces metabolic or biochemical alterations and would lead to cell death, and consequently, the alteration of the nervous system. The World Health Organization (WHO) has defined stroke as the fast clinical development of focal signs of alteration of cerebral function without any other apparent origin than the vascular one.[1]

Focusing on the nature of the lesion, stroke can be classified in two main groups, ischemic and hemorrhagic stroke. However, alternative classifications of this cerebrovascular disease can be used looking at other parameters such as stroke subtype, progression profile, neuroimaging characteristics, size and topography of the lesion, nature, and the mechanisms of induction and etiology.[2,3]

### 1.1.1. Ischemic Stroke

Ischemic stroke is the most common type of stroke, and represents about the 80% of all strokes.[2,4-6] This term includes also all those secondary encephalic alterations that lead to a failure of blood supply. Depending on the size and the affected territory, the classification is: focal brain ischemia, if affects one part of the brain, or global brain ischemia when the whole brain is injured. Among the focal brain ischemias, we can differentiate between transient ischemic attack (TIA) and cerebral infarction. TIA is defined as the focal or monocular cerebral dysfunction with symptoms that last for less than 24 hours, whose origin is a vascular insufficiency caused by an arterial thrombus or embolism, associated to arterial, cardiac or hematologic disease.[7] TIA patients present higher risk of subsequent major stroke (cerebral infarct) and other vascular episodes, mainly coronary, and the outcome of each individual is extraordinarily variable.

Attending to the etiology, the different ischemic stroke subtypes can be divided,[6]

- Atherothrombotic infarction: (~20%) Generally middle or large sized infarcts with cortical, subcortical, carotid or vertebro-basilar topography, in patients with presence of one or several cerebrovascular risk factors. It is imperative the presence of clinically generalized atherosclerosis, or the demonstration of occlusion or stenosis (> 50% occlusion or <50% plus two or more vascular risk factors) in cerebral arteries, with an established correlation to the patient's clinic.
- Lacunar infarction or small vessel disease: (~25%) small sized infarct (<15 mm of diameter), localized in the distribution territory of the penetrating arterioles. Although micro-atheromatosis and lipohialinosis of penetrating arterioles are the most frequent pathologic substrate in lacunar infarcts, other less frequent potential causes are cardiac embolism, arterial embolism, infectious arthritis or prothrombotic state.
- Cardioembolic infarction: (~20%) generally medium (1.5-3 cm of diameter) or large (>3 cm of diameter) sized infarcts, with symptoms frequently started during awakening. It is mandatory the presence of a demonstrated embolic origin, and the absence of significant concomitant arterial occlusion or stenosis.
- Infarction of undetermined etiology: (~30%) brain infarcts of medium or large size with more than two potential etiologies or unknown origin.
- Other causes (~5%)

### 1.1.2. Biochemistry of cerebral ischemia

The acute obstruction of one of the large brain arteries induces an instantaneous reduction of blood flow in the corresponding irrigation area (focal ischemia). But that reduction of blood supply is not homogeneous in the affected area, and can change within minutes or hours, especially if blood supply is reinstated.[8]

Two regions can be distinguished: The ischemic core is the portion of tissue closest to the affected blood vessel and where the ischemia becomes severe, and the so-called penumbra, where the reduction of blood flow is less severe, due to the blood supply carried out by collateral arteries of the non-ischemic neighbor tissue.[9] The impact of brain ischemia will depend on the level of the artery occlusion and duration of the reduction of blood flow, that is why time is a very important parameter in this disease.

After the onset of brain ischemia, a sequence of molecular events are triggered in the short and the long term, initiated with an energetic failure in cells, related to the interruption of oxidative phosphorylation processes and the deficient production of adenosine tri-phosphate (ATP) (Figure 1). The cessation of transmembrane ionic gradients due to the failure of sodium-potassium-ATPase pumps, and other ATP-dependent ionic pumps, is the key step of the physiopathological mechanisms in stroke, especially of cell death in the ischemic core, when the vascular occlusion lasts for few minutes.[10] Neurons and glial cells suffer an extreme depolarization because of the entrance of sodium, chloride, calcium and water into the cytoplasm,[11] and in addition, potassium leaves the cell, inducing a sudden increment of its extracellular levels.[12] The energetic failure and the associated ionic changes, originate an increment

in glutamate, a hyperexcitability of N-methyl- D-aspartate glutamatergic receptors (NMDA), and of α-amino- 3-hydroxy-5-methyl-4-isoxazol propionic acid receptors (AMPA), which induces an even higher increase of intracellular calcium (Figure 2).[13-15]

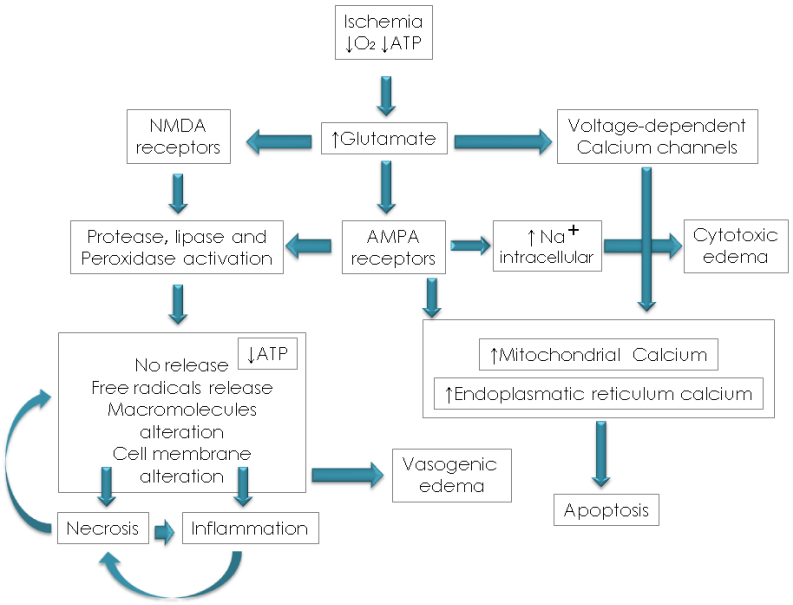


Figure 1: Sequence of main physiopathological events in cerebral ischemia.

The increase of intracellular calcium does not exclusively depend on the activation of glutamate receptors, but also in the stimulation of calcium voltage-dependent channels. Hyperexcitability causes a depolarization phenomenon in the periphery of the infarct, which increases the energetic cost while the membrane tries to re-polarize itself.[9,16,17] Calcium increment, together with acidosis and peri-infarct depolarization, contributes to initiate the damage, and after it, inflammation and activation of apoptotic phenomena contribute to increment the lesion.[15,18] During ischemia, and particularly during reperfusion, free

radicals are generated. These are highly reactive species produced at the initial and late stages of brain ischemia, following different physiopathological mechanisms. In first place, oxygen reactive species are produced by the metabolism of arachidonic acid and the activity of neuronal Nitric Oxide (NO) synthase (nNOS). During intermediate stages, free oxygen radicals are provided by the infiltration of neutrophils in the ischemic area. At later stages, they are produced via the synthesis and activation of inducible NO synthase enzymes (iNOS) and cycloxigenase-2(COX-2).[19,20]

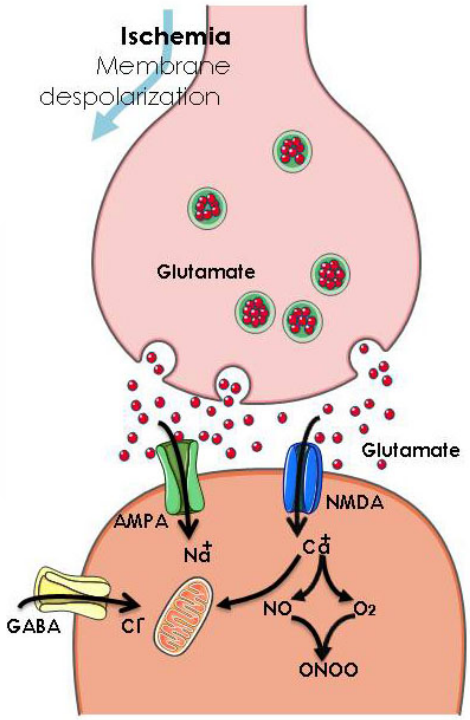


Figure 2: Glutamate role on the stimulation of AMPA and NMDA receptors.

Ischemic stroke triggers a series of complex molecular events, where the activation and the expression of genes

are included. Some of those events arise from the immediate reaction of neurons to damage,[21] and others are associated to cellular processes that determine the near fate of the affected neurons[22], or coordinate the repair mechanisms of tissues.[23,24]

However, ischemic cellular death can take place in two different ways. The most common one is necrosis,[25] which is the result of the acute energetic failure, and it is characterized by morphology changes and, in the end, cellular lysis, which also triggers inflammatory processes.[26] On the other hand, apoptotic or programmed cell death can be observed when energy-dependent intracellular mechanisms are activated, leading to cell degradation.[18,27]

### 1.1.3. The peri-infarct region

The introduction of the concept of ischemic penumbra by Astrup[10], and its subsequent development, has been crucial for the consideration of ischemic stroke from a *preventable catastrophe* to a *treatable disease*. The *time is brain* aphorism, and the consideration that stroke is a neurological emergency, as a result of the ischemic penumbra concept, has allowed patients to profit from fast attention by trained medical staff and specialized stroke units. The penumbra is classically defined as the hypoperfused tissue surrounding the ischemic core, where blood flow is too low to maintain electric activity but sufficient to preserve ion channels. However, this area is subjected to waves of deleterious metabolic processes propagated from the core to the neighboring tissue, including excitotoxicity, spreading depression, oxidative stress, and inflammatory response, which lead to the

expansion of the ischemic core and the subsequent worsening clinical outcome.

The most relevant definition of ischemic penumbra for clinical practice is based on neuroimaging techniques. It is widely accepted that brain tissue with reduced blood perfusion, as seen in MR perfusion-weighted imaging (PWI) but not included into the lesion core, as seen in MR diffusion weighted imaging (DWI), indicates potentially salvageable tissue. Thus, the combination of PWI and DWI images has led to the PWI/DWI mismatch concept.[28] Although it is generally accepted that hyperintense signal on DWI represents the lesion core, quantitative measurements of apparent diffusion coefficients (ADC) reveal that during ischemia, ADC values decline before energy metabolism fails, indicating that the increase in DWI signal intensity is not restricted to the infarct core[29]. Therefore, the discrimination between penumbra and infarct core by DWI is not always clear, because DWI signal increases in both sites. In addition, PWI-detectable flow decrease is pathophysiologically relevant only when interferes with the adequate oxygen supply to the tissue. Thus, the PWI/DWI mismatch includes not only the penumbra periphery, but also surrounding intact tissue.[28] Nowadays, neuroscientists are able to delineate the ischemic penumbra using alternatives to this hemodynamic concept. Among others, tissue hypoxia can be determined by MR spectroscopy, anoxic depolarization depicted by manganese enhanced MRI, tissue acidosis shown by pH-weighted MRI, and others. However, none of these methodologies is able to provide clear-cut threshold values to differentiate among ischemic core, penumbra, and surrounding intact brain tissue by themselves, and a multimodality approach is generally recommended.[28,29] Most of these MRI-based methods are unfortunately restricted to experimental models and

state-of-the-art brain imaging systems, and must be fully validated for the human brain before they can be translated into clinical practice.[30]

Although the definition of the penumbra by imaging techniques is currently of great value, in clinical terms an alternative definition of "tissue-at-risk", that is generally called peri-infarct region, may be more suitable for the development of new therapeutic approaches in stroke. The peri-infarct region is defined as a *no men's land* between the infarct core, with a front of toxic mediators of damage spreading out from it, and the healthy tissue, from where tissue's healing and repair mediators are trying to access to the affected but still viable tissue (Figure 3). It is clear that the peri-infarct definition and spatiotemporal dynamics do not necessarily match the specifications of the ischemic penumbra.

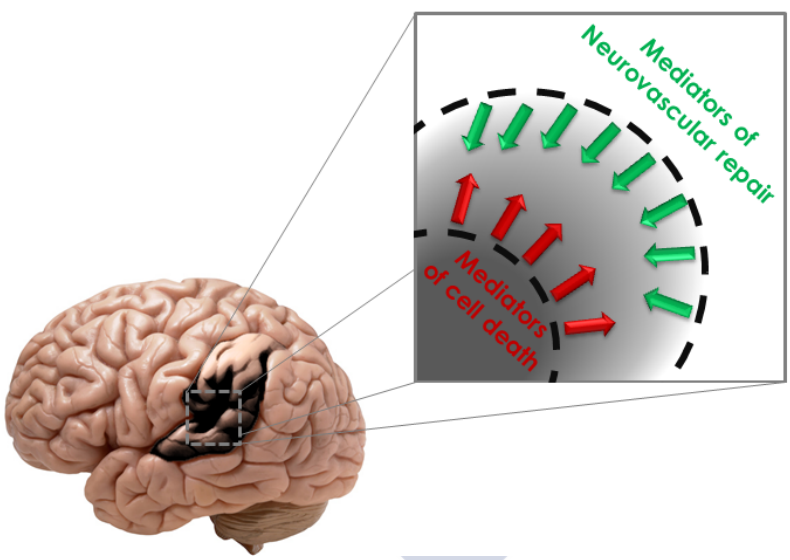


Figure 3: Peri-infarct region defined as the battlefield between mediators of damage, from the infarct core, and mediators of healing and repair from normal tissue. (Adapted from [31])

## 1.1.4. Therapeutic approaches for the treatment of stroke

### 1.1.4.1. Thrombolysis and neuro-interventionism

Pharmacological or mechanical (thrombectomy) thrombolysis are the strategies that report higher benefits for the patient, in terms of neurological outcome. The most common thrombolytic agent is the recombinant tissue plasminogen activator or rt-PA. Both therapies have pushed for the creation of stroke units inside hospitals, which have improved the management of stroke patients. Nevertheless only 3-7% of stroke patients are currently treated by these procedures. Such reduced numbers may be due to different factors, including the narrow therapeutic window and the high risks of hemorrhage transformation. Current neuroprotective strategies are required to work at both stages, by widening the therapeutic window and by reducing the associated risk factors.[32-36] The therapeutic window associated with intravenous thrombolytic treatment is 4.5 hours. The extension of this window may be possible by selecting candidate patients with a large *penumbral area* (the area of the brain susceptible to damage unless otherwise protected within the first 24-48 hours).[37]

In addition, reperfusion is associated with a higher rate of hemorrhagic events and the maintenance of the blood-brain barrier integrity (i.e. with metalloproteinase inhibitors), fluid homeostasis (by regulating aquaporin and inhibiting endothellin) and disabling free radicals after a reperfusion treatment, makes neuroprotective strategies during the acute phase of a stroke difficult to be viable.[38] An early treatment with anti-excitatory drugs or induction of hypothermia could also help to maintain the penumbra for

extended periods of time, hence extending the therapeutic window for reperfusion.[39]

1.1.4.2. Neuroprotection

Neuroprotection is a term that conglomerates a variety of strategies focused in reducing cell death after an ischemic event, without affecting tissue reperfusion. So far, a plethora of compounds have been proposed to block the pathway leading to ischemia-induced cell death at different steps. Most of these compounds have shown positive effects in experimental studies, although none of them have shown a clear beneficial effect in clinical studies.[40,41] Neuroprotective drugs can be classified into different groups, regarding their action mechanism.

a. Calcium blockers

Calcium plays an important role in stroke pathophysiology. The blockage of calcium channels stops neuronal calcium intake, hence reducing cell death. Nimodipine is an example of this family of compounds. With more than 200 published experimental studies, only half of them proved the efficacy of the drug. None of the members of this family of compounds have demonstrated a clear neuroprotective activity on clinical studies.[42,43] Among the reasons for this fact, overall the studies that generated positive results, animals were mostly treated within the first 15 minutes post-ischemia, which is not translatable to the clinical settings.

b. Glutamate antagonists

Glutamate is the main excitatory amino acid in the central nervous system. After an ischemic event, an excitotoxic response is generated leading to cell death. Glutamate activates NMDA and AMPA receptors. NMDA receptors

mediate cellular calcium and sodium intake. Several non-competitive blocking drugs against NMDA receptors have been synthesized, such as MK-801 (dizocilpine), which was used as a neuroprotective compound and rendered positive results in animal models of stroke. Nevertheless, the subsequent clinical trial had to be stopped due to adverse effects.[44]

NMDA competitive antagonist drugs have been also synthesized and used in animal models of stroke, like CGS 19755 (Selfotel) and GV15526 (Gavestinel). Although both compounds produced encouraging results in experimental studies, but they showed no effect in clinical trials.[45,46]

Natural NMDA antagonists, such as magnesium, have also been used as neuroprotective compounds. Magnesium sulphate has showed a brain infarct reduction up to 60% in animal models, treated even 6 hours after ischemia onset. Once again, these results showed no effect in clinical trials.[47]

As for NMDA, AMPA receptors have also been targeted for neuroprotective strategies. AMPA antagonists like ZK200755 have shown moderate neuroprotective effects in animal models. Results of its clinical trials have never been published.[38,42,48]

c. Plasmatic glutamate grabbers

Under normal physiologic conditions, glutamate present at the synaptic junction is captured by neurons and astrocytes through specific excitatory amino-acid transporters (EAATs). Nonetheless, under ischemic conditions these transporters do not function properly, and the massive release of this molecule lead to an accumulation of glutamate in the extracellular space.

EAATs are also present at the luminal side of endothelial cells in brain capillaries, and facilitate the passing of glutamate from the brain to blood. In this sense, it has been recently published that the increase of glutamate gradients between brain and blood facilitates the dumping of glutamate from the extracellular space to circulating blood, offering in this way an alternative strategy to protect brain cells during ischemia. Those strategies are based on metabolizing plasmatic glutamate by the action of the resident enzyme glutamate-oxaloacetate transaminase (GOT). This neuroprotective strategy has been successfully tested in animal models by our research group, leading to a significant reduction on brain infarct volume in animal models of stroke. In parallel, an association between elevated levels of GOT on blood and good outcome after stroke has been found in two clinical retrospective studies, pointing to the potential translationality of this neuroprotective strategy to the clinical setting.[49-52]

d. Antioxidants

Oxidative stress is another mechanism implicated on cell death after an ischemic event. Antioxidants could therefore play a role as neuroprotective drugs. The most successful antioxidant tested has been NXY-059. This drug reduced brain infarct by 66% in animal models, when injected 5 hours after occlusion. The first clinical trial generated positive results, improving patient's functional outcome. However a second clinical trial showed negative results. [53-55]

e. Phospholipid precursors: citicoline

Citicoline or CDP-choline is a precursor on the synthesis of phosphate-choline, which is integrated in the membrane of neurons. It has been shown that citicoline inhibits

norepinephrine and dopamine levels on the CNS, and restores mitochondrial ATPase activity.[56]

On animal models citicoline lowered phospholipase 2 activation after brain ischemia, reducing arachidonic acid formation and hence the production of free radicals; therefore inhibiting oxidative stress. Another effects claimed for this drug are its capacity to reduce excitotoxicity and the stimulation of brain plasticity.[57]

In preclinical studies, the treatment with citicoline immediately after reperfusion led to an improvement on functional deficits after a period of 28 days. A pool-data analysis published in 2002 showed a 33% increment in complete recovery after mild or severe stroke (NIHSS ≥ 8) when the treatment was started within the first 24 hours and maintained for 6 weeks.[40,58-60]

f. Nitric oxide pathway transduction regulators

One example of this kind of drugs is Lubezol, a compound capable of deregulate the glutamate-induced nitric oxide synthase pathway. This compound has shown hippocampal neuroprotection from nitric oxide toxicity. In experimental studies it has shown a 50 % infarct volume reduction upon injecting the drug 3 hours after ischemia induction. Nevertheless no clinical trial rendered positive results, and one of them was cancelled due to the mortality increase experimented in the treated group.[44] Several studies have been performed using other neuroprotective agents such as leukocyte inhibitors (Enlimomab), neuronal potassium channel activators (BMS-204352), membrane fluidity modifiers (Piracetam), opioid antagonists (Namefene), growth factors employed as intracellular calcium regulators (FGF), and much more. None of them

have shown the definitive efficacy of pharmacological neuroprotection.[44]

#### 1.1.4.3. Neurorepair

Neurorepair strategies involve the restoration of brain function, either by regeneration of damaged cerebral tissue (neurogereneration) or by the establishment of alternative neural pathways or synapses (brain plasticity). However, therapeutic window for those therapies is wider than for thrombolytic or neuroprotective approaches. The aim of the treatments for neurological function recovery after stroke is not restricted to neurons; it is more focused on the neurovascular unit, including procedures that enhance synaptogenesis and angiogenesis. Thus, neurorepair treatments may use stem cells, pro-neurogenic, pro-angiogenic and/or pro-synaptogenic drug delivery.

a. Neurogenesis after brain ischemia

In the adult brain there are niches for the production of neural stem cells,[61] localized in the subventricular region of the lateral ventricles (SVZ) and the dentate gyrus of the hippocampus (Figure 4). Under normal physiological conditions, the neuroblasts produced in the SVZ migrate to the olfactory bulb to differentiate in new neurons. After the induction of focal brain ischemia in the rat, an increase in neuroblast formation occurs in the ipsilateral hemisphere, and these neuroblasts migrate to regions surrounding the lesion.[62] This effect has been also shown in humans.[63] The enhancement of endogenous neurorepair mechanisms is one of the main goals on new therapies for the treatment of stroke.

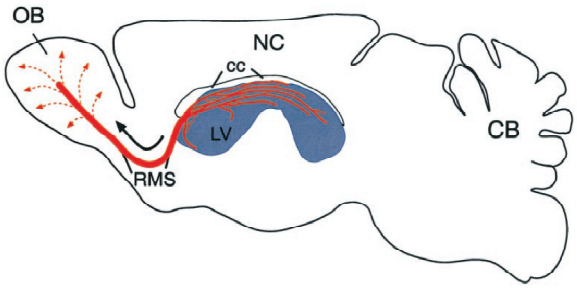


Figure 4: The SVZ–OB system (OB, olfactory bulb). Schematic sagital view of the adult rodent brain with the OB to the left and the cerebellum (CB) to the right. The SVZ is along the lateral wall of the lateral ventricle (LV, blue). New neurons are constantly produced throughout the SVZ. The young neurons become aligned into long chains (red lines) that form a complex network of interconnected paths throughout the SVZ. Many of these chains in the anterior SVZ connect with the RMS, which leads young neurons into the core of the olfactory bulb. Within the olfactory bulb, cells disperse radially (dotted lines) as individual cells and complete their differentiation into granule and periglomerular interneurons. NC, Neocortex; cc, corpus callosum. (Taken from[61])

Even though newborn cells are recruited after an ischemic insult, most of them do not get integrated into neuronal circuits. Several strategies have been used to enhance endogenous neurogenesis. Thus, a great number of newly differentiated neurons would be available, increasing the chance of survival and integration in neuronal networks, therefore improving functional recovery. Both cellular and pharmacological therapies have been used to achieve this goal by activating the phosphatidylinositol-3-kinase (PI3-Akt) pathway. This pathway is involved in cell survival, proliferation, differentiation and migration.[64]

b. Angiogenesis after brain ischemia

The development of the cerebral vascular system occurs mainly due to angiogenic processes. During adult life, endothelial cell proliferation ceases under normal physiological conditions. However, after an ischemic event brain capillaries surrounding the lesion proliferate, and new

vessels are formed between 2 and 28 days after the onset of stroke. [65-68]

The angiogenic process involves a multi-step procedure that comprises endothelial cell proliferation and migration, tubule formation, branching and anastomosis. Vascular Endothelial Growth Factor (VEGF) and its receptor (VEGFR2) initiate the angiogenic process, being angiopoietin 1 and 2 and their receptor (TIE-2) responsible for the maturation, stabilization and vascular remodeling [69]. VEGF and VEGF2 expression promotes vascular ramification, and the newly formed vessels are highly permeable. Meanwhile angiopoietins and TIE2 expression stimulate vessel maturation leading to the formation of fully functional brain blood vessels. VEGF treatment or therapies focused in producing VEGF, VEGF2, angiopoietin or TIE2 expression could increase the angiogenesis in the peri-infarct region.

The angiogenic process is essential for brain recovery after cerebral ischemia. In experimental studies both cellular and pharmacological therapies have been used to increase angiogenesis, promoting the functional recovery of ischemic animals.[70]

c. Neurogenesis & angiogenesis

Neurogenesis and angiogenesis after cerebral ischemia are not separated processes. Neurogenesis in the peri-infarct region cannot occur without angiogenesis, since the ultimate is responsible for restoring the oxygen and nutrient supply. Furthermore, endothelial cells produce growth factors that allow the neurons to survive, and that regulate metabolic activity of neural precursors. Endothelial cells secrete Stromal Cell-Derived Factor-1 (SDF-1), VEGF and Matrix Metalloproteinases (MMPs) that induce and facilitate neural progenitor cell migration to the injured site. On the

other hand, neural progenitor cells overexpress angiopoietin 2 and VEGFR2 leading to an increase in angiogenesis.[71]

Several in vitro and in vivo studies have shown the relationship between angiogenesis and neurogenesis. [71,72]. In animal models of ischemia, Tie2 inhibitors not only reduce angiogenesis, but also neuroblast migration to the peri-infarct area. On the other hand, neural progenitor cell grafted in the infarct region have demonstrated the induction of angiogenesis. These and other studies have reported that neurogenesis and angiogenesis are highly connected, and both promote neural remodeling and improve neurologic function after brain ischemia.[73,74]

d. The role of oligodendrocytes, astrocytes and axons in neurorepair

In the brain parenchyma there are not only neurons, but other cellular components as well (Figure 5). Oligodendrocytes, astrocytes and the development of functional axons are also involved on neurorepair. After an ischemic event, astrocytes proliferate forming a glial scar that surrounds the lesion and release proteoglycans that inhibit axonal growth. Hence there should be mechanisms for reducing glial scar formation, and also to stimulate axonal growth, leading to an efficient neurorepair.[75]

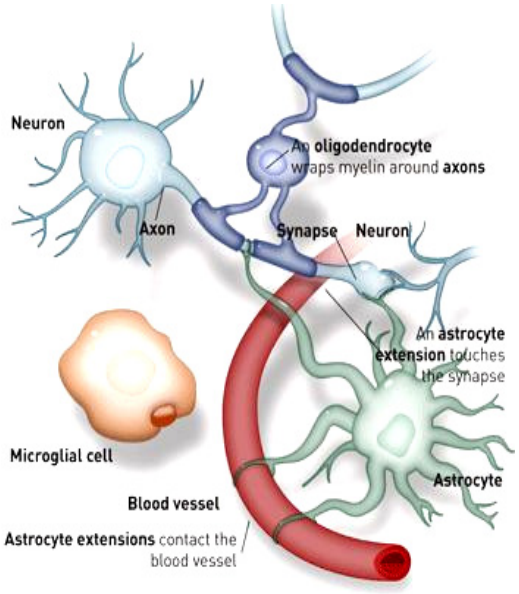


Figure 5: Cell structure of brain parenchyma (Adapted from [76])

## 1.2. Stem cell therapy

Research on stem cell therapies has been increasing from the last 40 years. This kind of therapies are specially attractive because stem cells interact directly to brain parenchyma cells whereas classical or pharmacological treatments depend on their pharmacokinetic profiles.[62] In this way, stem cells have emerged with a double role, not only as the key for revealing the insights of the neuroscience as well as new promising therapies for stroke, due to their self-renewal and multipotentiality properties.[77] However, the mechanisms mediating

ischemic stroke recovery using stem cells are still poorly understood.[78]

One of the potential mechanisms of stem cell therapy is cell replacement. Early studies have reported that after stem cell transplantation the number of grafted cells differentiated into mature neurons formed can vary. The origin of this variation lies in the source of the stem cell and also in the injection site. In this way, in recent preclinical studies, 34-60% of the injected cells were Neural Stem Cells (NSCs),[79] 30% Embryonic Stem Cells (ESCs)[80] or 2-20% for Mesenchymal Stem Cells (MSCs).[81,82] But sometimes, grafted cells remain undifferentiated close to the injury site, releasing growth and trophic factors [83,84] or even without entering the Cerebral Nervous System (CNS) inducing also benefits after stroke.[85] Regardless of this effect, this systemic cell administration can provoke that administered cells stay also in other organs, like spleen or liver, interacting with other cells from the immune system and leading into modulatory functions,[86] reducing at the same time, the post-ischemic inflammatory damage in stroke. [87-89] Nevertheless, apart from cell replacement, enhanced trophic support and immunomodulatory response, there are endogenous brain repair processes that stem cell can stimulate, such as angiogenesis, neurogenesis, synaptogenesis and white matter remodeling [62,90-93] inducing neurorestorative effects after ischemia.

In contrast to other pathologies, in stroke there is affected more than one brain cell population, involving also vascular cells in the ischemic region. This heterogeneity means that not only functional neuronal connections have to be reestablished; the vascular system has to be restored as well. In consequence, there is not an unique type of stem cells for stroke therapy, many of them have been tested

demonstrating beneficial effects: Embryonic Stem Cells (ESCs),[94-96] Neural Stem Cells (NSCs),[91,97,98] Induced Pluripotent Stem Cells (iPSCs),[99,100] Human Umbilical Cord Blood Cells (HUCBCs)[101,102] and Mesenchymal Stem Cells (MSCs). [82,103,104] Recent studies with iPSCs have shown powerful new opportunities for modeling human diseases offering hope for personalized regenerative cell therapies. However, the field is racing ahead, and some researchers are pausing to evaluate whether induced pluripotent stem cells are indeed the true equivalents of embryonic stem cells and whether subtle differences between these cells might affect their research applications and therapeutic potential.[105,106]

But, there are several parameters to take into account to elucidate the effective time point for stem cell therapy in preclinical or even clinical studies. An important factor to be considered is the use of autologous versus allogenic stem cells. The term autologous is referred to those from the same individual who is going to receive the treatment whereas allogenic cells are related to a donor. In spite of this, the less lineage specific the cells are, the less chances to have an immune response,[107] in fact, for example MSCs which can be harvested from a variety of mesenchymal tissues have different immune response depending on their origin.[108] Additionally to the immune response, several cases of tumorigenicity have been reported after stem cells therapies from different stem cell types. [109,110]

Very few preclinical studies have compared different routes of administration, and the choice among them depends on the organ target. First studies for cerebrovascular diseases explored the intraparechymal route with the main goal of determine the feasibility of replacing lost neurons and

rebuilding neural circuits,[111] meanwhile later studies showed that stem cells were not only able to survive after injection, as well as proliferate, differentiate and even migrate to the site of the injury.[112,113] However, intraparenchymal cell delivery normally is not the first choice because the injection is focused in one region and to reach that point it is necessary to damage brain tissue. On the other hand, vascular routes, intravenous (i.v.) and intra-arterial (i.a.), solve these pitfalls and they are becoming the most common cell delivery method. Tail vein, femoral and jugular veins are the most common ones for stem cell administration. Several groups have demonstrated that i.v. administration can reduce infarct size or induce functional recovery [82,101] when administrated 24h after stroke. Later studies also studied the biodistribution after i.v. injection and found out that depend on the cell type, between 1-5% of the injected cells reached arterial circulation.[114] One of the most interesting i.v. applications was for NSCs delivery. It's known that this kind of stem cells has the ability to differentiate into neurons, astrocytes and oligodendrocytes. At the early beginning of stem cell therapies their repairing mechanisms were assumed to be related to rebuild the neural structure, but in recent years it has been observed that the injured brain environment is not optimal for cell integration, so the recovery works through growth factor mediation or anti-immflamatory processes. [115] Nevertheless, it seems that if the brain is the target, it would be desirable to reach it with the most of the injected cells, and to achieve it the best delivery route is the i.a. administration. The first study showed that 21% of the injected Bone Marrow Stem Cells (BMSCs) were observed in the affected hemisphere, and this was also related with functional recovery in behavioral tests but not as an infarct volume reduction in the treated group. However,

administration route efficiency is also conditioned by the safety of the procedure and attending to this, i.a. administration has shown higher mortality than i.v. delivery. In a recent study, 41% of the animals died after an i.a. injection compared to 8% for i.v. delivery.[116] That's why this delivery route has been more explored recently and many studies have developed different injection strategies to minimize the risks.[117-120]

All these promising preclinical results progressed into early clinical trials of stem cell therapy in stroke. The effectiveness of different types of stem cells and delivery routes is also reflected in clinical studies which are exploring different combinations. So far, there is four published clinical trials of intracerebral cell therapy for stroke and one that is still ongoing,[121-123] one of intravenously administration [115,124-126] and three following intra-arterial delivery. [127-129] The main goals of these clinical trials were to demonstrate the safety and feasibility of stem cell therapy using different types of stem cells and routes of administration. Published results have reported that there were not enough patients enrolled in these studies to show benefits in terms of functional recovery after the treatment, but all of them demonstrated that stem cells are a promising, feasible and safe therapy for stroke.

However, the optimal conditions for applying stem cell therapies are still under discussion, fundamental questions related to cell type, characterization and dosage, therapeutic timing versus toxicity, or the relationship between biodistribution, fate and outcome are still on the bench, and preclinical studies should answer it first.

## 1.2.1.Mesenchymal Stem Cells

The term mesenchyme is related to embryonic connective tissue, derived from mesoderm, that can be differentiated into hematopoietic and connective tissue. Mesenchymal Stem Cells (MSCs) can be derived from almost all tissues in the body (Figure 6): bone marrow, placenta, muscle, skin, adipose tissue, umbilical cord, etc.[130]

The bone marrow derived cells (BM-MSCs) is the most studied type of MSCs. [131] They express a number of markers, none of which unfortunately are specific to MSCs, being $CD73^{+}$, $CD90^{+}$, $CD105^{+}$, $CD11b^{-}$, $CD14^{-}$, $CD19^{-}$, $CD79a^{-}$, $CD34^{-}$, $CD45^{-}$ and HLA-DR. It is generally agreed that rat MSCs do not express hematopoietic markers, as CD45, however cultured MSCs are uniformly and strongly positive for CD105, CD90 and CD73, regardless their passage or time in culture. MSCs can be differentiated into several cell types *in vitro* and can be expanded *in vitro*. These two properties make the mesenchymal stem cells attractive as a powerful source for tissue repair.[132,133] Moreover, MSCs have the potential to differentiate into adypocites, chondroblasts and osteoblasts[134] and their ability to be differentiated into myocytes, neuronal and glial cells has been already reported.[135-137]

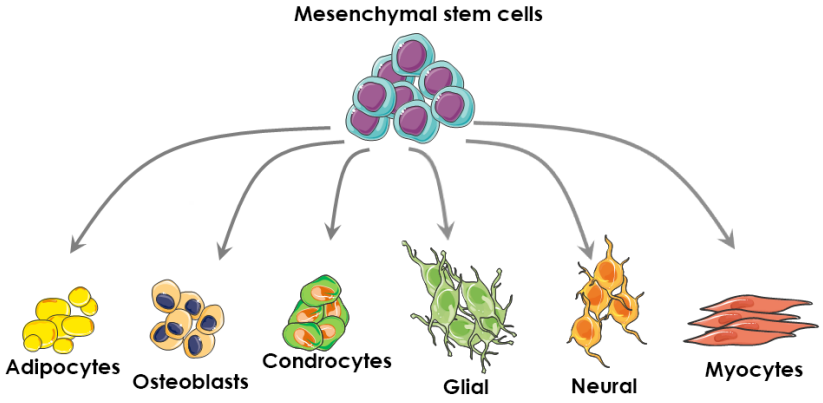


Figure 6: MSCs differentiation into different cell types.

MSCs are one of the best candidates for regenerative therapies, also in stroke, not only due to their multipotientiality, but mainly because their ability of releasing growth factors and their immunomodulatory abilities.[131] Several mechanisms of action of these cells in the ischemic brain have been described, mechanisms like transdifferentiation into cells of neural lineage[138-141] induction of neurogenesis,[142-144] angiogenesis,[142-144] synaptogenesis,[145] activation of endogenous restorative processes by producing cytokines and trophic factors,[142,146-148] regulating the Cerebral Blood Flow (CBF) and the Blood Brain Barrier (BBB),[146] and other neuroprotective mechanisms like the reduction of apoptosis, immflamation, demyelination and the increase of astrocyte survival.[101,142,143,149] Many preclinical studies reported functional recovery and infarct volume reduction after ischemic stroke, [131] which facilitates the leap into clinical trials.

### 1.2.2. Strengthen of endogenous stem cells and stroke recovery

Several studies in rodents and also in humans have reported that after a stroke event there is an endogenous stem cells migration towards the site of damage to contribute to the functional recovery.[150,151] These neural stem cells and their progeny activation and migration occur till the cells are integrated forming new functional neurons.[152,153] However, this endogenous contribution is not enough to overcome the consequences after stroke.

Several groups have demonstrated that direct administration of growth factors can enhance these endogenous processes like migration of NPCs, neurogenesis and angiogenesis. Factors such as vascular Endothelial Growth Factor (VEGF),[154-156] Epidermal Growth Factor (EGF),[157] Fibroblast Growth Factor (FGF) and Erythropoietin (EPO)[158] have been proved in stroke models with functional benefits. Moreover, the stimulation of the NPCs without affecting other cell types is being investigated. There are some approaches for this purpose by focalizing different treatments as poly(ethylene glycol) nano/microparticles carrying biomolecules[159] direct brain injection of functionalized hydrogel[158] or intraventricular infusion of biomolecules.[160]

Nevertheless, there is another way of growth factors delivery: stem cells. If the matter is target the proximity of the injury, as it has been specified at the beginning of this section, intra-arterial route of administration is the most efficient in terms of cell engraftment. But this binding can be also enhanced either by selecting a specific population of cells that endogenously express adhesion molecule or by modifying them to induce their expression.[161] However, it

is still necessary to demonstrate if those cells which have been bound to the endothelium, are able to migrate and target stroke lesions.

## 1.3. Animal models of ischemic stroke

Stroke is a focal neurologic deficit caused by an alteration in the cerebral blood circulation. Animal models for cerebral ischemia have been used for over 150 years trying to mimic the human pathology,[162] improving our understanding of the physiopathology of this disease. Numerous preclinical studies, mostly with neuroprotective drugs, have shown promising results for the treatment of stroke, however not all positive experimental outcomes were transferred to patients, in terms of a phase III clinical study so far.[163,164] However, the success of stroke studies in animals depends on the choice of the experimental model species. An inadequate selection of the specie and/or the experimental model may lead to limitations that compromise results and analysis.[165,166]

Numerous animal species have been used to study stroke, although the most common are rodents, due to the ease for inducing the cerebral ischemia, ease to monitor physiologic conditions and the reduced costs to obtain and maintain the animals for long periods of time.[163,166] We may not forget that in animal models of cerebral ischemia, most of variables are controlled in laboratory experiments and these conditions are quite different compared to a human going through a ischemic stroke process.[165]

Among rodents, the arterial and nerve supply of the rat is essentially similar to that of humans,[167] so rat is an appropriate animal for preclinical studies of brain ischemia. Firstly, and for a better understanding of cerebral ischemic models, it is necessary to have an anatomic knowledge about cerebral circulation in the rat. Basically, the head blood circulation depends on two systems: the carotid and the vertebrobasilar systems.[168]

- Carotid system. Right and left common carotid arteries (CCA) supply the head and the neck. Left arises from the arch of the aorta and right common artery is a continuation of the innominate artery. Each common carotid yields two branches, the external and internal carotid, both follow the same general direction to the head. External carotid (ECA) leads to occipital, superior thyroid, ascending pharyngeal, lingual and ascending palatine, meanwhile internal carotid artery (ICA) continues to reach the base of the skull. On its way to the brain, it branches into pterygopalatine (PPA) artery, which corresponds to a portion of the internal maxillary branch of the external carotid artery in humans. The cerebral portion of the internal carotid artery branches into the posterior communicating artery (PCoA), hypothalamic artery, anterior choroid artery, middle cerebral artery (MCA) and anterior cerebral artery (ACA). The main branch of posterior communicating artery is the posterior cerebral artery (PCA), which supplies the surface of the brain hemisphere, including the medial and lateral surfaces of the occipital lobe.

- Vertebrobasilar system: vertebral arteries arise from the anterior surface of the subclavian artery. When

entering the skull, both vertebral arteries join to form the basilar artery (BA). This artery is anastomosed to posterior communicating arteries from the carotid system.

Arteries from carotid and vertebrobasilar systems form a circle of communicating arteries, which protects the brain when the blood flow circulation is interrupted. This arterial circle, present in humans and also in rats, is called circle of Willis. The circle of Willis in rats is a buttonhole-like structure, formed by the anterior cerebral and posterior communicating arteries. Normally, another extra artery, the anterior communicating artery (ACA), bridges anterior cerebral arteries from both hemispheres closing the circle, however is quite common that the circle is not complete. Probably one of the most interesting things about the circle of Willis is that the blood flow circulation is overlapped, i.e., if one of the main arteries is occluded, the distal smaller arteries that it supplies can receive blood from other arteries, which is called collateral circulation.[167,169] (Figure 7)

Depending on the region affected by the diminution of cerebral blood flow (CBF), cerebral ischemic experimental models can be classified in global, focal or multifocal ischemia,[166] and attending to the duration of the ischemic insult, ischemia can be classified in transitory, if the artery occlusion is followed by reperfusion, or permanent ischemia, without artery reperfusion.[163] In this work we will focus on the focal cerebral ischemic model, which normally results in an ischemia in the cortex and striatum from occlusion or the middle cerebral artery, and it mimics the most common site of human stroke. In animal models of focal cerebral ischemia, the degree and distribution of CBF, and therefore infarction, depend on the duration and the

localization of the occlusion, as well on the collateral circulation.[170]

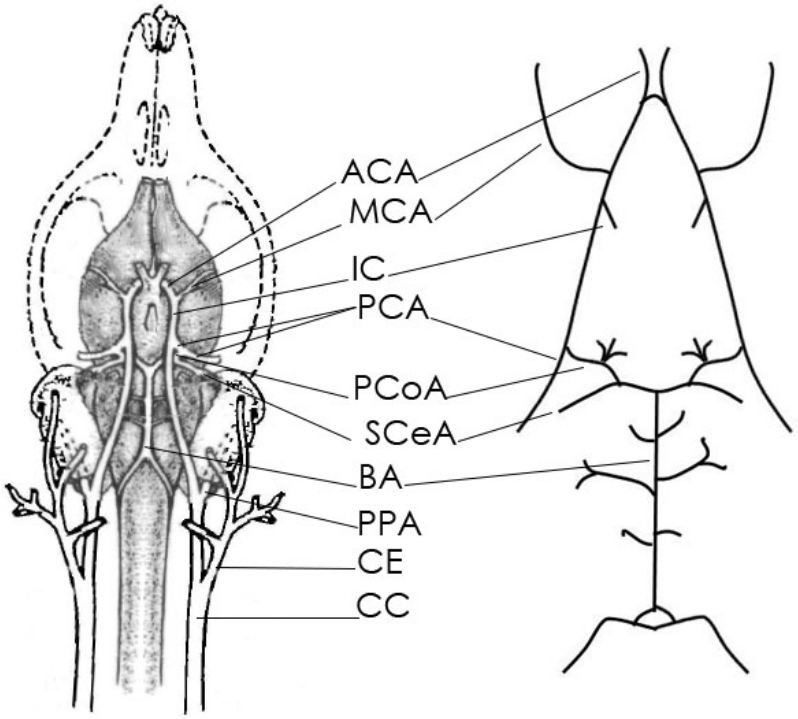


Figure 7: Diagrams of cerebrovascular anatomy in rats adapted from Longa et.al.[171]

A wide variety of animal models of focal cerebral ischemia have been investigated, and most of them involve craniotomy. A non-invasive method to produce permanent or transient middle cerebral artery occlusion (MCAO) is the intraluminal filament model, described in the late 1980s[171]. It is a widely used technique to study mechanisms of cellular injury and neuroprotection. Typically, the occlusion is performed by inserting a 4-0 nylon suture into the ICA of rats, advancing the thread cranially to block the MCA. In this work, from Longa et. al.,[171]

additional extracranial vessels such as vertebral arteries, contralateral ICA and ipsilateral ECA, were occluded to reduce collateral blood flow to the MCA territory, however those occlusions are not indispensable for intraluminal filament animal model.

Animal models of cerebral ischemia are designed to generate reproducible infarcts in a high throughput manner with a minimum of surgical manipulation, however therapeutic approaches have to be also optimized for each disease. Thus, optimal conditions for applying stem cell therapies for cerebral ischemia are still under discussion, fundamental questions related to cell type, characterization and dosage, administration route, therapeutic timing versus toxicity, or the relationship between biodistribution, fate and outcome are still on the bench.[172]

### 1.3.1. The blood brain barrier

Brain blood supply is governed by the carotid system, vertebrobasilar system and in the last term, by the arterial anastomosis of the circle of Willis.[173] Within them, cerebral microcirculation is constituted by three entities, endothelial cells, pericytes and astrocyte end-feet, which all together form the Blood Brain Barrier (BBB). BBB is a diffusion barrier, which selective excludes the influx of most compounds from blood to most parts of the brain.[174] Endothelial cells from BBB, which have been demonstrated by transmission electronic microscopic studies being the principal anatomic structure of the entity[169], differ from endothelial cells of the rest of the body by the absence of fenestrations, sparse pinocytic vesicular transport and more extensive tight junctions, which block the diffusion through the vascular wall. All systemic endothelial cells are

interconnected by tight junctions that normally have a low resistance (about 5-10 $\Omega/cm^2$), however in the BBB this resistance is a lot higher (2000 $\Omega/cm^2$) impeding the transference of small molecules as potassium ions.[169] Hydrophilic molecules flow across the BBB is limited but in contrast, small lipophilic substances such as $O_2$ or $CO_2$ diffuse freely depending on their gradient concentration.[174] Most of substances that must cross the BBB are not lipophilic and enter the brain via transporters. But apart from molecules, some cells can also cross the BBB. Under normal physiological conditions, lymphocytes entry into the central nervous system (CNS) across the BBB is kept at a low level. However, during inflammatory diseases, the circulating immunocompetent cells readily get access to the CNS.[175] In ischemic stroke, the effect of hypoxia-ischemia on the BBB has been extensively investigated. Hypoxia-ischemia sets in motion a series of events, which leads to disruption of the tight junctions and increased BBB permeability.[174] Several preclinical studies have elucidated that while experimental permanent occlusion of a cerebral artery is associated with a monophasic leakage of BBB, biphasic pattern of BBB leakage is believed to occur in a ischemia-reperfusion scenario.[176,177] This leakage must be considered not only as a source of disease complications like for example brain edema in ischemic stroke,[176] as well for treatment approaches, including stem cell therapies.

### 1.3.2. Mesenchymal Stem Cell therapy in animal models of ischemic stroke

Mesenchymal stem cells are an attractive therapeutic agent due to their ease of isolation, established safety and also because of their potential to target multiple pathways

involved in neuronal regeneration. A large number of preclinical and clinical trials have used systemic infusion of these cells, however it is still necessary to understand if transplanted MSCs can home to and engraft at ischemic and injured sites in the brain to exert their therapeutic effects. Several studies have described that MSCs can follow a leukocyte-like, multistep homing cascade (rolling, adhesion and transmigration) to connect with endothelial cells (ECs), however all *in vivo* and *in vitro* models have found several limitations.[178] Moreover, the *in vivo* mixed results of MSCs therapy efficacy is attributed to an incomplete understanding of MSCs biology and their fate following transplantation *in vivo*.

Functional improvement in animal models of focal cerebral ischemia when mesenchymal stem cells were transplanted either intravenously or intra-arterial has been demonstrated [179-182] however, there is not a preferred route of administration. Brain intraparenquimal and intraventricular administration routes are invasive, and it would be necessary several injection sites to cover the ischemic region. On the other hand, several groups have tracked labeled cells from different tissues and species donors administered i.v., evidencing the high rate of cell entrapment in peripheral organs and that reduced number of cells reached the brain.[114] Tail, jugular or femoral intravenous administrations are less invasive but most of cells remain trapped in lungs, liver and spleen.[183] Nevertheless, i.a. administration route would be the best candidate to direct most of the injected cells to the brain, especially on the region of the ischemic injury.[184] However, the fate of the injected cells following this route remains unknown due to the variable reported results found in literature. Thus, some studies have shown that approximately 21% of the delivered cells after an intra-

arterial injection were observed in the ipsilateral hemisphere,[103] however recent studies reported that 24h after injection 95% of the delivered cells were found in the spleen.[118] At this point, it is important to take into account that animal models of focal brain ischemia and the intra-arterial injection procedure are not the same for all these studies, which could explain differences on the cell distribution pattern after delivery. Apart from the cell distribution, most of them have agreed the main inconvenience for intra-arterial cell delivery in cerebral ischemia is the high animal mortality compared to other routes of administration.[183]

## 1.4. Non invasive imaging

There are many imaging modalities used in clinical and preclinical practice and the choice among them is based on multiple aspects including the nature of the specific diagnostic question, availability and cost-effectiveness. For one specific disease, parameters such as specificity, sensitivity, spatial resolution and radiation exposure will make more suitable one technique among others. However, for stem cell therapy the goal is double, not only is crucial to determine where the cells are, but to evaluate the pathological progress of the target organ as well.

For the recent development of cell-based therapies, imaging plays an important role on the follow-up of cell fate after administration and also on the response of the host to the treatment.

In the field of cell imaging, several techniques for non-invasive cell imaging in vivo have been developed, including Bioluminescence, Intravital Multiphoton Microscopy, Positron Emission Tomography (PET) and Magnetic Resonance Imaging (MRI) and all these imaging modalities are widely used in preclinical studies in stroke.

X-ray computed tomography (CT) and MRI are used for imaging the density and the intensity respectively, of the cerebral parenchyma and its anatomic structure in clinical procedures. The role of these imaging techniques is to identify the presence or absence or hemorrhage, detect ischemic tissue and differentiate the ischemic lesion from other diseases. However, MRI is considered the gold standard not only for the diagnosis in the acute phase of the stroke; as well to evaluate the progression of the pathology.[185]

### 1.4.1. Magnetic resonance imaging (MRI)

Nowadays, MRI is one of the most powerful medical diagnostic tools available due to its high resolution, but also because of the non-invasive and no ionizing radiation nature of the technique (Figure 8).

Each pixel of a MR image is the measurement of the nucleus spin magnetization, generated by the irradiation of the tissue at that position of space with a radiofrequency pulse (RF) in presence of an external magnetic field ($B_0$). In magnetic resonance imaging we do not measure to what extent nuclei (usually protons, represented by $^1H$) can be excited, but how they relax after excitation to return to a state of equilibrium. This effect, called free induction decay, is detected through the MRI coils and transformed into an

electrical signal that can be detected and further processed to generate an image.

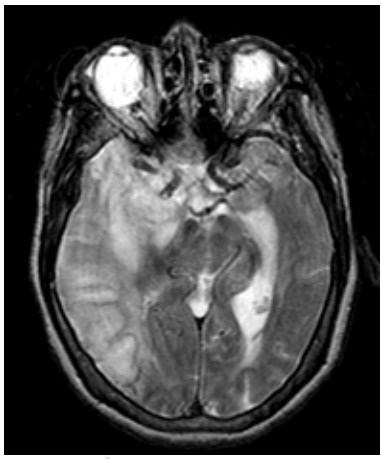

Figure 8: $T_2$ weighted magnetic resonance image.

There are two independent and simultaneous physical processes responsible for the relaxation of excited proton spins, but before, it would be necessary to define what spin magnetization vector is.

To describe MRI from a macroscopic point of view, we can suppose that we allocate a tissue into an external magnetic field ($B_0$) and that such tissue (Figure 9a.) can be divided in different parts, depending on how these parts are affected by the magnetic field (Figure 9b.), or in other words, in groups of spins that are experiencing the same magnetic field strength. Each of the delineated groups of spins can be represented by a global magnetization vector (Figure 9c.), which, at the same time contribute to form the net magnetization of the whole tissue (Figure 9d.).

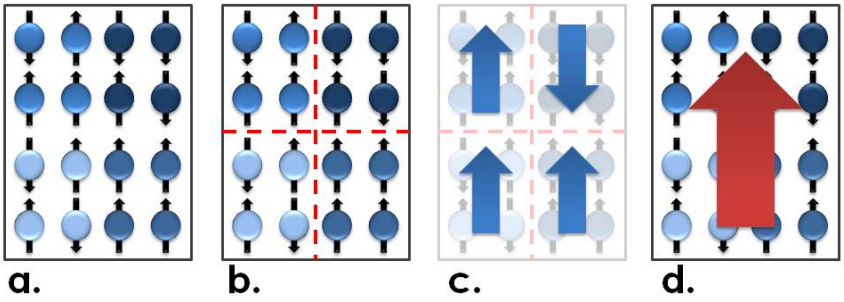


Figure 9: Description of spin magnetization vector.

Under $B_0$ condition, protons have an equilibrium longitudinal magnetization vector, parallel to this magnetic field (we consider $B_0$ and the net magnetization aligned along the Z axis). In this equilibrium, transversal components of the magnetization (perpendicular to $B_0$) are not detectable because nuclear spins are processing out-of-phase and their transversal components cancel each other. However, after an excitation of the spins by a RF excitation, the system is out of equilibrium in terms of longitudinal and transversal magnetization, and in this state, the transversal component of this vector can be detected. As we have already mentioned, there are two relaxation processes that bring the system back to equilibrium, each of them described by time constants, the Spin-Lattice relaxation or longitudinal relaxation ($T_1$) and the Spin-spin or transversal relaxation ($T_2$).

a. Spin-Lattice Relaxation $T_1$:
   This phenomenon is associated with the recovery of the thermodynamic equilibrium magnetization along $B_0$ and therefore with transitions between the Zeeman energy levels. To get back to equilibrium there is needed some energy dissipation into the surrounding tissue (lattice), and the emission is induced by fluctuations of the magnetic field, as a

result of the magnetic dipoles in the neighborhood variations (Brownian motion). As a consequence, $T_1$ is dependent on the strength of the static field and not only on the molecular mobility of the observed nucleus, on the surrounding dipoles as well. Mathematically, spin-lattice relaxation can be expressed as:

$$M_z = M_0 \left[1 - e^{\left(\frac{t}{T_1}\right)}\right]$$

C is a constant dependent on the flip angle of the RF pulse.

b. Spin-spin relaxation $T_2$ and effective spin-spin relaxation $T_2^*$:
Transversal magnetization is related to the loss of phase coherence in the nuclear precession after a RF excitation. If the net magnetization is placed in "xy" plane, it will rotate following one defined frequency called "Larmor frequency". But, apart from rotating, the net magnetization will start dephasing and each spin packages would have their own Larmor frequency. In this way, the time constant which describes the return to equilibrium of the transverse magnetization ($M_{xy}$) is called the spin-spin relaxation time ($T_2$).

$$M_{xy} = M_{0xy0}\left[e^{\left(\frac{t}{T_2}\right)}\right]$$

Two factors also contribute to this decay, molecular interactions (pure $T_2$ effect) and variations in $B_0$ (inhomogeneities). The combined time constant is called effective spin-spin relaxation and represented by $T_2^*$.

$$\frac{1}{T_2^*} = \frac{1}{T_2} + \frac{1}{T_{2\,inhom}}$$

Here, $T_1$ and $T_2$ have been described separately but both processes occur simultaneously. The full description of the magnetization vector behavior under different conditions is implemented in Bloch equations.

MR images are acquired using a pulse sequence (formed for radiofrequency pulses (RF) and gradient pulses). Depending on the pathologic condition or the composition of the tissue of interest, it will be necessary the use of one or another sequence to distinguish between what is called $T_1$ and $T_2$ weighted images, the two most common modalities of MRI in clinical practice. The differences between sequences rely on the choice of the acquisition parameters, mainly the repetition time (TR) and the echo time (TE), but also the contribution of the intrinsic tissue values of $T_1$ and $T_2$. However, sometimes for a more specific tissue detection or a change in an earlier stage of the disease, the combination of intrinsic relaxation times and sequence parameters is not enough for being visualized in MRI. It is needed an extra tool: MRI contrast agents.

### 1.4.2. Contrast agents for magnetic resonance imaging.

MRI contrast agents are mainly used for two purposes, enhance the natural contrast and /or obtain dynamic information about biological processes.

There are several options of MRI contrast agents, and parameters as pathology under study, target organ, therapeutic or diagnosis options, have to make the choice among them.

Particularly, for stem cell therapy, it would be ideal to monitor where and how these cell distribute. For different pathologies, also in ischemic stroke, the selected contrast agent to label stem cells has to achieve several goals:

- Specificity of the type of cell
- Ability to be detected at low concentrations
- Reasonable clearing period
- Stability
- Reduced toxicity

The most used contrast agent for cell tracking purposes verifying all previous conditions are magnetic nanoparticles (MNPs).

## 1.5. Superparamagnetic iron oxide nanoparticles

Cells are too small to be detectable using MRI, however the use of contrast agents to label them leads us to an *in vivo* real-time image of those cells. Superparamagnetic iron oxide nanoparticles are an excellent tool for stem cell tracking, not only for the high quality of the MR image, for the low toxicity and the ease for tagging as well.

The term nanoparticle is normally referred to particles with a size in the nano range, which corresponds to ca. 1-100nm. This reduced size gives them extraordinary properties compared to their counterparts, bulk materials. In this way, magnetic nanoparticles (MNPS) are nanoparticles made of ferro /ferrimagnetic materials, which exhibit superparamagnetic properties below certain dimensions

and above certain temperatures. To explain these properties several preliminary concepts will be introduced.

### 1.5.1. Magnetic materials

All materials are magnetic, but their response under an applied external magnetic field depends on their atomic structure and the temperature conditions. When a material is placed under a magnetic field of strength H, the individual atomic moments contribute to the overall magnetic response (B), which mathematically is expressed

$$B = \mu_0(H + M) \qquad \text{[Eq.1]}$$

Where $\mu_0$ is the permeability of free space, and *M* is the magnetization per unit of volume. It is possible to classify the materials according to their magnetic response under a magnetic field, or what is the same, to the volumetric magnetic susceptibility ($\chi$). Formally, this magnitude is defined as the induced magnetization in a material by a magnetic field H.

$$M = \chi \cdot H \qquad \text{[Eq.2]}$$

In this way, depending on the magnetic susceptibility it is possible to distinguish between:

a. Diamagnetism: it is a property common to all materials, but normally is very weak. In diamagnetic materials there are not unpaired electrons in their atoms and consequently, there is not net magnetic moment. When these types of materials are placed under a magnetic field, the magnetization produced is negative, so $\chi < 0$. As it is shown in Figure 10a, for zero field, the magnetization is also null.

b. Paramagnetism: The net magnetization of these materials is different from zero due to the unpaired electrons of their atoms. However, due to the non-magnetic interaction between the individual magnetic moments, the global process is randomized, and if the external field is removed, the magnetization is also zero. Under the influence of applied *H*, there is a partial alignment of the atomic magnetic moments in the direction of the field, resulting in a positive magnetization and as a consequence, the susceptibility becomes positive as well. (Figure 10b) Furthermore, this alignment is opposed to the randomizing effect of temperature, resulting in a correlation between temperature and magnetic susceptibility (Curie Law).

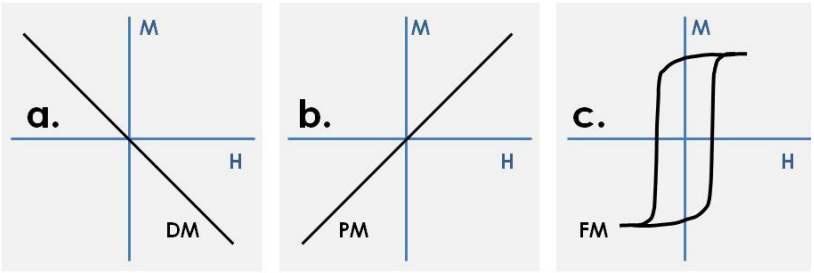


Figure 10: Magnetic responses for a diamagnetic material (a.), paramagnetic material (b.) and ferromagnetic material (c.)[186]

Hence, both diamagnetic and paramagnetic materials, exhibit the same behavior; no magnetization when the applied field is zero. Nevertheless, some other materials remain magnetic even without magnetic field presence. Those are ferromagnets, ferrimagnets and antiferromagnets.

a. Ferromagnets: these materials are characterized by the parallel alignment (Figure 11a.) of their atomic

moments, which results in a large net magnetization even when the external magnetic field is zero (Figure 10b). Two characterizing aspects of ferromagnetic materials are their spontaneous magnetization and the existence of a magnetic ordering temperature, called Curie temperature ($T_C$).

b. Ferrimagnets: In these materials the opposing atomic moments are unequal so that there is a remaining magnetization (see Figure 11c.). This phenomenon occurs when there are different ions in the material (such as $Fe^{2+}$ and $Fe^{3+}$). In this type of materials, the spontaneous magnetization is maintained below $T_C$ and they behave as paramagnetic materials above it.
c. Antiferromagnets: As in ferromagnetic materials, the atomic moments are opposed and equal, so the net moment is zero (see Figure 11b.). In this case, the critical temperature is $T_N$ (Néel temperature): above $T_N$ the magnetic susceptibility decreases with higher temperature and below it the susceptibility increases with temperature.

The behaviors previously described are also strongly dependent on the size of the material, so modifying the size it is possible to tune the magnetic response at a certain temperature.

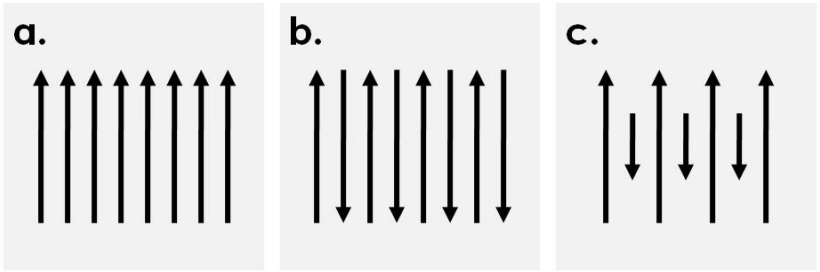


Figure 11: Alignment of magnetic dipoles for different types of magnetism. (a.) Ferromagnetism. (b.) Antiferromagnetism. (c.) Ferrimagnetism.

As presented before, a paramagnetic material is characterized by randomly oriented magnetic dipoles, which under an external magnetic field are aligned along the direction of the field. But when the field is switched off, all internal dipoles randomize again and no extra energy is needed to demagnetize the material, it goes back to equilibrium spontaneously, i.e. this type of material has no coercivity and no remanence.

However, ferromagnetic materials present the individual magnetic spins align parallel one to the other exhibiting a collective response even in the absence of the external applied magnetic field. In this absence of an applied magnetic field, a ferri or ferromagnetic material is divided into macroscopic magnetic domains. There is a specific direction of magnetization within each domain, but different from one domain to the other. When a magnetic field is applied to a multi-domain material, the domain walls move in response to the applied magnetic field, increasing the net magnetization of the crystal. As the applied field is increased, the magnetization increases until saturation is reached, when the crystal consists of a single magnetic domain with its magnetization aligned to the field (Figure 12). In this way, the saturation magnetization ($M_S$) is a

property of the material and can be related to the magnetic distribution and ordering. If the applied magnetic field is now reduced to zero, the magnetization will decrease to $M_R$, which is the remnant magnetization, and in order to reduce the magnetization to zero, a reverse field has to be applied. The value of this reverse field is called coercivity $H_c$. Increasing the reverse field saturates the sample in the reverse direction, and so on, giving a hysteresis loop, which describes the relationship between the applied field and the magnetization.[187]

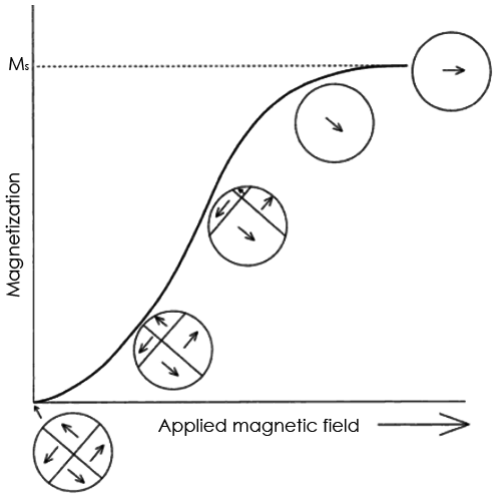


Figure 12: The behavior of the domain distribution in a multidomain grain during various stages of magnetization. $M_s$ is the saturation magnetization where the grain consists of a single domain magnetized in the direction of the applied magnetic field. (Adapted from [187])

The difference between a magnet and the material to which magnets are attracted is the size of the magnetic domains. Thus, the shape of the M-H curves is partially determined by the size of the material, in this case, the size of the particle. In large particles (>1μm) there is a multi-domain ground state, which causes a narrow hysteresis loop due to the small energy needed to make the domain

walls move. On the other hand, smaller particles (100nm - 1μm) have wider hysteresis loops. At lower sizes (10-100nm) it is possible to observe superparamagnetism, in which the magnetic moment of the particle acts as a whole and is free to fluctuate in response to thermal energy (Figure 13). At the same time, the individual atomic moments maintain their ordered state relative to each other, leading to a non-hysteretic M-H curve, where $H_C=M_R=0$.

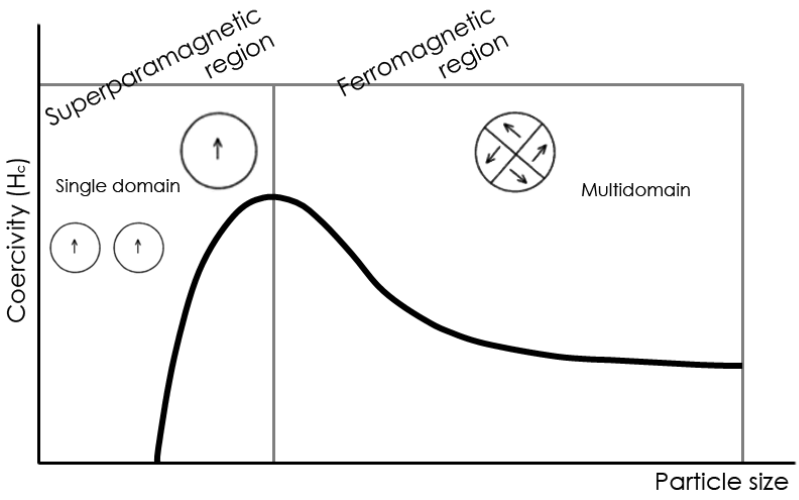


Figure 13: Variation of coercivity during transition from multi-domain ferromagnetism to single-domain superparamagnetism. (Adapted from [188])

## 1.5.2. Superparamagnetism

Superparamagnetism was firstly and theoretically described by Neel (1949), who demonstrated that $H_C$ approaches zero when particles become very small, due to thermal fluctuations of very small particles, preventing the existence of a stable magnetization.

As a consequence of the reduced size of the particles, the basic mechanism of superparamagnetism is based on the relaxation time ($\tau$) of the net magnetization of a magnetic particle (Brown 1963):

$$\tau = \tau_0 \cdot e^{\left[\frac{\Delta E}{k_B T}\right]} \qquad \text{[Eq.3]}$$

Where, $\Delta E$ is the energy barrier for moment reversal, $k_B T$ is the thermal energy and the pre-exponential factor $\tau_0$ is in the order or $10^{-10}$ – $10^{-12}$ s, only weakly dependent on temperature and is inversely proportional to the jump attempt frequency of the particle magnetic moment between opposite directions of the magnetization easy-axis. For non-interacting particles the factor $\tau_0$ is in the order of $10^{-10}$ – $10^{-12}$ s, and only weakly dependent on temperature. The energy barrier has several origins, including both intrinsic and extrinsic effects such as the magneto-crystalline and shape anisotropies. The simplest case is given by $\Delta E=KV$, where K is the anisotropy energy density and V is the particle volume. For small particles $\Delta E$ is comparable to $k_B T$ at room temperature. It should be noted that, for a given material, the observation of superparamagnetism is dependent not only on temperature, but also on the measurement time $\tau_m$ of the experimental technique used. As shown in Figure 14 (a.), if $\tau << \tau_m$ the flipping is fast relative to the experimental time window and the particles appear to be paramagnetic, while for $\tau >> \tau_m$ (Figure 14 b.) the flipping is slow and such a state is called a blocked state. The blocking temperature $T_B$ can be obtained assuming $\tau=\tau_m$ and is associated to the energy barrier; hence, $T_B$ increases when the size of the particle also increases.

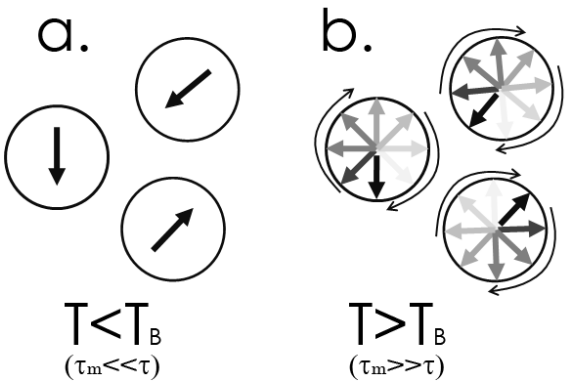


Figure 14: Illustration of the concept of superparamagnetism, where the circles depict three magnetic nanoparticles and the arrows represent the net magnetic moment direction in those particles. (a.) the net moments are quasi-static and (b.) the moment reversals are so rapid that in zero external field the time averaged-net moment on the particles is zero. (Adapted from [189]) .

### 1.5.3. Superparamagnetic iron oxide nanoparticles (SPIOs)

Nanotechnology refers to the field of science and engineering dedicated to materials, having dimensions in the range of 100nm or less.[190,191] Although new, the starting of nanomaterials dates back to 1959, when Richard P. Feynman forecasted the advent of nanomaterials. In one of his lectures at California Institute of Technology he said, *there is plenty of room at the bottom*, and suggested that scaling down to nanolevel and starting from the bottom was the key to future technology and advancement[192]. One of these advancements of nanotechnology can be found in biological applications, because a variety of bioprocesses also occur at the nanoscale level. Fluorescent biological labels, drug and gene delivery, bio detection of pathogens, detection of proteins, probing of DNA structures, tissue engineering, tumor destruction via heating,

separation and purification of biological molecules and cells, MRI contrast enhancement or phagokinetic studies are some of the applications of nanomaterials to biology or medicine.[190] Along this way, superparamagnetic iron oxide nanoparticles (SPIOs) with appropriate surface chemistry have been used for numerous *in vitro and in vivo* applications, such as cell separation, drug delivery, hyperthermia, detoxificacion of biological fluids, immunoassay, tissue repair and MRI contrast enhancement.

SPIOs have been the most extensively investigated MNPs for biomedical applications due to their excellent biocompatibility and ease of synthesis. Normally they are composed of a core of nanocrystalline magnetite ($Fe_3O_4$) or maghemite ($\gamma$–$Fe_2O_3$) wrapped with a polymeric coating[193]. Indeed, magnetite is particularly suitable for its use in magnetic resonance (MR), as it has been isolated from certain birds, fish and bacteria, in which its interaction with the earth magnetic field has been found to play a critical role in navigation.[194]

Maghemite is formed from the oxidation of magnetite and is similar to it, possessing cation vacancies. Both, magnetite and maghemite have similar magnetic and relaxation properties. They have a face/centered cubic packing of oxygen that allows fast electron hopping or continuous exchange of electrons between irons occupying interstitial tetrahedral (surrounded by 4 oxygen atoms) and octahedral (surrounded by 8 oxygen atoms) sites. All tetrahedral holes are filled by $Fe^{3+}$ ions, and octahedral sites are filled by the remaining $Fe^{3+}$ and $Fe^{2+}$ ions (or vacancies). The magnetic properties of this material arise from the ferrimagnetic alignment of the iron ions. The tetrahedral $Fe^{3+}$ ions are aligned in one direction, and all the octahedral ions are aligned in the opposite direction. In magnetite, the

octahedral and tetrahedral $Fe^{3+}$ ions cancel each other and the magnetic moment is due to uncompensated octahedral $Fe^{2+}$ ions. In maghemite, the moment arises from uncompensated octahedral $Fe^{3+}$ ions[195].

Numerous chemical methods can be used to synthesize magnetic nanoparticles for medical imaging applications: microemulsions, sol-gel synthesis, sonochemical reactions, hydrothermal reactions, hydrolysis and thermolysis of precursors, flow injection synthesis and electrospray synthesis. The synthesis of superparamagnetic nanoparticles is a complex process because of their colloidal nature. The main chemical challenge is to define the experimental conditions, leading to a monodisperse population of magnetic grains of suitable size. The second critical point is to select a reproducible process without any complex purification procedure, such as ultracentrifugation, size-exclusion chromatography, magnetic filtration or flow field gradient. However, the most common and the easiest method for the production of magnetite nanoparticles is the chemical coprecipitation technique of iron salts[196].

#### 1.5.3.1. Synthesis of SPIONs: Chemical coprecipitation method.

This technique is probably the simplest and the most efficient chemical pathway to obtain magnetic nanoparticles. Iron oxides (either $Fe_3O_4$ or $\gamma Fe_2O_3$) are usually prepared by aging a stoichiometric mixture of ferrous and ferric salts in aqueous medium, the chemical reaction may be written as

$$Fe^{2+} + 2Fe^{3+} + 8OH^- \rightarrow Fe_3O_4 + 4H_2O$$

According to the thermodynamics of the reaction, complete precipitation of $Fe_3O_4$ should be expected at a

pH between 8-14, with a 2:1 ratio ($Fe^{3+}/Fe^{2+}$) in non-oxidizing oxygen environment. However, magnetite is not very stable and it is sensitive to oxidation, transforming into maghemite in the presence of oxygen:

$$Fe_3O_4 + 2H^+ \rightarrow \gamma Fe_2O_3 + Fe^{2+} + H_2O$$

However, oxidation in air is not the only way to transform magnetite into maghemite; also the pH of the suspension has a big influence.

The main advantage of the coprecipitation method is that a large amount of particles can be synthesized at the same time. However, the control of the particle size distribution is limited because only kinetic factors are influencing the growth of the crystal. The size and shape of the particles can be tailored adjusting the pH, ionic strength, temperature, nature of salts or the ratio between $Fe^{II}/Fe^{III}$, and also the addition of chelating organic anions (oleic acid, citric acid,…) or polymer surface complexing agents (dextran, polyvinyl alcohol,…). Other external parameters as the mixing rate and the order on adding the reagents have also an influence in those parameters.

#### 1.5.3.2. Surface modifications of MNPS

Due to the high Brownian mobility of MNPs, they will constantly collide and can aggregate if any attractive interaction is present. Nanoparticle interactions are originated mainly due to 4 different phenomena: Van der Waals forces (attractive), electrostatic forces (attractive or repulsive), steric hindrance (repulsive) and the hydrophobic effect.

There are two methods to stabilize MNPs, by adding a ligand or by exchanging ligands. On one hand, ligand

addition is in general performed by using an amphiphilic molecule, which hydrophobically interacts with the non-polar surfactant. On the other hand, ligand exchange involves total replacement of the non-polar ligands by a polar surfactant.[197]

There are 3 different approaches to stabilize magnetic nanoparticles by adding a ligand: monomeric stabilizers (carboxylates, phosphates or sulfates), inorganic materials (silica, gold or gadolinium, providing not only stability but also helping in binding various biological ligands to the surface as well) and polymeric stabilizers. In this approach, it is possible to distinguish between *in situ* coatings, where nanoparticles are coated during the synthesis, and post-synthesis coatings. In the literature, the most common coatings are dextran, carboymethylated dextran, carboxydextran, arabinogalactan, glycosaminoglycan, starch, sulfonated styrene-divinylbencene, PolyEthylene Glycol (PEG), PolyVinyl Alcohol (PVA), poloxamers and polyoxamines,[196] although the selection of the coating will be conditioned by the biological application of the coated nanoparticle.

#### 1.5.3.3. Superparamagnetic nanoparticles for cell labeling and cell tracking

MRI contrast agents for in vivo cell tracking are being widely investigated. Transplanted cells not only have the potential to replace damaged cells, but also to produce growth and trophic factors, or stimulate the release of such factors from host brain cells, enhancing endogenous brain repair processes. Many issues for stem cell therapy are still in the bench like therapeutic window, cell type, delivery route and *in vivo* monitoring of their migration pattern. The possibility to track the transplanted cells could help to

clarify all these questions and improve stem cell therapies for different pathologies.[198]

MRI contrast agents for cell tracking require nanoparticles with special characteristics as high magnetization values and small and narrow size distribution. Thermal decomposition and chemical coprecipitation methods are the most extended procedures. Coprecipitation technique is probably the simplest and most efficient chemical route to obtain magnetic nanoparticles. As it was previously mentioned, the main advantage is that a large amount of particles can be synthesized easily and economically.[199] But for biological applications not only the magnetic properties are important, a specific surface coating of the magnetic particles is also needed, which has to be biocompatible.[196]

Among all the coating possibilities, dextran is one of the most widely polymers used as magnetic nanoparticle coating due to its biocompatibility. It is a polysaccharide polymer composed exclusively of $\alpha$–D-glucopyranosyl units with varying degrees of chain length and branching. In 1982, Molday and Mackenzie were the first who reported the formation of magnetite in presence of dextran 40000.[200] The synthesis of dextran coated nanoparticles is an *in situ* procedure, and the effect of reducing the terminal glucose of dextran upon the formation and stability of dextran-coated superparamagnetic nanoparticles has demonstrated to be significant for particle size, coating stability and magnetic properties.[199] For cell labeling applications, dextran coated nanoparticles normally need to be combined with transfection agents or the use of electroporation techniques to increase the tagging efficiency.[201-204]

Other methods to synthesize coated magnetic nanoparticles need more than one step. Jain et al. [205] developed a novel oleic acid (OA)-Pluronic-stabilized iron oxide magnetic nanoparticle formulation, and characterized it as a drug carrier system for anticancer agents. The hydrophobic drugs would partition into the OA shell surrounding the iron oxide nanoparticles, and the polymer (Pluronic) would anchor at the interface of the OA shell to confer an aqueous dispersity to the formulation. [205] Pluronic (Poloxamer) and Tetronic (Poloxamines) are a family of amphiphilic nonionic block polymers. More in detail, Pluronic block polymer consists of a hydrophobic poly(ProPylene Oxide) (PPO) chain flanked on each side with hydrophilic Poly(Ethylene Oxide) (PEO) chains, meanwhile Tetronic block polymer contain four PPO-PEO chains connected together at the PPO subunits to form a star shape structure (Figure 15).[206] Because Pluronic and Tetronic are a family of polymers, they vary structurally, as well as in the ratio of hydrophobic PPO and hydrophilic PEO segments in the polymer chain and in molecular weight [207]. Moreover, FDA and EMEA have approved the use for some of the linear PEO-PPO-PEO triblocks in food, pharmaceutical and agricultural industries[208] and also Pluronic has been already used as iron oxide nanoparticle coating, and their applications on cell labeling experiments point out that no transfection agents are needed.[205,209]

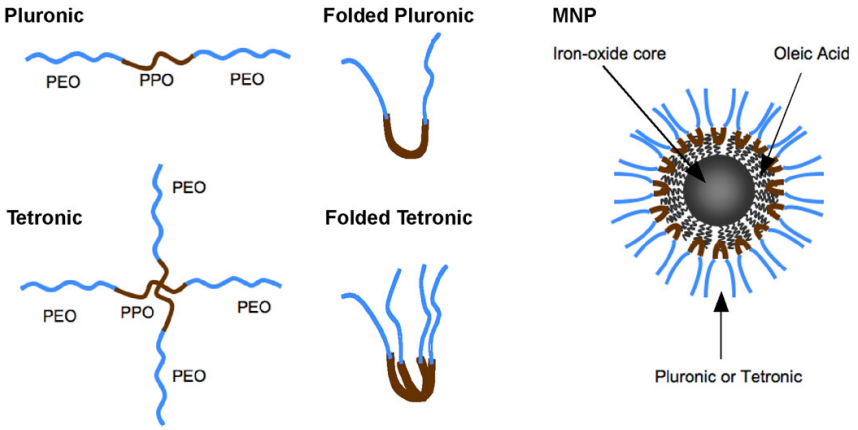


Figure 15: Schematic of MNPs. Each particle contains an iron-oxide core coated with OA and is coated with either Pluronic (single PEO-PPO-PEO subunit) or Tetronic (two PEO-PPO-PEO subunits). The PPO subunit from the copolymers adsorbs onto the OA rendering the MNPs dispersible in aqueous solution. (Pluronic and Tetronic are registered trademarks of BASF SE, Ludwigshafen, Germany.) Adapted from [207]

In addition, when considering MNPs enabled MRI cell tracking, there are other parameters with high impact on the success of applying this method:[210] the amount of nanoparticle uptake,[211,212] reactive oxygen species, [213-215] the specific nanoparticle localization in the cell, [210] and the impact of transfection agents (TA).[210,216]

TAs are macromolecules possessing an electrostatic charge and normally are used for non-viral transfection of DNA into the nucleus.[216,217] There are different types of TAs available, including polyamines (as PoLy-Lysine –PLL-), lipid-based agents (as lipofectamine) and heat-activated dendrimers. Usually, TAs have net positive z-potential, but it depends on the type of agent and their molecular weight.[218] However, TAs when added to cell medium are toxic to the cells, and the toxicity is proportional to the concentration in culture medium. Their importance to tag non phagocytic cells with dextran coated nanoparticles

has already been shown [201,204,219,220] but it is necessary to determine the appropriate ratio nanoparticles/TAs to efficiently label cells and minimize toxic-side effects.[216,221]

Several studies have demonstrated the migration capacity of injected stem cells under normal and pathological conditions. Specific cell tracking is a successful application of SPIONs in MRI. The ability of load cells with enough MNPs *in vitro* has provided a useful technique to label and track cells in vivo by MRI. The detection limit will be conditioned by the type or MNPs and the cell load.[222]

#### 1.5.3.4. Magnetic vectorization

Recent works have studied the influence of the administration route on the efficacy of stem cell therapy, suggesting that improved methods for cell delivery to targeted areas would lead to better outcomes.[223] Several studies have already demonstrated its applicability for cell therapy for spinal cord injury [224] and magnetic vectorization of labeled endothelial progenitor cells after an intra-arterial injection in the common carotid artery in mice.[225] In order to increase the amount of injected cells close to the ischemic lesion, magnetic vectorization of cells tagged with superparamagnetic nanoparticles could be a good approach. However, the hypothesis of directing most of injected cells to the brain in order to decrease infarct size and increase functional recovery after an ischemic event was not yet demonstrated.[183]

# Section II

USC
UNIVERSIDADE
DE SANTIAGO
DE COMPOSTELA

# 2. Hypothesis

Cell based therapies show great promise in the treatment of certain, so far incurable, pathologies like stroke. To determine the success of these cell therapies, non-invasive monitoring of the cells is required, and MRI is one of the most appropriate tools to do it because of its excellent soft tissue contrast and high resolution. By tagging cells with MRI contrast agents such as superparamagnetic nanoparticles, MRI can provide anatomical and pathological information and also the possibility of visualize and track cells in vivo.

In this thesis we hypothesized that it is possible to synthesize biocompatible superparamagnetic nanoparticles for *in vivo* cell tracking. Superparamagnetic nanoparticles-tagged cells can be monitored *in vivo* by MRI and guided with magnetic fields without harmful effects, providing information of the cellular fate after different routes of administration. Moreover, the nanoparticle labeling will allow us to study therapeutic effects in an animal model of ischemic stroke based on the localization of the cells after delivery.

USC
UNIVERSIDADE
DE SANTIAGO
DE COMPOSTELA

# 3. Objectives

The present work will be structured in 4 sections, and the main objectives are:

1. Superparamagnetic nanoparticles:
    - Synthesis and characterization of superparamagnetic nanoparticles as contrast agents for MRI.

2. *In vitro* validation:
    - Biological validation of our synthesized superparamagnetic nanoparticles: *In vitro* evaluation of cellular well-being after labeling and MRI cell detection.
    - *In vitro* feasibility of magnetic vectorization of labeled cells.
    - Long term evaluation of labeled cells: harmful effects in the cells and MR signal after proliferation.

3. Cell tracking in animal models of ischemic stroke:
    - Animal models of ischemic stroke and its relationship with administration routes for stem cell delivery.
    - *In vivo* feasibility of magnetic vectorization of labeled cells.
    - *In vivo* cell tracking of mesenchymal stem cells following intra-arterial and intravenous administration.

4. Neurorepair mediated by stem cell therapy:
    - Stem cell therapy in ischemic stroke: Neuroreparation mediated by intra-arterial and intravenous injection of mesenchymal stem cells in an animal model of ischemic stroke.

# Section III

## Synthesis of superparamagnetic nanoparticles for cell labeling

USC
UNIVERSIDADE
DE SANTIAGO
DE COMPOSTELA

# 4. Synthesis of superparamagnetic nanoparticles coated with different polymers as contrast agents for MRI

## 4.1. Hypothesis

In order to develop an efficient, effective and minimally invasive cell tracking system for MRI, this chapter presents the synthesis procedure and physicochemical characterization of 3 different coated superparamagnetic nanoparticles. Magnetic cores were synthesized following the chemical coprecipitation method previously described, an *in situ* procedure was performed for dextran-coated superparamagnetic nanoparticles, while Pluronic F127 and Tetronic 908- coated magnetic nanoparticles were obtained following a two step synthesis method.

## 4.2. Materials and methods

### 4.2.1. Reagents

Iron (III) chloride reagent grade 97% (157740, *Sigma-Aldrich*), iron (II) chloride 98% (372870, *Sigma-Aldrich*), ammonia solution 28-30% for analysis (1.05423, *Merk*), dextran from Leuconostoc spp. (31389. *Sigma-Aldrich*), Oleic Acid >99% (O1008. *Sigma-Aldrich*), Pluronic F-127 (P2443. *Sigma-Aldrich*), Tetronic 908 (Basf) and chloroform (1.02447. *Merk*). Deionized water purged with nitrogen gas was used in the synthesis and formulation of magnetic nanoparticles.

### 4.2.2. Synthesis of dextran coated superparamagnetic nanoparticles

Dextran magnetic nanoparticles were prepared following the protocol described elsewhere[226] with slight modifications. Aqueous solutions of 0.1M Fe(III) and 0.1M Fe(II) in a ratio 2:1 were mixed (stirring ratio 400 rpm) under $N_2$ atmosphere and T=60°C. After 15 minutes, 100 mg of dextran in 5 mL of water were added to the mixture. Next, 5 mL of 5M ammonia solution was added and mixed for 15 minutes to form iron oxide nanoparticles. The final solution was cooled down to room temperature and finally, the suspension was dialyzed (D0530, *Sigma-Aldrich*) against distilled water (DW).

### 4.2.3. Synthesis of Pluronic F127 and Tetronic 908 coated superparamagnetic nanoparticles

Pluronic F127 (P127) and Tetronic 908 (T908)- coated magnetic nanoparticles were prepared through a two step

procedure following the protocol described elsewhere [205] with several modifications. Briefly, in order to form the magnetic core, aqueous solutions of 0.1M Fe(III) and 0.1M Fe(II) in volume ratio 2:1 were mixed (stirring ration 400 rpm) under $N_2$ atmosphere and room temperature. Ammonium hydroxide (5mL 5M) was added drop by drop to produce the particles. After 10 minutes, 46 µL of oleic acid (OA) was added and the temperature was raised to 80°C and maintained for 20 minutes under $N_2$ atmosphere. The solution was cooled down to room temperature and the suspension was washed with magnetic separation using DW (pH=9.5).

For nanoparticle polymer coating a phase change is needed. After removing all the water from the magnetic cores prepared in the previous step, 5.5 mg of nanoparticles in 4 mL of chloroform were sonicated for 5 minutes. This solution was mixed with 40 mg of polymer and stirred again for 5 minutes. After cholorform evaporation, DW was added and the mixture was placed for 1h shacking. Under ambient conditions, the MNPs were washed three times with distilled water and separated using a rare earth magnet.

### 4.2.4. Magnetic nanoparticle characterization

Dynamic Light Scattering (DLS): For measuring the particle size of the OA coated magnetic cores and dextran, Pluronic and Tetronic coated nanoparticles, each coated sample was dispersed in DW, while for measuring OA-coated nanoparticles the samples were dispersed in chloroform. Dynamic light measurements were performed by means of an ALV-5000F (ALV-GmbH, Germany) instrument with vertically polarized incident light (θ = 488 nm) supplied by a diode-pumped Nd:YAG solid-state laser

(Coherent Inc., CA, USA) and operated at 2 W, and combined with an ALV SP-86 digital correlator with a sampling time of 25 ns to 100 ms. Measurements were made at an angle θ = 90° to the incident beam, as appropriate for particles smaller than the light wavelength. The intensity scale was calibrated against scattering from toluene.. Each experiment was repeated at least three times. Sampling time was 5-10 min for each run in order to define an optimal correlation function. The correlation functions were analyzed by the CONTIN method to obtain the intensity distributions of decay rates (Γ).From the decay rate distributions the apparent diffusion coefficients $D_{app}=\Gamma/q^2$, $q=(4\pi n_s/\lambda)\sin(\theta/2)$ were derived, being $n_s$ the solvent refractive index. Values of the apparent hydrodynamic radius were calculated from the Stokes-Einstein equation.

Transmission Electron Microscopy (TEM): For measuring the size and determining the shape of the MNPS, TEM samples were prepared by evaporating a drop of the nanoparticles dispersion of the particles on a carbon-coated cooper grid without staining and imaged using a TEM microscope model Philips CM-12 operating at 120 kV. The NIH ImageJ software was used to calculate the mean particle diameter from TEM images. Diameters of ca. 40 particles were measured.

X-Ray Diffraction (XRD): A structural analysis of dextran coated and non-coated nanoparticles were performed by X-ray diffraction (XRD) data. The samples were measured on a Philips powder diffractometer fitted with Philips PW1710 control unit, vertical Philips PW1820/00 goniometer and FR590 Enraf Nonius generator. The instrument was equipped with a graphite diffracted beam monochromator and copper radiation source ($\lambda(K\alpha 1)=1.5406$Å), operating at 40

kV and 30mA. The X-Ray powder diffraction pattern (XRPD) was collected by measuring the scintillation response to CuKα radiation versus the 2θ value over a 2θ range of 10-80°, with a step size of 0.02° and counting time of 2 s per step.

Zeta-potential: Polymer-coated MNPs were measured using a Zetasizer NanoZS instrument (Malvern) equipped with a red laser (633 nm) in backscatter mode.

Vibrating Sample Magnetometer (VSM): Magnetic properties of SPIONs were recorded on a vibrating sample magnetometer (VSM) from Quantum Design TM. Hysteresis loops (magnetization vs. applied external magnetic field plots) of synthesized SPIONs were recorded at 5 and 300 K and a maximum applied magnetic field of 50000 Oe. Saturation (Ms), and remanent (Mr) magnetizations, and coercitive field (Hc) were subsequently derived from experimental data.

Fourier-transform infrared (FTIR): 59.5 mg of potassium bromide and 1mg of MNPs were mixed. This mixture was dried in a vacuum for 3 days and subsequently pressed to form a pellet and mounted in FTIR spectrometer (Varian FTIR 670). The spectra were obtained at a resolution of 4 $cm^{-1}$ and 64 scans were accumulated for each sample.

Inductive coupled plasma optical emission spectroscopy (ICP-OES): The iron concentration was determined by ICP-OES (Varian Inc., Palo Alto, USA). Hereto, the nanoparticles were dissolved in 1mL of 37% HCl after which 4 mL of DW were added. The intensity of the emission wavelength for iron at 238.204 nm was measured and compared to a standard solution. ICP_OES was performed at the Material Science Institute (MTM), KU Leuven.

Thermal gravimetric analysis (TGA): This analysis was performed at imec (Leuven, Belgium) on a Q5000IR (TA instruments, New Castle, DE, USA) under nitrogen atmosphere to study the organic coating of the MNPs. First, 100 µL of MNPs were slowly heated to 80ºC to remove all solvents. Next, temperature was increased to 850ºC at a heating rate of 20ºC/min. Using the software provided by the manufacturer (Universal Analysis 2000, 4.5 A), the weight difference was analyzed before and after burning off the organic coating.

Magnetic Resonance Imaging (MRI): Samples were prepared using an agar phantom holder following the protocol described elsewhere [227]. Triplicates of dextran, Pluronic F127 and Tetronic 908 coated nanoparticles, 4 concentrations for each type of nanoparticle were measured. MRI studies were conducted on a 9.4 T MR system (Bruker Biospin, Ettlingen, Germany) with 440 mT/m gradients, using a combination of a linearly polarized birdcage resonator of 7 cm of diameter for signal transmission and a 2x2 arrayed pick-up surface coil for signal detection. T2-weighted images were typically acquired using a Multi-Slice Multi-Echo (MSME) sequence (3 averages with a train of 16 echoes of 7.32 ms Echo time and a repetition time of 5.4 s. The whole agar phantom was covered with 14 consecutive axial slices of 1 mm thickness with a field-of-view (FOV) of 75x75 mm (with saturation bands to suppress the signal outside the FOV) and an in-plane resolution 0.75mm/pixel. Post-processing of all images was performed using ImageJ software (Rasband, W. NIH).

# 4.3. Results

## 4.3.1.Dextran coated magnetic nanoparticles.

### 4.3.1.1. Iron oxide core

Magnetic nanoparticles were synthesized in the presence of dextran through the chemical coprecipitation method. TEM micrographs (Figure 16) confirmed the spherical shape of the dextran-coated magnetic nanoparticles. The mean particle size using this technique was 3.7±0.8 nm.

The crystal structure (Figure 17) of MNPs determined by XRD showed peaks at 2θ positions of ca. 30.2º; 35.6º; 43.2º; 57.1º; 62.7º, corresponding to the (220), (311), (400), (511) and (440) planes of magnetite respectively with a lattice parameter of 8.33±0.02 Å. It was also possible to determine the core size of the dextran coated nanoparticles from XRD data. The calculated cristallite size (Figure 17) was 4.8±0.5 nm.

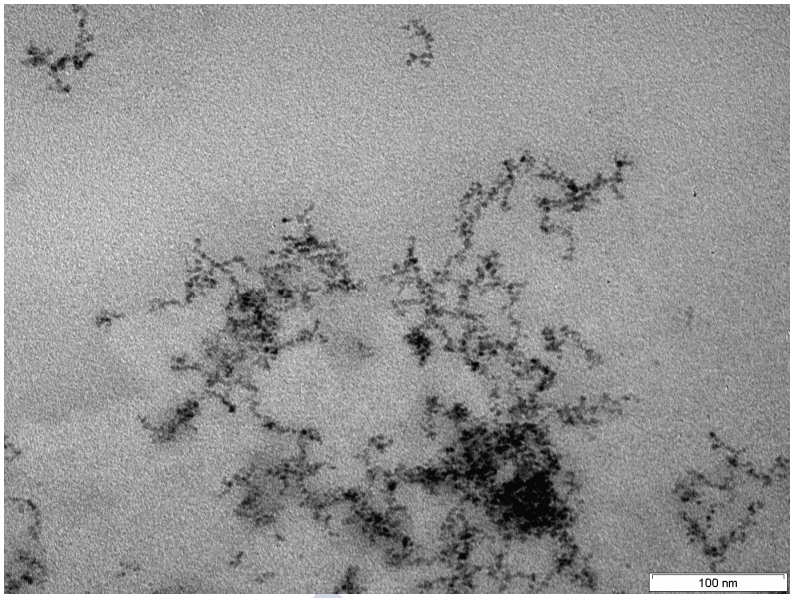


Figure 16: TEM image of dextran Coated Nanoparticles.

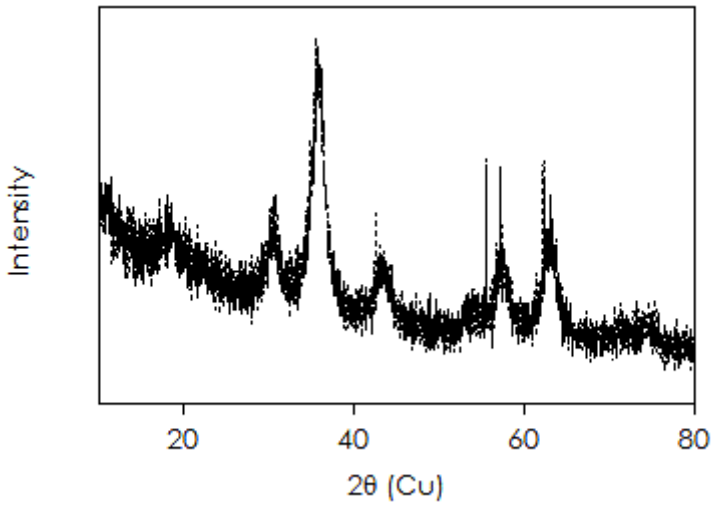


Figure 17: XRD spectrum of dextran coated nanoparticles

4.3.1.2. Dextran coated nanoparticles.

The hydrodynamic size measured by DLS was 94±3 nm. Z-potential of these coated particles dispersed in DW was negative, with values of ca. -11±3 mV. The presence of the polymeric coating on the nanoparticles was further confirmed by TGA and FITR. The TGA data showed two peaks corresponding to mass losses at approximately 280ºC and 322ºC, close to polymer loss temperature of dextran (289ºC), demonstrating that about 66 wt % of dextran can be found in the nanoparticles (Figure 18). The FTIR spectrum exhibits several polysaccharide characteristic absorption bands, at 3351 $cm^{-1}$ due to the O-H stretching. Vibrational modes $\upsilon$(C-H) and $\delta$(C-H) correspond to 2906 $cm^{-1}$, 1420 $cm^{-1}$ and 1380 $cm^{-1}$. Water molecular bending is assigned to 1620 $cm^{-1}$; 1145 $cm^{-1}$ and 1010 $cm^{-1}$ peaks due to C-O vibrations and the small peaks at 908 $cm^{-1}$, 877 $cm^{-1}$ and 746 $cm^{-1}$ corresponding to $\alpha$-glucopyranose ring deformation modes (Figure 19). There are also two absorption bands at 578$^{-1}$ and 430 $cm^{-1}$ corresponding to Fe-O vibration modes.

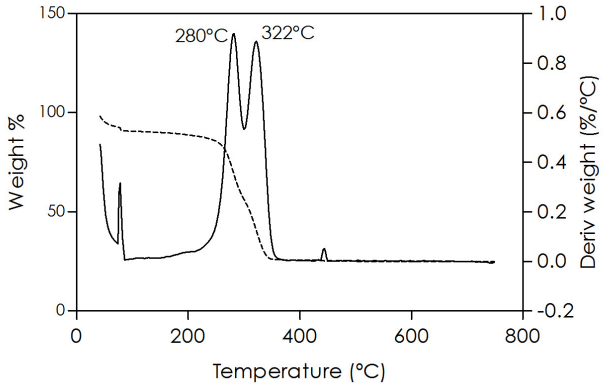


Figure 18: TGA spectrum of dextran polymer and dextran coated NPs.

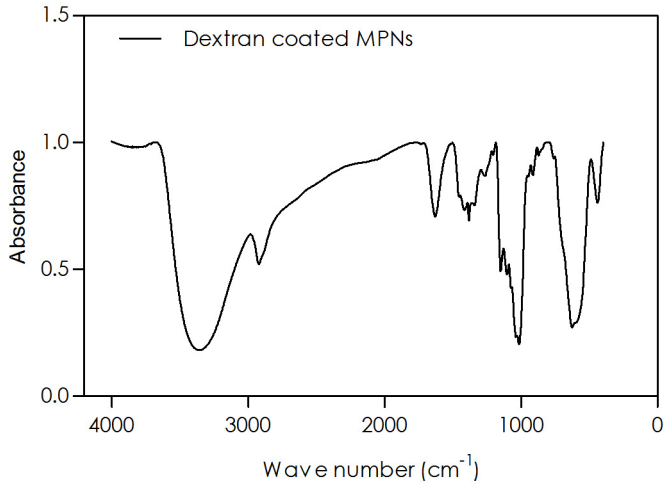


Figure 19: FTIR spectrum of Dextran coated nanoparticles.

VSM data showed that Dextran coated nanoparticles exhibited superparamagnetic behavior (Figure 20).

MRI contrast in T2* weighted images of 4 different concentrations of dextran coated nanoparticles were measured: 0.19mM; 0.09mM; 0.05mM and 0.02mM (Figure 21). The relaxation rate ($R_2$) was plotted versus the concentration of iron. A linear relationship was found between $R_2$ and the MNPs concentration, enabling the calculation of the transverse relaxivity ($r_2$) (the slope). The $r_2$ for dextran coated magnetic nanoparticles resulted in 699±4 $mM^{-1}s^{-1}$.

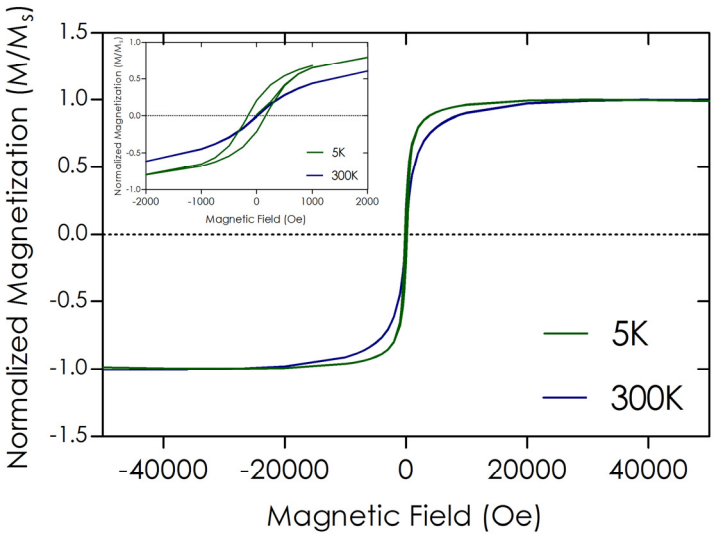


Figure 20: VSM results of dextran coated magnetic iron oxide nanoparticles.

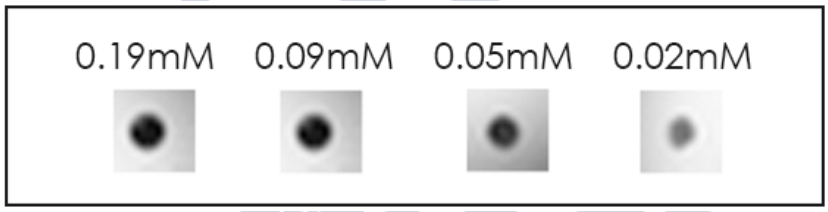


Figure 21: MRI T2 weighted of dextran-coated nanoparticles for each concentration.

## 4.3.2. Polymer coated magnetic nanoparticles: Pluronic F127 and Tetronic 908.

### 4.3.2.1. Core

Pluronic and Tetronic-coated MNPs were prepared following a two step procedure. First, magnetic cores were synthesized and next the polymer coating was added. Magnetic cores coated with oleic acid were obtained

through the chemical coprecipitation method, obtaining spherical MNPs (Figure 22). The core size was 8.6±1.4 nm determined through TEM. The core size was also determined by XRD spectrum data and by DLS, being 7.7±0.8 nm and 7.3±0.8 nm respectively.

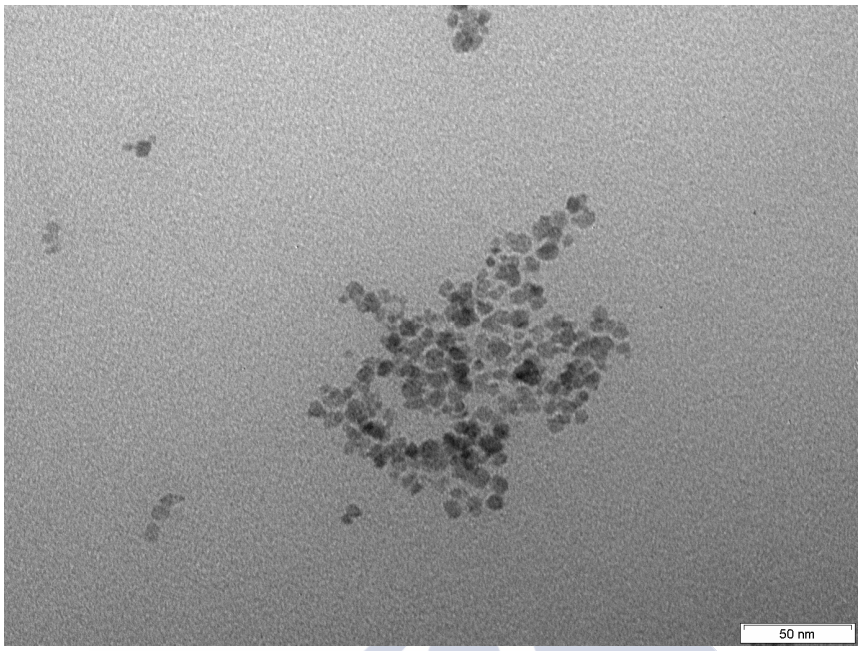


Figure 22: TEM picture of superparamagnetic nanoparticle cores.

The core crystal structure determination using XRD (Figure 23) showed peaks at 2θ positions of approximately 30.2º; 35.6º; 43.2º; 57.1º; 62.7º, corresponding to the (220), (311), (400), (511) and (440) planes of magnetite respectively with a lattice parameter of 8.361±0.004 Å. Data obtained through VSM measurements showed that the cores exhibited superparamagnetic behavior at room temperature (Figure 24).

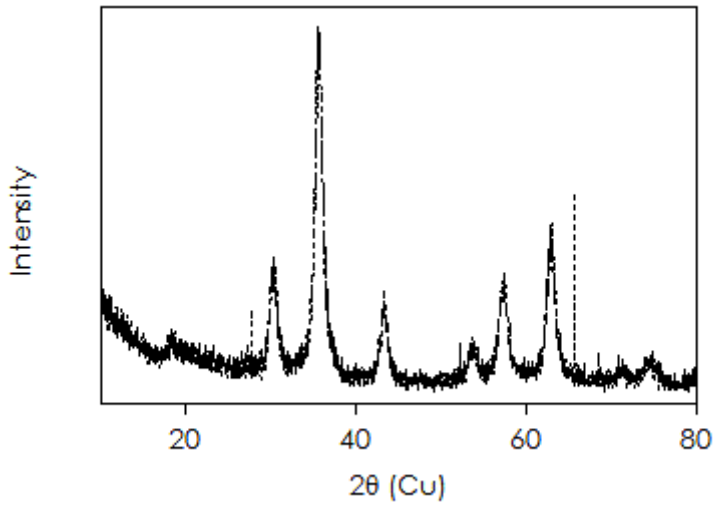


Figure 23: XRD spectrum of magnetic nanoparticle cores synthesized through chemical coprecipitation method.

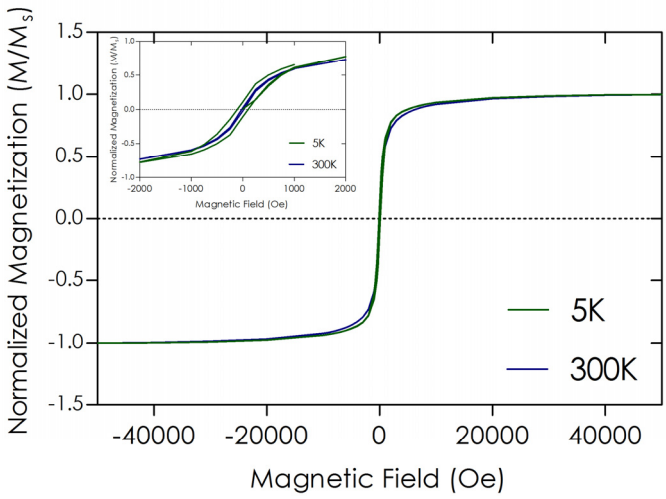


Figure 24: Magnetization versus magnetic field plots for magnetic cores of superparamagnetic nanoparticles.

The presence of oleic acid attached to the surface of the nanoparticle was evaluated through TGA. In Figure 25A two

peaks can be observed at 179ºC and 213ºC, which is near to the boiling or decomposition point of the oleic acid chains (239ºC) (figure not shown). This corresponded to a mass loss percentage of 17,14%. The main peak was observed at ca. 356.51ºC with a 25.49 wt% of mass loss percentage.

4.3.2.2. Pluronic F127 and Tetronic 908 coated magnetic nanoparticles.

After coating the magnetic cores with Block copolymers, the hydrodynamic size measured by DLS was 154±6 nm for Pluronic-coated nanoparticles, and 180±6 nm for Tetronic-coated nanoparticle. Z-potential of these coated particles dispersed in DW was negative for both, being -18±3 mV and -24±3 mV respectively.

TGA of Pluronic coated iron oxide nanoparticles indicated the presence of the polymer and the oleic acid. TGA showed two peaks approximately 262ºC (19.1 wt%) and 313ºC (35.5 wt%), close to oleic acid and pure Pluronic F127 boling points respectively. For Tetronic 908 coated nanoparticles the behavior is similar. TGA data also showed two peaks, first one at about 260ºC (26.3%) corresponding to oleic acid and second one at 311ºC (42 wt%) corresponding to pure Tetronic 908. (Figure 25 B and C)

FTIR spectrum (Figure 26) exhibited similar peaks for Pluronic and Tetronic coated superparamagnetic nanoparticles and oleic acid coated cores. Two broad peaks at approximately 440 $cm^{-1}$ and 610 $cm^{-1}$ corresponded to Fe-O vibration modes, and ca. 1430 $cm^{-1}$ and 1600 $cm^{-1}$ specific for symmetric and asymmetric stretching vibrations of $COO^-$ respectively. Additionally, the peaks at 1700 $cm^{-1}$ and 3400 $cm^{-1}$ can be attributed to the stretching vibration of the hydroxyl groups on the surface of the magnetite

nanoparticles. It was also possible to identify the asymmetric $CH_2$ and the symmetric $CH_2$ stretching bands at 2850 $cm^{-1}$ and 2920 $cm^{-1}$ respectively. The difference between the polymer coated and uncoated nanoparticles in FTIR data was the peak at 1100 $cm^{-1}$, typical for symmetric stretching vibrations of C-O-C bonds.

MRI contrast in T2 weighted images of 4 different concentrations of nanoparticles coated with Pluronic F127 (0.36mM; 0.18mM; 0.09mM; 0.04mM) and Tetronic 908 (0.45mM; 0.22mM; 0.11mM; 0.06mM) copolymers are shown in Figure 27. The relaxation rate ($R_2$) was plotted versus the concentration of iron, and a linear relationship was found between $R_2$ and the MNPs concentration, enabling the calculation of the transverse relaxivity ($r_2$) for each coated MNPs. The $r_2$ For Pluronic F-127 coated magnetic nanoparticles resulted in 398±12 $mM^{-1}s^{-1}$ and for Tetronic 908 coated MNP 330±20 $mM^{-1}s^{-1}$.

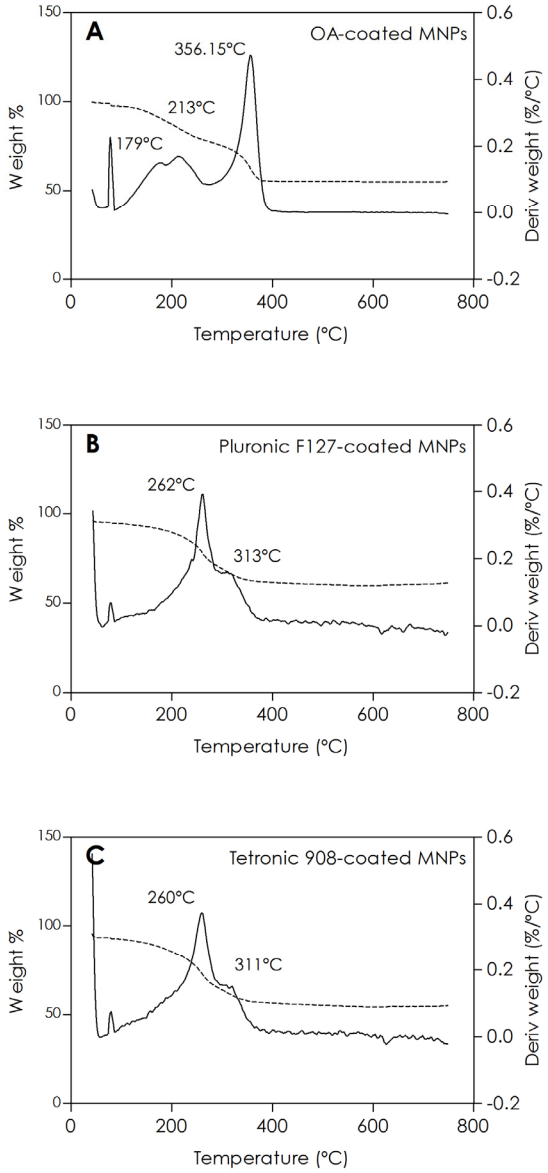


Figure 25: TGA of Oleic acid-coated MNPs (A), Pluronic F127-coated nanoparticles (B) and TGA of Tetronic 908-coated nanoparticles (C).

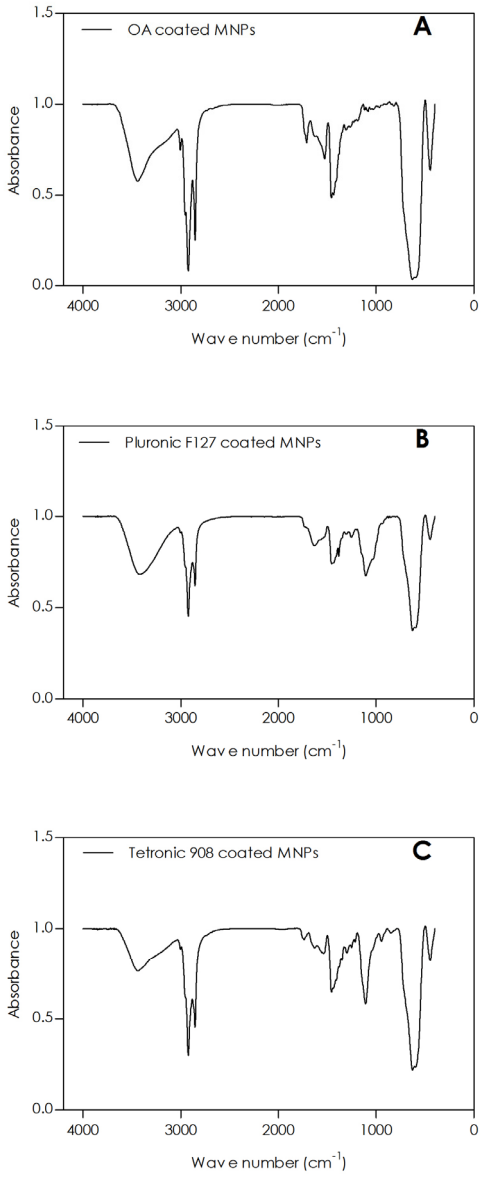


Figure 26: Oleic acid-coated cores (A), Pluronic F127-coated nanoparticles (B) and Tetronic 908-coated nanoparticles (C).

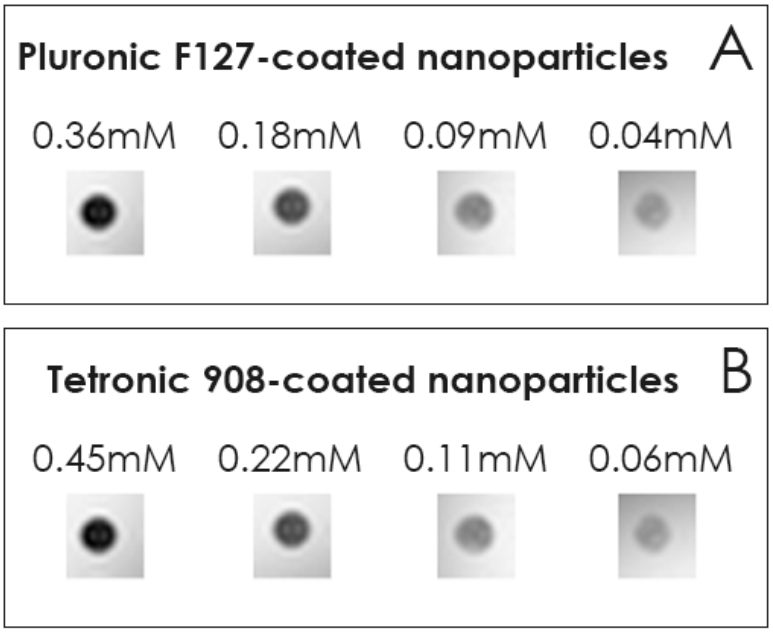


Figure 27: MRI T2 weighted of (A) Pluronic F127- and (B) Tetronic 908-coated nanoparticles for each concentration.

## 4.4. Discussion

The chemical coprecipitation method used for the magnetic nanoparticle synthesis was chosen because it is considered the easiest method to produce superparamagnetic nanoparticles. The main lack of this method is the big influence in the final particle size of several parameters such as temperature, pH, presence of oxygen in the reaction, stirring speed or $Fe^{3+}/Fe^{2+}$ molar ratio. Special care must be taken for a robust and reproducible NP synthesis, because the particle formation takes place when the ammonium hydroxide is added drop by drop, which is a tricky process to control.

### 4.4.1. Dextran coated superparamagnetic nanoparticles.

Since non coated nanoparticles have a large surface area to volume ratio, they tend to aggregate in order to reduce their surface energy.[199] However these nanoparticles can be stabilized with high molecular weight polymers such dextran. TEM image of dextran coated nanoparticles showed a regular distribution of sizes and shape of the synthesized particles. It wass possible to identify the core (spherical dark spots) but the polymer chains of dextran have too low density for contributing to contrast in the image and therefore cannot be observed. It has to be mentioned that it was not possible to take a micrograph of single dextran coated nanoparticles due to the aggregative nature of this polymer already previously reported[226].

Because dextran coated nanoparticles synthesis is a single step method, it was not possible to measure exclusively magnetic cores and dextran coated particles separated and all determinations were performed on dextran coated nanoparticles. However, several techniques as TEM and XRD are appropriate to measure the core size in presence of the coating material. Using TEM, the mean experimental size was 3.7±0.8 nm, a close value to core sizes already published following similar synthesis methods (4.11±0.85 nm).[226] Moreover, the crystallite size value from XRD spectrum using the Scherrer equation was 4.8±0.5 nm, in agreement with TEM results. Indeed, grain size should be smaller than TEM (multiple crystals, defects in crystals, amorphous shell). Normally, the grain size obtained from the XRD data should be smaller than the sizes measured from the TEM micrographs, due to several reasons: First, the outer layer of the MNPs tend to be amorphous due to the

curvature of the particles. This amorphous layer is detected by TEM, but does not contribute to the XRD diffractograms. Secondly, crystal defects can form within the MNPs crystal structure distorting the XRD data. Additionally, a MNP can be made up of several crystals, all of course being smaller than the size measured through TEM. A possible reason for the unexpected larger grain size can be attributed to the both methods, where size analysis based on TEM has a limited sample size, whereas the XRD data is taken from larger samples. Overall, both experimental values are in concert with each other. It is also important to mention that the standard deviation derived from the TEM measurement and therefore the size distribution is adequate considering that they were synthesized following the chemical coprecipitation method.

The crystalline structure from XRD data reflects a magnetite and/or maghemite crystal with a cubic spinel structure. Magnetite can be easily oxidized in air to form maghemite,[228] making it difficult to distinguish between them. This even can occur during sample preparation. The maghemite phase is known to exhibit few extra peaks at 23.77° (210) and 26.10° (211), and these peaks may be used to distinguish it from magnetite phase, however the intensity of these peaks are very weak (5%) for the positive identification of the maghemite phase.[229] Our XRD experimental spectrum of synthesized MNPs did not exhibit those diffraction peaks, but this fact does not guarantee that the sample is a single-phase maghemite, considering the previous point made. With regard to the calculated lattice parameter from XRD spectrum, the value 8.33±0.02 A is closer to maghemite (8.3515 A –JCPDS 39 1346-) than to magnetite (8.396 A –JCPDS 19 629-), what suggests that the obtained cores through chemical coprecipitation method

in presence of dextran are mostly composed of maghemite.

Moreover, the size of the dextran-coated nanoparticles was measured by DLS with a mean size 94±3 nm is in agreement with previous works.[230] Apart from the size, the surface charge is an important factor to take into account in terms of nanoparticle stability. The synthesized dextran-coated nanoparticles are stable in distilled water and negatively charged (-11±3 mV), a remarkable aspect to take into account for further *in vitro* and *in vivo* experiments in terms of not only cell labeling, but also of protein binding as well.[231,232]

To study the nature of the nanoparticle coating, FTIR and TGA were performed. FTIR spectrum demonstrated the presence of dextran and magnetite. The peak at 3351$cm^{-1}$ is attributed to the stretching vibrations of –OH, which is assigned to $OH^-$ absorbed by iron oxide nanoparticles or leftover water from KBr preparation. Also vibrational modes $\upsilon$(C-H) and $\delta$(C-H) at 2906 $cm^{-1}$, 1420 $cm^{-1}$ and 1380 $cm^{-1}$, water molecular bending due to C-O vibrations at 1620 $cm^{-1}$, 1145 $cm^{-1}$ and 1010 $cm^{-1}$ and small peaks at 908 $cm^{-1}$, 877 $cm^{-1}$ and 746 $cm^{-1}$ corresponding to $\alpha$-glucopyranose ring deformation modes (Figure 18) demonstrated the presence of dextran in the sample. The two absorption bands at 578 $cm^{-1}$ and 430 $cm^{-1}$ corresponding to Fe-O vibration modes verify the presence of the iron oxide core. However, it is necessary to look of TGA data for a better understanding of the dextran coated magnetic nanoparticles. TGA data indicates the presence of two close peaks (280ºC and 322ºC), demonstrating that the 66% of total weight of the sample was dextran, which points towards a thick and dense coating of the MNPs, this result agrees with other published works.[199,233] However, those two peaks also

show that the high stability of the sample is also conditioned for the presence of free dextran, which would be more easily detached (therefore 280ºC) and nanoparticle-attached dextran (more difficult to unbound, 322ºC). In this sense, 32.44 wt % would correspond to free dextran and 33.57 wt% to nanoparticle bonded one. Together, the results of FTIR and TGA, confirm the presence of dextran coating on the magnetic nanoparticles and also free polymer increasing the stability of the suspension.

Magnetic characterization of the MNPs showed the relative magnetization curve as a function of magnetic field at 5K and 300K. The absence of hysteresis loop at 300K indicated the characteristic superparamagnetic behavior of the particles. This means that these particles have non-interacting domains, so no magnetic clustering and high magnetization saturation, an important aspect for MRI contrast enhancement.[199] To assess the transverse relaxivity measured by MRI and therefore that those particles are suitable as MRI contrast agents, $T_2$-weighted images were acquired. Four different concentrations of dextran coated nanoparticles were measured and all parameters, such as echo time, repetition time and resolution were adjusted to obtain a well-defined exponential decay. The higher concentration (0.19mM) of particles could not be adjusted to an exponential decay because there were not enough data points to perform the adjustment. The relaxivity $r_2$ of dextran-coated particles from this data was 699±4 $mM^{-1}s^{-1}$.

### 4.4.2. Pluronic F127 and Tetronic 908 coated superparamagnetic nanoparticles.

The iron oxide nanoparticles formation through chemical coprecipitation method is a fast reaction, and happens when the ammonium hydroxide is added to iron salts mixture. After the formation of iron oxide nanoparticles, oleic acid is added in order to create an OA shell surrounding the iron oxide nanoparticle, which will be used as an anchor for further polymer functionalization. However, due to the excess of OA for the coating process, a multilayer of OA on the surface of the nanoparticles is formed, making them hydrophilic like. This multilayer is not stable, so a deep DW wash process will turn them into their natural hydrophobic state, and easily dispersible in organic solvents. This full procedure, including chemical coprecipitation, OA coating and nanoparticle washing results in OA-coated iron oxide nanoparticles nicely dispersed in chloroform.[205]

The oleic acid coated nanoparticles were found to be spherical in TEM micrographs, and it was also possible to measure their size, being this one about 8.6±1.4 nm. DLS and XRD nanoparticle sizes were 7.7±0.8 nm and 7.3±0.8 nm respectively. It is expectable that standard deviation (SD) of TEM size determination is higher than XRD and DLS due to the number of total counts taken into account to calculate the mean. However, OA-coated nanoparticles size determination was similar for all techniques, and also consistent with previous studies.[205,234]

In accordance with dextran-coated MNPs XRD spectrum, the position and intensities of OA-coated nanoparticles peaks matched well with magnetite and/or maghemite crystals with a cubic spinel structure. Apart from the fact

that the peaks at 23.77º (210) and 26.10º (211) are not observed, it is not possible to reassure that the sample is pure magnetite. The calculated lattice parameter from XRD spectrum is about 8.361±0,004 Å, which is in between maghemite (8,3515 A –JCPDS 39 1346-) and magnetite (8,396 A –JCPDS 19 629-), exhibiting, as a consequence, the presence of both phases.

The magnetization curve of these OA-coated nanoparticles at room temperature showed not coercivity and remanence, indicating that the sample is superparamagnetic at room temperature.

With regard to the functionalization with Pluronic F127 and Tetronic 908 of OA-coated nanoparticles, DLS size determination were performed, as it was not possible to measure through TEM pictures the size of the polymer coated nanoparticles. Tetronic coated MNPs are slightly bigger compare to Pluronic, 120±6 nm and 154±6 nm respectively and these values are in consonance with other block copolymers coated nanoparticles.[207] Z-potential was negative for both, Pluronic F127 coated MNPs were -18±3 mV and -24±3 mV for Tetronic 908 coated MNPs, which confirms the stability of the nanoparticles and prevents aggregation for storage[235].

TGA of OA-, Pluronic F127- and Tetronic 908- coated nanoparticles was performed to quantify OA and polymer contents. For all formulations the percentage of oleic acid present in the MNPs went from 19% to 26%, and the amount of polymer was 35.5% for Pluronic F127 and 42% for Tetronic 908. Because these preparations were washed through magnetic separation, these percentages correspond just to attached polymer. Nevertheless, FTIR spectrums showed that OA-, Pluronic F127- and Tetronic 908-coated MNPs

have all peaks at same wave numbers except for 1100 $cm^{-1}$, which is not present in OA-coated nanoparticles. It has been published that broad bands around 1250-1000 $cm^{-1}$ are due to the $CH_2$ rocking and C-O-C stretch vibrations of Pluronic. The well-defined band at 1100 $cm^{-1}$ is typical for a block copolymer in the optimal formulation in which OA completely covers the iron oxide nanoparticle surface.[205]

MRI T2* weighted images were acquired to calculate the transverse relaxivity and evaluate if these particles are suitable as MRI contrast agents for cell tracking. Four different concentrations of each polymer coated nanoparticles were measured and all parameters, such echo time, repetition time and resolution were adjusted to obtain a well-defined exponential decay. As happened before for dextran coated MNPs, the higher concentrations (0.36 mM for Pluronic F127- and 0.45 mM for Tetronic 908-coated MNPs) of particles cannot be adjusted to an exponential decay because there were not enough data points to perform the adjustment. On the other hand lower concentration data points described a nice adjustment. With this data it was also possible to determine the relaxivity $r_2$ of Pluronic F-127 and Tetronic 908- coated particles, being 398±12 $mM^{-1}s^{-1}$ and 330±20 $mM^{-1}s^{-1}$ respectively. It was expected that both values are similar because they have common magnetic cores, similar coatings and almost equal DLS sizes.

## 4.5. Conclusions

In conclusion, 3 types of superparamagnetic nanoparticles coated with different polymers have been developed. After a careful chemical coprecipitation synthesis processes, spherical-shaped maghetite/maghemite nanoparticles exhibiting superparamagnetic behavior at room temperature were obtained. Two methods were described for core synthesis and polymer coating; *in situ* dextran coated MNPs and two step procedure for Pluronic F127 and Tetronic 908 coating. Both processes resulted in clustered, well-coated and nicely dispersed nanoparticle suspensions in aqueous solutions, being biocompatible and suitable as a MRI contrast agent. Overall, this has resulted in an easy method to produce water-stable superparamagnetic nanoparticles with different size and coatings, which will be essential for next biological and biomedical applications.

# Section IV

## *in vitro* validation

USC
UNIVERSIDADE
DE SANTIAGO
DE COMPOSTELA

In this section we present the *in vitro* validation of the superparamagnetic nanoparticles synthesized in the previous chapter. *In vitro* studies are divided in three chapters, where different aspects of the cell labeling process will be detailed.

As we have mentioned in the introduction section, several studies have demonstrated the need of transfect agents for an efficient labeling process. In previous test (data not shown) we have observed that Pluronic F127- and Tetronic 908-coated MNPs do not need Transfect Agents (TAs), while TAs are indispensable for dextran-coated labeling. Thus, in the first chapter of this section (Chapter 4) we have evaluated the use of TAs for dextran-coated MNPs previously synthesized and its influence in mesenchymal stem cells.

Considering these transfection agent results, in Chapter 5 we have studied the MNPs influence in the well-being of two types of cells. Rat mesenchymal stem cells and the multi-potent neural progenitor cell line C17.2. were used for the in vitro evaluation due to their therapeutic potential. Here, different concentrations and incubation times were evaluated to elucidate which of our synthesized MNP is the most suitable for further *in vivo* cell tracking experiments.

However, prior to *in vivo* studies, in the last chapter of this section we have studied the long-term evolution of the MRI signal of labeled mesenchymal stem cells. We have evaluated *in vitro* how the proliferation rate affects the MRI detection limit and if the labeling has a long-term harmful effect in the cells. In addition, we have also evaluated the magnetic vectorization in vitro with MSCs labeled with our MNPs.

USC
UNIVERSIDADE
DE SANTIAGO
DE COMPOSTELA

# 5. Mesenchymal stem cells labeled with Dextran coated MNPs: Transfection agents evaluation

## 5.1. Hypothesis

The purpose of this chapter is to evaluate the use of Transfect Agents (TAs) for labeling mesenchymal stem cells with dextran-coated magnetic nanoparticles (D-MNPs) and to study the bio-influence of the TA and MNPs in the cells.

## 5.2. Materials & Methods

Seven different conditions were studied: Control, 3 concentrations of Poly-L-Lysine hydrobromide (PLL) (0 μg/mL; 0.75 μg/mL and 1.5 μg/mL) and 2 concentrations of D-MNPs (200 μg/mL and 100 μg/mL) for each PLL condition (n=3 for each condition). To evaluate the viability, two control groups were included, 1) 1.5μg/mL of PLL in cell medium (No D-MNPs) and 2) lysed cells.

### 5.2.1. Cell lines

All experiments were performed using Mesenchymal Stem Cells (MSCs) purchased from Cultrex, Trevigen and were cultured in IMDM (78%), Fetal bovine serum (10%), Horse serum (10%), Penicillin-Streptomycin (1%) all from Gibco Invitrogen, and Amphotericin-B (1%) from Sigma-Aldrich. Cell passage numbers between 7 and 18 were used in these experiments.

### 5.2.2. Dextran-coated superparamagnetic nanoparticles

Dextran coated MNPs (D-MNPs) were synthesized in the Clinical Neuroscience Research Laboratory following the *in situ* protocol described in Chapter 3.

### 5.2.3. Preparation of Poly-L-lysine hydrobromide-coated D-MNPs

Two concentrations of Poly-L-lysine hydrobromide (PLL) (Sigma-Aldrich) were studied: 0.75 μg/mL and 1.5μg/mL. One hour prior to cell incubation, the D-MNPs were mixed with MSCs medium and with 0.75 or 1.5 μg/mL PLL and vigorously shaken.

### 5.2.4. Cell labeling with PLL-coated D-MNPs

Cells were labeled following the protocol described elsewhere [227] with slight modifications. MSCs were incubated with different concentrations of PLL (0; 0.75 and 1.5μg/mL) and D-MNPs (200 and 100 μg of Fe/mL) for 24h. The D-MNP containing medium was removed and the cells were 3 times washed with 1.5 mL of Phosphate Buffered Saline (PBS without $Mg^{2+}$ and $Ca^{2+}$, Gibco Invitrogen) to

remove non-attached MNPs. After washing, the cells were left overnight (12h) in 1mL of fresh medium. The following day the medium was removed, cells were washed once with 1.5mL of PBS, and 0.5mL of EDTA-trypsin (Gibco Invitrogen) was added to detach the cells from the well. The trypsin was neutralized with fresh medium and the detached cells were collected in a Falcon tube. After a mild centrifugation, the supernatant was discarded and the cells were resuspended in fresh medium.

### 5.2.5. Proliferation

To determine the proliferation rate, total cell count was performed with Trypan Blue staining and a Neubauer chamber. Samples were diluted 1:5 with PBS and 1:2 with Trypan Blue.

### 5.2.6. Cell viability assay: Lactate Dehydrogenase Assay (LDH)

For assessing the viability of the cells after labeling compared to control, supernatants from last 12h (fresh medium incubation) were collected in eppendorf tubes. A negative control of lysed cells was also included (death) following manufacturer protocol for lysis. After a mild centrifugation of the supernatants, 75 μL were mixed in a 96 well plate with 150 μL LDH reagents following the manufacturer protocol (Lactate Dehydrogenase Assay Kit. Sigma-Aldrich). After 20 minutes incubation, the plate was read in Synergy2 (Biotek) at 490 nm. To calculate the viability rate respect to control, next equation was applied.

$$Viability\ [\%\ control] = \frac{LDH_{lysed} - LDH_{exposed}}{LDH_{lysed} - LDH_{control}} \cdot 100$$

### 5.2.7. Intracellular iron determination

An amount of 100.000 cells per condition were dissolved in 1mL of 37% HCl (Hydrochloric acid fuming 37% extra pure, Merk) and then 4 mL of DIW was added to reach total volume of 5mL. Iron concentration was determined by inductive coupled plasma optical emission spectroscopy (ICP-OES) (Varian Inc). The intensity of the emission line at 238.204 nm was measured for iron and compared to a standard solution. ICP-OES was performed at the Material Science Institute (MTM), KU Leuven.

### 5.2.8. Prussian Blue staining

Prussian Blue staining was performed to demonstrate the uptake of the D-MNPs by the cells. Labeled cells were planted and after 8h, were washed with PBS and incubated for 20 minutes with a mix of equal parts of aqueous solution of 20% HCl (Hydrochloric acid fuming 37% extra pure, Merk) and aqueous solution of 10% Potassium ferrocyanide Trihydrate (KFe(CN)6.3H2O, FW 422.2, Sigma-Aldrich). After incubation, cells were washed 3 times with PBS and photographs were taken using an inverted microscope (Olympus IX51).

### 5.2.9. Transmission electron microscopy (TEM)

To assess the localization of the D-MNPs in the cell, TEM images of cells were taken. Fixation and postfixation of 500.000 cells were carried out in 2% glutaraldehyde in sodium cacodylate buffer and in 1% $OsO_4$ in the same buffer. Inclusion was done in Spurr's epoxy resin. Semithin sections (0.5 µm) were stained with Toluidine blue and ultrathin sections (100 nm) were stained with uranyl acetate and lead citrate.

### 5.2.10. Magnetic resonance imaging of labeled cells

Agar phantom were made following the procedure described elsewhere.[227] 100.000 cells per condition were scanned in a Bruker Biospec 9.4 T small animal MR scanner (Bruker, Biospin) equipped with actively shielded gradients (400 mT/m). A quadrature radio-frequency transmit-recive resonator was used for data acquisition. T2-weighted images were acquired using a MSME sequence of 10.26 ms echo time, 3 s repetition time, 16 echoes, 14 slices, 1 average, FOV of 7.5 cm x 7.5cm and matrix size of 256 x 256. T2*-weighted images were acquired using a MGE sequence of 4.44 ms echo time, 6.75 ms echo spacing, 1.8 s repetition time, 16 echoes, 14 slices, 2 averages, FOV of 7.5cm x 7.5cm and a matrix size of 256 x 256. Post-processing was performed using ImageJ software (Rasband, W. NIH).

### 5.2.11. Flow cytometry of MSCs

The characterization of MSCs after labeling was performed by flow cytometry analysis. MSCs ($0.25x10^6$ cells) were washed with 50 μL of PBS and stained by incubation (15 minutes) with 5 μL CD90-FITC and 5 μL CD45-PE (BD Pharmigen) antibodies. Firstly, MSCs were separated by their forward and side scattering signal characteristics. MSCs were characterized as CD90+/CD45- cells. For analysis 20.000 cell events were acquired in a BD FACS Aria I (BD Bioscience), and data were analyzed with the use of FACSDiva software (BD Biosciences).

### 5.2.12. Statistical analysis

The statistical analyses of the data were performed using GraphPad Prism 5.01(GraphPad Software, Inc) and mean and standard deviation are presented.

## 5.3. Results

### 5.3.1. Cellular internalization of the MNPs

The amount of internalized iron oxide nanoparticles was determined by ICP and results are plotted in (Figure 28). PLL alone does not increase the Fe signal measured by ICP, which can be observed in control (2.32±0.04 pg/cell) and control+PLL (2.34±0.02 pg/cell). D-MNPs internalization is PLL dose dependent; no PLL labeling group showed similar values than controls, 2.75±0.02 pg/cell for 200 μg/mL D-MNPs and 2.57±0.05 pg/cell for 100 μg/mL D-MNPs. Increasing the PLL concentration in cell medium enhances the uptake, being for 0.75 μg/mL of PLL about 6.1±0.2 pg/cell for 200 μg/mL D-MNPs and 5.27±0.14 pg/cell for 100 μg/mL D-MNPs. For the highest PLL concentration studied (1.5 μg/mL), experimental values were 10.4±0.5 pg/cell for 200 μg/mL D-MNPs and 9.9±0.3 pg/cell for 100 μg/mL D-MNPs.

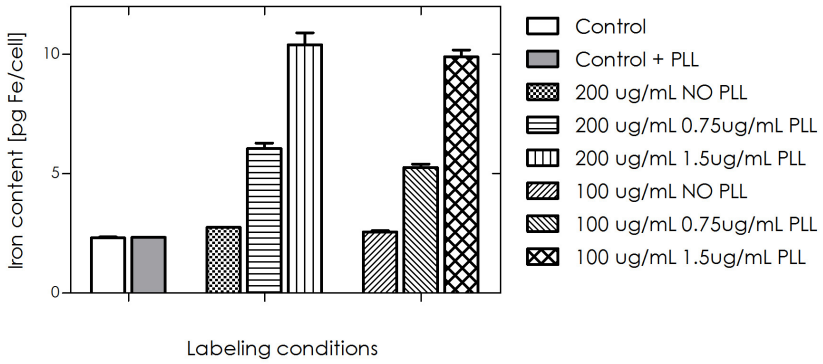


Figure 28: Iron content of D-MNPs labeled and non-labeled MSCs.

### 5.3.2. Magnetic resonance imaging of labeled cells

To assess the D-MNPs internalized contrast, MRI of labeled and control cells was performed. $T_2$ and $T_2$* maps were calculated from $T_2$ and $T_2$* weighted images respectively and $R_2$ and $R_2$* relaxivities were obtained for each concentration using ImageJ software.

Hence, $R_2$ were similar for Control, No PLL 200 μg/mL D-MNPs and No PLL 100μg/mL D-MNPs, being 5.0±0.2 $s^{-1}$, 4.9±1.1 $s^{-1}$ and 5.2±1.2 $s^{-1}$ respectively. For 200 μg/mL D-MNPs, $R_2$ = 7.1±1.4 $s^{-1}$ for 0.75μg/mL and $R_2$ = 8.6±0.8 $s^{-1}$ for 1.5μg/mL. And for 100 μg/mL D-MNPs, $R_2$ = 7.2±0.8 $s^{-1}$ for 0.75μg/mL and $R_2$ = 7.1±1.9 $s^{-1}$ for 1.5μg/mL. Experimental values are plotted in Figure 29, and MSCs T2-weighted images are shown in Figure 30.

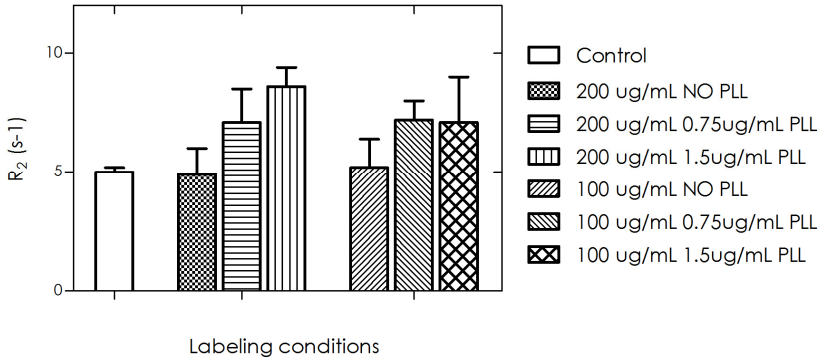


Figure 29: $R_2$ values [$s^{-1}$] of D-MNPs labeled and non-labeled MSCs.

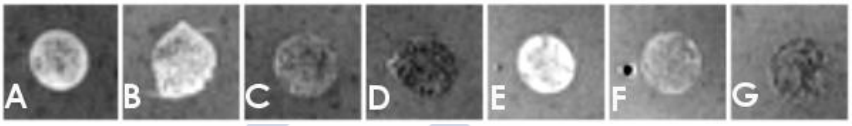


Figure 30: T2-weigthed images of MSCs. (A) Control; (B) 200 μg/mL of D-MNPs and No PLL, (C) 200 μg/mL of D-MNPs and 0.75 μg/mL of PLL, (D) 200 μg/mL of D-MNPs and 1.5 μg/mL of PLL, (E) 100 μg/mL of D-MNPs and No PLL, (F) 100 μg/mL of D-MNPs and 0.75 μg/mL of PLL, (G) 100 μg/mL of D-MNPs and 1.5 μg/mL of PLL.

Accordingly to $T_2$* maps, $R_2$* for Control cells was 15±4 $s^{-1}$. For 200 μg/mL D-MNPs was: 24±5 $s^{-1}$for No PLL, 38±5 $s^{-1}$ for 0.75 μg/mL of PLL and 64.8 ±0.6 $s^{-1}$ for 1.5 μg/mL of PLL. For 100 μg/mL D-MNPs, $R_2$ values were: 20±5 $s^{-1}$ for No PLL, 35±6 $s^{-1}$ for 0.75μg/mL of PLL and 51±9 $s^{-1}$ for 1.5μg/mL of PLL. Experimental values are plotted in Figure 31 and MSCs T2-weighted images are shown in Figure 32.

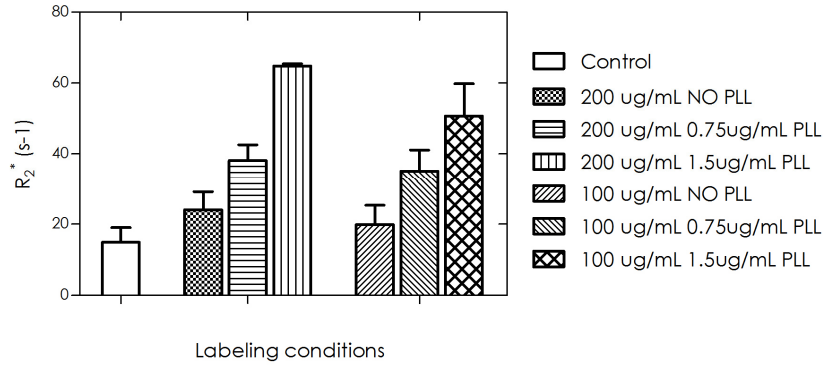


Figure 31: R2* values [s-1] of D-MNPs labeled and non-labeled MSCs.

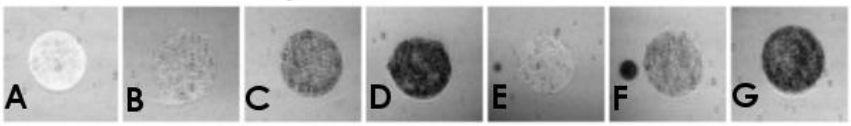


Figure 32: T2*-weigthed images of MSCs. (A) Control; (B) 200 μg/mL of D-MNPs and No PLL, (C) 200 μg/mL of D-MNPs and 0.75 μg/mL of PLL, (D) 200 μg/mL of D-MNPs and 1.5 μg/mL of PLL, (E) 100 μg/mL of D-MNPs and No PLL, (F) 100 μg/mL of D-MNPs and 0.75 μg/mL of PLL, (G) 100 μg/mL of D-MNPs and 1.5 μg/mL of PLL.

## 5.3.3. Optical microscopy and TEM

Two microscopic techniques were used to assess the cellular labeling. The most common is Prussian Blue staining, which shows the MNPs in a blue color in bright field microscopy imaging. Control and No PLL conditions showed no Prussian Blue Figure 33((A), (B), (C), (D)), therefore no cell labeling. Under PLL presence, Prussian Blue staining can be observed, revealing also a dependence between amount of PLL and blue staining as can be seen in Figure 33 (E, F, G, H). For 100 μg/mL of D-MNPs results were similar (Data not shown).

Apart from optical microscopy, transmission electron microscopy was performed. There were no particles in the cells for the No PLL group (Figure 34 (A)). For the rest of the groups, D-MNPs were engulfed in cellular compartments and distributed along the cell. MSCs labeled with 1.5 μg/mL of PLL and 200 μg/mL of D-MNPs are shown in Figure 34 (B), where black circular dots can be observed within the cell cytoplasm. It was also possible to zoom into one labeled cell (see Figure 35 (A), (B), (C)), and the particle pattern inside the endosomes can be observed in Figure 35(C). One important result is that all particles observed were fully internalized and not attached to the cell membrane.

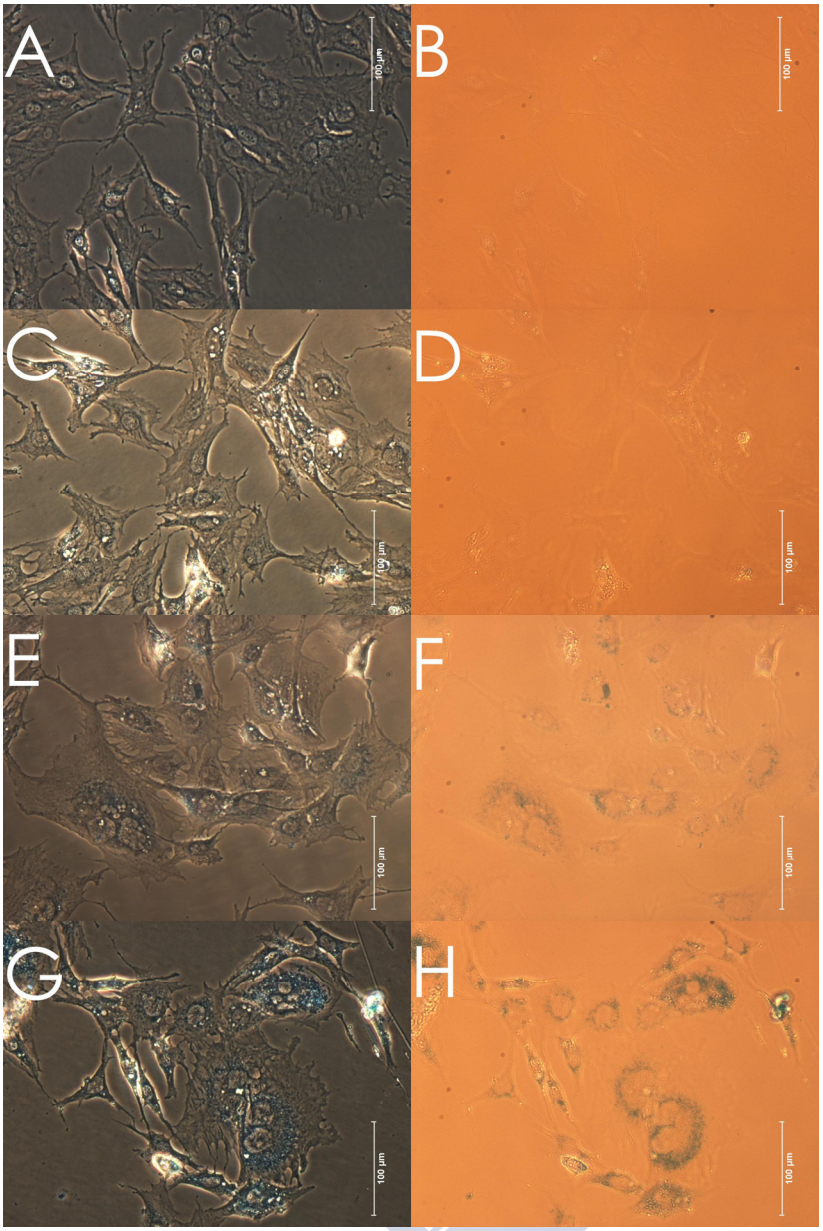


Figure 33: Prussian Blue staining of MSCs. (A) Control cells in phase contrast, (B) Bright field of Control cells, (C) Phase contrast 200 µg/mL D-MNPs and NO PLL, (D) 200 µg/mL D-MNPs and NO PLL in Bright field, (E) Phase contrast 200 µg/mL D-MNPs and 0.75 µg/mL, (F) 200 µg/mL D-MNPs and 0.75 µg/mL in bright field, (G) Phase contrast 200 µg/mL D-MNPs and

1.5 μg/mL PLL and (H) 200 μg/mL D-MNPs and 1.5 μg/mL PLL in bright field.

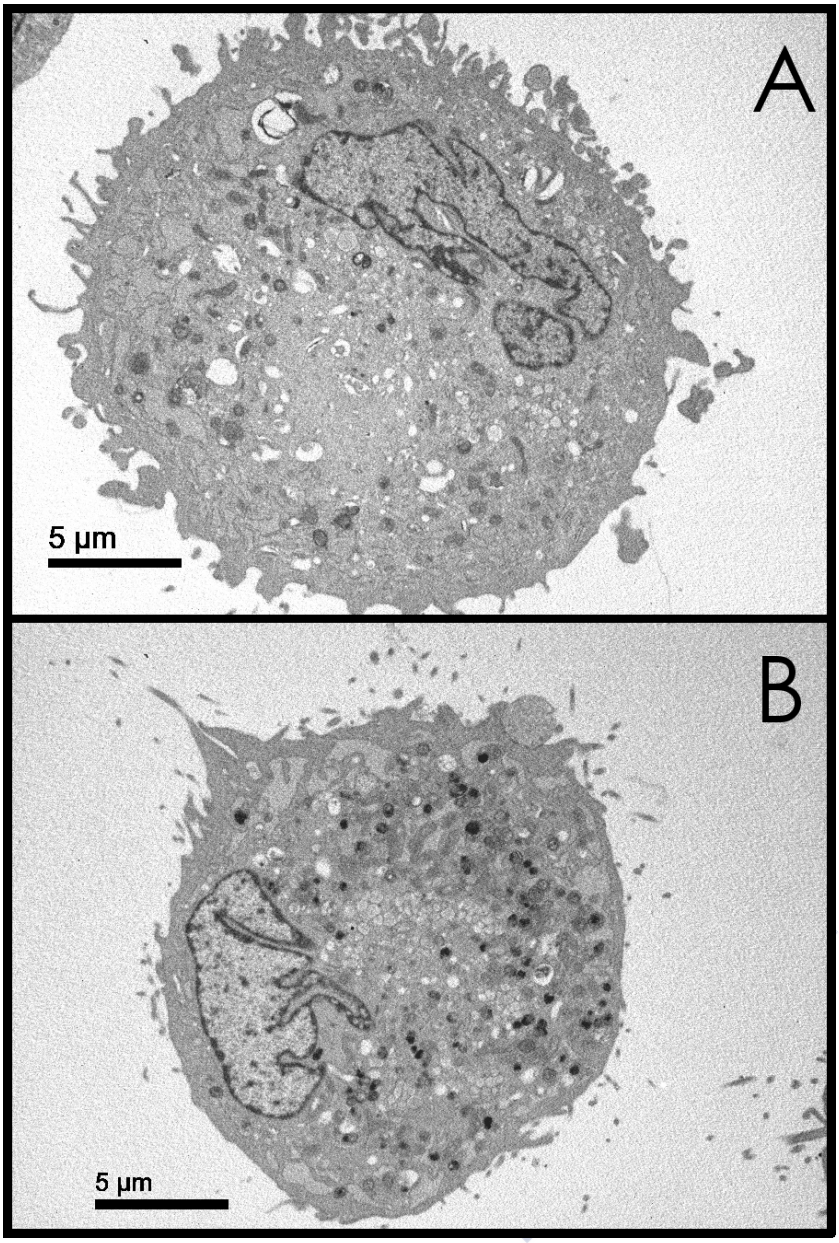


Figure 34: TEM micrographs of (A) No PLL 200 μg/mL D-MNPs, (B) 1.5 μg/mL PLL and 200 μg/mL of D-MNPs.

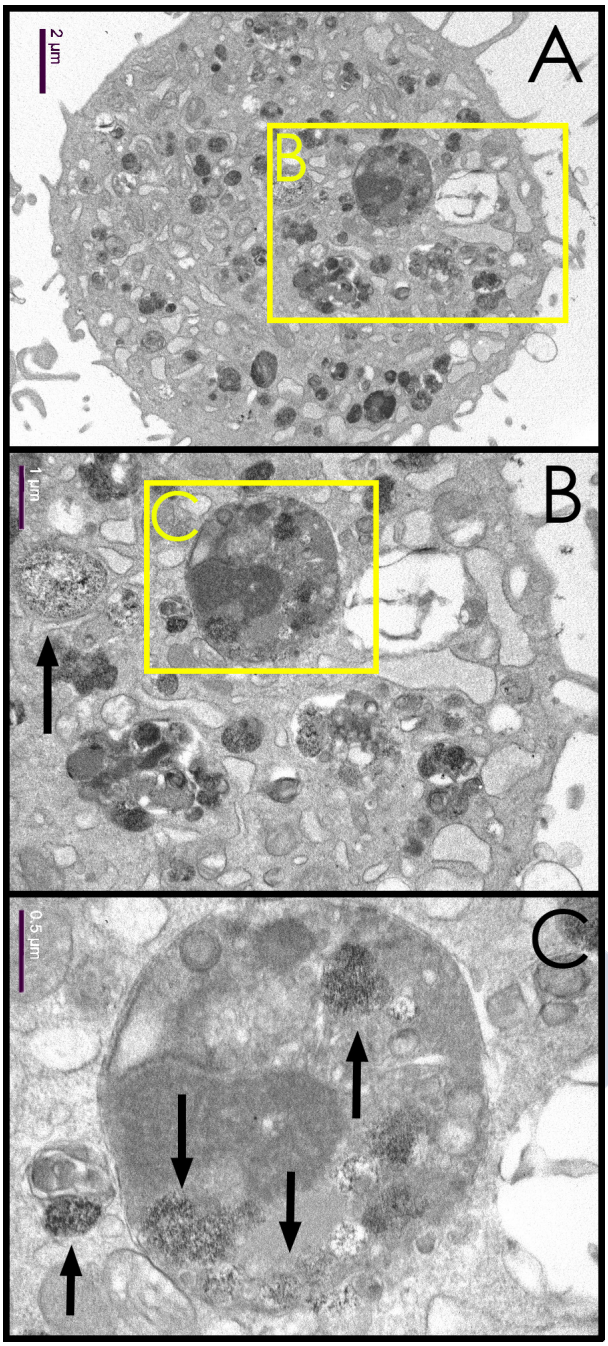


Figure 35: TEM micrographs of 1.5 µg/mL of PLL and 200 µg/mL of D-MNPs (A) one labeled cell, (B) 200x zoom of A, (C) 400x zoom of A.

## 5.3.4. Effect of the MNPs internalization on the cells

Proliferation rate experimental data is referred to control group (100%). There are no significant differences between all groups in terms of proliferation 12h after full D-MNPs internalization, see Figure 36.

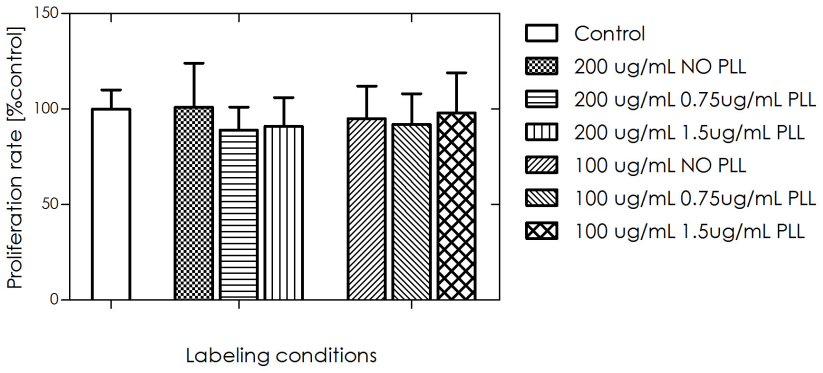


Figure 36: Proliferation rate for D-MNPs labeled and non-labeled MSCs.

Moreover, LDH viability assay performed at same timepoint showed that there are not significant differences between control group and the rest of the conditions. As it is shown in Figure 37, experimental values of control are slightly increased for the presence of PLL and/or D-MNPs but there is not a statistical difference between conditions.

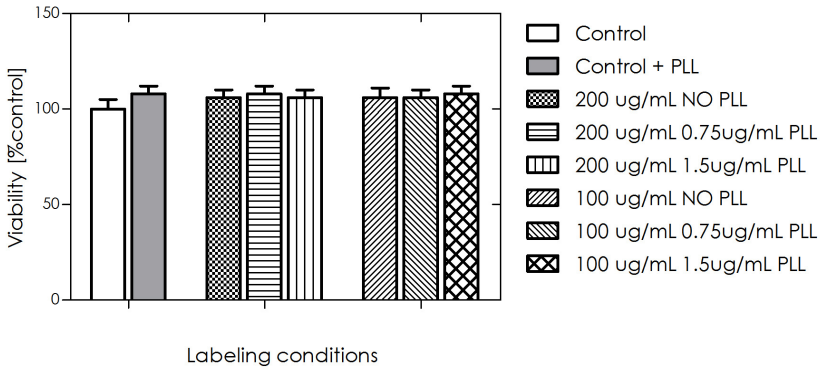


Figure 37: Viability rate [% respect control] for D-MNPs labeled and non-labeled MSCs.

To evaluate phenotypic changes in MSCs after cell tagging, CD45 and CD90 markers for flow cytometry were used to characterize labeled and non-labeled MSC. Figure 38 shows the results for the control and for highest concentration of D-MNPs, 200 μg/mL. There were no differences between all labeling conditions; all groups were negative for CD45 and positive for CD90, as can be observed in Figure 38 (blue). Conditions of 100 μg/mL showed the same behavior (data not shown). It can also be noted that the shape of side scattering (SSC), in Figure 38 is different depending on the condition, and this can be correlated with the amount of PLL and therefore with internalized MNPs. Control and No PLL are more similar between them than 0.75 μg/mL PLL, and 1.5 μg/mL PLL is the most different one. SSC is influenced by the complexity of the sample, pointing out the amount of internal organelles. The more PLL combined with D-MNPs, the more cellular uptake and as a consequence, the higher will be the SSC in flow cytometry.

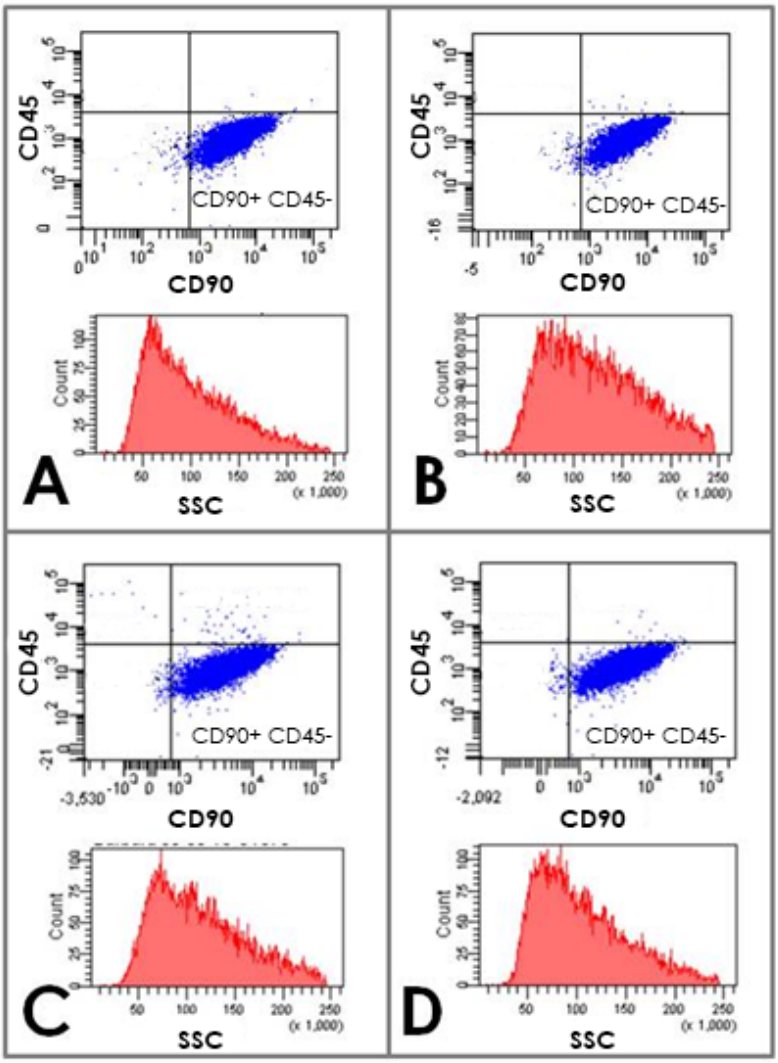


Figure 38: Flow cytometry for CD45 and CD90 markers in MSCs (A) control group, (B) 1.5 μg/mL of PLL for 200 μg/mL of D-MNPs, (C) 0.75 μg/mL of PLL for 200 μg/mL of D-MNPs and (D) No PLL for 200 μg/mL of D-MNPs.

## 5.4. Discussion

In this chapter we have assessed the use of D-MNPs synthesized in the previous chapter as contrast agents for MRI. After D-MNPs characterization, all data suggested their potential for cell tagging; however it was necessary to demonstrate their use, not only because of the magnetic properties, but also to the biocompatibility after labeling as well.

It is known that dextran coated superparamagnetic nanoparticles should be combined with transfect agents for an efficient cell labeling, but the use and concentration of these TAs is limited due to their toxicity[215,236]. In order to assess the labeling capacities of D-MNPs alone or combined with Poly-L-lysine (PLL), different labeling conditions were studied *in vitro*.

PLL is a polycationic amine. The combination of excessive amounts of polycations with cells results in pore formation in the membrane and an intracellular ionic embalance that can ultimately lead to cell death.[216] However, PLL use is widely extended and accepted for nanoparticle cell labeling based upon the toxicity profile and iron content per cell for certain concentrations.[216,227,237-239] To evaluate the optimal cell tagging, 3 concentrations of PLL (No PLL; 0.75 μg/mL and 1.5 μg/mL) combined with 200 and 100 μg/mL of D-MNPs were studied in MSCs culture. The selection of MSCs for *in vitro* labeling validation was made based on their inherent therapeutic capacities and on the promising preclinical results in ischemic stroke.

Our results show that cellular uptake is mainly governed by PLL concentration. The uptake profile is the same for 200 and 100 μg/mL D-MNPs concentrations, and is the amount

of PLL that makes the difference between groups. No PLL conditions showed similar values to the control, meaning no labeling occurs without transfection agents. On the other hand, the highest cell uptake is reached for the highest PLL concentration. For the two D-MNPs concentration studied (200 and 100 μg/mL), double amount of PLL is reflected in almost double amount of internalized iron; For 200 μg/mL of D-MNPs, 6.1±0.2 pg/cell and 10.4±0.5 pg/cell for 0.75 μg/mL and 1.5 μg/mL respectively, and in the other case, for 100 μg/mL of D-MNPs, 5.27±0.14 pg/cell and 9.9±0.3 pg/cell for 0.75 μg/mL and 1.5 μg/mL respectively. But this numerical data must be supported by other technique that shows where those MNPs are, in essence to demonstrate that the measured iron is internalized.

Prussian Blue staining is designed for qualitative detection of MNPs in labeled cells, but using this technique is not possible to discriminate if they are in the cell or attached to the surface. TEM and confocal microscopy are the gold-standard techniques for this task, but because of the non-fluorescent nature of our D-MNPs confocal microscopy will not determine whether D-MNPs are fully internalized. For taking TEM micrographs of labeled and non-labeled cells no staining was needed. A black circular dot distribution along the cytoplasm can easily be observed in labeled cell slices Figure 34 (B) and Figure 35, and going more in detail, D-MNPs can be observed encapsulated in small cellular vesicles. Moreover, no particles are attached to the cell membrane or new endosome-shapes are being formed, what means that the labeling protocol is highly efficient; uptake process has finished and all particles are inside the cell. At this point, it is important to keep in mind that the ultimate goal of cell labeling is to inject and track these cells *in vivo*. Surface associated MNPs of injected cells could result in uncontrolled label transfer to cells of the host,

leading to unspecific contrast and possible misinterpretation of MRI. However, TEM micrographs confirm that labeled cells are Trojan-horse-like; the host will not distinguish between labeled and non-labeled cells, because all D-MNPs are fully internalized.

The efficient cellular uptake and the dependence with the amount of PLL were also seen in MRI. 5000 cells/μL loaded with 5-10 pg/cell can be properly detected in $T_2$ and $T_2$* weighted images in MRI. This is in consonance with other studies that suggested that the minimum concentration for in vivo cell visualization is 2-5 pg/cell. [212,239,240]

Regarding the MNPs biocompatibility, optical and transmission electron microscopy also showed that cells exhibit normal external morphology and internal organelle distribution, as was reported in previous studies.[215,239,241] It is also important to mention at this point that labeled cells were replanted to perform Prussian Blue staining, assessing their further viability. Additionally, cell proliferation after PLL and/or D-MNPs incubation was not affected compared to control group as can be noted in Figure 36. It is well known that high concentrations of PLL are toxic, and can lead to cell death,[215,236] but in our experiments we have seen that under 0.75 μg/mL and 1.5 μg/mL of PLL incubation, the proliferation rate is not diminished after cell labeling.

Furthermore it is also crucial to study the toxicity-viability induced by PLL and/or D-MNPs. LDH viability assay is a widely used procedure which, measuring the amount of cytoplasmic LDH released into the medium, evaluates cell viability as well as a function of membrane integrity. However, it has been described that MNPs presence in medium induces artifacts in several viability assays, also in LDH, mainly due to the interactions between the particles

and the reagents from the assay.[242,243] Nevertheless, our labeling protocol is compatible with LDH assay; cell viability can be evaluated once the labeling medium is removed and fresh medium is added and incubated for 12h. As it has been already mentioned, after the labeling process, MNPs are fully internalized so no free particles can be found in cell medium, and therefore no interaction can occur with the LDH assay. At this point, in regard to LDH viability results, there are no significant differences between groups. This result is in concert with the proliferation data and the TEM pictures, assessing that the incubation with these amounts of PLL and/or D-MNPs does not have a harmful effect on the cells.

Addressing to the phenotype characterization, labeled and non-labeled cells exhibited a similar surface markers profile in flow cytometry analysis, negative for the hematopoietic marker CD45 and positive for the mesenchymal progenitor marker CD90. So no adverse effect was detected in MSCs after PLL and/or D-MNPs incubations with regard to CD45 and CD90, which is in agreement with previous published studies using D-MNPs.[236,244]

## 5.5. Conclusions

This chapter has demonstrated that our synthesized dextran-coated superparamagnetic nanoparticles in combination with a transfection agent as Poly-L-lysine can be sufficiently taken up by potential therapeutic cells as mesenchymal stem cells. The labeling protocol ensured a full internalization of the PLL coated D-MNPs without affecting the wellbeing of the cells. The relatively high uptake rate depends on the PLL concentration, and cells can be properly detected in MRI, providing promising results for further *in vivo* applications. In conclusion, the results of this study showed that our synthesized dextran coated superparamagnetic nanoparticles combined with 1.5 µg/mL of PLL are an efficient and biocompatible MRI contrast agent for cell tracking.

USC
UNIVERSIDADE
DE SANTIAGO
DE COMPOSTELA

# 6. Dextran-, Pluronic F127- and Tetronic 908-coated superparamagnetic nanoparticles: *In vitro* validation

## 6.1. Hypothesis

The aim of the present chapter is to evaluate the biocompatibility of our synthesized dextran-, pluronic F127- and tetronic 908-coated MNPs in 2 different cell types, MSCs and C17.2., combining D-MNPs with PLL for an efficient cellular uptake. Moreover, we will study the influence of the incubation time and MNPs concentration in the well-being, in the uptake, and therefore in the MRI signal produced by these labeled cells.

## 6.2. Materials & Methods

### 6.2.1. Cell lines

Mesenchymal Stem Cells (MSCs) were purchased from Cultrex, Trevigen and cultured in IMDM (78%), Fetal bovine serum (10%), Horse serum (10%), Penicillin-Streptomycin (1%) all from Gibco Invitrogen, and Amphotericin-B (1%) from Sigma-Aldrich. Cell passage numbers between 7 and 18 were used in these experiments.

Multi-potent neural progenitor cell line C17.2 were characterized by Markus Auswendt and kindly donated by Prof. Mathias Hoehn (Max-Planck Institute, Cologne, Germany) and cultured in DMEM (78%), Fetal bovine serum (10%), Horse serum (5%), Penicillin-Streptomycin (1%) all from Gibco Invitrogen, and Amphotericin-B (1%) from Sigma-Aldrich.

### 6.2.2. Dextran-, Pluronic F127- Tetronic 908-coated superparamagnetic nanoparticles

Dextran coated MNPs (D-MNPs), Pluronic F127 coated MNPS (P-MNPs) and Tetronic 908 coated MNPS (T-MNPs) were synthesized in the Clinical Neuroscience Research Laboratory following the protocols described in chapter 3.

### 5.2.3. Preparation of Poly-L-lysine hydrobromide-coated D-MNPs

One hour prior to cell incubation, different concentrations of D-MNPs (500 and 250 μg/mL) were mixed with MSCs or C17.2 mediums and with 1.5 μg/mL PLL (Sigma-Aldrich) and vigorously shaken.

### 6.2.3. Cell labeling with MNPs

Cells were labeled with 3 different types of MNPs, as it has been mentioned before. Two concentrations (500 and 250 μg/mL for D-MNPs and 35 and 15 μg/mL for P-MNPs and T-MNPs) respectively; and two incubations times (24h and 6h) were studied in this chapter (n=6 for each condition). Labeling protocol was the same for all groups.

Cells were labeled following the protocol described elsewhere [227] with slight modifications, already used in the previous chapter. Cells were incubated with different concentrations of MNPs for 6h or 24h. The MNP containing medium was removed and the cells were 3 times washed with 1.5 mL of Phosphate Buffered Saline (PBS without $Mg^{2+}$ and $Ca^{2+}$, Gibco Invitrogen) to remove non-attached MNPs. After washing, the cells were left overnight (12h) in 1 mL of fresh medium. The following day the medium was removed, cells were washed once with 1.5mL of PBS and 0.5mL of EDTA-trypsin (Gibco Invitrogen) was added to detach the cells from the well. The trypsin was neutralized with fresh medium and the detached cells were collected in a Falcon tube. After a mild centrifugation, the supernatant was discarded and the cells were resuspended in fresh medium.

### 6.2.4. Proliferation

To determine the proliferation rate, total cell count was performed with Trypan Blue staining and a Neubauer chamber. Samples were diluted 1:5 with PBS and 1:2 with Trypan Blue.

### 6.2.5. Cell viability assay: Lactate Dehydrogenase Assay (LDH)

For assessing the viability of the cells after labeling compared to control, supernatants from last 12h (fresh medium incubation) were collected in eppendorf tubes. A negative control of lysed cells was also included. After a mild centrifugation of the supernatants, 75µL were mixed in a 96 well plate with 150µL LDH reagents following the manufacturer protocol (Lactate Dehydrogenase Assay Kit. Sigma-Aldrich). After 20 minutes incubation, the plate was read in Synergy2 (Biotek) at 490nm. To calculate the viability rate respect to control, next equation was applied.

$$Viability\ [\%\ control] = \frac{LDH_{lysed} - LDH_{exposed}}{LDH_{lysed} - LDH_{control}} \cdot 100$$

### 6.2.6. Intracellular iron determination

An amount of 100.000 cells per condition was dissolved in 1 mL of 37% HCl (Hydrochloric acid fuming 37% extra pure, Merk) and then 4 mL of DIW was added to reach total volume of 5 mL. Iron concentration was determined by inductive coupled plasma optical emission spectroscopy (ICP-OES) (Varian Inc). The intensity of the emission line at 238.204 nm was measured for iron and compared to a standard solution. ICP-OES was performed at CACTUS-Lugo (University of Santiago de Compostela).

### 6.2.7. Prussian Blue staining

Prussian Blue staining was performed to demonstrate the uptake of the MNPs by the cells. Labeled cells were planted and after 8h, were washed with PBS and incubated for 20 minutes with a mix of equal parts of aqueous solution of 20%

HCl and aqueous solution of 10% Potassium ferrocyanide Trihydrate (KFe(CN)6.3H2O, FW 422.2, Sigma-Aldrich). After incubation, cells were washed 3 times with PBS and photographs were taken using an inverted microscope (Olympus IX51).

### 6.2.8. Transmission electron microscopy (TEM)

To assess the localization of the D-MNPs in the cell, TEM images of cells were taken. Fixation and postfixation of 500.000 cells were carried out in 2% glutaraldehyde in sodium cacodylate buffer and in 1% $OsO_4$ in the same buffer. Inclusion was done in Spurr's epoxy resin. Semithin sections (0.5 µm) were stained with Toluidine blue and ultrathin sections (100 nm) were stained with uranyl acetate and lead citrate.

### 6.2.9. Magnetic resonance imaging of labeled cells

Agar phantom was made following the procedure described elsewhere.[227] 100.000 cells per condition were scanned in a Bruker Biospec 9.4 T small animal MR scanner (Bruker, Biospin, Ettlingen, Germany) equipped with actively shielded gradients (400 mT/m). A quadrature radio-frequency transmit-receive resonator was used for data acquisition. T2-weighted images were acquired using a MSME sequence of 10.26 ms echo time, 3 s repetition time, 16 echoes, 14 slices, 1 average, FOV of 7.5 cm x 7.5cm and matrix size of 256 x 256. T2*-weighted images were acquired using a MGE sequence of 4.44 ms echo time, 6.75 ms echo spacing, 1.8 s repetition time, 16 echoes, 14 slices, 2 averages, FOV of 7.5cm x 7.5cm and a matrix size of 256 x

256. Post-processing was performed using ImageJ software (Rasband, W. NIH).

### 6.2.10. Statistical analysis

The statistical analysis of the data was performed using GraphPad Prism 5.01 (GraphPad Software, Inc). For descriptive analyses, means and standard deviations were calculated for the normally distributed continuous variables. For confirmatory analyses one-way ANOVA was performed to calculate overall p-values for the comparison of the different groups for each variable. The global significance level for all statistical test procedures was chosen as $\alpha$=0.05.

## 6.3. Results

Thirteen conditions were studied for each type of cell. Every group and the nomenclature assigned are presented below:

*<Polymer>-MNPs <Concentration> <Incubation time>*

- Control
- D-MNPs 500 24h: Cells labeled with 500 μg/mL D-MNPs with1.5 μg/mL of PLL incubated for 24 h.
- D-MNPs 500 6 h: Cells labeled with 500 μg/mL D-MNPs with1.5 μg/mL of PLL incubated for 6 h.
- D-MNPs 250 24 h: Cells labeled with 250 μg/mL D-MNPs with1.5 μg/mL of PLL incubated for 24 h.
- D-MNPs 250 6h: Cells labeled with 250 μg/mL D-MNPs with1.5 μg/mL of PLL incubated for 6 h.
- P-MNPs 35 24h: Cells labeled with 35 μg/mL P-MNPs incubated for 24 h.
- P-MNPs 35 6h: Cells labeled with 35 μg/mL P-MNPs incubated for 6 h.
- P-MNPs 15 24h: Cells labeled with 15 μg/mL P-MNPs incubated for 24 h.
- P-MNPs 15 6h: Cells labeled with 15 μg/mL P-MNPs incubated for 6 h.
- T-MNPs 35 24h: Cells labeled with 35 μg/mL P-MNPs incubated for 24 h.
- T-MNPs 35 6h: Cells labeled with 35 μg/mL P-MNPs incubated for 6 h.
- T-MNPs 15 24h: Cells labeled with 15 μg/mL P-MNPs incubated for 24 h.
- T-MNPs 15 6h: 15 μg/mL P-MNPs incubated for 6 h.

## 6.3.1. Cellular internalization of the MNPs

The amount of internalized iron oxide nanoparticles was determined by ICP and results are shown in Table 1 and Figure 39. All labeling conditions showed variable amount of iron internalization depending on MNPs concentration in the medium and also on the incubation time.

| | **MSCs** | | **C17.2** | |
|---|---|---|---|---|
| | *Mean [pg]* | *SD* | *Mean [pg]* | *SD* |
| Control | 0.4 | 0.1 | 0.4 | 0.0 |
| D-MNPs 500 24h | 15 | 2 | 9.3 | 1.6 |
| D-MNPs 250 24h | 8.7 | 0.9 | 8.4 | 0.1 |
| D-MNPs 500 6h | 7.7 | 0.9 | 4.8 | 0.7 |
| D-MNPs 250 6h | 5.9 | 0.9 | 5.1 | 0.3 |
| P-MNPs 35 24h | 36.8 | 1.4 | 28 | 7 |
| P-MNPs 15 24h | 16.2 | 0.4 | 9.7 | 0.8 |
| P-MNPs 35 6h | 39 | 3 | 33 | 3 |
| P-MNPs 15 6h | 8.9 | 0.5 | 12.7 | 0.8 |
| T-MNPs 35 24h | 37 | 3 | 39 | 1 |
| T-MNPs 15 24h | 9.9 | 1.5 | 14 | 2 |
| T-MNPs 35 6h | 36 | 4 | 16.7 | 1.5 |
| T-MNPs 15 6h | 12.4 | 1.4 | 8 | 3 |

Table 1: Iron content per cell [pg]

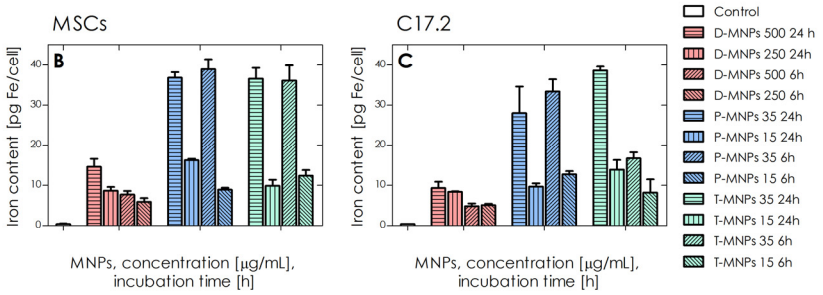


Figure 39: Iron internalization [pg/cell] for all labeling conditions.

### 6.3.2. Magnetic resonance imaging of labeled cells

To assess the contrast generated by MNPs internalization, MRI of all labeling conditions was performed. $T_2$ and $T_2$* maps were calculated from $T_2$ and $T_2$* weighted images respectively, and $R_2$ and $R_2$* relaxivities were obtained for each condition using ImageJ. $R_2$* values are shown in Table 2 and plotted in Figure 40. Moreover, the contrast generated by the labeled and non-labeled cells can be observed in the first echo of $T_2$* weighted images in Figure 41 and Figure 42 for MSCs and C17.2 respectively.

| | **MSCs** | | **C17.2** | |
|---|---|---|---|---|
| | *Mean* $[s^{-1}]$ | *SD* | *Mean* $[s^{-1}]$ | *SD* |
| Control | 32 | 5 | 31 | 5 |
| D-MNPs 500 24h | 69 | 23 | 60 | 3 |
| D-MNPs 250 24h | 57 | 17 | 59 | 5 |
| D-MNPs 500 6h | 62 | 21 | 41 | 7 |
| D-MNPs 250 6h | 47 | 14 | 40 | 12 |
| P-MNPs 35 24h | 69 | 24 | 63 | 24 |
| P-MNPs 15 24h | 60 | 21 | 66 | 5 |
| P-MNPs 35 6h | 71 | 32 | 53 | 14 |
| P-MNPs 15 6h | 78 | 29 | 58 | 12 |
| T-MNPs 35 24h | 53 | 26 | 57 | 31 |
| T-MNPs 15 24h | 69 | 10 | 67 | 11 |
| T-MNPs 35 6h | 72 | 16 | 62 | 8 |
| T-MNPs 15 6h | 72 | 22 | 48 | 8 |

Table 2: $R_2$* of different label conditions determined by MRI in an agar phantom with concentrations of 500 cell/μL.

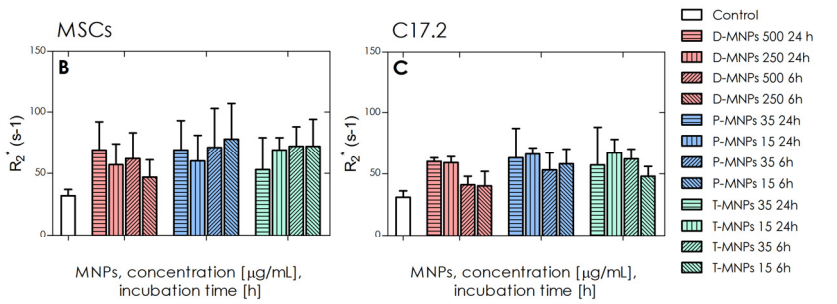


Figure 40: $R_2$* of different label conditions. determined by MRI in an agar phantom with concentrations of 500 cell/µL.

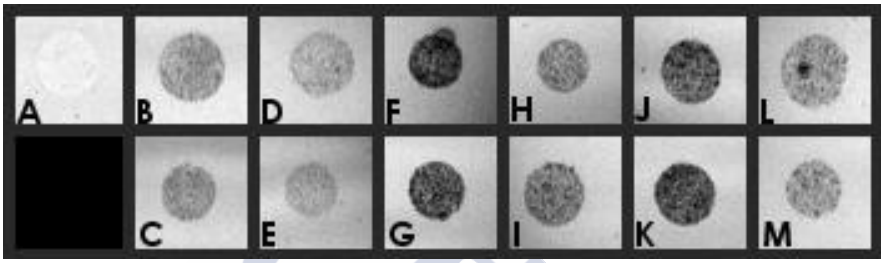


Figure 41: First echo of $T_2$* weighted images of MSCs for all conditions: (A) Control, (B) D-MNPs 500 24h, (C) D-MNPs 500 6h, (D) D-MNPs 250 24h, (E) D-MNPs 250 6h, (F) P-MNPs 35 24h, (G) P-MNPs 35 6h, (H) P-MNPs 15 24h, (I) P-MNPs 15 6h, (J) T-MNPs 35 24h, (K) T-MNPs 35 6h, (L) T-MNPs 15 24h and (M) T-MNPs 15 6h.

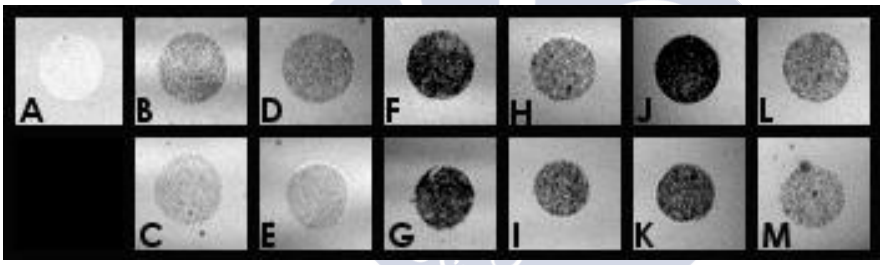


Figure 42: First echo of $T_2$* of C17.2 for all conditions: (A) Control, (B) D-MNPs 500 24h, (C) D-MNPs 500 6h, (D) D-MNPs 250 24h, (E) D-MNPs 250 6h, (F) P-MNPs 35 24h, (G) P-MNPs 35 6h, (H) P-MNPs 15 24h, (I) P-MNPs 15 6h, (J) T-MNPs 35 24h, (K) T-MNPs 35 6h, (L) T-MNPs 15 24h and (M) T-MNPs 15 6h.

In the same way, R2 values are shown in Table 3 and plotted in Figure 43. Moreover, the contrast generated by the labeled and non-labeled cells can be observed the first echo of T2 weighted images in Figure 44 and Figure 45 for MSCs and C17.2 respectively.

| | **MSCs** | | **C17.2** | |
|---|---|---|---|---|
| | *Mean [s⁻¹]* | *SD* | *Mean [s⁻¹]* | *SD* |
| Control | 8,3 | 2,1 | 5,6 | 2,3 |
| D-MNPs 500 24h | 10,2 | 1,2 | 9,1 | 0,3 |
| D-MNPs 250 24h | 11,0 | 0,8 | 9,4 | 0,5 |
| D-MNPs 500 6h | 11,2 | 2,7 | 9,2 | 0,8 |
| D-MNPs 250 6h | 10,6 | 2,5 | 8,3 | 2,3 |
| P-MNPs 35 24h | 16,0 | 2,3 | 12,1 | 0,4 |
| P-MNPs 15 24h | 12,4 | 0,1 | 8,9 | 0,5 |
| P-MNPs 35 6h | 13,3 | 1,0 | 11,4 | 2,5 |
| P-MNPs 15 6h | 10,8 | 3,1 | 8,0 | 4,4 |
| T-MNPs 35 24h | 13,4 | 0,8 | 15,3 | 0,9 |
| T-MNPs 15 24h | 11,7 | 2,0 | 10,4 | 0,4 |
| T-MNPs 35 6h | 10,1 | 1,8 | 11,6 | 1,7 |
| T-MNPs 15 6h | 12,1 | 1,8 | 8,6 | 0,5 |

Table 3: $R_2$ of different label conditions determined by MRI in an agar phantom with concentrations of 500 cell/μL.

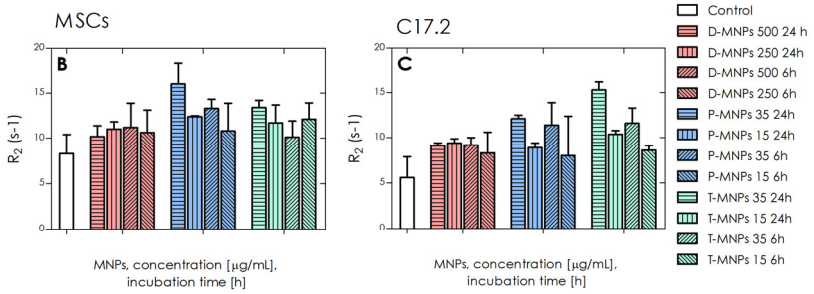


Figure 43: $R_2$ of different label conditions determined by MRI in an agar phantom with concentrations of 500 cell/μL.

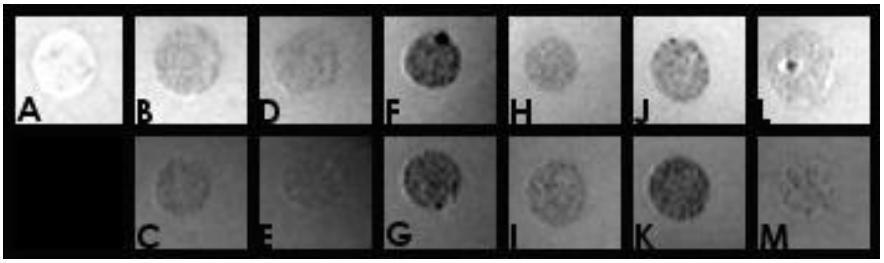


Figure 44: First echo of $T_2$ of MSCs for all conditions: (A) Control, (B) D-MNPs 500 24h, (C) D-MNPs 500 6h, (D) D-MNPs 250 24h, (E) D-MNPs 250 6h, (F) P-MNPs 35 24h, (G) P-MNPs 35 6h, (H) P-MNPs 15 24h, (I) P-MNPs 15 6h, (J) T-MNPs 35 24h, (K) T-MNPs 35 6h, (L) T-MNPs 15 24h and (M) T-MNPs 15 6h.

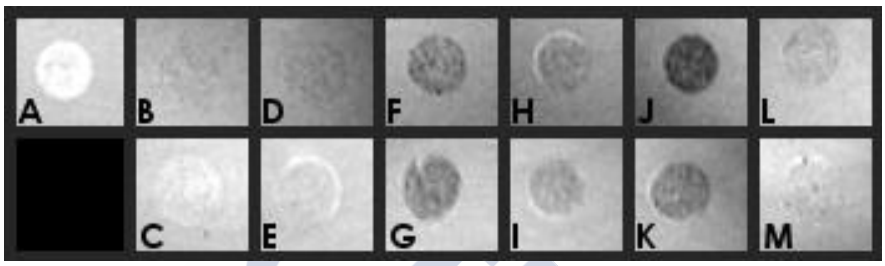


Figure 45: First echo of $T_2$ of C17.2 for all conditions: ((A) Control, (B) D-MNPs 500 24h, (C) D-MNPs 500 6h, (D) D-MNPs 250 24h, (E) D-MNPs 250 6h, (F) P-MNPs 35 24h, (G) P-MNPs 35 6h, (H) P-MNPs 15 24h, (I) P-MNPs 15 6h, (J) T-MNPs 35 24h, (K) T-MNPs 35 6h, (L) T-MNPs 15 24h and (M) T-MNPs 15 6h.

### 6.3.3. Optical microscopy and TEM

In order to assess and visualize the MNPs uptake, Prussian Blue staining and TEM micrographs were taken. All labeling conditions and cell types showed Prussian Blue staining, supporting ICP and MRI quantitative data Figure 46 and Figure 47.

These results were further confirmed by TEM. All incubation conditions for MSCs and C17.2 resulted in cell labeling with all different MNPs. In addition, TEM pictures showed a nucleus free of MNPs and a variable number of MNPs in the cytoplasm (Figure 48). Cellular vesicles containing D-MNPs exhibit a circular shape in where MNPs are condensed (Figure 49(A)), meanwhile vesicles morphology for P-MNPs and T-MNPs is not well defined, as it can be observed Figure 49 for P-MNPs.

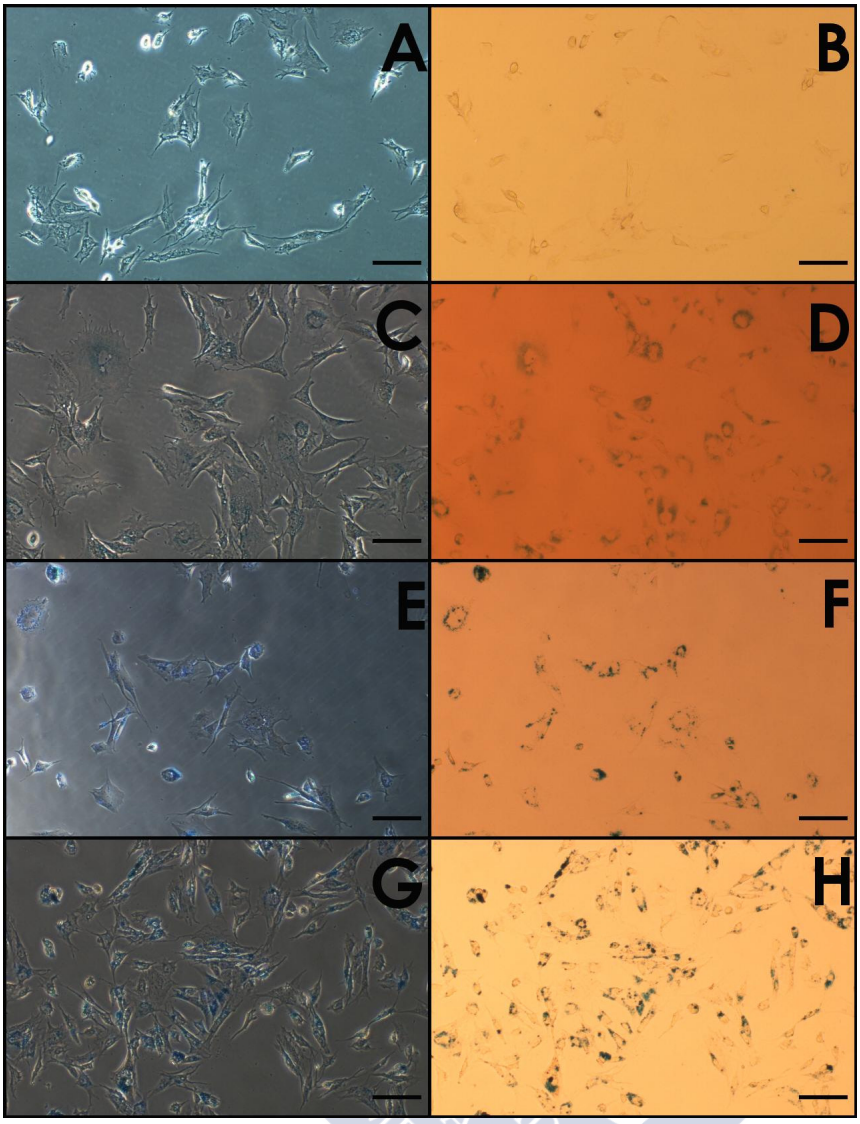


Figure 46: Prussian Blue staining of MSCs. (A) Phase contrast microscopy of control cells, (B) Bright field microscopy of control cells, (C) Phase contrast microscopy of D-MNPs 500 24h, (D) Bright field microscopy of D-MNPs 500 24h, (E) Phase contrast microscopy of P-MNPs 35 24h, (F) bright field microscopy of P-MNPs 35 24h, (G) Phase contrast microscopy of T-MNPs 35 24h, (H) Bright field microscopy of T-MNPs 35 24h. (Scale bar 100μm)

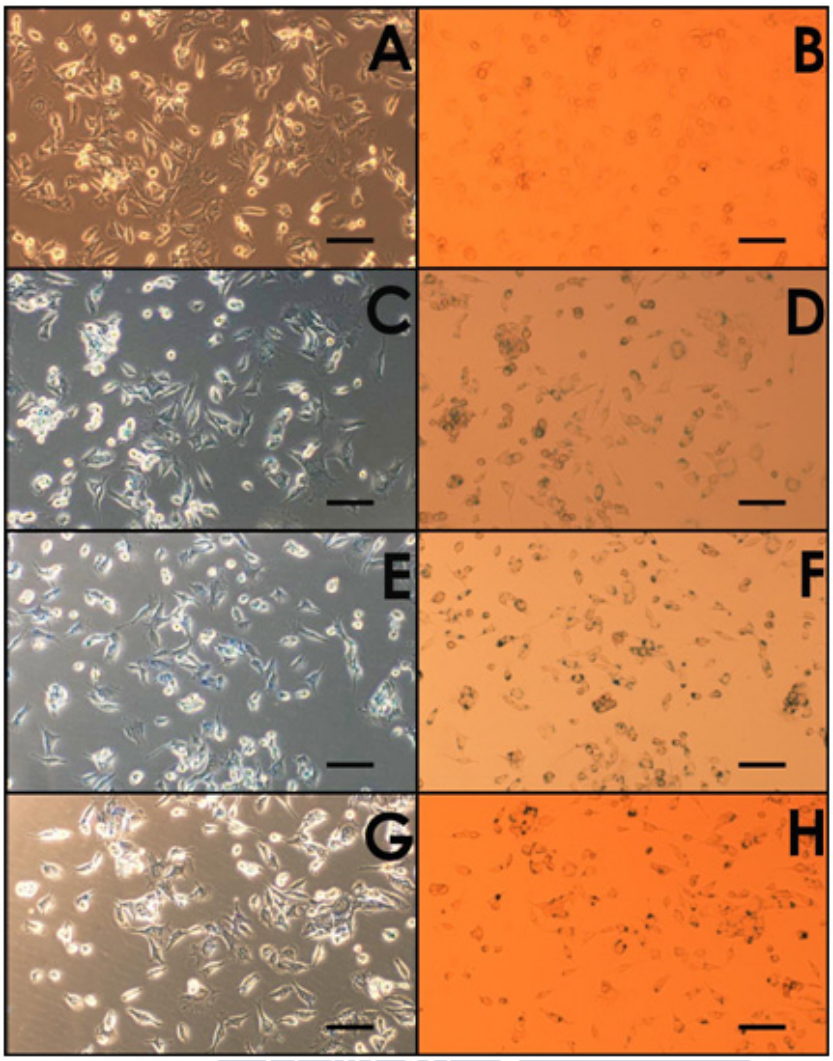


Figure 47: Prussian Blue staining of C17.2. (A) Phase contrast microscopy of control cells, (B) bright field microscopy of control cells, (C) Phase contrast microscopy of D-MNPs 500 24h, (D) Bright field microscopy of D-MNPs 500 24h, (E) Phase contrast microscopy of P-MNPs 35 24h, (F) Bright field microscopy of P-MNPs 35 24h, (G) Phase contrast microscopy of T-MNPs 35 24h, (H) Bright field microscopy of T-MNPs 35 24h. (Scale bar 100μm)

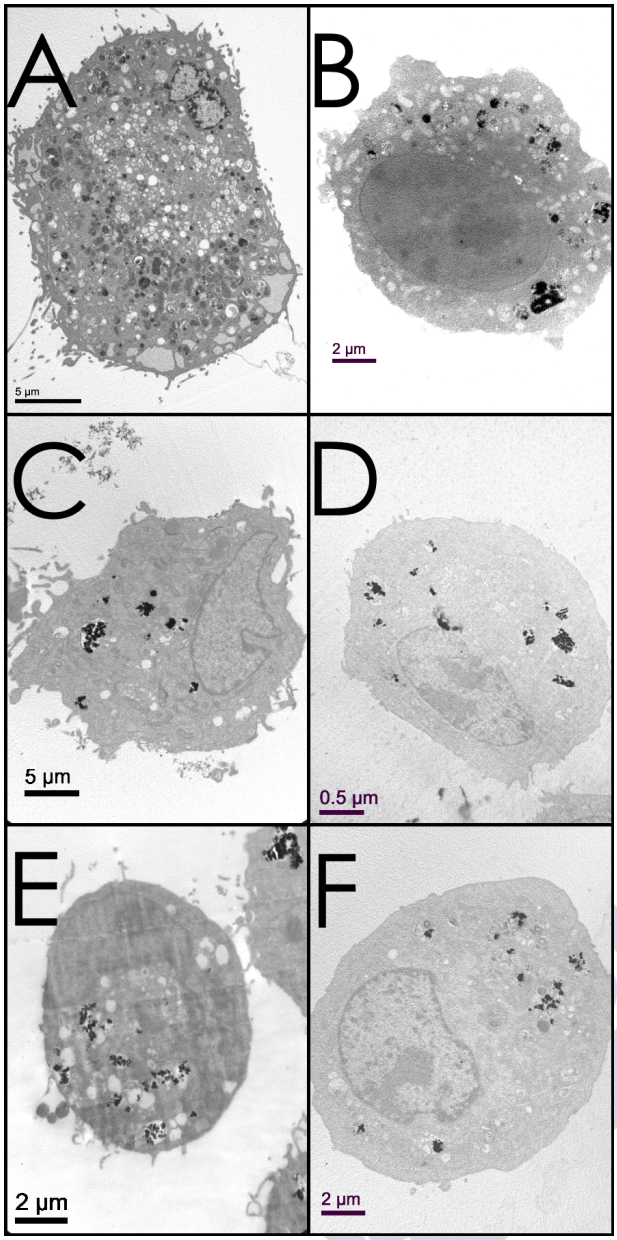


Figure 48: (A) MSC labeled with D-MNPs 500 24h, (B) MSCs labeled with P-MNPs 35 24h, (C) MSCs labeled with T-MNPs 35 24h, (D) C17.2 labeled with D-MNPs 500 24h, (E) C17.2 labeled with P-MNPs 35 24h, (F) C17.2 labeled with T-MNPs 35 24h

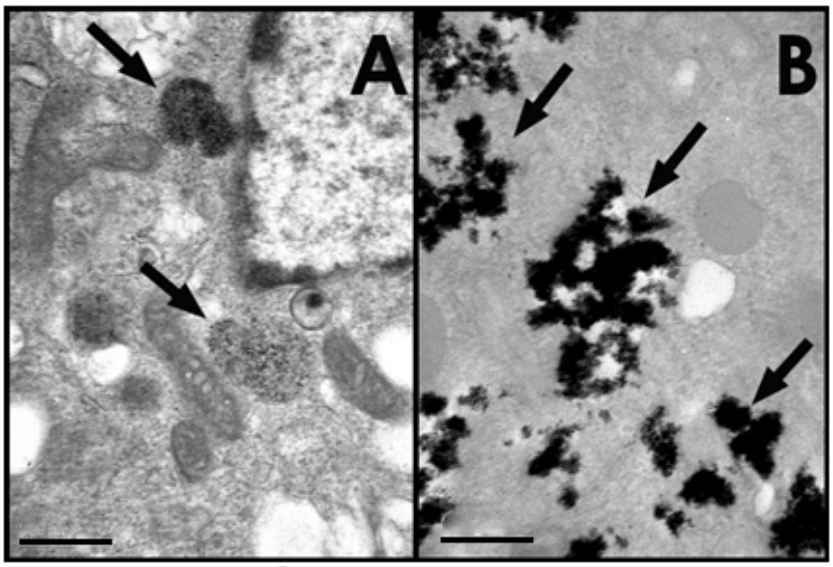


Figure 49: MNPs internalized. (A) PLL coated D-MNPs internalized in an endosome in the cellular cytoplasm (1.5 µg/mL PLL and 500 µg/mL D-MNPs incubated for 24h), (B) P-MNPs internalized in an endosome in the cellular cytoplasm (35 µg/mL of P-MNPs incubated for 24h). (Scale bar 500 nm)

## 6.3.4. Effect of the MNPs internalization in the cells

Proliferation rate experimental data is referred to control group (%). Experimental values are shown in Table 4 and plotted in Figure 50 (A) and (B). For the highest concentrations of MNPs there is a reduction in proliferation rate respect to control for both cell types.

| | MSCs | | C17.2 | |
|---|---|---|---|---|
| | *Mean [%]* | *SD* | *Mean [%]* | *SD* |
| Control | 100 | 18 | 100 | 4 |
| D-MNPs 500 24 h | 67 | 19 | 80 | 15 |
| D-MNPs 250 24h | 84 | 22 | 66 | 20 |
| D-MNPs 500 6h | 86 | 10 | 84 | 22 |
| D-MNPs 250 6h | 102 | 9 | 76 | 10 |
| P-MNPs 35 24h | 46 | 9 | 62 | 4 |
| P-MNPs 15 24h | 51 | 11 | 91 | 26 |
| P-MNPs 35 6h | 61 | 16 | 66 | 9 |
| P-MNPs 15 6h | 87 | 2 | 67 | 16 |
| T-MNPs 35 24h | 44 | 4 | 50 | 19 |
| T-MNPs 15 24h | 73 | 5 | 55 | 10 |
| T-MNPs 35 6h | 75 | 6 | 65 | 7 |
| T-MNPs 15 6h | 62 | 17 | 79 | 3 |

Table 4: Proliferation rate [%] respect to control.

Moreover, LDH viability assay showed that there are not significant differences between control group and any labeling condition for MSCs and well as for C17.2 (Table 5 and Figure 50 (C) and (D)).

| | MSCs | | C17.2 | |
|---|---|---|---|---|
| | *Mean [%]* | *SD* | *Mean [%]* | *SD* |
| Control | 100 | 2 | 100 | 4 |
| D-MNPs 500 24 h | 96 | 2 | 102 | 4 |
| D-MNPs 250 24h | 95 | 2 | 102 | 3 |
| D-MNPs 500 6h | 97 | 3 | 100 | 3 |
| D-MNPs 250 6h | 98 | 1 | 98 | 5 |
| P-MNPs 35 24h | 97 | 1 | 97 | 4 |
| P-MNPs 15 24h | 95 | 1 | 100 | 3 |
| P-MNPs 35 6h | 98 | 2 | 98 | 3 |
| P-MNPs 15 6h | 100 | 2 | 98 | 3 |
| T-MNPs 35 24h | 96 | 2 | 100 | 3 |
| T-MNPs 15 24h | 97 | 2 | 100 | 3 |
| T-MNPs 35 6h | 100 | 2 | 98 | 3 |
| T-MNPs 15 6h | 99 | 2 | 100 | 3 |

Table 5: Viability [%] respect to control.

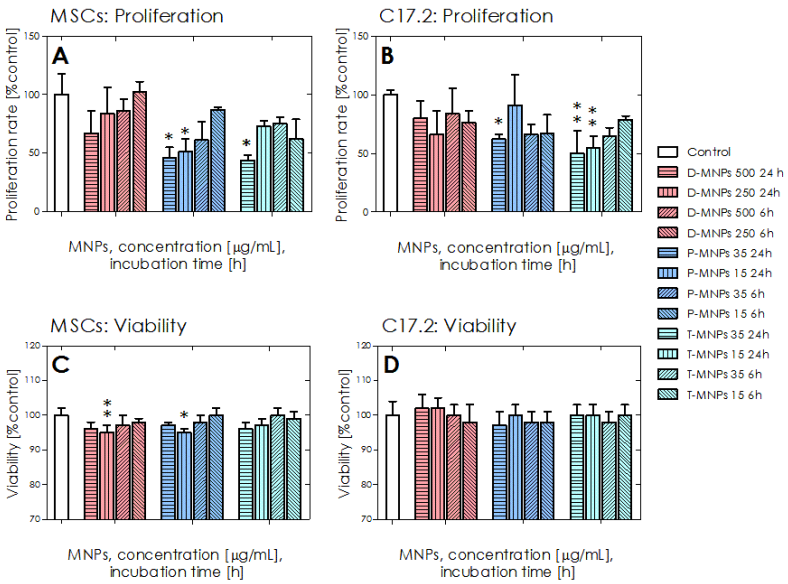


Figure 50: (A) Proliferation rate (respect to control %) for MSCs after labeling, (B) Proliferation rate (respect to control %) for C17.2 after labeling, (C) Viability rate (respect to control %) for MSCs after labeling and (D) Viability rate (respect to control %) for MSCs after labeling. (* $p<0.05$; ** $p<0.01$)

## 6.4. Discussion

In this chapter we have successfully validated the use of our synthesized dextran-, pluronic F127- and tetronic 908-coated superparamagnetic nanoparticles for in vitro applications. Previously we had reported the dependence on transfect agents as PLL for D-MNPs cellular internalization, and here we have proven that no transfection agent is needed for P-MNPs and T-MNPs cell labeling. However, besides transfect agent influence findings, other parameters such as incubation time, MNPs

concentration or cell type were also studied in order to find out the best labeling conditions. But, the best scenario requires not only the best MRI signal, which actually is the main goal as MRI contrast agents; but must also maintain the well-being of the cells, as they will be used as treatment agents in a potential therapy for stroke.

One of the most direct parameters that can be influenced by the presence of MNPs is cell proliferation. With regard to the proliferation rate of labeled cells, PLL coated D-MNPs do not significantly affect their proliferative capacity compared to control for both types studied, MSCs and C17.2. Viability is slightly reduced for these conditions, but it only has statistic significance for D-MNPs 250 24h in MSCs ($p<0.05$). On the other hand, P-MNPs and T-MNPs have a similar behavior between them. For both cell types, the highest concentration (35 μg/mL) and the longest incubation time (24h), reduce the proliferation up to 45-60%, for P-MNPs ($p<0.05$) and also for T-MNPs ($p<0.01$). In addition, the lowest concentration (15 μg/mL) of P-MNPs reduces the proliferation of MSCs to 51% ($p<0.05$) and also T-MNPs for C17.2 to 55% ($p<0.01$). Twelve hours after labeling, LDH viability assay shows a reduction in all conditions being statistic significant just for MSCs labeled with P-MNPs 250μg/mL for 24h. As it has been mentioned before we can attribute this fact to an artifact (higher concentration does not show a significant effect) and not as a viability reduction. In general, the proliferation after labeling is reduced and depends on the incubation time as well as in the concentration of MNPs in medium. For MSCs it is possible to observe a trend, proliferation rate decreases with the increase of incubation time and MNPs concentration for all coated MNPs. In the case of C17.2, same trend can be observed for T-MNPs, meanwhile standard deviations of D-MNPs and P-MNPs are too high to

show this effect. In regard to viability 12h after labeling, there are no significant differences between groups in terms of LDH release.

In order to perform Prussian Blue staining, harvested cells were replanted again. With this staining it is possible to observe that all studied conditions showed MNPs, which can be observed through optical microscopy in blue color Furthermore, the fact of replant the cells also indicates that the behavior of labeled cells is the same as controls, they get attached to the well and enabling Prussian Blue staining.

Other way to evaluate the wellbeing of labeled cells and also demonstrate the MNPS presence is based on their morphology in TEM micrographs. There were no differences in morphology observed by TEM and all coated MNPs are encapsulated in vesicles along the cytoplasm. As it was demonstrated in the previous chapter, we can assess that the labeling protocol used is highly efficient to tag cells with MNPS, and no MNPS were observed attached to the cellular membrane. Particularly, the endosomes of cells labeled with P-MNPs and T-MNPs showed big clustering of MNPs where individual particles (cores) cannot be easily observed. On the other hand, endosomes containing D-MNPs are more regular in shape and present a uniform dotted pattern, where MNPs cores can be observed.

The MNP internalization is variable depending on the MNPs type. We have already reported the dependency on PLL for D-MNPs internalization, however for this study the concentration has been kept constant (1.5μg/mL). However, it is possible to observe the dependency on concentration and incubation time for both types of cells labeled with PLL coated D-MNPs.

The dependency on concentration is more remarkable for P-MNPs and T-MNPs, where the amount of MNPs during the incubation process is decisive. The more concentration, the more internalization value with one exception, T-MNPs 35μg/mL 6h, which showed similar values to 15 μg/mL. Nevertheless, it is important to remark that MNP internalization of P-MNPs and T-MNPs (for 35 μg/mL) are 2, 3 or even 4 times higher than D-MNPs (for 500 μg/mL). This could be explained based on two factors, on one hand the nature of the coating and, on the other hand on terms of MNPs stability in cell medium. Considering the small size of all these MNPs, it is not possible to observe clustering or aggregation after MNPs dispersion in cell medium by optical microscopy, but P-MNPs and T-MNPs could be precipitating onto the cells facilitating the uptake. TEM images indicate that Pluronic and Tetronic coated MNPs could be micro-aggregated due to the irregular morphology of the endosomes observed. This idea would be also supported by ICP data, which revealed a strong dependence on the MNPs concentration in medium for this kind of particles, suggesting that higher uptake would occur because more particles precipitate onto the cell. Clusters of P-MNPs and T-MNPs would be big enough to lay onto the cells and facilitate the uptake, and small enough to be washed after labeling and grant full MNPs internalization, as it was observed in TEM micrographs.

Iron internalization can be related to MRI relaxation values. Relaxation rates $R_2$* of labeled cells did not reflect the differences in terms of MNPs internalization. This fact can be explained due to the high concentration of labeled cells (500 cells/μL) for the phantom. In $T_2$* weighted images, the signal decays so fast that the adjustment to an exponential decay is based on 2-4 experimental points (others are zero). In order to perform a better exponential decay adjustment

it would be necessary to reduce the cell concentration (therefore the iron concentration in the phantom) or the echo time of the MRI sequence (MGE).

Overall, in this chapter we have evaluated our synthesized MNPs, which enable efficient and non-invasive imaging of cells in MRI. D-MNPs, P-MNPs and T-MNPs demonstrated their use for cell labeling at different concentrations and incubation times without a short-term harmful effect for the most of the studied conditions. However, a long-term cellular wellbeing evaluation would be necessary to assess their further use for in vivo cell tracking studies.

In this way, as mesenchymal stem cells have demonstrated their potential use in cerebrovascular diseases, also in stroke, we will consider MSC for further in vivo studies of cell tracking. Moreover, in this chapter we had validated our 3 synthesized coated MNPs as suitable MRI contrast agents for these cells. However, among all possibilities, PLL- coated D-MNPs offer several advantages in terms of cell labeling compared to P-MNPs and T-MNPs for further *in vivo* studies. MNP uptake for D-MNPs is concentration/incubation time dependent and stable in terms of internalization, as it has been shown here and in the previous chapter. It is possible to detect cells labeled with this kind of particles in MRI with relatively low amount of internalized nanoparticles (about 10pg/cell) and from 100μg/mL to 500μg/mL D-MNPs concentrations, there is not significant influence on proliferation and toxicity. The cytoplasmic distribution in endosomes of regular shape is also crucial because after proliferation, cells will split the internalized MNPs, being daughter cells also detectable by MRI. Another important point to take into account is the ease on the *in situ* synthesis of D-MNPs, because further *in vivo* studies will require a high amount of them.

## 6.5. Conclusions

In the present chapter, we have evaluated the *in vitro* short-term biocompatibility of D-MNPs, P-MNPs and T-MNPs by labeling MSCs and C17.2 cells. In general terms, the internalization behavior was the same for both types of cells. Cellular uptake is conditioned by concentration and incubation time for PLL coated D-MNPs meanwhile P-MNPs and T-MNPs internalization depends mostly on the MNPs concentration in cell medium. MNPs influence on the cellular wellbeing is dependent on the internalized iron, reducing proliferation and viability for cells with more than 28 pg/cell and once again, we have demonstrated that the labeling protocol used is highly efficient for full MNPs internalization, providing reliable MRI values for labeled cells.

Based on these results, for further *in vitro* and *in vivo* studies we will choose dextran-coated MNPs due to its ease for synthesis, stable cell labeling, reduced cellular toxicity, high MRI signal of cells labeled and nanoparticle endosomal distribution observed by TEM in the cellular cytoplasm. However, we have studied short-term biocompatibility, a long-term *in vitro* study of proliferation, viability and MRI signal evolution is needed for further *in vivo* studies.

# 7. Long-term study of mesenchymal stem cells labeled with PLL-Dextran coated superparamagnetic nanoparticles

## 7.1. Hypothesis

So far, we have developed 3 different coated superparamagnetic nanoparticles, and we have already demonstrated their short-term biocompatibility for cell tracking. However, a long-term evaluation of labeled cells and how the proliferation rate influences the MRI signal are needed prior to *in vivo* cell tracking studies. Additionally, the study of magnetic field influence on the cells after magnetic vectorization is needed. In this way and considering previous results, the main goal of this chapter is the long-term biocompatibility study and the evaluation of the MRI signal clearance with the proliferation of rat mesenchymal stem cells labeled with PLL-Dextran coated superparamagnetic nanoparticles for further cell tracking and magnetic vectorization in vivo.

## 7.2. Materials & methods

### 7.2.1. Cell lines

All experiments were performed using Mesenchymal Stem Cells (MSCs) purchased from Cultrex, Trevigen and were cultured in IMDM (78%), Fetal bovine serum (10%), Horse serum (10%), Penicillin-Streptomycin (1%) all from Gibco Invitrogen, and Amphotericin-B (1%) from Sigma-Aldrich. Cell passage numbers between 7 and 18 were used in these experiments (n=3 for each condition).

### 7.2.2. Dextran-coated superparamagnetic nanoparticles

Dextran coated MNPs (D-MNPs) were synthesized in the Clinical Neuroscience Research Laboratory following the *in situ* protocol described in chapter 3.

### 7.2.3. Preparation of Poly-L-lysine hydrobromide-coated D-MNPs

One concentration of PLL (Sigma-Aldrich) was used: 1.5μg/mL. One hour prior to cell incubation, D-MNPs were mixed with MSCs medium and 1.5 μg/mL PLL and vigorously shaken.

### 7.2.4. Cell labeling with PLL-coated D-MNPs

Cells were labeled following the protocol described elsewhere [227] with slight modifications. MSCs were incubated with 1.5 μg/mL of PLL combined with D-MNPs (100 μg/mL) for 24h. The D-MNP containing medium was removed and the cells were 3 times washed with 1.5 mL of

Phosphate Buffered Saline (PBS without $Mg^{2+}$ and $Ca^{2+}$, Gibco, Invitrogen) to remove non-attached MNPs. After washing, the cells were left overnight (12h) in 1 mL of fresh medium. The following day the medium was removed, cells were washed once with 1.5 mL of PBS and 0.5 mL of EDTA-trypsin (Gibco Invitrogen) was added to detach the cells from the well. The trypsin was neutralized with fresh medium and the detached cells were collected in a Falcon tube. After a mild centrifugation, the supernatant was discarded and the cells were resuspended in fresh medium. These cells, control and labeled, were named as "Plant 0".

To evaluate the effect of the D-MNPs dilution, control and labeled cells from "Plant 0" were replanted in fresh medium. After 48h, the cells were washed once with 1.5 mL of PBS and 0.5 mL of EDTA-trypsin (Gibco Invitrogen) was added to detach the cells from the well. The trypsin was neutralized with fresh medium and the detached cells were collected in a Falcon tube. After a mild centrifugation, the supernatant was discarded and the cells were resuspended in fresh medium. These control and labeled cells were named as "Plant 1".

Control and labeled cells from "Plant 1" were replanted in fresh medium. After 48h, the cells were washed once with 1.5mL of PBS and 0.5mL of EDTA-trypsin (Gibco Invitrogen) was added to detach the cells from the well. The trypsin was neutralized with fresh medium and the detached cells were collected in a Falcon tube. After a mild centrifugation, the supernatant was discarded and the cells were resuspended in fresh medium. These control and labeled cells were named as "Plant 2". Timeline scheme of these Plants 0, 1 and 2 can be observed in Figure 51.

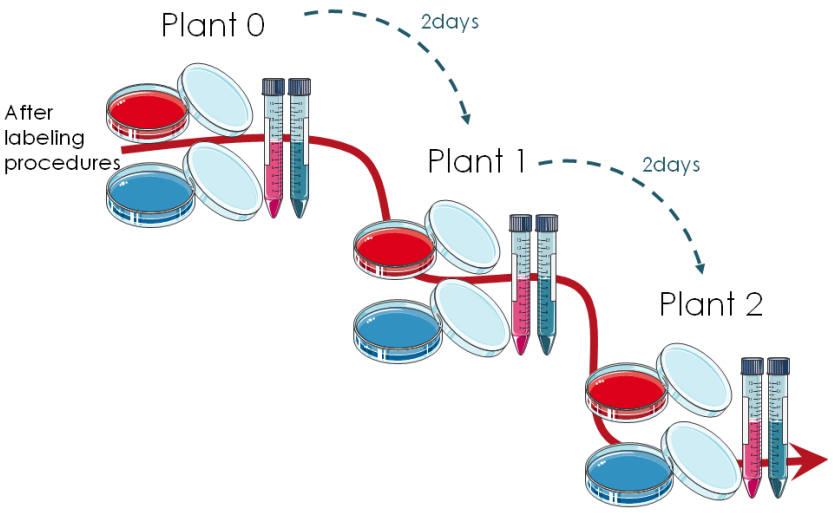


Figure 51: Timeline of Plant 0, Plant 1 and Plant 2 for *in vivo* experiments.

### 7.2.5. Proliferation

To determine the proliferation rate of Plant 0, Plant 1 and Plant 2, total cell count was performed with Trypan Blue staining and a Neubauer chamber. Samples were diluted 1:5 with PBS and 1:2 with Trypan Blue.

### 7.2.6. Cell viability assay: Lactate Dehydrogenase Assay (LDH)

For assessing the viability of the cells after labeling compared to control, supernatantswere collected in eppendorf tubes. LDH ciability assay was performed for Plant 0 (12h after labeling), Plant 1 (3 days after labeling) and Plant 2 (5 days after labeling). A negative control of lysed cells was also included. After a mild centrigufation of the supernatants, 75µL were mixed in a 96 well plate with 150µL LDH reagents following the manufacturer protocol (Lactate Dehydrogenase Assay Kit. Sigma-Aldrich). After 20

minutes incubation, the plate was read in Synergy2 (Biotek) at 490nm. To calculate the viability rate respect to control, next equation was applied.

$$Viability\ [\%\ control] = \frac{LDH_{lysed} - LDH_{exposed}}{LDH_{lysed} - LDH_{control}} \cdot 100$$

### 7.2.7. Intracellular iron determination

An amount of 200.000 cells per condition and Plants were dissolved in 1mL of 37% HCl (ref) and 4mL of DW was added to reach total volume of 5mL. Iron concentration was determined by inductive coupled plasma optical emission spectroscopy (ICP-OES) (Varian Inc). The intensity of the emission line at 238.204 nm was measured for iron and compared to a standard solution. ICP-OES was performed at the Material Science Institute (MTM), KU Leuven.

### 7.2.8. Prussian Blue staining

Prussian Blue staining was performed to demonstrate the uptake of the D-MNPs by the cells in all time points (Plant 0, Plant 1, Plant 2). Cells were washed with PBS and incubated for 20 minutes with a mix of equal parts of aqueous solution of 20% HCl (Hydrochloric acid fuming 37% extra pure, Merk) and aqueous solution of 10% Potassium ferrocyanide Trihydrate (KFe(CN)6.3H2O, FW 422.2, Sigma-Aldrich). After incubation, cells were washed 3 times with PBS and photographs were taken using an inverted microscope (Olympus IX51).

### 7.2.9. Magnetic resonance imaging of labeled cells

Agar phantom was made following the procedure described elsewhere.[227] 100.000 cells per group were scanned in a Bruker Biospec 9.4 T small animal MR scanner (Bruker, Biospin, Ettlingen, Germany) equipped with actively shielded gradients (400 mT/m). A quadrature radio-frequency transmit-recive resonator was used for data acquisition. T2*-weighted images were acquired using a MGE sequence of 4.44 ms echo time, 6.75 ms echo spacing, 1.8 s repetition time, 16 echoes, 14 slices, 2 averages, FOV of 7.5 cm x 7.5 cm and a matrix size of 256 x 256. Post-processing was performed using ImageJ software (Rasband, W. NIH).

### 7.2.10. Flow cytometry of MSCs

The characterization of MSCs after labeling was performed by flow cytometry analysis in timepoint Plant 0 and Plant 2. MSCs (250.000 cells) were washed with 50 μL of PBS and stained by incubation (15 minutes) with 5 μL CD90-PerCP, 2.5 μL CD45-PE (BD Pharmigen) and 1 μL of CD73-APC (Inmunostep) antibodies. Firstly, MSCs were separated by their forward and side scattering signal characteristics. MSCs were characterized as CD90+CD73+/CD45- cells. For analysis 20.000 cell events were acquired in a BD FACS Aria I (BD Biosciences) and data were analyzed with the use of FACSDiva software (BD Biosciences).

### 7.2.11. Angiogenic assay: Matrigel.

Tube formation was assayed by using Matrigel (BD Pharmigen). Angiogenic assay medium was prepared with 95% IMDM (Gibco. Invitrogen) and 5% FBS (Gibco.

Invitrogen). 300 μL of Matrigel (4°C) per well was added in a 24-well plate and it was further incubated for 30 min till full solidification. 80.000 labeled and non-labeled MSCs dispersed in angiogenic assay medium were placed and well distributed in each well. After 6h incubation, pictures of tubular structures were taken by using and inverted microscope (Olympus IX51).

### 7.2.12. Cellular protein determination: Bradford assay.

Total protein quantification was determined by Bradford techniques.[245] 400 μL of 0.2% NaOH (Sodium Hydroxide pellets PA-ACS-ISO. Panreac) was added to each well and plate was placed under shaking for 4h at room temperature. Standard curve was generated from different concentrations of Bovine Serum Albumin (BSA) (Cell Culture Grade, pH 7.0, Lyophilized Powder, GE Healthcare Life Sciences). 10 μL of each sample was mixed with 190 μL of distilled water and 50 μL of Protein Assay Dye Reagent Concentrate (Bio-Rad) and plate was read in Synergy2 (Biotek) at 595 nm.

### 7.2.13. Vascular endothelial growth factor (VEGF) determination: ELISA kit assay.

VEGF concentrations of MSC control and labeled mediums were measured with a Quantikine VEGF ELISA kit (R&D Systems) following the manufacturer's protocol. VEGF values are corrected for the amount of total cell protein calculated by Bradford techniques.

### 7.2.14. *In vitro* magnetic vectorization

To investigate the effects of a magnetic field *in vitro*, two experiments were performed: 2D and 3D vectorization assays.

For 2D vectorization experiments, several neodymium magnets (0.3T) were placed and stuck below a culture dish (diameter 100mm) as is shown in Figure 52. After placing the magnets, 150.000 cells were added to each well and 4 conditions were studied, non-labeled cells with and without magnet, and D-MNPs labeled cells with and without magnet. Dishes were placed under intense shaking for 30 min and after that moved into the incubator for 4 h. Afterwards, magnets were removed, cells were washed once with PBS and Prussian Blue staining was performed.

For 3D vectorization experiments, 100 μL of Matrigel (4ºC) was added to small eppendorfs and incubated for 1 h till full solidification. One neodymium magnet (1T) was placed below the tip of the eppendorf (Figure 53), 50.000 cells in cell medium were added onto the solidified Matrigel, and samples were taken to incubator for 4h. Two groups were studied, non-labeled and labeled cells. After 4h incubation, MRI of eppendorf was performed to evaluate the cell migration through the Matrigel. MRI setup was the same as the mentioned in 7.2.9, $T_2$ weighted images were acquired using a RARE sequence of rare factor 4, echo time 22.5ms, repetition time of 5133 ms, 1 average, and 1 echo image. FOV of 28.8 mm x 28.8 mm and a matrix size of 192x192. Post processing was performed using ImageJ software (NIH).

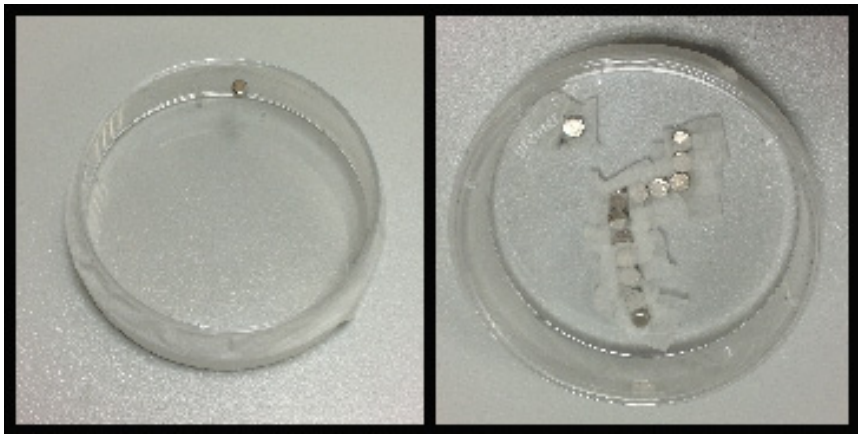

Figure 52: Neodiymium magnets (0.3T) distributed for 2D vectorization studies.

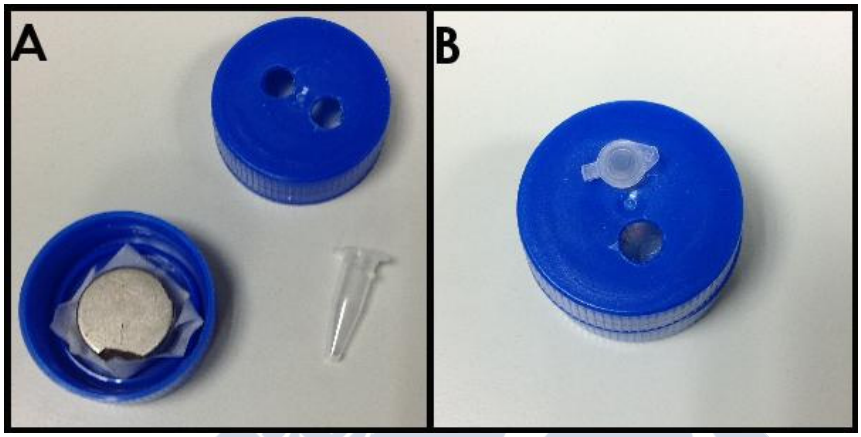


Figure 53: Neodymium magnet (1T) for 3D vectorization experiments.

## 7.3. Results

Biocompatibility of MSCs labeled with D-MNPs was evaluated for further *in vivo* applications. Since the main goal of the use of MRI contrast agents for cell tracking is to

monitor the cells after injection, the long-term evaluation of the biocompatibility of these MNPs is determined by their rapid clearance. Thus, considering rate proliferation of MSCs and internalized iron, the endpoint of our study was 5 days after cell labeling.

### 7.3.1. Cellular internalization and MNPs clearance

The amount of internalized iron nanoparticles was determined by ICP. Three times 150.000 labeled and non-labeled cells from "Plant 0" were replanted and harvested 48 h later, corresponding to "Plant 1". Three times 150.000 labeled and non-labeled cells from "Plant 1" were replanted and harvested 48 h later, corresponding to "Plant 2". In this way, the amount of internalized iron was 0.25±0.13 pg/cell for control and for MSCs labeled with D-MNPs was 7.7±0.7 pg/cell for "Plant 0", 2.4±0.2 pg/cell for "Plant 1" and 0.90±0.09 pg/cell for "Plant 2". (Figure 54 (A))

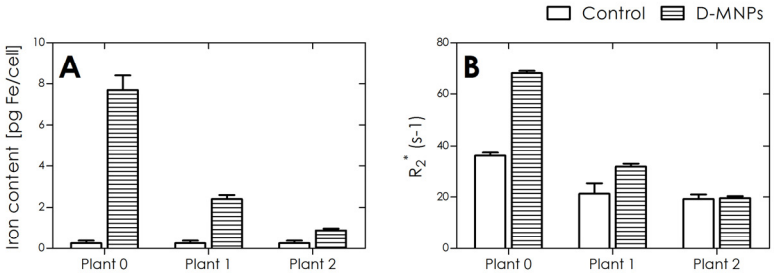


Figure 54: (A) Iron content of labeled and non-labeled MSCs for different timepoints (Plant 0, Plant 1 and Plant 2). (B) $R_2^*$ of labeled and non labeled MSCs for different timepoints ((Plant 0, Plant 1 and Plant 2).

### 7.3.2. Magnetic resonance imaging of labeled cells and MNPs clearance

In order to assess the contrast generated by MNPs internalization and to study the clearance of the signal, MRI of labeled cells and non-labeled cells at different timepoints was performed. $T_2$* maps were calculated from $T_2$* weighted images and $R_2$* relaxivities were obtained for each condition. Experimental results are plotted in Figure 54(B). Thus, for "Plant 0" $R_2$* was 36.0±1.2 $s^{-1}$ for control and 68.0±0.9 $s^{-1}$ for D-MNPs. For "Plant 1" $R_2$* was 21±4 $s^{-1}$ for control and 31.8±1.1 $s^{-1}$ for D-MNPs, and for "Plant 2" $R_2$* was 19±2 $s^{-1}$ for control and 19.6±0.8 $s^{-1}$ for D-MNPs. Clearance effect can also be observed in Figure 55.

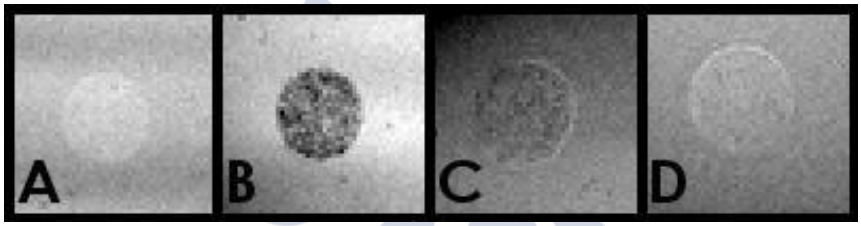


Figure 55: First echo of $T_2$* weighted images of (A) control, (B) "Plant 0" of labeled MSCs with D-MNPs, (C) "Plant 1" of labeled MSCs with D-MNPs and (D) "Plant 2" of labeled MSCs with D-MNPs.

### 7.3.3. Internalization and clearance assessed by Prussian Blue staining

Cell labeling was assessed by Prussian Blue staining. Same trend as ICP and MRI results was observed. "Plant 0" exhibited a great amount of MNPs internalization and this staining was reduced for "Plant 1", as can be noted in Figure 56 (C), (D), (E) and (F). In "Plant 2" Prussian Blue staining was similar to control, whereas almost no MNPs were in the cells (Figure 56 (A) and (B) for control and (G) and (H) for "Plant 2").

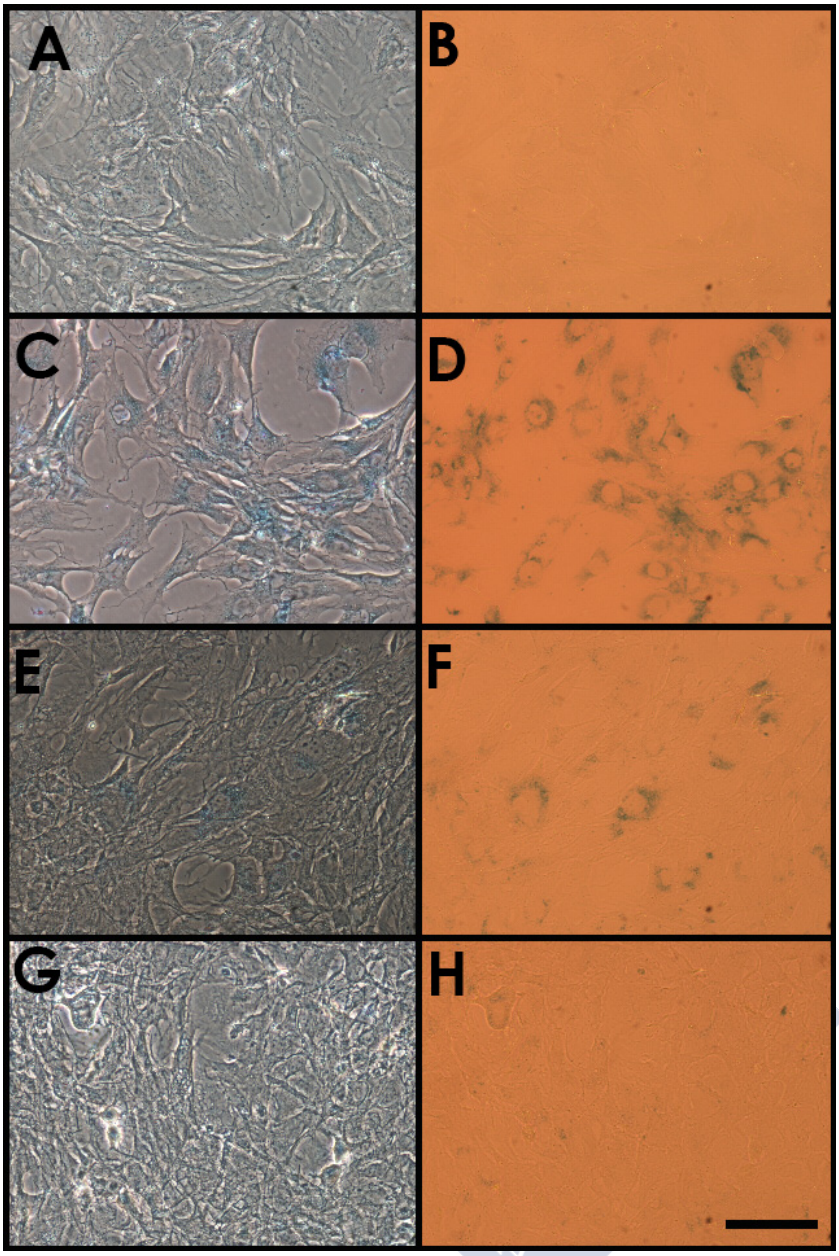


Figure 56: Prussian Blue staining (A) Phase contrast Control, (B) Bright field Control, (C) Phase contrast Plant 0 D-MNPs, (D) Brightfield Plant 0 D-MNPs, (E) Phase Contrast Plant 1 D-MNPs, (F) Bright field Plant 1 D-MNPs, (G) Phase contrast Plant 2 D-MNPs and (H) Bright field Plant 2 D-MNPs.

### 7.3.4. Long-term effect of D-MNPs internalization in MSCs in proliferation rate and viability

Proliferation rate experimental data is referred to control group (100%) for each timepoint (Figure 57 (A)). There were no significant differences between control and D-MNPs for each plant in terms of proliferation.

Moreover, as it can be observed in Figure 57 (B) there were not significant differences between control and D-MNPs in terms of viability (referred to control %) measured by LDH assay.

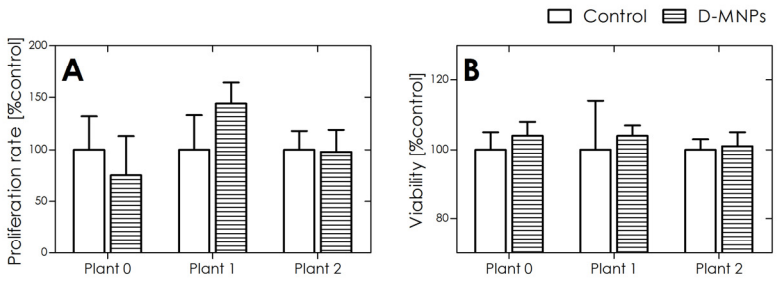


Figure 57: (A) Proliferation rate and (B) Viability for control and D-MNPs.

### 7.3.5. Long-term effect of D-MNPs internalization in MSCs in cell phenotype and angiogenic capacity

In order to evaluate phenotypic long-term changes after labeling, CD45, CD90 and CD73 markers for flow cytometry were studied for "Plant 0" and "Plant 2". There were no differences between groups for all conditions studied, meaning that after 5 days all conditions of MSCs were $CD90^{+}/CD73^{+}$ and $CD45^{-}$.

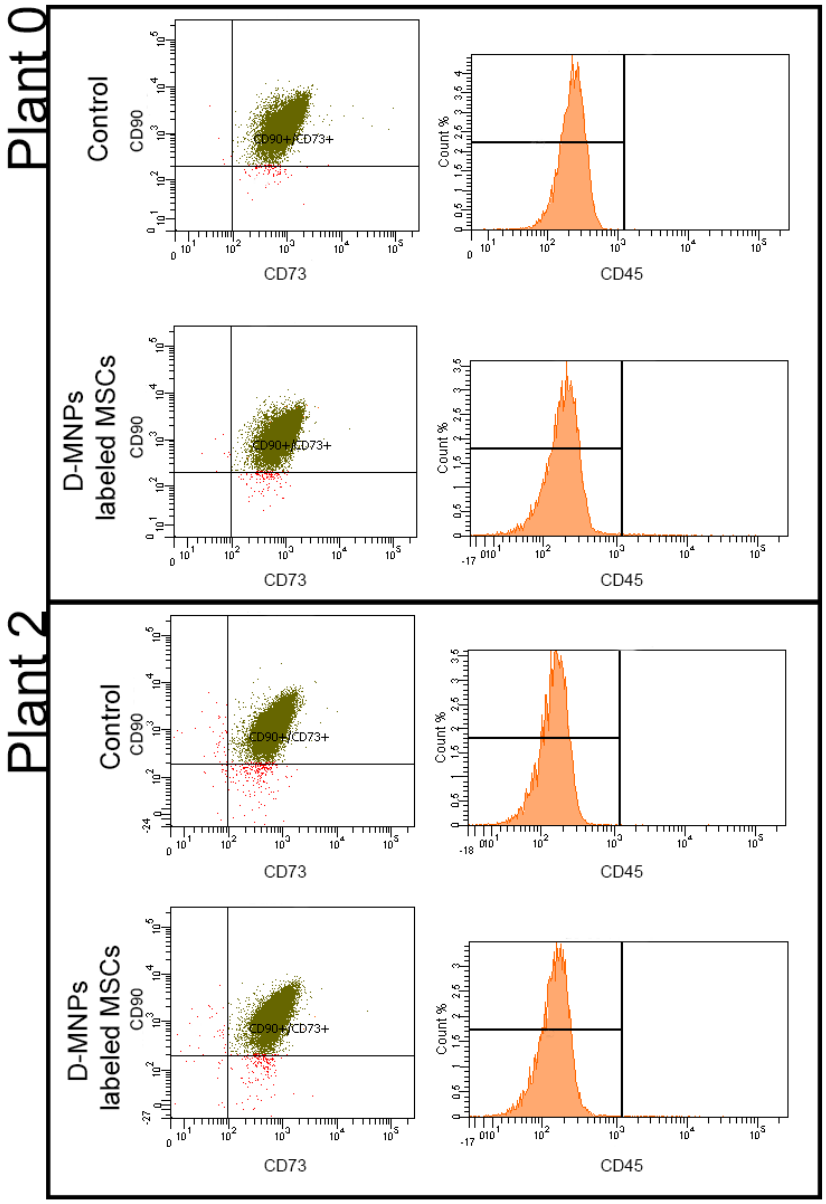


Figure 58: Flow cytometer graphs for Plant 0 and Plant 2 of non-labeled MSCs (control) and D-MNPs labeled MSCs for $CD90^{+}/CD73^{+}$ and $CD45^{-}$ analysis.

The angiogenic capacity of labeled MSCs was also studied. There were no differences observed between control and D-MNPs labeled cells after labeling (Plant 0) and after 5 days labeled (Plant 2) (Figure 59).

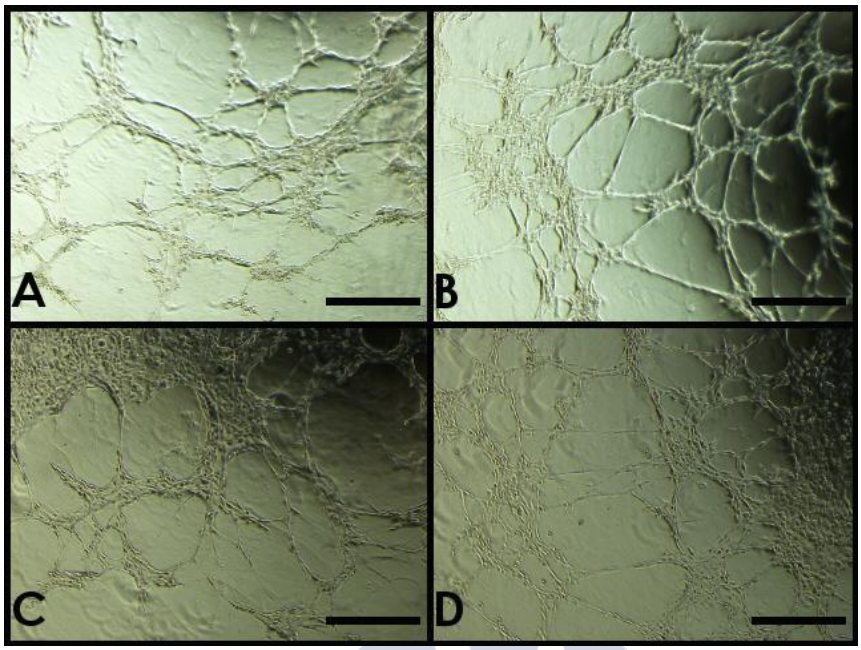


Figure 59: Matrigel angiogenic assay. (A) Control "Plant 0", (B) D-MNPs "Plant 0", (C) Control "Plant 2", (D) D-MNPs "Plant 2".

### 7.3.6. Long-term effect of D-MNPs internalization in MSCs in VEGF release

To determine the amount of VEGF release per microgram of protein, Bradford assay and VEGF ELISA assay were performed for each timepoint. For "Plant 0" 0.33±0.04 pg/μg protein for control and 0.40±0.05 pg/μg protein for D-MNPs was found. For "Plant 1" 0.27±0.04 pg/μg protein for control and 0.37±0.07 pg/μg protein for D-MNPs was obtained, and for "Plant 2" it was 0.52±0.07 pg/μg protein for control and 0.53±0.07 pg/μg protein for D-MNPs was measured. There

were no differences between control and D-MNPs for each timepoint as it can be seen in Figure 60.

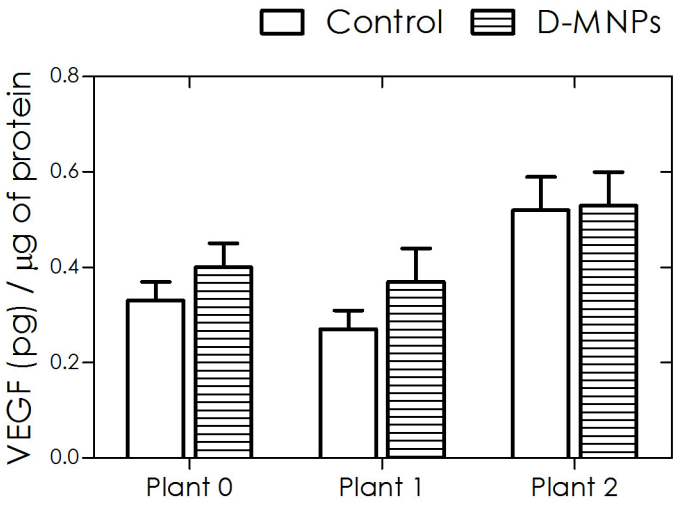


Figure 60: VEGF release pg/µg of protein for different timepoints (Plant 0, Plant 1 and Plant 2)

### 7.3.7. Magnetic vectorization of MSCs labeled with D-MNPs

2D magnetic vectorization experiment demonstrated the cellular magnetic guidance towards the magnet. Figure 61 (A) and (B) showed control MSCs evenly dispersed along the dish, which was also de case with MSCs labeled with D-MNPs but without the presence of the magnet (Figure 61 (C) and (D)). A similar pattern distribution occurred under neodymium magnet presence for control, being non-labeled MSCs (Figure 62 (A)). The distribution of labeled cells under the presence of a magnet was totally different; cells were attached to the well only at the regions where the

magnet was placed. This phenomenon is clearly visible in Figure 62(B), (C) and (D).

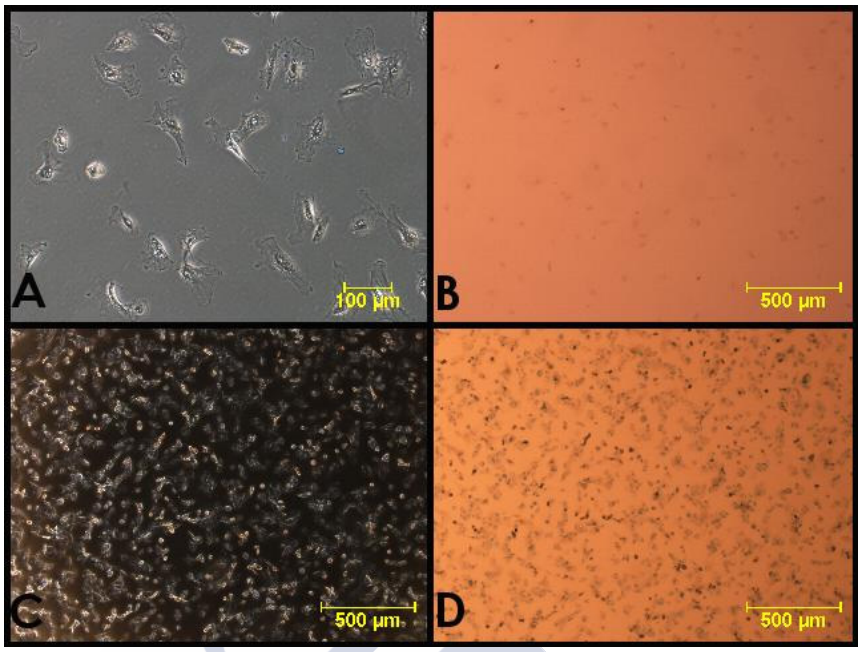


Figure 61: Optical microscopy of 2D magnetic vectorization. (A) Control through phase contrast microscopy without magnet, (B) Control through bright field without magnet, (C) D-MNPs through phase contrast microscopy without magnet, (D) D-MNPs through bright field without magnet.

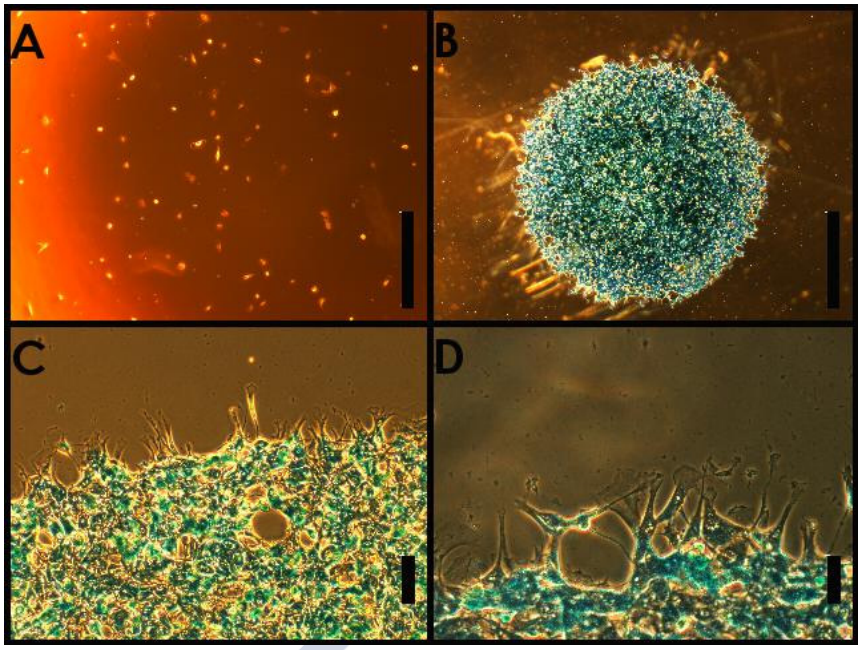


Figure 62: Bright field optical microscopy of 2D magnetic vectorization. (A) Control (scale bar 500 μm), (B) D-MNPS with magnet (scale bar 1 mm), (C) D-MNPS with magnet (scale bar 100 μm), (D) D-MNPS with magnet (scale bar 50 μm).

In spite of 2D magnetic vectorization, in a 3D environment our results showed that labeled MSCs are not able to migrate through Matrigel even under the presence of a 1T magnet. In Figure 63 (B) it is possible to observe the brownish color in the interface between cell medium and Matrigel (black arrows) corresponding to labeled cells. Meanwhile in Figure 63 (A) non-labeled cells have a pale color. To evaluate the migration through Matrigel, MR images of control and D-MNPs were acquired (Figure 64). A difference between labeled and non-labeled cells was determined by the hypointense signal for D-MNPs in Figure 64 (A) and (C) compared to control groups Figure 64 (B) and (D). However, when evaluating the migratory

capacities through Matrigel, no differences between D-MNPs with and without magnet presence were observed.

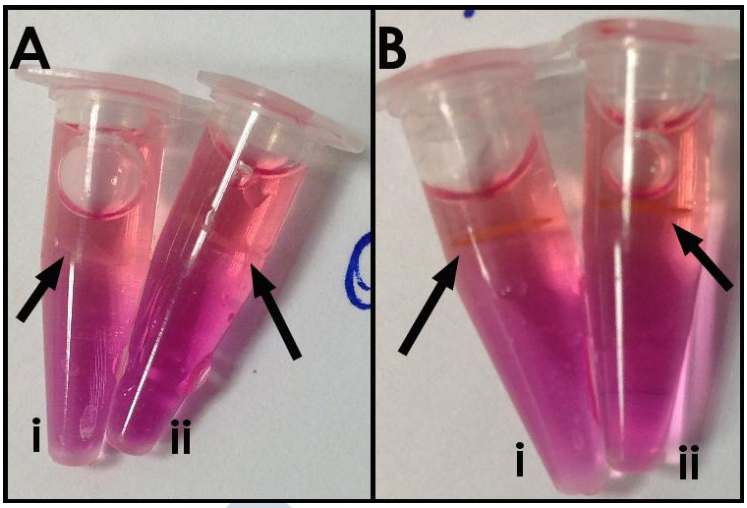


Figure 63: 3D magnetic vectorization. (A) (i) Control without magnet, (A) (ii) Control with magnet, (B) (i) D-MNPs without magnet, (B) (ii) Control with magnet.

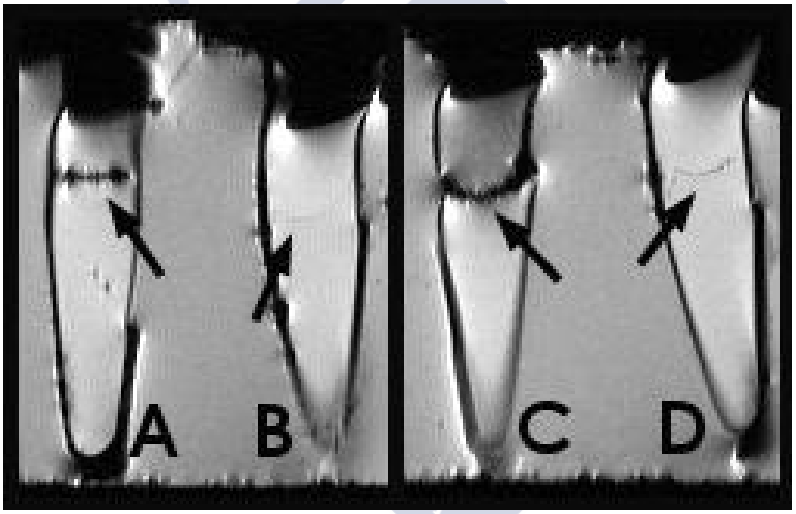


Figure 64: $T_2$-weighted images of 3D magnetic vectorization for (A) D-MNPs cells without magnet, (B) Control cells without magnet, (C) PLL-MNPs cells after placing 1T magnet, and (D) Control cells after placing 1T magnet.

## 7.4. Discussion

The aim of MRI cell tracking is to follow injected cells *in vivo* and, in order to achieve this goal, contrast agents as superparamagnetic nanoparticles must be used. However, parameters such as number of injected cells and amount of MNPs per cell are critical for cell tracking. Moreover, it is important to take into account that cells are active systems, i.e. they proliferate, which means that initial MRI signal can be cleared after cellular proliferation. In this chapter we have studied the clearance of MRI signal induced by the proliferation of MSCs labeled with D-MNPs and PLL.

Cells were labeled with 1.5μg/mL of PLL combined with 100μg/mL of D-MNPs based on our previous results from Chapter 4 and Chapter 5. Internalization values for "Plant 0" were similar to previous ones, and it was possible to observe in Figure 54 (A) how iron concentration per cell was reduced after replants and therefore, proliferation. This trend could also be noted in Figure 54 (B) and Figure 55 for T2* MRI signal. D-MNPs cells could be detected in "Plant 0" and "Plant 1" meanwhile MRI signal from "Plant 2" was too close to control to be detected. As we have mentioned before, the lower detectability limit for labeled cells is between 2-5 pg Fe/cell,[212,239] and, in "Plant 1" our labeled cells are loaded with 2.4±0.2 pg/cell and still can be detected in MRI. For "Plant 2" internalized iron was higher than control however it was not possible to distinguish between control and labeled cells in MRI $T_2$*. This dilution effect is also showed in Prussian Blue staining for different replants, Figure 56.

Signal clearance is not only important to track injected cells, but also crucial for the cell wellbeing in an effective therapy. Prussian Blue staining requires replant control and

labeled cells, and as could be observed, morphology of labeled cells was similar to control for all replants. With regard to proliferation and viability data there are not significant differences between control and D-MNPs, what points out that long-term labeling did not show any harmful effect on the cells.

Furthermore, phenotypically, MSCs express a number of markers, none of which unfortunately, are specific for MSCs.[132,133,246] However, in order to evaluate phenotypic changes after labeling, CD45, CD90 and CD73 markers were studied. All cells for all time points studied were $CD45^-$, $CD90^+$ and $CD73^+$. No phenotypic influence after labeling on a 5 days following was found. Angiogenic capacity was evaluated using Matrigel, and tubular formations were observed for short-term labeled cells with a high amount of D-MNPs and also for long-term labeled cells with almost no internalized MNPs.

Additionally, vascular endothelial growth factor release was determined. It is known that once MSCs have entered the microenviroment of injured tissues, many factors, including cytokines, toxins of infectious agents and hypoxia can stimulate the release of many growth factors by MSCs. This includes VEGF, which could promote the development of fibroblasts, endothelial cells and tissue progenitor cells, and carried out tissue regeneration and repair.[247] That is why the study of the influence of cell labeling with D-MNPs on VEGF release is very important. In our experiments, we have observed that labeled cells and non-labeled cells secrete same levels of VEGF for all time points of evaluation, as can be observed in Figure 60. Therefore, D-MNPs labeled cells would potentially have the same benefits than non-labeled cells in terms of VEGF production.

During the last years, the use of superparamagnetic nanoparticles combined with magnetic fields for enhancing targeted delivery of stem cells has been widely investigated. Several *in vivo* studies have shown that this method could improve migration of intravenously injected stem cells. [223,248,249] However, prior to an *in vivo* study it is necessary to evaluate the wellbeing of the labeled cells after being under magnetic forces. First approach explored was a 2D setup where the influence of the magnet can be easily observed. In normal cell culture conditions, it takes about 4h for MSCs to get attached to the culture dish. For our 2D experiments, we added labeled and non-labeled cells to each culture dish and placed it under vigorously shaken for 30 minutes. Without magnet presence, this agitation produced a homogeneous cell distribution along the well for labeled and non-labeled cells (Figure 61), meanwhile under magnetic fields presence the distribution is governed by the location of the neodymium magnets for D-MNPs labeled cells. Further incubation for 4h indicated no harmful effect after magnetic guidance because all cells are attached to the well in the proximal regions of the magnet (Figure 62 (B), (C) and (D)). However, for further in vivo applications, cellular magnetic vectorization will occur in a 3D environment, different from liquid conditions. For this purpose, Matrigel granted us the tridimensional background where cells can survive and migrate under a magnet action, and a higher magnetic field produced by a 1T neodymium magnet. Considering this setup, it was not possible to observe any migration through Matrigel for labeled cells by MRI, which would point out the safety of 3D magnetic vectorization for a non-liquid environment. The effective use of Matrigel for migration and invasion studies has been performed previously where labeled human dermal lymphatic microvascular endothelial cells migrate

through in response to metastatic MDA-MB-231 breast cancer cells under hypoxic conditions.[250]

## 7.5. Conclusions

In this chapter, we have validated the *in vitro* long-term biocompatibility of D-MNPs by following labeled MSCs over time till full MNPs clearance. Our results showed that labeled cells did not differ from control cells in terms of proliferation rate and viability after 5 days, as well as the maintenance of $CD45^-$, $CD90^+$ and $CD73^+$ cellular phenotype. Angiogenesis capacity in Matrigel was not altered by the presence of internalized D-MNPs, as well as VEGF release measurements did not exhibit differences between control and labeled cells. Under the labeling conditions studied and for cell tracking applications, MRI can easily detect labeled cells 3 days after being tagged. From then, MRI signal is affected by the clearance of the internalized D-MNPs due to proliferation, being only possible to detect MNPs loaded cells by ICP. Moreover, we have proven the efficacy of cellular magnetic vectorization in a liquid environment without harmful effects for future targeted delivery of stem cells. Overall, our results suggest that MSCs loaded with D-MNPs are a promising tool for cell tracking and cellular magnetic vectorization *in vivo* without cellular harmful effects.

USC
UNIVERSIDADE
DE SANTIAGO
DE COMPOSTELA

# Section V

## *In vivo* animal models of ischemic stroke and cell tracking

USC
UNIVERSIDADE
DE SANTIAGO
DE COMPOSTELA

This *in vivo* section is divided in two chapters. On one hand, in Chapter 7 we have optimized the experimental conditions and procedures for stem cell administration in an animal model of ischemic stroke. On the other hand, in Chapter 8, ischemic and non-ischemic animals were injected following different administration routes to evaluate if the pathologic condition has an influence in the fate of the delivered cells, assessed by magnetic resonance imaging and histological techniques.

USC
UNIVERSIDADE
DE SANTIAGO
DE COMPOSTELA

# 8. Animal models of focal cerebral ischemia and their influence on the intra-arterial administration route for stem cell therapy

## 8.1. Hypothesis

One of the main goals of this chapter is to find the least invasive and most reproducible animal model of focal ischemia in rats. We will explore the different variations of tMCAO model in order to find out the most efficient and the safest protocol for intra-arterial delivery of mesenchymal stem cells. In this chapter we will study the *in vivo* distribution of labeled stem cells after an intra-arterial injection and how cerebral blood flow can affect the brain distribution of administered cells.

Furthermore, we have also demonstrated that tagged cells can migrate *in vitro* under presence of magnetic fields, so in this chapter we will explore the influence of magnetic fields after intra-arterial injection of labeled stem cells in order to increase their presence in the brain.

## 8.2. Materials & Methods

### 8.2.1. Cell labeling preparation

#### 8.2.1.1. Cell lines

All experiments were performed using Mesenchymal Stem Cells (MSCs) purchased from Cultrex, Trevigen and were cultured in IMDM (78%), Fetal bovine serum (10%), Horse serum (10%), Penicillin-Streptomycin (1%) all from Gibco Invitrogen, and Amphotericin-B (1%) from Sigma-Aldrich. Cell passage numbers between 7 and 18 were used in these experiments.

#### 8.2.1.2. Dextran-coated superparamagnetic nanoparticles

Dextran coated MNPs (D-MNPs) were synthesized in the Clinical Neuroscience Research Laboratory following the *in situ* protocol described in chapter 3.

#### 8.2.1.3. Preparation of Poly-L-lysine hydrobromide-coated D-MNPs

1.5µg/mL of Poly-L-lysine hydrobromide (PLL) (Sigma-Aldrich) was used. One hour prior to cell incubation, D-MNPs were mixed with cell medium and with 1.5 µg/mL PLL and vigorously shaken.

#### 8.2.1.4. Cell labeling with PLL-coated D-MNPs

MSCs were labeled following the protocol previously described [227] with slight modifications. Cells were incubated with 1.5 µg/mL PLL and 100 µg/mL of D-MNPs for 24h. The MNP containing medium was removed and the cells were 3 times washed with 1.5 mL of Phosphate Buffered Saline (PBS without $Mg^{2+}$ and $Ca^{2+}$, Gibco

Invitrogen) to remove non-attached MNPs. After washing, the cells were left overnight (12h) in 1mL of fresh medium. The following day the medium was removed, cells were washed once with 1.5mL of PBS and 0.5mL of EDTA-trypsin (Gibco Invitrogen) was added to detach the cells from the well. The trypsin was neutralized with fresh medium and the detached cells were collected in a Falcon tube. After a mild centrifugation, the supernatant was discarded and the cells were resuspended in PBS 1X. Cell count was performed with Trypan Blue staining and a Neubauer chamber. Samples were diluted 1:5 with PBS and 1:2 with Trypan Blue.

#### 8.2.1.5. Cell preparation for intra-arterial injection

Labeled cells were harvested and counted just before being injected. Different amount of cells were injected in order to study the cell tracking and the safety of the procedure. Cell numbers vary from $2.5x10^5$ to $1x10^6$ MSCs.

### 8.2.2. Animal management

In this study we have used 113 Wistar rats (Harlan) with a weight of 288±9 g. Animals were kept at controlled conditions of temperature (22±1°C) and humidity (60±5%), with a 12/12 hours light/dark cycle, and granting free access to food (commercial chow pellets) and tap water. For surgery and MRI, rats were anesthetized with sevoflurane (3% in 70% $N_2O$ and 30% $O_2$). Rectal temperature was monitored and maintained at 37±0.5°C with a feedback controlled heating system (1025 system, SA Instruments). At the end of the procedures animals were sacrificed under deep anesthesia (8% sevoflurane). Experimental protocols were approved by the local Animal Care Committee according to the Spanish and European Union (EU) rules

(86/609/CEE, 2003/65/CE, 2010/63/EU, RD 1201/2005 and RD53/2013).

### 8.2.3. Model of focal transient ischemia in the rat

Transient focal ischemia was induced in rats by intraluminal occlusion of the middle cerebral artery (tMCAO), performed as previously described[171] with several modifications. In order to monitor the relative cerebral blood flow (CBF) during the surgery, a laser-Doppler flow probe (tip diameter 1 mm) attached to a flow meter (PeriFlux 5000; Perimed AB) was located over the thinned skull, over the middle cerebral artery territory (approximately 4 mm lateral to bregma).

Under a surgical microscope, common carotid, external carotid, and the internal carotid arteries of the left side were dissected from connective tissue through a midline neck incision. Left external carotid and pterygopalatine arteries were separated and tied with 6-0 silk sutures, showing a CBF reduction of 20% measured by laser Doppler. A silicon rubber-coated monofilament (403512PK5Re; Doccol Corporation) was inserted through the external carotid into the left common carotid artery and advanced into the internal carotid 17-20 mm from the bifurcation to occlude the origin of the MCA. The intraluminal filament was removed after 45 minutes of occlusion. Only animals with a CBF reduction higher than 60% and with reperfusion after occlusion were included in the studies. To perform tMCAO, both vertebral arteries remained intact all surgical procedures.

To study the influence of the collateral blood flow on labeled cells distribution after i.a. injection ipsilateral and

contralateral common carotids will remain open and/or closed during different stages of tMCAO.

### 8.2.4. Intra-arterial administration of stem cells

Cells were administrated 4h after the reperfusion of the ACM. Several arterial cerebral blood flow configurations based on ipsilateral common carotid (Ip-CC) and contralateral common carotid (Con-CC) arteries were evaluated after tMCAO for intra-arterial delivery of stem cells (Figure 65):

a. Con-CC is ligated during tMCAO. Ip-CC remains closed after MCA reperfusion. Intra-arterial stem cell delivery is performed with Ip-CC closed.
b. Con-CC is ligated during tMCAO. Ip-CC remains closed after tMCAO. At the moment of the injection Ip-CC is opened and remains opened after the stem cell delivery.
c. Con-CC is ligated during tMCAO. Ip-CC is reperfunded at the same time than middle cerebral artery. Ip-CC is opened before, during and after the injection.
d. Con-CC is intact during tMCAO. Ip-CC is reperfunded at the same time than middle cerebral artery. Ip-CC is opened before, during and after the injection.

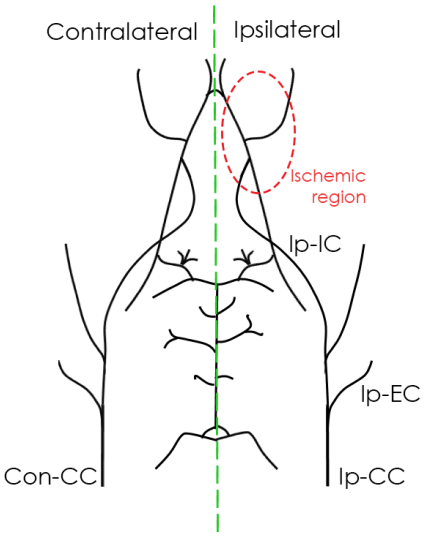


Figure 65: Diagram of cerebrovascular anatomy of rats.

All these different conditions for the common carotid artery will be further explained in Results and Discussion section; however Table 6 summarizes the main aspects of each protocol:

| Conditions | Con-CC closed during tMCAO | Ip-CC is opened from MCA reperfusion till the injection | Ip-CC is opened during the injection | Ip-CC remains opened after the injection |
|---|---|---|---|---|
| a | Yes | No | No | No |
| b | Yes | No | Yes | Yes |
| c | Yes | Yes | Yes | Yes |
| d | No | Yes | Yes | Yes |

Table 6: Common carotid configurations for animal models of tMCAO and intra-arterial delivery of labeled stem cells.

Intra-arterial injections of MSCs were performed following identical protocol for all surgery combinations. Briefly, a 0.28 mm ID & 0.61 mm OD catheter (Smiths) connected to a 30G needle and a 1 mL syringe was inserted into the stump

of ECA through an incision on the vessel under the operation microscope, and was tightened to ECA by a 6-0 silk suture. The catheter went forward into ICA till reach the branch of common and internal carotid. This tube was filled with heparinized physiological saline to prevent air bubble and blood coagulation. (At this point it was possible to observe a small blood reflux in the catheter if the common carotid would be opened). The syringe was filled with labeled cells in PBS and using slow hand injection over 15 minutes, 300 µL of cells in PBS were delivered into the internal carotid.

## 8.2.5. Animals and drug administration

### 8.2.5.1. Antiplatelets administration

The influence of antiplatelets on cell distribution was studied following the specifications described elsewhere.[251] Adiro tablets (Bayer) were dissolved in potable water and administrated at 100 mg/kg· day for 4 days, previous to intra-arterial stem cell delivery.

### 8.2.5.2. Anticoagulant administration

Similar to antiplatelets, anticoagulant effect was also studied in combination with MSCs administration. For such purpose, animals after tMCAO were injected with mesenchymal stem cells dispersed in a mixture of 450 µL of PBS 1X and 50 µL of Heparin 5000 unit/5mL (Mayne Pharma) prior to be injected. Doses were calculated following these studies.[252,253]

### 8.2.6. Laser Doppler flow monitoring of cerebral blood flow

Transcranial laser Doppler flow (TLDF) was used to monitor the cerebral blood flow during the surgery procedure of intra-arterial stem cell administration. Three optic fiber probes were placed onto the squamosal part of the temporal bone of the rat skull. In order to facilitate the positioning of the fiber, this bone was slightly smooth over and fibers were attached to the bone using conventional glue. Optical probes were distributed along the squamosal bone to cover different branches of ACM. Cerebral blood flow was monitored prior the injection, during it and for 1h after stem cell delivery.

### 8.2.7. In vivo magnetic vectorization

All different conditions for intra-arterial delivery specified in section 8.2.4 were assessed for magnetic vectorization. In order to study the magnetic guidance of labeled stem cells, a rare magnet (Supermagnete. Webcraft GmbH) of about 1T and dimensions of 50.8 cm x 50.8 cm x 25.4 cm was used. Rats were anesthetized with sevoflurane (3% in 70% N2O and 30% O2) and rectal temperature was monitored and maintained at 37±0.5 °C during all procedure. Prior to injection, rat neck and head were placed onto the magnet in supine position, so that parietal part of rat head was in contact with the magnet. Surgery and stem cell delivery was performed under magnetic field presence and maintained for 4 hours after injection.

### 8.2.8. Magnetic resonance imaging

Infarct size, angiography and cell tracking were assessed by magnetic resonance imaging. Magnetic resonance

imaging studies were conducted on a 9.4 T horizontal bore magnet (Bruker BioSpin, Ettligen, Germany) with 20 cm wide actively shielded gradient coils (440 mT/m). Radio-frequency transmission was achieved with a birdcage volume resonator; signal was detected using a four-element surface coil, positioned over the head of the animal, which was fixed with a teeth bar, earplugs, and adhesive tape. Transmission and reception coils were actively decoupled from each other. Gradient-echo pilot scans were performed at the beginning of each imaging session for accurate positioning of the animal inside the magnet bore.

Apparent diffusion coefficient maps were acquired using a spin-echo echo-planar imaging sequences with the following acquisition parameters: FOV 24 x 16 $mm^2$, image matrix 96 x 64 (isotropic in plane resolution of 200mm/pixel), 14 consecutive slices of 1mm thickness, repetition time 4 s, 4 averages, echo time 26.91 ms, spectral bandwidth 200 KHz and 7 *b*-values: 0; 300; 600; 900; 1200; 1600 and 2000 $s/mm^2$. Diffusion-weighted images were acquired during the ACM occlusion.

To evaluate the status of the ACM occlusion in a noninvasive manner, the TOF-MRA was performed. The MRA scan was performed with a 3D Flash sequence with the following acquisition parameters: FOV 30.72 x 30.72 x 14 $mm^3$, image matrix 256 x 256 x 58 (in plane resolution 120 mm/pixel x 120 mm/pixel x 241 mm/pixel), repetition time 15 ms, 2 averages, echo time 2.5 ms and excitation pulse angle of 20º. MRA was performed during ACM occlusion and 4h after stem cell injection.

$T_2$-weighted images were acquired using a multislice multiecho spin-echo sequence with the following

acquisition parameters: FOV 19.2 x 19.2 $mm^2$, image matrix 192 x 192 (isotropic in-plane resolution of 100 µm/pixel x 100 µm/pixel), 14 consecutive slices of 1mm thickness, repetition time of 3 s, and 16 echoes with 9 ms of echo time. $T_2$-weighted images were acquired 24h after the onset of the ischemia.

$T_2$*-weighted axial images were acquired using a multi gradient echo sequence with the following acquisition parameters: FOV 19.2 x 19.2 $mm^2$, image matrix 192 x 192 (isotropic in-plane resolution of 100 µm/pixel ), 14 consecutive slices of 1mm thickness, repetition time of 1.5 s, and 16 echoes with 2.9 ms for the first echo time and 3.28 ms of echo spacing. $T_2$*-weighted coronal images were acquired using previous parameters with different in plane geometry: FOV 25.6 x 19.2 $mm^2$ and image matrix 128 x 96 (isotropic in-plane resolution of 200 µm/pixel). $T_2$*-weighted images were acquired 4h after the stem cell delivery.

Post-processing of all images was performed using ImageJ software (Rasband, W. NIH).

### 8.2.9. In vitro evaluation of cell aggregation with different serums

5mL of blood was extracted from tail vein in a Wistar rat prior being sacrificed under sevofluorane overdose (8%). 1h after being extracted, blood is centrifuged for 7 minutes at 3000 rpm to obtain the blood serum.

Two different serums were tested: Wistar serum and fetal bovine serum (Invitrogen, Gibco); 2 types of cells: MSCs and C17.2 and 4 different conditions for each one were studied. For C17.2/MSCs: Normal cell medium (See Chapter 5), PBS 1x, DMEM/IMDM respectively (Invitrogen. Gibco) + 20%

Wistar serum and DMEM/IMDM respectively + 20% fetal bovine serum (FBS). $1x10^5$ cells per well were planted under each previous condition in a 6 well plate and pictures with an inverted optical microscope were taken. (Olympus IX51)

## 8.3. Results and discussion

### 8.3.1. Animal models of focal ischemia and intra-arterial delivery route for stem cell therapy

Animal models of stroke and their treatment are indispensable prior clinical trials. However, several therapies for acute stroke have proven effective in reducing lesion size in animal models while being clinically ineffective in humans.[162,254] So far, animal models in rodents satisfy all basic requirements needed to induce, manipulate and treat diseases like stroke. Nevertheless, it is obvious that there can never be one model that mimics all types of strokes because the pathogenesis of stroke is multifaceted with overlapping and interacting mechanisms.[255] For this study we have selected focal stroke model, mimicking clinical situations of stroke with atherosclerosis, thrombus and embolus.

Transient intraluminal occlusion of the middle cerebral artery is one of the most wide extended protocols to induce cerebral ischemia in rats. Craniotomy is not needed, and as a consequence, intraluminal occlusion of MCA is a good model to also study cerebral edema induced by the ischemia. Normally, infarcts affect to cortex and striatum and it is highly reproducible. Variability in infarct size or

distribution is due to the slightly differences on the filament position during the tMCAO. However, several parameters as ligature of common carotids (one or both) or their reperfusion after the tMCAO can be modified in order to minimize collateral circulation and therefore, variability.

Before discussing different tMCAO protocols and their implications in intra-arterial administration of labeled stem cells, it would be useful to identify the circle of Willis and their integrants in the images obtained from magnetic resonance angiography (MRA). Axial MRA images of rat brain are a stack of 58 slices where all brain is mapped. In Figure 66 it is shown different slices from a MRA of a healthy rat. Internal carotids are pointed with orange arrows in Figure 66(A) meanwhile in (B), (C) and (D) it is possible to observe their branches: middle (green) and anterior (magenta) cerebral arteries in different slices.

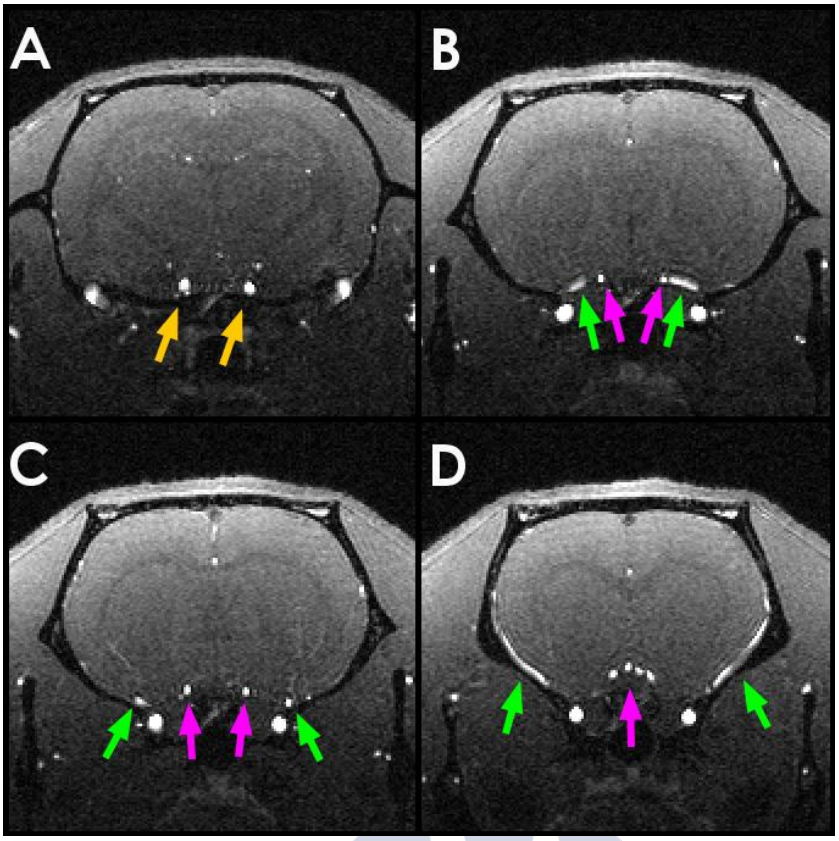


Figure 66: MR angiography of a healthy Wistar rat. (A) Orange arrows correspond to internal carotids of both sides, (B) (C) and (D) Green and magenta arrows correspond to middle cerebral arteries (MCA) and anterior cerebral arteries (ACA) respectively of both hemispheres in different slices.

Normally, MRA is shown as a z-projection, i.e. a coronal image, and from this point of view it is possible to observe the circle of Willis of the rat. This representation is useful to assess the occlusion of the MCA during tMCAO; however we may not forget that this is a projection and because of it several arteries would be overlapped in some parts of their way (Figure 67).

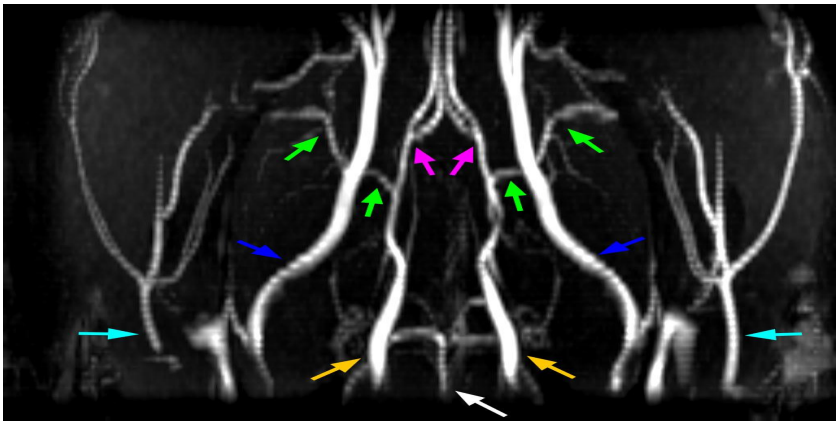

Figure 67: Coronal projection of a MR angiography of a healthy Wistar rat. Orange arrows correspond to internal carotids. Green arrows correspond to middle cerebral arteries. Magenta arrows correspond to anterior cerebral arteries. Cyan arrows correspond to external carotid arteries. Blue arrows correspond to pterygopalatin arteries. White arrow corresponds to basilar artery.

As it has been mentioned before, one of the most extraordinary characteristics of Willis circle is the blood flow compensations if an occlusion event happens. Under normal conditions, blood flow in the posterior communicating arteries, which connect carotid system with vertebrobasilar system, is negligible. However, if a subject has an incomplete circle of Willis, or if is under an occlusion of one or two of the cerebral or carotid vessels, the flow can be redirected to perfuse deprived areas.[256] This arterial system plasticity could also have an influence on the intra-arterial route of administration, because the directions of the flows in each artery could vary if one of the arteries is maintained closed.

Thus, to perform an occlusion of the middle cerebral artery using an intraluminal filament it is necessary to tie the ipsilateral common carotid artery. External carotid will be closed with a permanent suture, the filament will be inserted through it and will advance into the internal carotid

artery. In order to avoid that the filament can go through pterygopalatin (PPA) artery, instead through middle cerebral artery; PPA will be also tied with a permanent suture. Cerebral blood flow is monitored during all surgery procedure; when CC is tied, about a 20% reduction of CBF is registered and when MCA is occluded, the CBF drops 60% more. The Doppler probe position onto the skull of the rat to acquire these measurements is deeply critical. Coyle and Jokelainen[257] published a study where they demonstrated that MCA and ACA of Wistar rats are not independent arteries, i.e. their branches are anastomosed, as it can be observed in Figure 68.

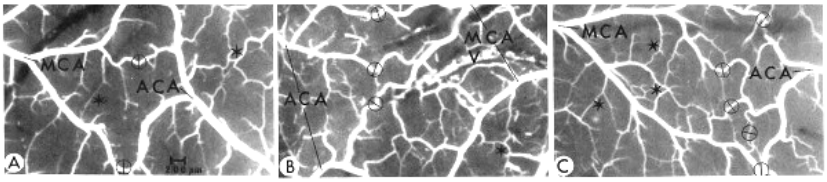


Figure 68: Patterns of rat cerebral arterial collaterals made visible with Vultex. (A) and (C) demonstrate collateral units composed of end-to-end rami. Inter- and intra-arterial anastomoses indicated by circles and stars respectively Stars outside the unit's boundary in A and C indicate intra-arterial anastomoses are not confined within a unit. R is a view of a vascular complex with end-to-side branches. Vein(V). x 15. Adapted from [257].

So, because of this arterial anastomoses and for an accurate measurement of CBF reduction on MCA, Doppler probe should be placed onto the main branch of the MCA, or the measurement will be mainly conditioned by collateral flow. In our experiments, and in order to discriminate where the intraluminal filament is and which brain regions are affected by the reduced blood flow, we have performed MR angiography and diffusion weighted images (DWI) meanwhile the filament was inserted. In that way, Figure 69 and Figure 70 shows MRA images for a

typical intraluminal filament occlusion. Figure 69 (A) assess the presence of IC for contralateral hemisphere (Orange arrow) meanwhile no signal is observed for ipsilateral IC, due to the ligature of CC. In Figure 69(B) it is possible to note that no MRA signal for MCA of ipsilateral hemisphere can be detected due to the occlusion, meanwhile ACA of the same side can be noted. Moreover, in coronal projection of MRA (Figure 70), it is possible to observe where the filament is. In this experiment, intraluminal filament is well-positioned occluding the MCA.

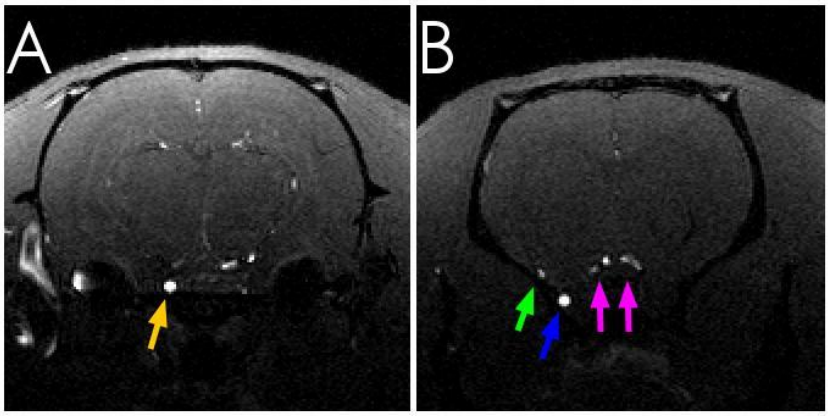


Figure 69: MRA slices during tMCAO. (A) Orange arrow points contralateral IC, meanwhile ipsilateral IC cannot be visualized because of ipsilateral CC ligature. (B) Blue arrow points out contralateral PPA artery, Green arrow points contralateral IC artery and Magenta arrows point ACAs from both sides.

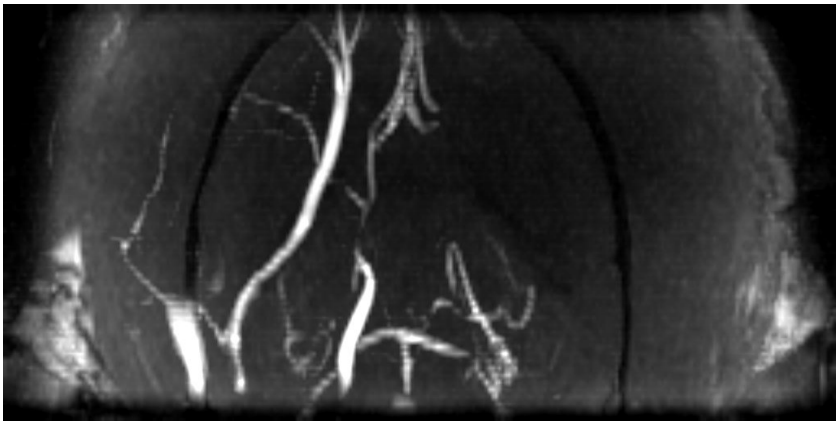

Figure 70: Coronal projection of MRA during tMCAO.

Besides, in order to evaluate the extent and localization of the hypoperfunded brain region, MR DWI was performed. It is important to note that in clinical practice MR DWI infarct region are displayed as hyperintense signal in MRI[258] while preclinical displays are normally hypoinense. This is because clinical MR images normally present the image for the higher "b" value of the sequence (DWI) while preclinical images are normally maps (Apparent diffusion coefficient, ADC), resulted from the adjustment of all "b" values to an exponential decay. So, for the previous animal, ADC maps are shown in grayscale in Figure 71 and color scale in Figure 72. In regard to these maps, tMCAO is affecting to MCA territory where a reduction of the cerebral blood flow (CBF) can be noted in cortex and striatum (dark in grayscale, black-purple-blue in color scale).

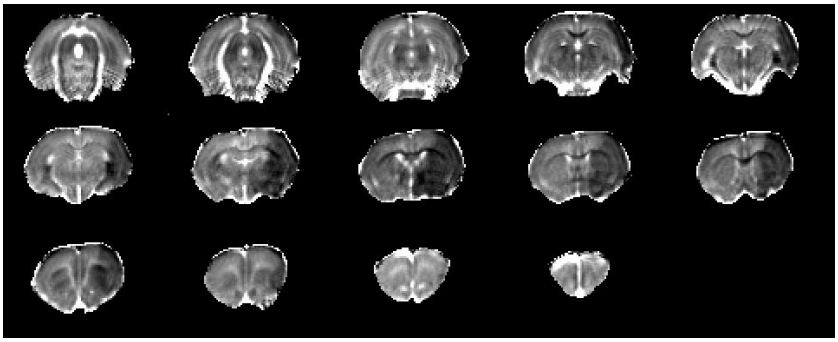

Figure 71: ADC of a Wistar rat during tMCAO. Coefficient diffusion values: grayscale (0.3-2.0) $\cdot 10^{-3}$ $mm^2/s$.

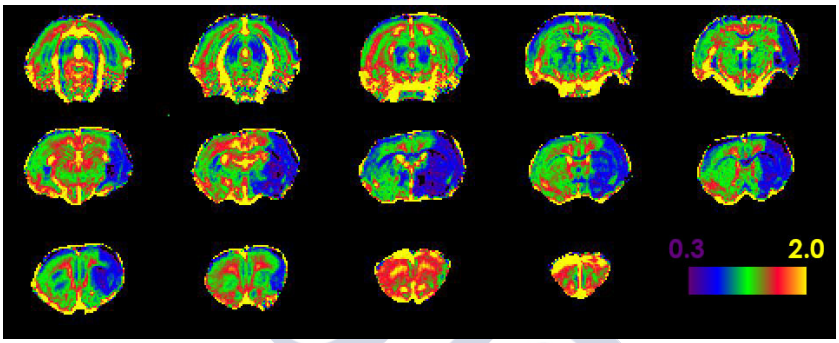


Figure 72: ADC maps of a Wistar rat during tMCAO. Coefficient diffusion values: color scale (0.3-2.0) $\cdot 10^{-3}$ $mm^2/s$.

Our occlusion of the MCA lasts 45 minutes, and after that time this artery is perfused. So far, all procedures of tMCAO are identical for all variations we are going to go through in next section, and as we have mentioned before, mentioned variations involve exclusively the contralateral and ipsilateral common carotid arteries. We may not forget that the main goal of this part is to find out the most efficient and the safest route for intra-arterial delivery of stem cells in an animal model of ischemic stroke. So, in order to assess the efficiency and safety of the procedure, animas will be scanned following $T_2$ and $T_2$* sequences in MRI to evaluate the presence, the absence and the

distribution of injected cells labeled with dextran coated superparamagnetic nanoparticles (Figure 73).

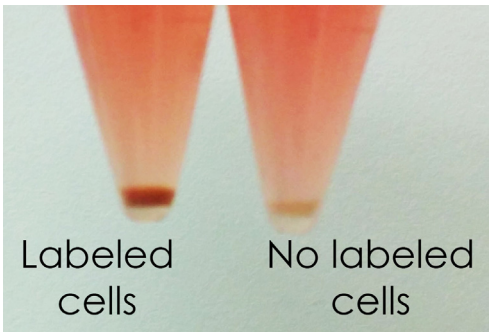


Figure 73: Pellet color differences between labeled cells and no labeled cells.

### 8.3.2. Analysis of different conditions for i.a. delivery in an animal model of cerebral ischemia

a. Contralateral common carotid is ligated during tMCAO. Ipsilateral common carotid remains closed after middle cerebral artery reperfusion. Intra-arterial stem cell delivery is performed with ipsilateral common carotid closed.

This is condition "a" from Table 6. During tMCAO, contralateral common carotid is closed in order to reduce the collateral flow and in this way, the brain will receive blood through vertebrobasilar system. Thus, after 45 minutes of occlusion, the intraluminal filament is pulled out perfunding the MCA, sutures of ipsilateral external carotid and common carotid are tightened while contralateral CC is reperfunded too.

Cannulation of EC is performed and the artery is flushed with heparinized saline to prevent blood clots formation.

The syringe is filled for the intra-arterial delivery of $1x10^6$ labeled mesenchymal stem cells dispersed in PBS. After the injection, the catheter is removed and EC is tied with a suture. (Figure 74)

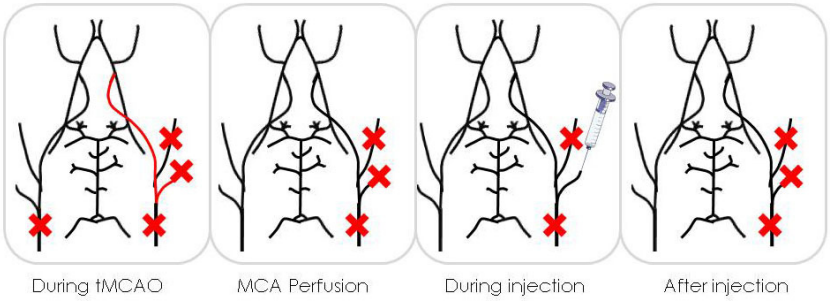


Figure 74: Scheme of animal procedures of tMCAO and intra-arterial cannulation for stem cell delivery following condition "a".

Results showed a high variability in this protocol for intra-arterial delivery: 9 rats did not show labeled cells in the brain (Figure 75), while following the same procedure it was possible to detect labeled cells in other 6 animals (Figure 76).

As we have seen in previous chapters, in phantoms for MRI, labeled cells can be observed as hypointensity signal in $T_2$* weighted images. A dark dotted pattern along the left brain hemisphere in Figure 76 denotes labeled cells presence.

The high variability on cell detection following this procedure could be explained by the circle of Willis compensation flows. Ipsilateral common carotid has been maintained closed since the tMCAO started, and arterial system (contralateral common carotid artery and vertebrovasilar system) had compensated the cerebral blood flow reduction. Because Willis circle might not be the same for all subjects and the direction of the blood flow

after an ischemic event is not well-defined, the most plausible explanation is that the cerebral blood flow is blocking the entrance of the labeled cells in those cases where cells were not detected by $T_2$* weighted images in MRI.

On the other hand, the safety of this injection model is high because both groups of animals, with and without labeled cells in brain after the injection, survived after all procedures.

Consequently, this animal model of cerebral ischemia and intra-arterial injection is not a valid model due to its high variability and low efficiency for brain cell delivery. Our results suggest that an extra blood pumping is needed to push the cells after intra-arterial delivery. Thus, in next section we will study condition "b" from Table 7:Table 6

| Conditions | Con-CC closed during tMCAO | Ip-CC is opened from MCA reperfusion till the injection | Ip-CC is opened during the injection | Ip-CC remains opened after the injection | Evaluation |
|---|---|---|---|---|---|
| a | Yes | No | No | No | No |
| b | Yes | No | Yes | Yes | ? |

Table 7: Evaluation of Ip-CC configuration "a" for animal models of tMCAO and intra-arterial delivery of labeled stem cells.

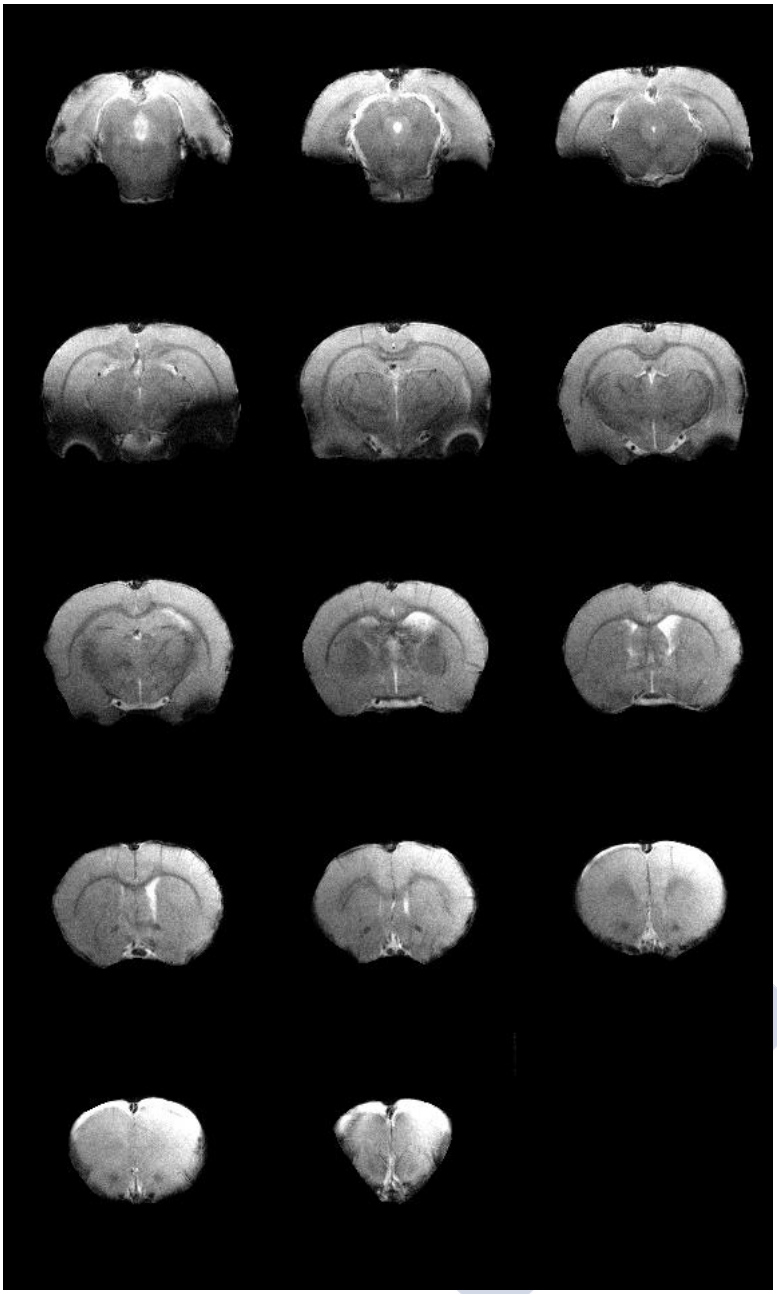

Figure 75: MR $T_2$*-weighted image 4h after intra-arterial injection of labeled MSCs following delivered route condition "a". No labeled cells were observed after the injection.

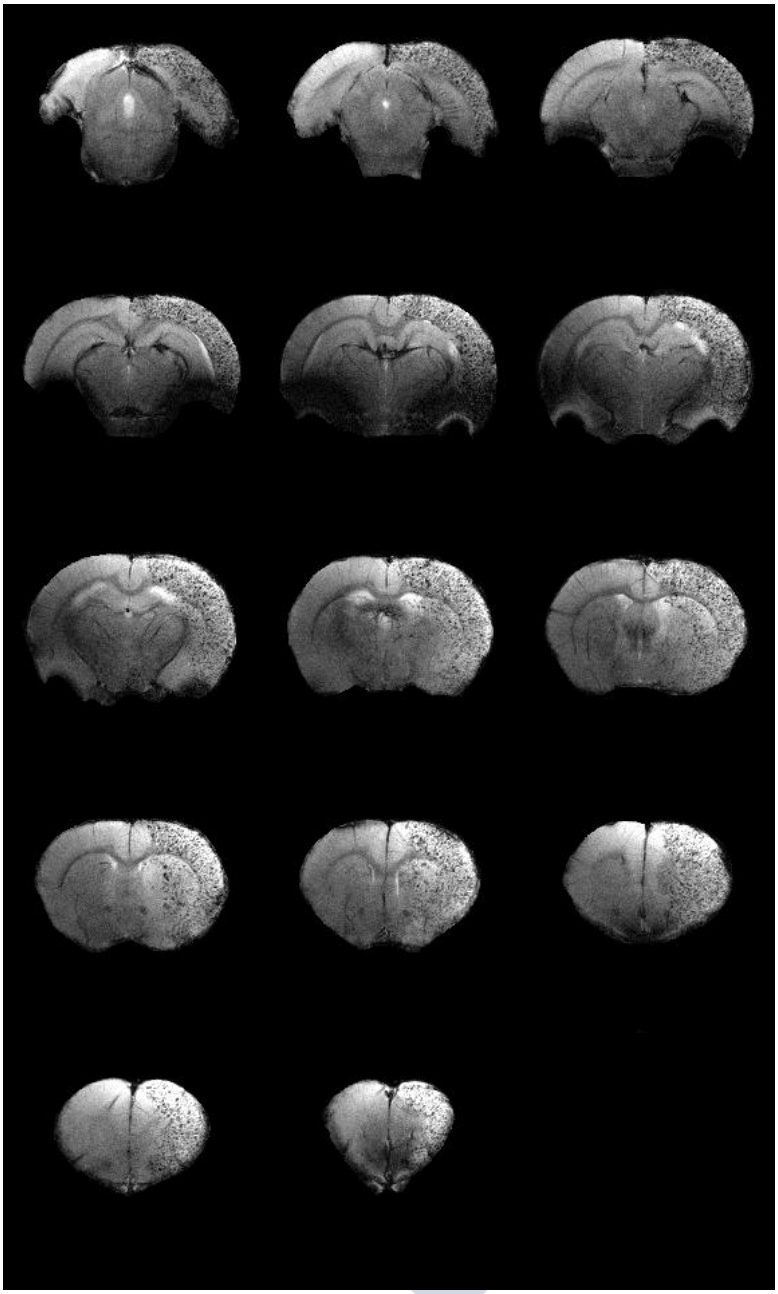

Figure 76: MR $T_2$*-weighted image 4h after intra-arterial injection of labeled MSCs following delivered route condition "a". Labeled cells can be observed along right hemisphere (dotted pattern).

b. Contralateral common carotid is ligated during tMCAO. Ipsilateral common carotid remains closed after tMCAO. At the moment of the injection Ipsilateral common carotid is opened and remains opened after the stem cell delivery.

Here, we will study condition "b" from Table 6. During tMCAO, contralateral common carotid artery is closed in order to reduce the collateral flow and in this way, the circle of Willis will receive blood flow through vertebrobasilar system. Thus, after 45 minutes of occlusion, the intraluminal filament is pulled out perfunding the MCA, sutures of ipsilateral external carotid and common carotid are tightened while contralateral CC is reperfunded too.

Cannulation of EC is performed and suture of Ip-CC is opened, perfunding this artery and all its branches. After it, it is possible to observe blood reflux coming from this vessel entering the EC. As it has been done before, EC artery is flushed with heparinized saline to prevent blood clots formation at the end of the catheter. The syringe is filled with $1x10^6$ labeled mesenchymal stem cells dispersed in PBS for intra-arterial delivery. After the injection, the Ip-CC is temporally ligated to remove the catheter, then EC is tied with a suture and Ip-CC is opened again. (Figure 77)

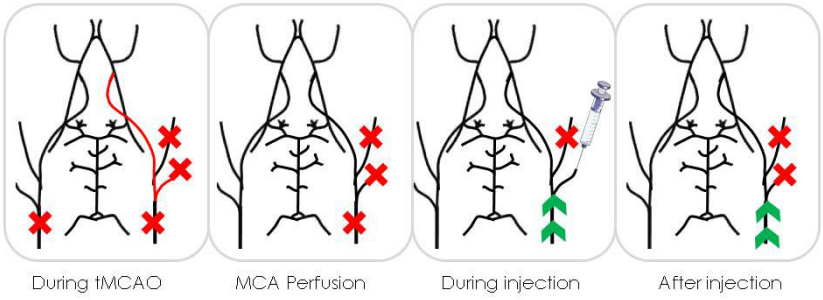


Figure 77: Scheme of animal procedures of tMCAO and intra-arterial cannulation for stem cell delivery following condition "b".

We have found labeled cells in $T_2$* weighted MRI after this procedure for intra-arterial administration in all cases (Figure 78), however, 6 over a total of 8 animals died within 7 days; 4 of them the night after the injection and 2 animals the 4th and 7th day after the injection respectively. Most of the animas died during the night so was not possible to scan them; however, our hypothesis to explain this high mortality was that animals suffered from intracerebral hemorrhage. Ip-CC was closed for 4 hours prior the injection, which could induce damage on the vessel. During and after the injection, the artery and therefore all its branches are opened and carrying blood again. The blood pressure on damage vessels could induce their rupture and consequently, blood extravasations to the parenchyma. It was possible to scan one animal before it was dead and, for this particular case, our hypothesis was confirmed. 7 days after cerebral ischemia and intra-arterial stem cell delivery several hemorrhages were found scattered along the brain in MRI (Figure 79 and Figure 80 (C) and (D)).

These hypointensities could be a misinterpretation of labeled stem cells that migrate into the brain after 7 days instead an hemorrhage, however, by using $T_2$ and $T_2$* MRI sequences it is possible to distinguish between hemorrhages and our labeled cells. Labeled cells can be barely detected in $T_2$ weighted images, as it was already showed in MRI phantoms in Chapters 5 and 6, meanwhile hemorrhages can be easily reported using both sequences. For a better understanding of this fact, Figure 80 shows it. Figure 80 (A) corresponds to $T_2$ weighted images 24h after the injection and Figure 80 (B) corresponds to $T_2$* at the same timepoint, where labeled cells can be observed in $T_2$* sequence while not in $T_2$. On the other hand, after 7 days several hypointensities can be observed in both, $T_2$ and $T_2$* (Figure 80 (C) and (D)) with a higher blooming effect than

in Figure 80(B), denoting the hemorrhage nature of the MR signal.

In general, this procedure for intra-arterial delivery is efficient in terms of directing labeled cells to brain however it presents a high mortality rate, which makes this protocol not valid for intra-arterial administration route. Overall, our results suggest the need of blood which pumps the injected cells to the brain; however ipsilateral common carotid artery perfusion must be performed sooner to prevent vessel damage. Thus, in next section we will study condition "c" from Table 8 to overcome these pitfalls.

| Conditions | Con-CC closed during tMCAO | Ip-CC is opened from MCA reperfusion till the injection | Ip-CC is opened during the injection | Ip-CC remains opened after the injection | Evaluation |
|---|---|---|---|---|---|
| a | Yes | No | No | No | No |
| b | Yes | No | Yes | Yes | No |
| c | Yes | Yes | Yes | Yes | ? |

Table 8: Evaluation of Ip-CC configuration "a" and "b" for animal models of tMCAO and intra-arterial delivery of labeled stem cells.

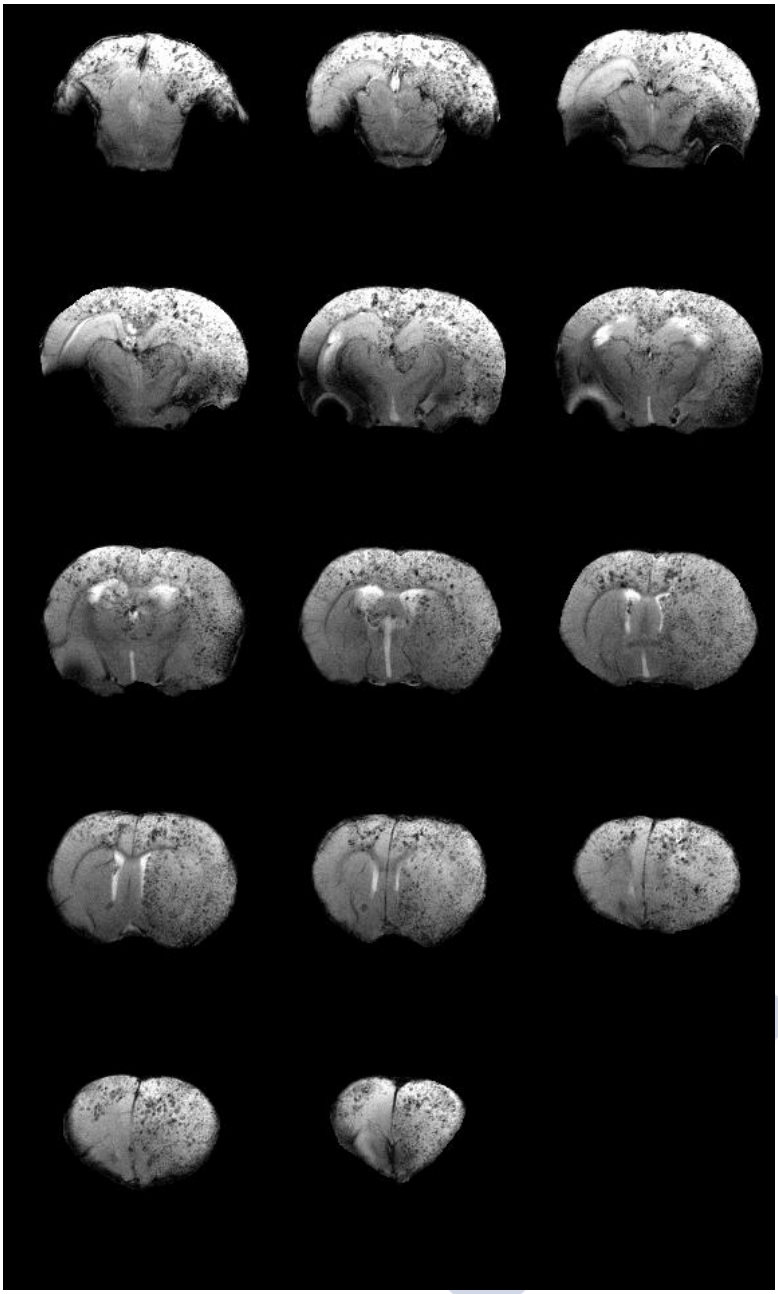

Figure 78: 3rd echo of MGE sequence 24h after intra-arterial injection of labeled MSCs following delivered route condition "b".

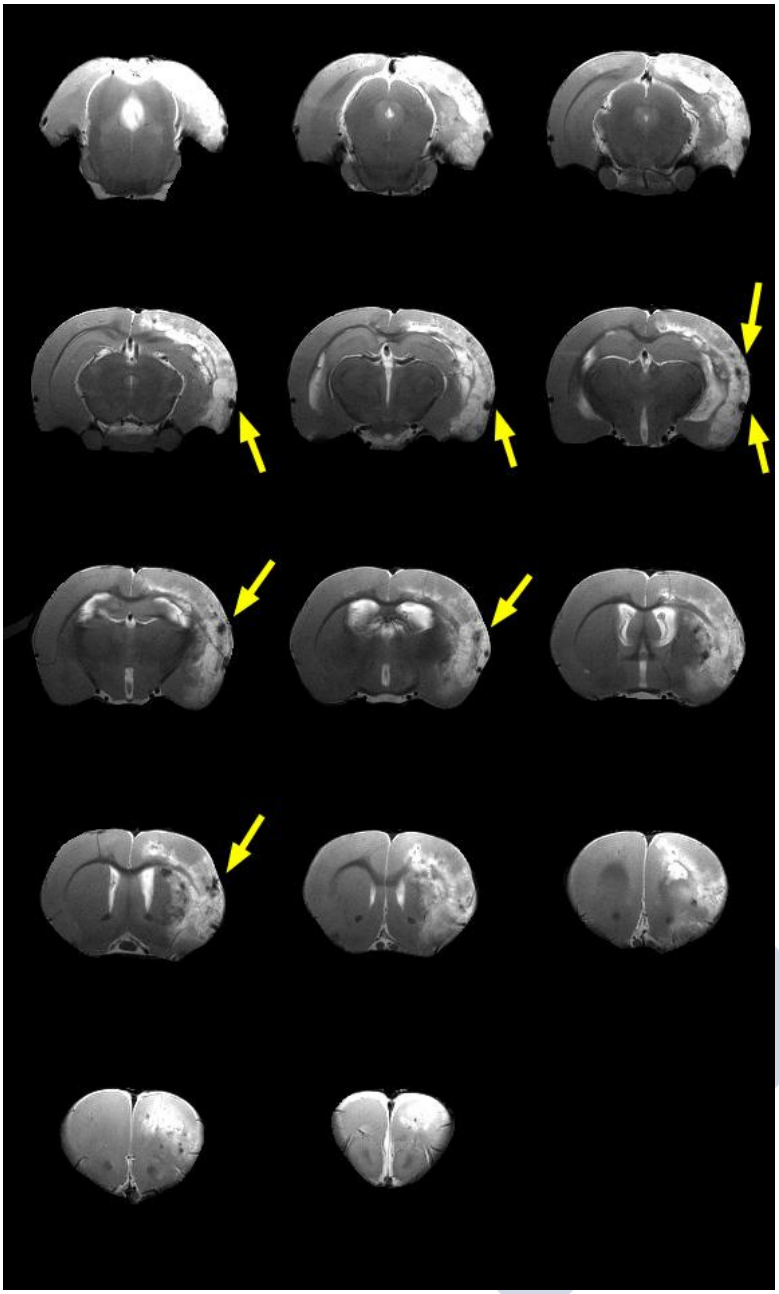

Figure 79: $T_2$ weighted MRI 7 days after the onset of cerebral ischemia and MSCs injection.

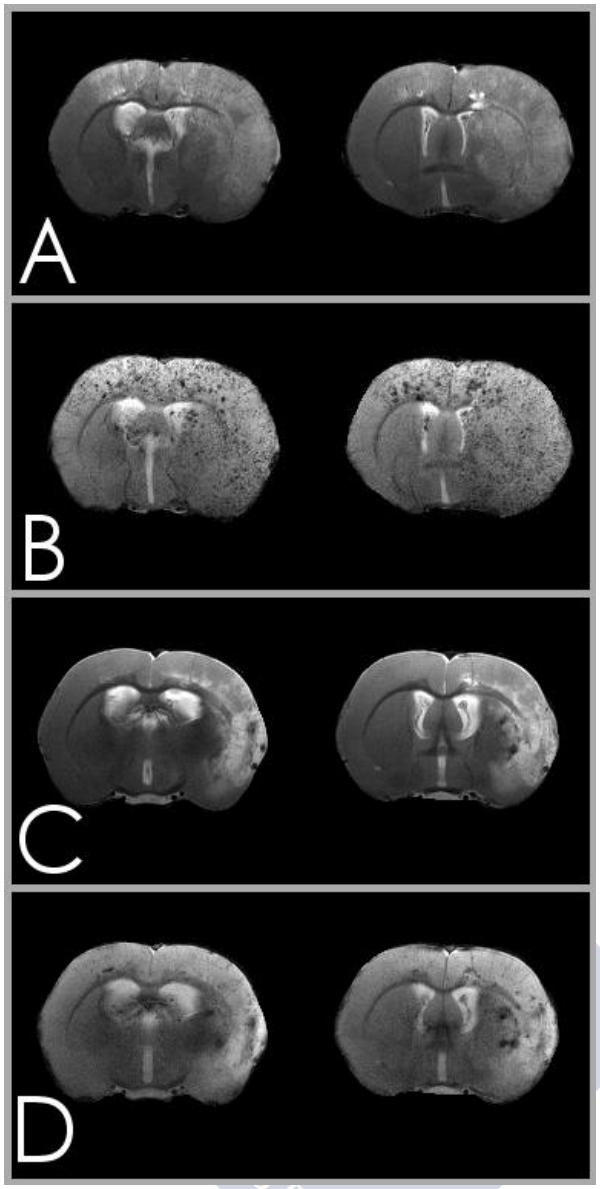


Figure 80: (A) $T_2$ weighted images of Wistar rat brain 24h after cerebral ischemia and MSCs injection, (B) $T_{2^*}$ weighted images of Wistar rat brain 24h after cerebral ischemia and MSCs injection, (C) $T_2$ weighted images of Wistar rat brain 7 days after cerebral ischemia and MSCs injection and (D) $T_{2^*}$ weighted images of Wistar rat brain 7 days after cerebral ischemia and MSCs injection.

c. Contralateral common carotid is ligated during tMCAO. Ipsilateral common carotid is reperfunded at the same time than middle cerebral artery. Ipsilateral common carotid is opened before, during and after the injection.

Considering results from previous sections, here we will consider condition "c" of Table 8, where contralateral CC will be closed exclusively during tMCAO while ipsilateral CC will be reperfunded after tMCAO and it will remain open during all further procedures.

Once animal was cannulated, EC artery was flushed with heparinized saline to prevent blood clots formation at the end of the catheter. The syringe was filled with $1x10^6$ labeled mesenchymal stem cells dispersed in PBS. In order to perform the intra-arterial injection, Ip-CC will be open helping the cells migrate into the brain. After the injection EC is tied with a suture. (Figure 81)

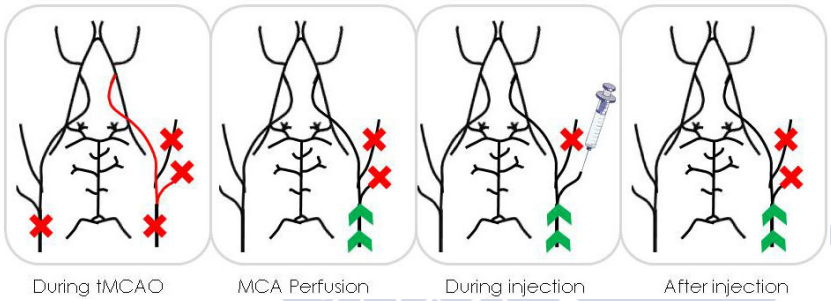


Figure 81: Scheme of animal procedures of tMCAO and intra-arterial cannulation for stem cell delivery following condition "c".

This procedure for intra-arterial administration is efficient in terms of cell administration because all animals (12) showed hypointense dotted signal in $T_2$*-weighted images. However, all of them had difficulties for breathing when woke up from anesthesia, and several (6) died few hours

after being injected. For a better understanding of this procedure results, we are going to focus on one animal which was being scanned when died. MRI showed dispersed cells along the brain as it was reported in previous sections, but performing a coronal $T_2$*-weighted scan, cells did also appear in the cerebellum (Figure 82 (A), (B)). To discard hemorrhagic events, $T_2$ weighted images were acquired and a hyperintense signal was observed, not only in the territory of MCA, as well in the cerebellum, which could be related to ischemias in this region.

Our hypothesis of why cells migrate not only to the brain, along the cerebellum as well is based on the posterior communicating artery flows. Vertebrobasilar system is connected to carotid system through these arteries. When an occlusion of both common carotids is performed (for tMCAO model), posterior communicating arteries provide the blood to the brain from vertebrobasilar system. These arteries must adapt to new situation increasing their caliber for this blood supply. However, when the cell injection is performed, the distribution along the brain and cerebellum is going to depend on the CBF distribution in the circle of Willis, and in this particular case, cells migrated towards cerebellum. In order to avoid this distribution, it is necessary to have an extra blood supply apart from the provided by vertebrobasilar system. For tMCAO surgery is necessary that the ipsilateral common carotid remains closed, because the intraluminal filament will pass through the external carotid and advance through the internal carotid to reach the middle cerebral artery. But there is still a possibility for reducing the vertebrobasilar incoming flow: the contralateral common carotid artery. Normally, we close this artery to avoid collateral flow during tMCAO and therefore more stable ischemic lesions after tMCAO. However, due to the nature of the intra-arterial injection we

will study the influence of the contralateral common carotid incoming flow for labeled stem cell delivery in the next section.

On the other hand and apart from cell distribution, one million cells for intra-arterial delivery could be inducing ischemia, as it can be early detected in Figure 82(C) and (D). We have chosen 1 million cells for intra-arterial delivery based on recent studies, which have been injecting from 1 million to 30 million cells[117-120,182,184,259-261]; however, not all of these studies have tracked the cells after being injected assessing the efficiency and safety of the route. So, considering MRI of the last injected animals and before assessing the influence of the contralateral common carotid artery flows, we will inject different amount of labeled cells ($1x10^6$ cells, $0.5x10^6$ cells and $0.25x10^6$ cells), in order to evaluate the well-being of the animal and the cell distribution in MRI.

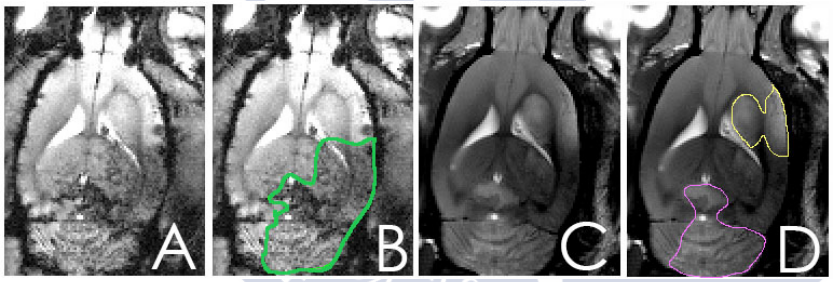


Figure 82: (A) and (B) same slice of the 5th echo of MGE sequence 4h after intra-arterial injection of $1x10^6$ labeled MSCs following delivered route condition "c". In (B) hypointense signal produced by labeled cells is delimitated in green. (C) and (D) are $T_2$ weighted MR images of same slice 4h after intra-arterial injection of $1x10^6$ labeled MSCs following delivered route condition "c". Yellow line and Pink line in (D) would correspond to ischemic lesion produced by tMCAO and region where labeled cells were found respectively.

In Figure 83 intra-arterial injections of $1x10^6$ cells (A), $0.5x10^6$ cells (B) and $0.25x10^6$ cells (C) were performed. It was not

observed cerebellar ischemia for less than one million cells injection, and $0.25x10^6$ labeled cells can still be observed after intra-arterial injection. With regard to the safety of the injection, in next sections we will further study the influence of the injections into the CBF for these amounts of cells.

Thus, considering all these findings, in next section we will study the distribution of $0.25x10^6$ labeled cells after an intra-arterial injection without contralateral common carotid artery occlusion. We will also evaluate the localization and the possibility of ischemic injuries induced by the injection. Hence, in next section we will study condition "d" from Table 9; Ip-CC is reperfunded after perfunding the MCA, during the injection and remains open after it in order to push the cells to the brain, but maintaining contralateral CC intact during all procedures.

| Conditions | Con-CC closed during tMCAO | Ip-CC is opened from MCA reperfusion till the injection | Ip-CC is opened during the injection | Ip-CC remains opened after the injection | Evaluation |
|---|---|---|---|---|---|
| a | Yes | No | No | No | No |
| b | Yes | No | Yes | Yes | No |
| c | Yes | Yes | Yes | Yes | No |
| d | No | Yes | Yes | Yes | ? |

Table 9: Evaluation of Ip-CC configuration "a", "b" and "c" for animal models of tMCAO and intra-arterial delivery of labeled stem cells.

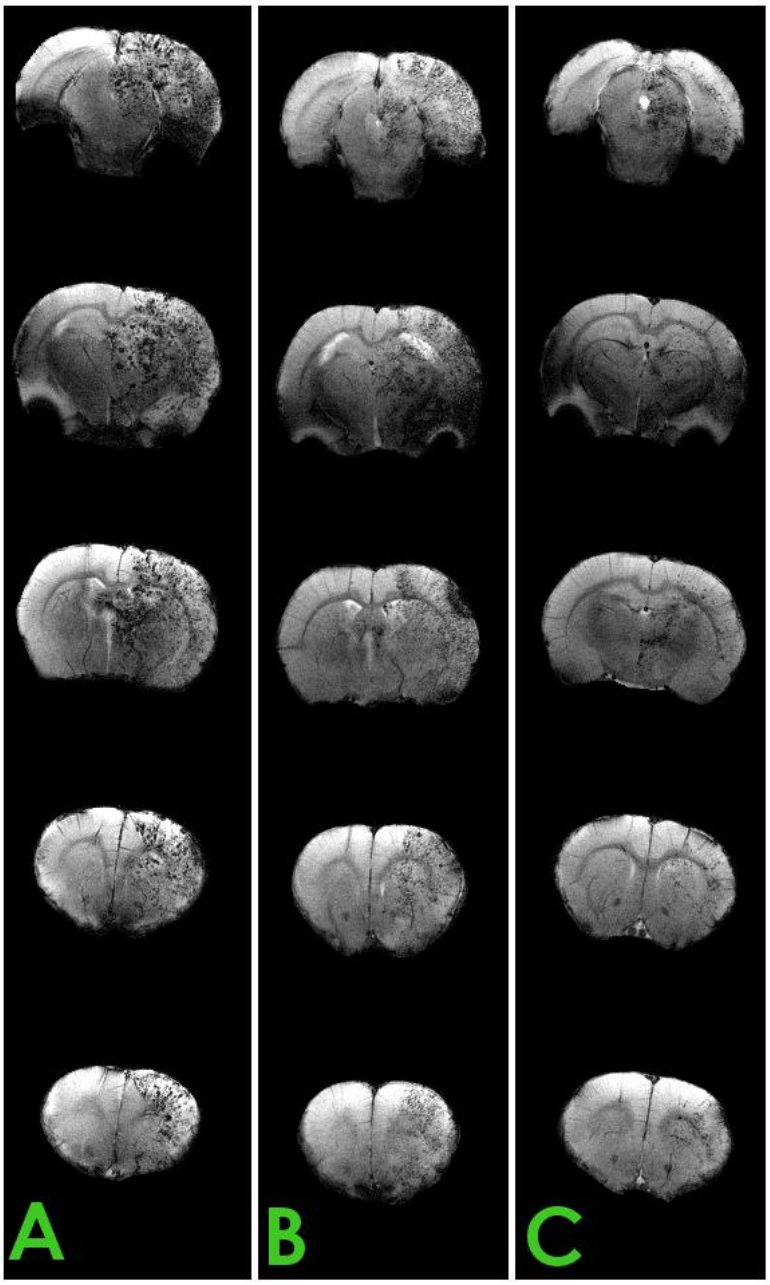


Figure 83: $T_2$* weighted images of different slices of a Wistar rat with cerebral ischemia 4h after the injection of (A) $1x10^6$ labeled MSCs, (B) $0.5x10^6$ labeled MSCs and (C) $0.25x10^6$ labeled MSCs.

d. Contralateral common carotid is intact during tMCAO. Ipsilateral common carotid is reperfunded at the same time than middle cerebral artery. Ipsilateral common carotid is opened before, during and after the injection.

Surgery for tMCAO and further cannulation for intra-arterial delivery of labeled MSCs is only performed in the left side. Ipsilateral common carotid is occluded during tMCAO procedure, and furthermore is temporally ligated to insert and pull out the cannula for the MSCs intra-arterial delivery. $0.25x10^6$ labeled cells were dispersed in 300 µL of PBS and injected through EC as previously described. Ipsilateral common carotid is open before, during and after the procedure. 3 animals were included for these experiments and all of them survived.

Figure 84 shows one of the animals 4h after being injected following this route. As we had expected, hypointense dotted pattern signal is more reduced than in previous procedures due to the lower amount of injected cells ($0.25x10^6$ now versus $1x10^6$ before), however all slices do display labeled cells. We have also performed coronal scans ($T_2$* and $T_2$) in order to evaluate the cell distribution in the cerebellum and possible ischemic regions (Figure 85). No labeled cells were found in cerebellum in $T_2$*(Figure 85 (A)) and also no hyperintensity signal in $T_2$ was detected (Figure 85 (B)), i.e. no ischemia in the cerebellum was observed.

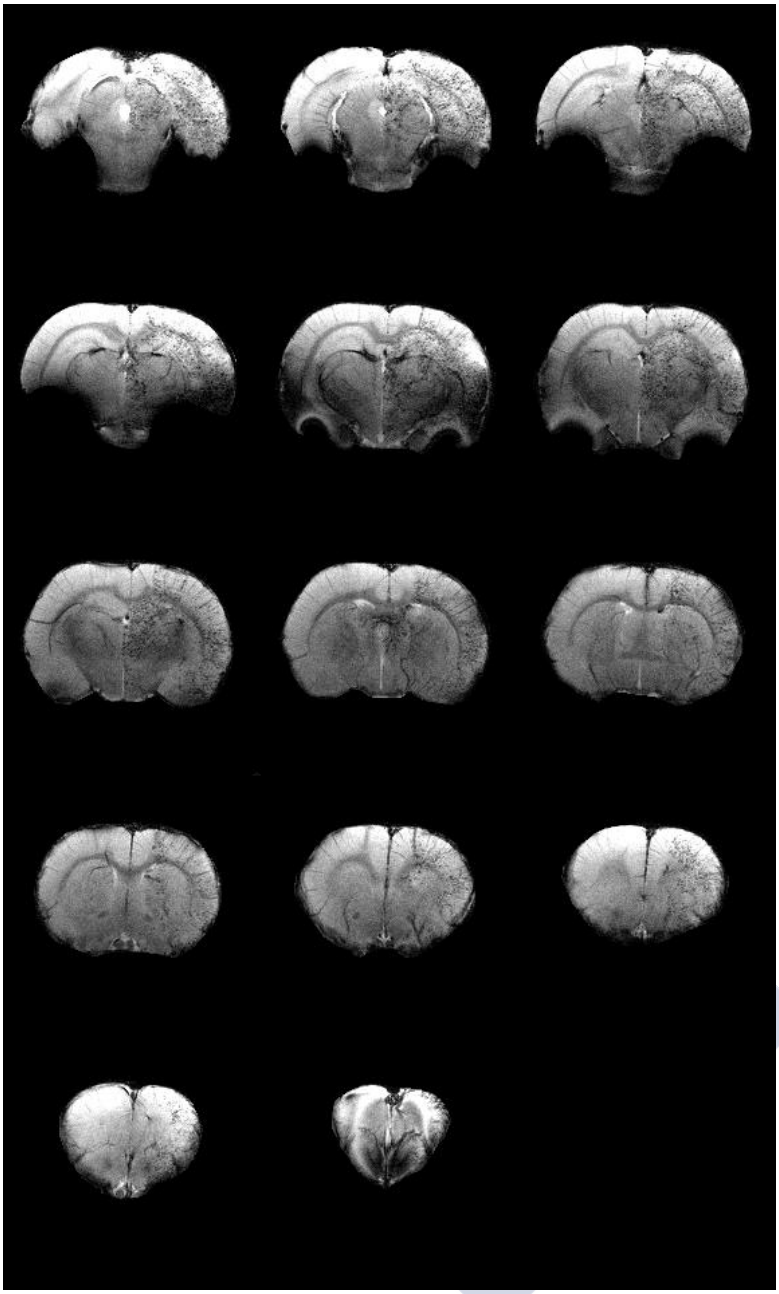

Figure 84: $T_2$* weighted images 24h after intra-arterial injection of labeled MSCs following delivered route condition "d".

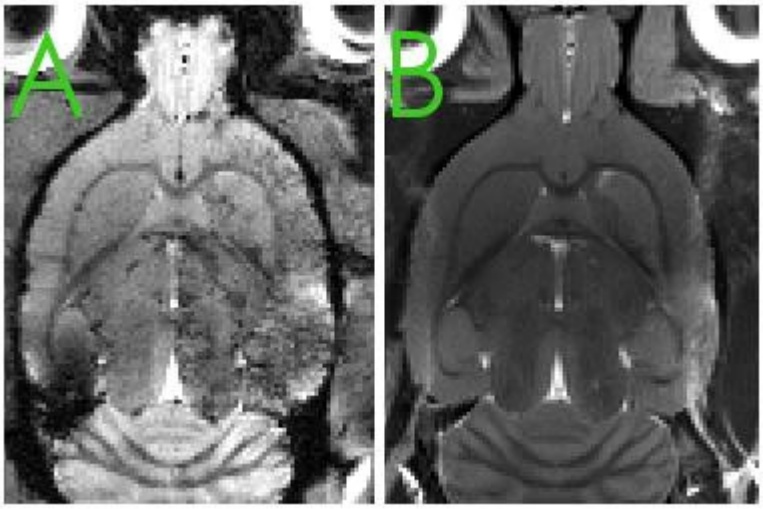


Figure 85: (A) $T_2$* weighted image of a coronal slice 4h after labeled MSCs injection; labeled cells are spread in the right brain hemisphere and no cells are observed in the cerebellum. (A) $T_2$ weighted image of same coronal slice 4h after labeled MSCs injection; it can be observed a shadow in the right ventricle which could be ischemic lesion after tMCAO.

Eventually, surgery of tMCAO performed exclusively on the left side allowed a uniform cell distribution along the brain after intra-arterial delivery. With contralateral common carotid artery opened during tMCAO, posterior communicating arteries contribute to the cerebral blood flow; however vertebrobasilar system is not the unique source of blood supply for deprived areas. When tMCAO is over and intraluminal filament is pulled out from middle cerebral artery, ipsilateral common carotid is perfunded to prevent vessel necrosis and therefore hemorrhagic transformation.[262] As we had observed in previous sections, it is necessary an extra blood flow to push the injected cells to brain, so during the injection common carotid flow will further transport them. Labeled cells were not observed in cerebellum and multifocal ischemias produced by them either.

In regard to the safety of the procedure, all animals survived after injection and their behavior after waking up from anesthesia was normal; they did not present difficulties for breathing or exploring the cage. Hence, gathering all these data, this is the safest and most efficient model of ischemic stroke and intra-arterial administration of mesenchymal stem cells in Wistar rat.

However, after these results two questions are still on the bench. On one hand it is necessary to evaluate if the magnetic vectorization of labeled cells could increase the amount of cells in the animal brain following intra-arterial delivery without compromise the safety, and on the other hand, if cells after an intra-arterial injection with or without magnetic vectorization could provoke occlusions that can lead to multifocal ischemias.

### 8.3.3. Magnetic vectorization *in vivo*

In chapter 7, we have already demonstrated that mesenchymal stem cells labeled with dextran coated nanoparticles can be magnetic vectorizated in a 2D environment without harmful effects on the cells.

In this section we will discuss if 1T magnet can guarantee or increase the amount of labeled cells in the brain after an intra-arterial injection. Previous studies have used 0.3 T magnets[223] however, considering that the adhesive force follows an exponential decay with the distance, as it can be noted in Figure 86 (1T Magnet data sheet, article Q-51-51-25-N, Supermagnete) we have selected the rare magnet with the highest magnetization available to cover most of the brain with the highest adhesive possible force.

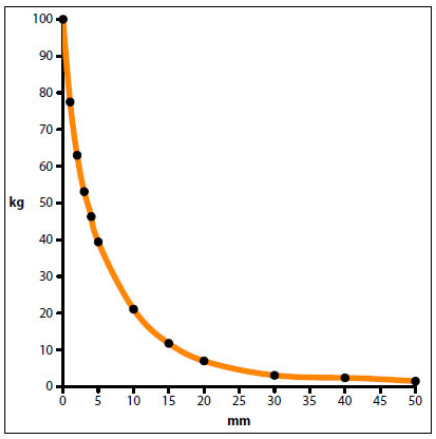


Figure 86: Adhesive force in ration to the air gap between magnet and a steel plate. (1T Magnet data sheet, article Q-51-51-25-N, Supermagnete)

Under sevofluorane anesthesia, the head and the neck of the animal were placed on to the magnet as it is shown in Figure 87 prior to be injected. After cell administration, animals stayed in contact with the magnet for 4 extra hours, and then magnetic vectorization was evaluated in MR $T_2$* weighted images, as it was done before for cell tracking in animal models of stroke. *In vivo* conditions are quite different from *in vitro*, however timing for magnetic vectorization was chosen based on *in vitro* experiments; where MSCs in culture get attached to the flask or well after 4h.

We have studied the influence of the magnet for all previous tMCAO-injection conditions and no differences with and without magnet were observed, however we went through the different possibilities.


Figure 87: Wistar rat positioning for magnetic vectorization experiments.

For the first condition "a" without the magnet, where common carotid is not pumping the cells and therefore, the cells not always reach the brain, magnetic vectorization did not contribute to attract labeled cells to brain region. No differences were found after an intra-arterial injection of one million cells with and without the magnet. So, all seem to point out that applied magnetic forces were not enough to attract injected cells to the brain, but maybe they could hold the cells if eventually they enter into the magnetic field.

In order to prove last hypothesis, conditions "b" and "c" were evaluated. The major inconvenience of these conditions is the high mortality associated to the procedure as it was previously reported. For these cases, the magnet effect on the cells did not reduce the mortality and no differences on labeled cell distribution along the brain were observed either (data not shown).

Then, 4h after cerebral ischemia, $0.5x10^6$ labeled MSCs were injected following "d" condition. No differences were observed 4h after injection in MRI as it can be observed in Figure 88 with and without magnet. Cell brain distribution is not exactly the same with and without magnet considering the hypointense signal in $T_2$* weighted images, but these pattern asymmetries could be more influenced by the differences on the brain vessel ramifications than by the magnet presence because no cell pattern associated to magnetic field lines was observed. If magnetic field would have a macroscopic influence on the cell retention, it would be expectable that as closer to the magnet as higher would be the hypointensities in $T_2$* weighted images, however no differences in cell distribution were observed for both groups.

To elucidate the mechanism that holds the cells in the brain of the animal and allow us to detect labeled cells at least 4h after being injected, several experiments were performed following condition "d". Next table summarizes all approaches performed:

| Hypothesis | Approach |
|---|---|
| Cellular aggregation prior to injection | Reduce cell concentration<br>Controlled delivery rate<br>Manual-Infusion pump<br>Increase catheter length<br>Cell passage number |
| Cellular aggregation after injection | Antiaggregant administration<br>Antiplatelet administration |
| Cell specificity | MSCs and C17.2 |
| MNPs specificity | Dextran-MNPs and PluronicF127-MNPs |
| Serum reactivity | *In vitro* aggregation |

Table 10: Approaches to elucidate the mechanism of cellular entrapment after intra-arterial delivery.

On one hand, cells could be aggregating before being injected. To avoid this, we change the cellular concentration in PBS before injection changing total injected volume from 300 µL to 1 mL. What we found is that cell distribution for 1 mL was similar to 300 µL but an important brain edema after injection was observed for 1 mL.

In this way, and maintaining 300µL of injection, instead of performing the administration by manual injection a micro-infusion-pump was used for stem cell delivery. Injection was performed for 15 minutes but following a constant delivery that could overcome the bolus-like manual injection. No differences were observed between manual and pump-controlled administration.

Other approach we also considered was the possibility of cell precipitation into the syringe. Because the duration of the injection was 15 minutes and the length of the catheter was 20cm, we hypothesized that cells could precipitate in the syringe, aggregate and what we were actually injecting were cell aggregates instead of a single-cell suspension. To overcome this we have used a 2 m length catheter and prior to injection it was filled up with the cells in PBS. However, no differences were observed changing the length of the catheter.

We have also evaluated if the passage number of the injected cells could have an influence onto the cellular retention in brain, but no differences were observed between passage number 7 and 18.

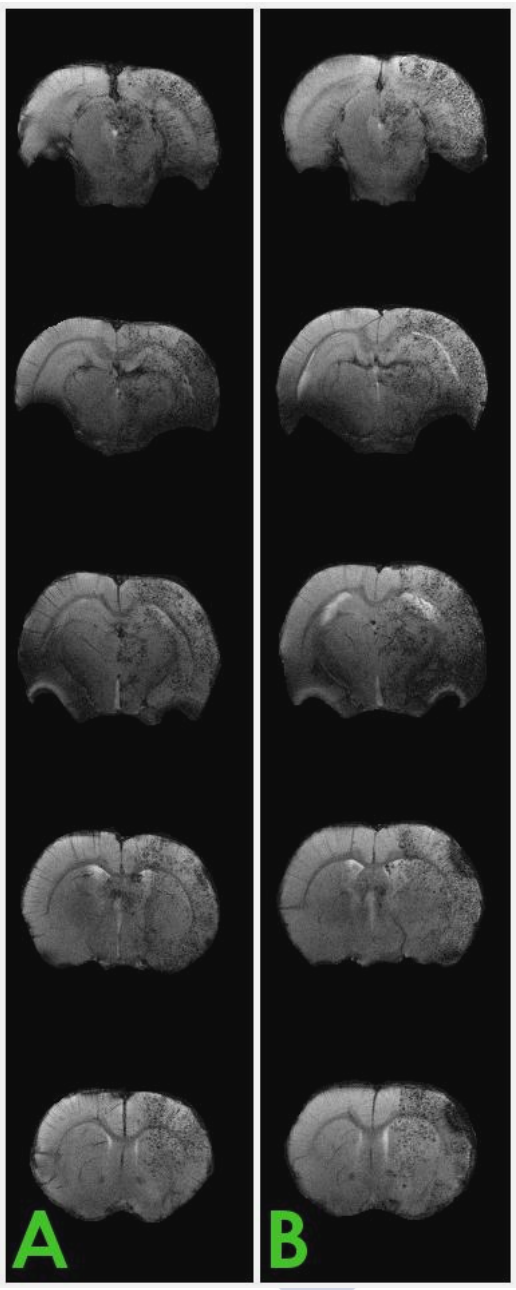


Figure 88: $T_2$* weighted images 4h after 0.5x$10^6$ labeled MSCs intra-arterial injection of (A) Wistar rat 4h after onset of cerebral ischemia with

magnet, (B) Wistar rat 4h after onset of cerebral ischemia without magnet.

After all these changes related to cellular status before injection and no differences observed between them, we thought that maybe was not a consequence of cellular aggregation prior to injection, but a reaction after being injected. To prove this hypothesis, 3 different experiments were performed. Our first hypothesis was coagulation problems mostly due to the injection surgery, but also for using PBS for cell delivery, although most of cellular administration studies use this vehicle for injecting the cells.[117,182,259,260] Cells were dispersed in heparinized PBS and injected following the intra-arterial delivery procedure, however 4h after injection it was possible to observe cells in the rat brain in MR $T_2$* weighted images. Secondly, we thought about the possibility of platelet aggregation as a consequence of the injection. To overcome this fact, animals were pretreated with antiplatelets (Adiro) and labeled cells in PBS were intra-arterially administered. Once more, no differences in cellular detection through MRI were observed after antiplatelet pre-administration.

So far, we have tested all these hypothesis of cellular detection 4h after injection using mesenchymal stem cells labeled with dextran-coated superparamagnetic nanoparticles. In order to demonstrate if the entrapment effect is dependent on the type of injected cells we evaluated the injection of neural stem cells C17.2 labeled with dextran-coated MNPs already characterized in Chapter 6. No differences were observed between C17.2 and MSCs in MR $T_2$* weighted images 4h after an intra-arterial injection.

Moreover, in section 3, we have demonstrated that for the labeling protocol used,[227] all magnetic nanoparticles for cell labeling are inside the cell, not attached to the surface, so MNPs should not be a parameter which explains the entrapment. However, we also used MSCs labeled with Pluronic F127-coated MNPs to confirm this hypothesis. No differences of cellular entrapment in the animal brain were observed between MSCs labeled with dextran or pluronic F127 coated MNPs, so it was also verified that the type of MNPs does not have an influence on injected cell detection.

Finally, considering that the MSCs we have used are from a donor rat, it could be that injected cells are reacting with animal serum once injected, as it was reported in other study.[263] To prove this hypothesis, we cultured MSCs and C17.2 cells in IMDM and DMEM respectively using 20% Wistar serum or 20% FBS. Pictures of all groups were taken and no aggregation was observed for any group after 1 and 6 hours, concluding that MSCs either C17.2 aggregates in Wistar serum (data not shown).

In light of these results, magnetic vectorization after an intra-arterial delivery of labeled mesenchymal stem cells in an animal with cerebral ischemia is not needed. For those animal models that cells not always end up in the brain, magnetic vectorization resulted not effective, and for those that cells always end up in the brain, magnetic cell guidance did not increase the amount of cells in the brain. We have also studied several factors that could influence the cell entrapment in the brain; however none of the investigated approaches gave us an explanation of the mechanism. In order to elucidate this natural vectorization, it would be necessary to study MSCs administration in healthy animals to evaluate if molecular ischemic processes

have an influence on the entrapment, and this will be one of the objectives of the next chapter.

### 8.3.4. Monitoring of cerebral blood flow for an intra-arterial injection of labeled mesenchymal stem cells in healthy rats

So far, we have reported the most efficient and the safest route for intra-arterial administration, and also that magnetic vectorization does not increase the amount of cells in brain from a macroscopic point of view. However, it is still necessary to demonstrate if the injection of labeled cells can affect the CBF.

We have observed that for several tMCAO & intra-arterial injection procedures cells can migrate into the cerebellum producing an ischemic lesion that can be early observed in $T_2$ weighted images (Figure 81). We assume that the hyperintense signal in the cerebellum was a consequence of the injection, because tMCAO occlusions do not affect that territory.

In non-ischemic animals and following the last injection procedure "d", we would evaluate the cell entrapment in healthy brains. We would also assess if MSCs provoke multifocal ischemias by monitoring the CBF during the injection and studying $T_2$ weighted images 24h after cell delivery. At this point, because stem cell administration is going to be performed in healthy animals, if MRI reveals ischemic lesions, they would be a consequence from the MSCs injection unambiguously.

Thus, 6 healthy animals were used for studying the CBF changes as consequence of the injection, and 3 different conditions were evaluated: PBS; $1x10^6$ MSCs and $0.25x10^6$

MSCs. For an optimal monitoring, prior to injection 3 doppler probes were placed onto the squamosal bone in the skull and cannulation surgery was performed as previously described following "d" condition. (Figure 89)

CBF was monitored during all procedure. 24h after MSCs administration MR $T_2$ weighted images were acquired to assess focal/multifocal ischemias due to the intra-arterial cellular injection. Results of transcranial Doppler flow measurements and $T_2$ weighted images 24h after the injection are shown in Figure 90, Figure 91 and Figure 92 for PBS, $1x10^6$ MSCs and $0.25x10^6$ MSCs respectively.

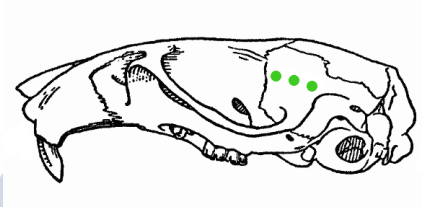

Figure 89: Lateral view of the skull of a rat (adapted from[264]). Color dots shows the different Doppler probes position onto the squamosal bone for monitoring CBF before, during and after the mesenchymal stem cell intra-arterial administration.

The measurement of the CBF in three different regions was performed following the same procedure for all animals. (Figure 89)

In order to evaluate the safety of the procedure, first group of study was an intra-arterial delivery of 300 µL of vehicle (PBS). As it can be noted in the graph of Figure 90, CBF was constant during all procedure for all of the 3 probes used. All profiles did not show peaks and valleys during the injection and after it either. MR $T_2$ weighted images were performed 24h after injection, and no hyperintensities were observed along the brain (Figure 90), confirming the safety of this intra-arterial administration route.

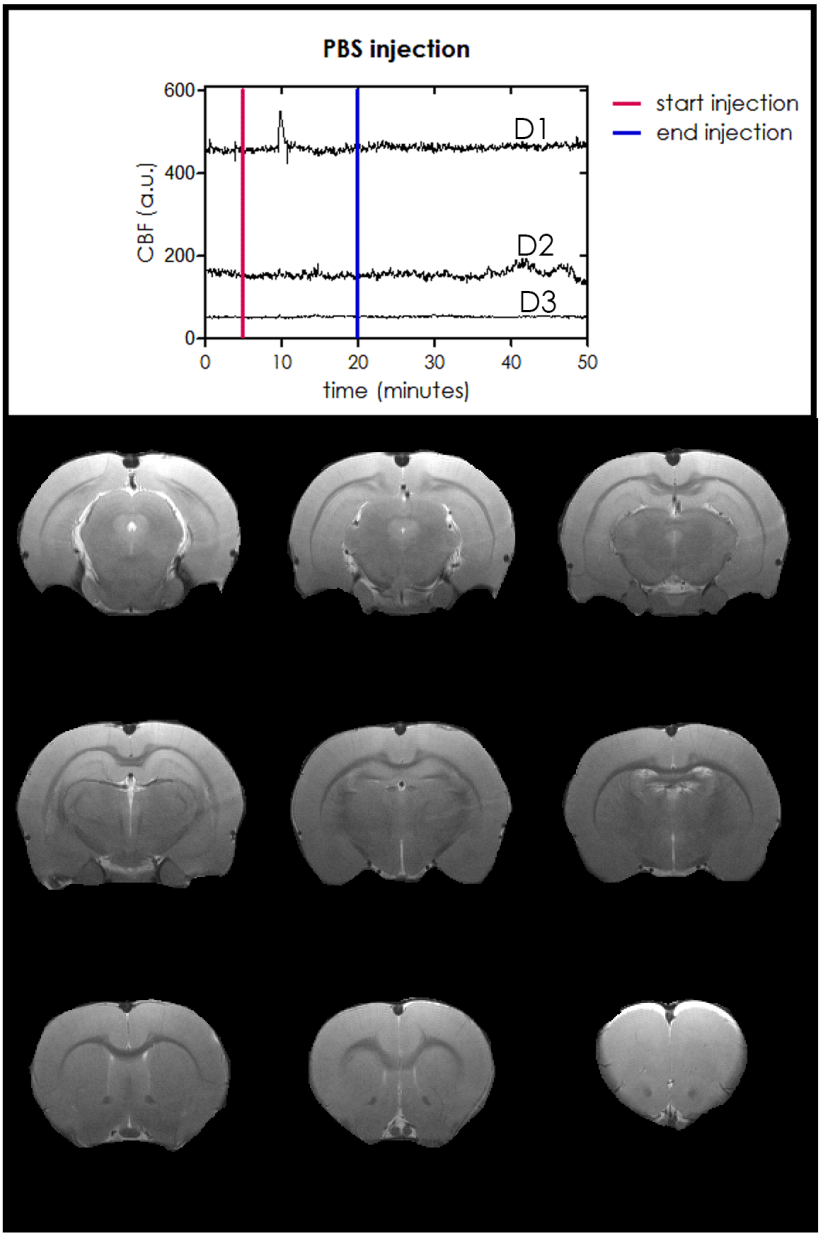


Figure 90: CBF for 3 Doppler probes (D1, D2, D3) measured before, during and after the injection of PBS; and MR $T_2$ weighted images of several slices 24h after the injection.

In previous sections we had reported that most of animals which had been injected with $1x10^6$ cells after tMCAO, died short after stem cell delivery. In order to elucidate if injected cells can provoke ischemic lesions and consequently the animal death, 2 healthy animals were considered for these injections. One of them died 6h after the injection and the other survived 24h. CBF monitoring of this animal is shown in the graph of Figure 91. Unlike PBS administration, for one million cell delivery it is possible to observe peaks and valleys during the injection for all Doppler measurements. What is also interesting in this graph is the CBF reduction that can be observed in the three of them after the cell administration; however it is more evident for the upper profile line (going from approximately 150 to 100). CBF was monitored for 40 minutes more after finishing the cell delivery, but no changes were observed after it. Considering these Doppler profiles, it would be expectable to observe hyperintensities in MR $T_2$ weighted images 24h after the injection. In effect, in Figure 91 it is possible to observe multifocal ischemic regions (hyperintensity in $T_2$ weighted images) distributed along the brain. Most of them were found in the hemisphere where the cannulation and administration was performed, however due to the circle of Willis some hyperintensities were also observed in the contralateral hemisphere. For an injection of one million cells, Doppler flow monitoring showed a reduction in the CBF which was further confirmed by the presence of multifocal ischemic lesions in $T_2$ weighted images 24h after the mesenchymal stem cells administration.

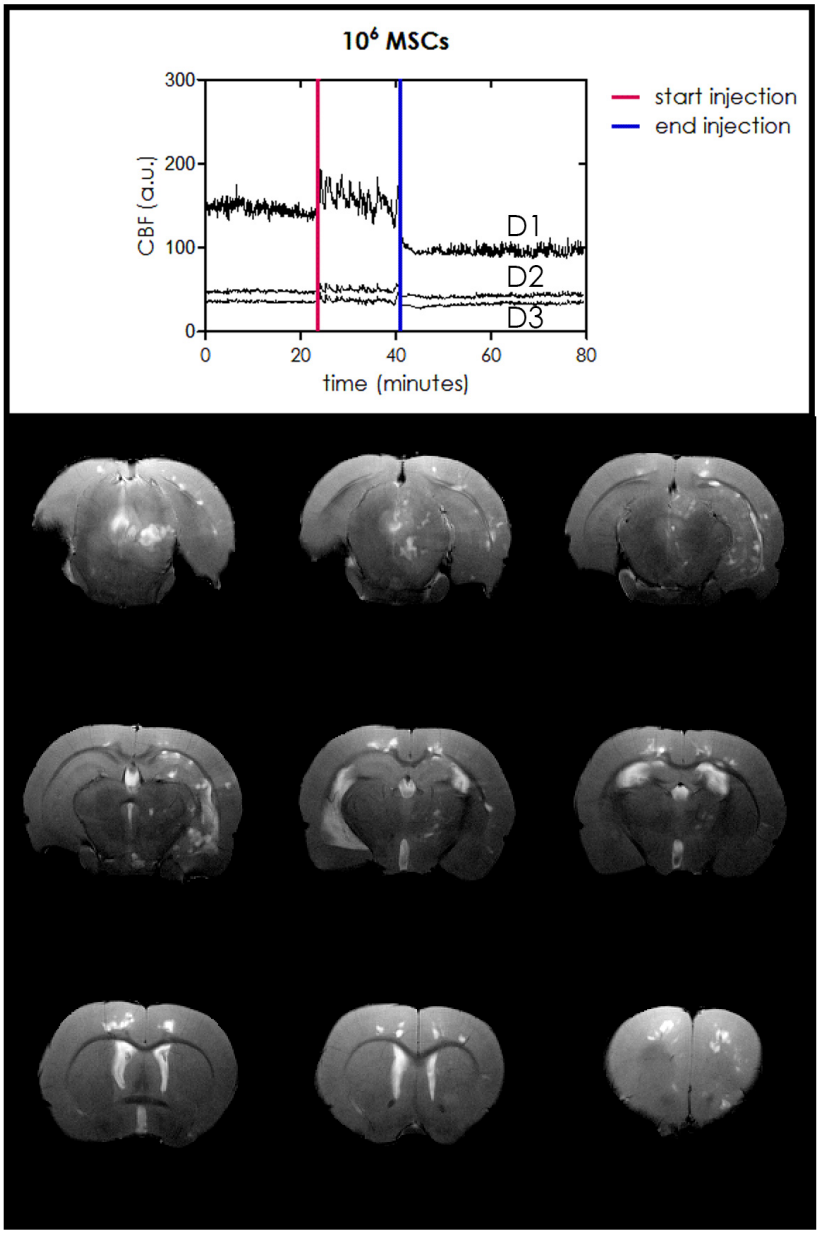


Figure 91: CBF for 3 Doppler probes (D1, D2, D3) measured before, during and after the injection of $10^6$ MSCs; and MR weighted images of several brain slices 24h after the cell delivery.

We have already reported that no animals with cerebral ischemia died after an intra-arterial injection of $0.25x10^6$ mesenchymal stem cells. In this section we have studied if those injections can vary the CBF in 3 healthy rats. In regard to Doppler measurements in Figure 92, in this animal it is also possible to observe peaks and valleys during the injection; however no reduction in CBF was measured after stem cell delivery. For the upper CBF monitoring, baseline is more horizontal than for the other two, however the slope observed for these last ones seems to be originated in the measurement itself and not as a consequence of the injection. MR $T_2$ weighted images of this animal 24h after the injection showed big subcortical ischemic lesions in the same hemisphere and cortical lesions in the contralateral side of the brain. So, for this animal laser Doppler measurements did not report a reduction in the CBF but ischemic events were observed 24h later. This underestimation took place because Laser Doppler flowmetry has an excellent temporal resolution but not sufficient spatial resolution. CBF monitoring is limited to the proximity of the probe, in surface and also in depth, being the subortical region out of the range of measurement. Thus, deep ischemic lesions could not be detected by this technique.

However, not all animals injected with $0.25x10^6$ MSCs showed significant ischemic events. In Figure 93 it is possible to observe one animal 24h after $0.25x10^6$ MSCs intra-arterially delivered. Hyperintensities noted with green arrows correspond to a lesion consequence of one Doppler probe positioning, and orange arrows point out 3 focal ischemias that could be produced by the cell injection. Comparing Figure 92 with Figure 93, the degree of ischemic events after $0.25x10^6$ cells injection is quite different, which could point out the big influence of the circle of Willis structure on the

cell distribution and even multifocal ischemias due to the intra-arterial delivery of MSCs.

Hence, this procedure for intra-arterial delivery route is highly reproducible and safe for vehicle injection, however for mesenchymal stem cell administration multifocal injuries were observed in MR $T_2$ weighted images in all groups. Animals which were injected with $1x10^6$ MSCs showed bigger lesions or died, while animals injected with $0.25x10^6$ mesenchymal stem cells had variable size multifocal ischemias along the brain. Moreover, laser Doppler flowmetry is a good technique to monitor CBF in a specific region onto the brain surface; however it is not enough to elucidate deep ischemic lesions after an intra-arterial stem cell delivery.

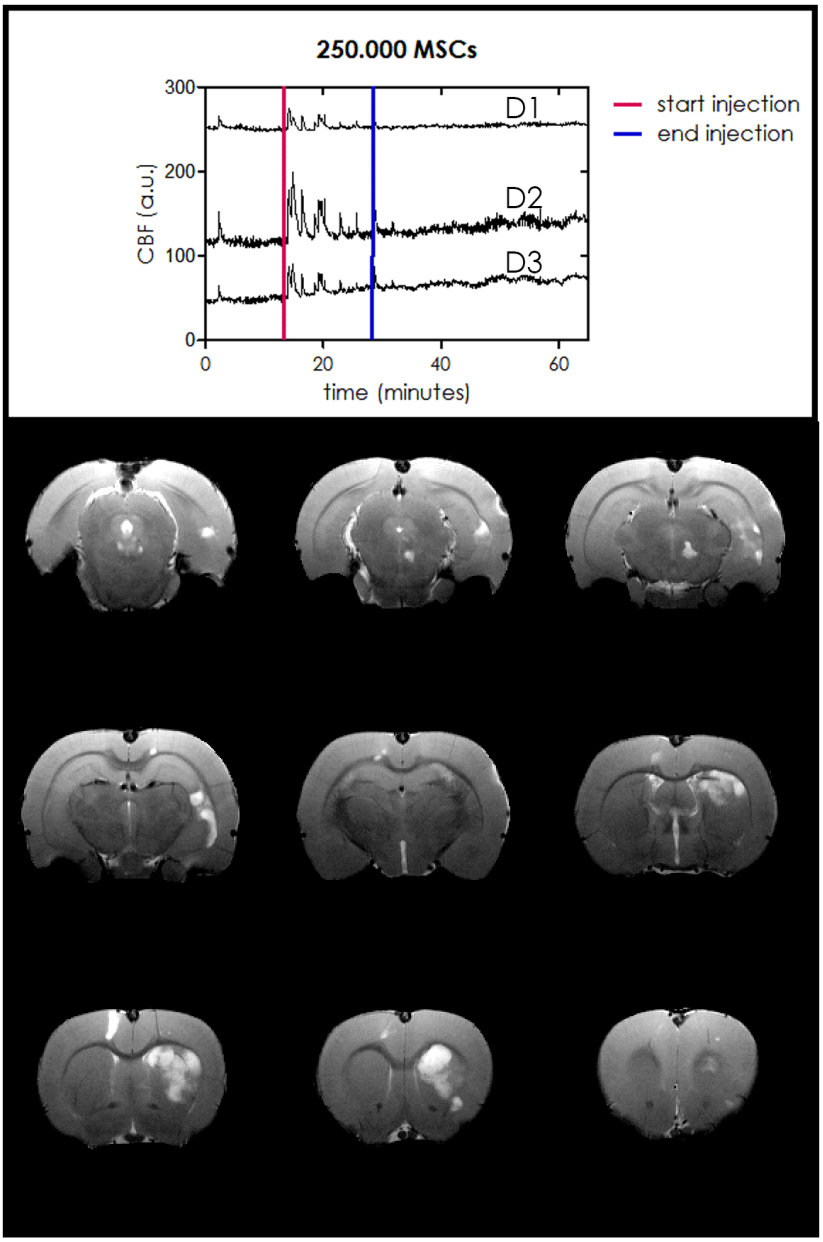


Figure 92: CBF for 3 Doppler probes measured before, during and after the injection of $0.25x10^6$ MSCs; and MR $T_2$ weighted images of several brain slices 24h after the cell delivery.

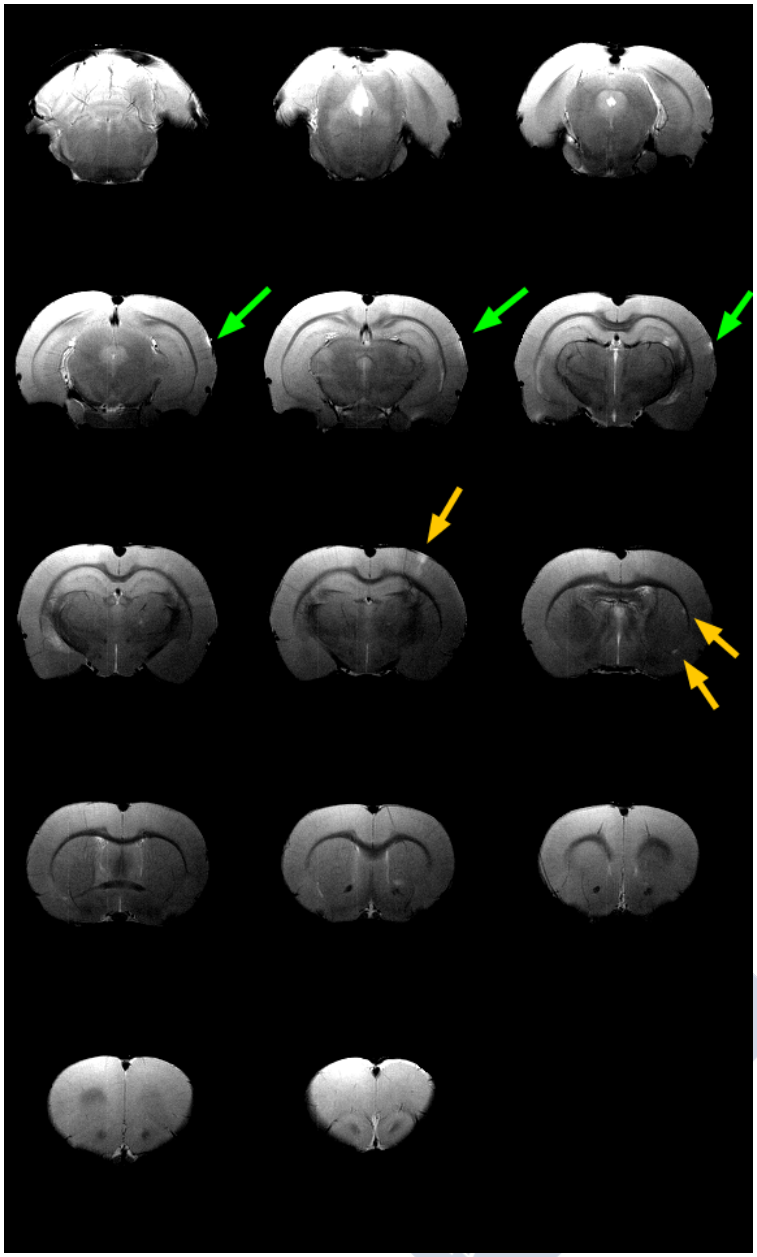

Figure 93: MR $T_2$ weighted images 24h after $0.25x10^6$ MSCs intra-arterial delivery. Green arrows point lesion induced by positioning the Doppler probes and orange arrows point ischemic lesions produced by $0.25x10^6$ cells intra-arterially administrated.

## 8.4. Conclusions

This chapter shows the different combinations of animal models of ischemic stroke and intra-arterial administration routes for mesenchymal stem cells delivery. In order to elucidate which model was the most efficient and the safest for an intra-arterial injection, we have used mesenchymal stem cells labeled with our dextran-coated superparamagnetic nanoparticles characterized in previous chapters. By using them, we have observed the circle of Willis compensating flow adaptation after an ischemic event and the great importance of the tMCAO procedure for a successful intra-arterial administration.

Thus, for an efficient intra-arterial delivery, during tMCAO surgery is necessary to maintain intact the contralateral common carotid artery and, after perfunding the occluded middle cerebral artery of ipsilateral side, ipsilateral common carotid must be also opened. Intra-arterial stem cell delivery will be produced through the ipsilateral external carotid and heart pumping will carry the delivered cells to the brain territory.

These injected cells can be detected in the ischemic brain for more than 4h after injection, and their presence is not increased by the use of external magnetic fields, as magnetic vectorization. Moreover, we have demonstrated that monitoring of CBF by transcranial laser Doppler is not enough to assess the safety of the intra-arterial delivery, and healthy animals injected with $0.25x10^6$ MSCs showed multifocal ischemic lesions 24h after the stem cell administration, evidencing that injected cells could be inducing focal ischemias.

USC
UNIVERSIDADE
DE SANTIAGO
DE COMPOSTELA

# 9. Cell tracking of mesenchymal stem cells

## 9.1. Hypothesis

In previous sections we have developed dextran-coated superparamagnetic nanoparticles for cell labeling and further cell tracking for MRI. This system, cell-MNPs, let us to monitor the cells once being injected and was used to assess the efficiency for intra-arterial administration after tMCAO.

The aim of this chapter is to track labeled mesenchymal stem cells following intra-arterial (i.a.) and intravenous (i.v.) routes in healthy and ischemic animals to assess if ischemic condition has an influence on the biodistribution of the injected cells, evaluated by MRI and histological techniques.

## 9.2. Materials & Methods

### 9.2.1. Cell labeling preparation

#### 9.2.1.1. Cell lines

All experiments were performed using Mesenchymal Stem Cells (MSCs) purchased from Cultrex, Trevigen and were cultured in IMDM (78%), Fetal bovine serum (10%), Horse serum (10%), Penicillin-Streptomycin (1%) all from Gibco Invitrogen, and Amphotericin-B (1%) from Sigma-Aldrich. Cell passage numbers between 7 and 18 were used in these experiments.

#### 9.2.1.2. Dextran-coated superparamagnetic nanoparticles

Dextran coated MNPs (D-MNPs) were synthesized in the Clinical Neuroscience Research Laboratory following the *in situ* protocol described in chapter 4.

#### 9.2.1.3. Preparation of Poly-L-lysine hydrobromide-coated D-MNPs

1.5µg/mL of Poly-L-lysine hydrobromide (PLL) (Sigma-Aldrich) was used. One hour prior to cell incubation, D-MNPs were mixed with cell medium and with 1.5 µg/mL PLL and vigorously shaken.

#### 9.2.1.4. Cell labeling with PLL-coated D-MNPs and CFSE

MSCs were labeled following the protocol described elsewhere[227] with slight modifications. Cells were incubated with 1.5 µg/mL PLL and 100 µg/mL of D-MNPs for 24h. The MNP containing medium was removed and the cells were 3 times washed with 1.5 mL of Phosphate Buffered Saline (PBS without $Mg^{2+}$ and $Ca^{2+}$, Gibco

Invitrogen) to remove non-attached MNPs. After washing, the cells were left overnight (12h) in 1mL of fresh medium.

The following day the medium was removed, and CFSE (Carboxyfluorescein succinimidyl ester) labeling was performed following the manufacture instructions (CellTrace CFSE Cell Proliferation Kit for flow cytometry, LifeTechnology). Then, cells were washed once with 1.5mL of PBS and 0.5mL of EDTA-trypsin (Gibco Invitrogen) was added to detach the cells from the well. The trypsin was neutralized with fresh medium and the detached cells were collected in a Falcon tube. After a mild centrifugation, the supernatant was discarded and the cells were resuspended in PBS 1x. Cell count was performed with Trypan Blue staining and a Neubauer chamber. Samples were diluted 1:5 with PBS and 1:2 with Trypan Blue. $0.5x10^6$ labeled cells were injected in order to study the cell tracking following different administration routes.

### 9.2.2. Animal management

In this study we have used 8 Wistar rats (Harlan) with a weight of 288±9 g. Animals were kept at controlled conditions of temperature (22±1 °C) and humidity (60±5%), with a 12/12 hours light/dark cycle, and granting free access to food (commercial chow pellets) and tap water. For surgery and MRI, rats were anesthetized with sevoflurane (3% in 70% $N_2O$ and 30% $O_2$). Rectal temperature was monitored and maintained at 37±0.5 °C with a feedback controlled heating system (1025 system, SA Instruments). At the end of the procedures animals were sacrificed under deep anesthesia (8% sevoflurane). Experimental protocols were approved by the local Animal Care Committee according to the Spanish and European Union (EU) rules

(86/609/CEE, 2003/65/CE, 2010/63/EU, RD 1201/2005 and RD53/2013).

### 9.2.3. Model of focal transient ischemia in the rat

Transient focal ischemia was induced in rats by intraluminal occlusion of the middle cerebral artery (tMCAO), performed as previously described[171] with several modifications. In order to monitor the relative cerebral blood flow (CBF) during the surgery, a laser-Doppler flow probe (tip diameter 1 mm) attached to a flow meter (PeriFlux 5000; Perimed AB) was located over the thinned skull, over the middle cerebral artery territory (approximately 4 mm lateral to bregma). Only animals with a CBF reduction higher than 60% and with reperfusion after occlusion were included in the studies. To perform tMCAO, both vertebral arteries and contralateral common carotid artery remained intact all surgical procedures.

Under a surgical microscope, common carotid, external carotid, and the internal carotid arteries of the left side were dissected from connective tissue through a midline neck incision. Left external carotid and pterygopalatine arteries were separated and tied permanently with 6-0 silk sutures, showing a CBF reduction of 20% measured by laser Doppler. A silicon rubber-coated monofilament (403512PK5Re; Doccol Corporation) was inserted through the external carotid into the left common carotid artery and advanced into the internal carotid 17-20 mm from the bifurcation to occlude the origin of the MCA. The intraluminal filament was removed after 45 minutes of occlusion. Common carotid artery was perfunded immediately after removing the intraluminal filament.

## 9.2.4. Intraparenchymal injections in healthy rats

Labeled cells with CFSE and labeled cells with dextran-coated superparamagnetic nanoparticles and CFSE were injected in each hemisphere following stereotactic injections in 3 healthy animals (Figure 94). Under sevofluorane anesthesia (3%), 100.000 mesenchymal stem cells in sterile PBS (total volume of 10 µL) were administered to the rat brain hemispheres at the locations of 0.6 mm posterior, 2.9 mm lateral to the bregma, and 5.0 mm deep to the skull surface in a rat stereotactic apparatus, after drilling a hole in the parietal bones. The injection was performed using a 30G needle in 10 min, MSCs were delivered at a rate of 1 µL/min using a micro-pump, and the needle was kept in this position for an additional 10 min and then retrieved slowly out of the brain.

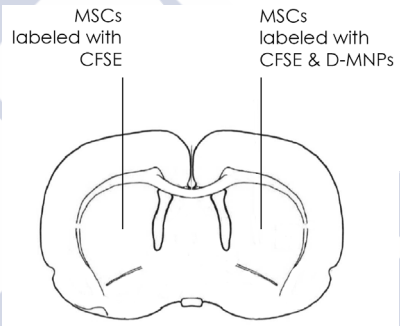


Figure 94: Representative scheme of intraparenchymal injection of MSCs labeled cells.

## 9.2.5. Systemic administration delivery routes

Cells were administrated 4h after the perfusion of the ACM in those animals that went under tMCAO.

#### 9.2.5.1. Intra-arterial injection

Cannulation for intra-arterial delivery of labeled MSCs is performed in the left side following the same procedure for healthy and ischemic rats. Animals that went under tMCAO have already pterigopalatin and external carotid arteries closed, however it is necessary to tie these arteries in healthy rats.

Ipsilateral common carotid is temporally ligated to insert the cannula for the MSCs intra-arterial delivery. A 0.28 mm ID & 0.61 mm OD catheter (Smiths) connected to a 30G needle and a 1 mL syringe was inserted into the stump of ECA through an incision on the vessel under the operation microscope, and was tightened to ECA by a 6-0 silk suture. The catheter went forward into ICA till reach the branch of common and internal carotid. This tube was filled with heparinized physiological saline to prevent air bubble and coagulation. Common carotid is opened and a small blood reflux in the catheter can be observed. The syringe was filled with labeled cells in PBS and using slow hand injection over 15 minutes, $0.5x10^6$ labeled cells in 300 µL of PBS were delivered into the internal carotid. When the injection is finished, common carotid is temporally ligated to remove the catheter. EC is tied and common carotid is opened again.

#### 9.2.5.2. Intravenous injection

Intravenously administration was performed through the jugular vein. A 0.5 cm incision was made in the animal's neck just above the clavicle 1 cm to both left and right of the midline. Subcutaneous fat was cut and the jugular vein was revealed. A 30G gauge needle was used for every injection since after withdrawal; the puncture rapidly closes

preventing bleeding. One million cells in 300 µL of PBS were administered manually in less than 1 min.

### 9.2.6. Magnetic resonance imaging *in vivo*

Cell tracking was assessed by magnetic resonance imaging. Magnetic resonance imaging studies were conducted on a 9.4-T horizontal bore magnet (Bruker BioSpin, Ettligen, Germany) with 20 cm wide actively shielded gradient coils (440 mT/m). Radio-frequency transmission was achieved with a birdcage volume resonator; signal was detected using a four-element surface coil, positioned over the head of the animal, which was fixed with a teeth bar, earplugs, and adhesive tape. Transmission and reception coils were actively decoupled from each other. Gradient-echo pilot scans were performed at the beginning of each imaging session for accurate positioning of the animal inside the magnet

$T_2$-weighted images were acquired using a multislice multiecho spin-echo sequence with the following acquisition parameters: FOV 19.2 x 19.2 $mm^2$, image matrix 192 x 192 (isotropic in-plane resolution of 100 µm/pixel x 100 µm/pixel), 14 consecutive slices of 1mm thickness, repetition time of 3 s, and 16 echoes with 9 ms of echo time. $T_2$-weighted images were acquired 24h after the onset of the ischemia.

$T_2$*-weighted images were acquired using a multi gradient echo sequence with the following acquisition parameters: FOV 19.2 x 19.2 $mm^2$, image matrix 192 x 192 (isotropic in-plane resolution of 100 µm/pixel x 100 µm/pixel), 14 consecutive slices of 1mm thickness, repetition time of 1.5 s, and 16 echoes with 2.9 ms for the first echo time and 3.28 ms of echo spacing.

Post-processing of all images was performed using ImageJ software (Rasband, W. NIH).

### 9.2.7. Tissue processing

Rats were anesthetized under sevofluorane (8%), perfused transcardiacally with 4% paraformaldehyde (PFA) in 0.1 M PBS, the brains were removed, postfixed (4% PFA, 4°C, 24 h), and included in paraffin.

#### 9.2.7.1. Tissue processing for Prussian Blue staining and CFSE detection

Prussian Blue staining was performed to colocalize D-MNPs with the CFSE labeled cells. Paraffin sections of 10 µm were deparaffinized in xylol and rehydrated in graded alcohol series. The sections were then washed with phosphate buffer saline (PBS 1X) and incubated for 20 minutes with a mix of equal parts of aqueous solution of 20% HCl (Hydrochloric acid fuming 37% extra pure, Merk) and aqueous solution of 10% Potassium ferrocyanide Trihydrate ($KFe(CN)6.3H2O$, FW 422.2, Sigma-Aldrich). After incubation, slides were washed 3 times with PBS and were mounted with fluorescence mounting medium (Life Technologies). Photographs were taken using an inverted microscope (Olympus IX51).

#### 9.2.7.2. Tissue processing for fluorescence optical microscopy

Paraffin sections of 10 µm were deparaffinized in xylol and rehydrated in graded alcohol series. The sections were then washed with phosphate buffer saline (PBS 1X), heated at 99°C in Citrate buffer (Dako) for 20 min and washed again with PBS 1x. Slides were incubated first with Rabbit polyclonal antibody to CD31 (Abcam) (1:25), normal horse

serum (15%), Trition X-100 (0.2%) and PBS overnight. The slides were then incubated at room temperature for 1h with biotinylated horse anti-Rabbit IgG antibody (Vector) (1:200) and PBST. After 3 washes with PBST, slides were incubated with dylight 594 streptavidin (Vector) (1:500) and PBST. And finally for nucleus staining, 10 µL of Hoechst (Invitrogen) in 60mL of PBS 1x were added to the slides and incubated for 15 min and washed afterwards with PBS. Slides were mounted with fluorescence mounting medium (Life Technologies). Photographs were taken using an inverted microscope (Olympus IX51).

#### 9.2.7.3. Tissue processing for transmission electronic microscopy

Rats were sacrificed under sevofluorane anesthesia (8%) and samples of brain cortex and striatum were taken immediately after the animal death. Fixation and postfixation were carried out in 2% glutaraldehyde in sodium cacodylate buffer and in 1% $OsO_4$ in the same buffer. Inclusion was done in Spurr's epoxy resin. Semithin sections (0.5 µm) were stained with Toluidine blue and examined under optical microscope to select brain regions for further TEM analysis and ultrathin sections (100 nm) were stained with uranyl acetate and lead citrate.

## 9.3. Results & Discussion

Stem cells offer tremendous potential to treat stroke and other neurological diseases; however the translation from pre-clinical to clinical studies presents several challenges and one of them is the selection of an adequate

administration route for cell delivery. Monitoring cell localization and study the fate after administration is essential to elucidate underlying mechanisms of stem cell therapy.

In this chapter we will monitor the fate of labeled cells following two types of administration routes; intra-arterial delivery, following the procedure described in the previous chapter and, intravenous administration route through jugular vein. As we have mentioned before, MRI is the best technique to monitor injected cells due to the soft tissue contrast and non-invasiveness of the procedure, however a complementary technique would be useful to demonstrate that MR hypointensities in $T_2$* weighted images correspond to labeled cells and not to free particles. Immnunohistochemistry will assess the co-localization of cells and magnetic nanoparticles *ex vivo*.

Because there is not a specific marker for MSCs that let us an unequivocal identification of the administered cells, MSCs will be labeled with a fluorescent cell staining dye prior to be injected. CFSE is a fluorescent dye, used for in vitro and in vivo labeling of cells to trace multiple generations; however in this work the dye will be used to distinguish between injected cells and host cells in brain tissue *ex vivo*. This dye labeling is performed in vitro, prior to the injection, diffusing easily into cells and binding covalently to intracellular amines *in vitro*, resulting in stable and well-retained fluorescent staining. Apart from CFSE, MSCs will be also labeled with our synthesized dextran-coated superparamagnetic nanoparticles, which will provide MRI contrast as well Prussian blue staining for *ex vivo* detection. Thus, we will be able to correlate *in vivo* MRI signal with Prussian blue and CFSE signal *ex vivo*. In vitro

assessing of D-MNPs and CFSE labeling of MSCs is shown in Figure 95.

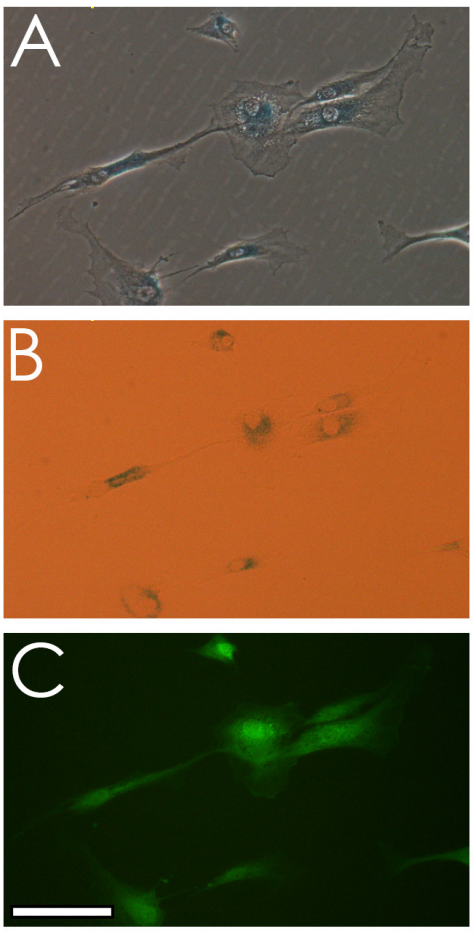


Figure 95: MSCs labeled with D-MNPs and CFSE (A) Phase contrast microscopy; (B) Prussian blue staining of D-MNPs through bright field optical microscopy and (C) fluorescent microscopy for observing CFSE labeling.

### 9.3.1. Intraparenchymal administration route

So as to assess the efficacy of these different labels on mesenchymal stem cells, our first *in vivo* approach was an intraparenchymal injection. Actually, this administration

route was one of the early delivery routes and was also used for stem cell therapy, however due to the high invasiveness of the technique we will consider stereotactic injections to co-localize cells and D-MNPs, and not as an administration route for cell tracking studies or further stem cell therapy experiments.

In this way, MSCs labeled with CFSE were injected in the left brain hemisphere, and MSCs labeled with CFSE and D-MNPs in the right hemisphere of a healthy animal (Figure 94). After the injection, the animal was scanned in MRI and $T_2$* and $T_2$ weighted images were acquired, corresponding to Figure 96 and Figure 97 respectively. As we expected, only cells labeled with D-MNPs can be detected after the injection in MRI. Moreover, it is possible to note in $T_2$ and $T_2$* weighted images the needle track for cell delivery in the left hemisphere, corresponding to CFSE labeling (green arrow), being this trace attributed to a small bleeding due to the injection itself. Collateral effects from craniotomy and intraparenchymal injection can be also noted in $T_2$ and $T_2$* (red asterisks). D-MNPs labeled cells can be easily observed in both sequences due to the high concentration of cells in a reduced brain volume producing similar hypointensities in both sequences, however blooming effect for $T_2$* weighted images can be noted.

In the previous chapter we had demonstrated that cells labeled with D-MNPs can be visualized by MRI after an intra-arterial administration. In this section we have seen that non-labeled cells do not present hypointensities in $T_2$ or $T_2$*, while D-MNPs labeled cells following the same route of administration do present negative contrast in both sequences, making them visible in MRI 4h after being injected.

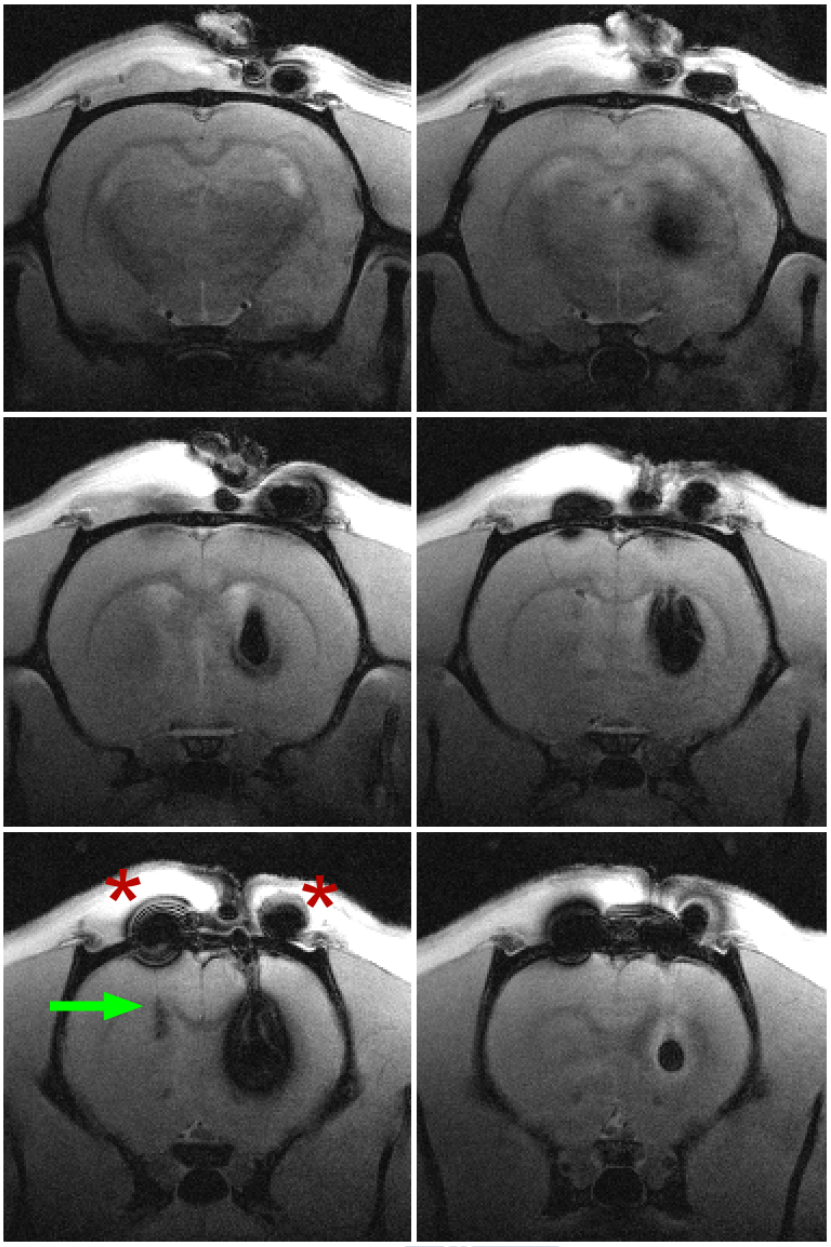

Figure 96: MR $T_2$* weighted images of an intraparenchymal injection of MSCs. Left hemisphere was injected with MSCs labeled with CFSE and right hemisphere was injected with MSCs labeled with CFSE and D-MNPs. Green arrow shows the needle trajectory for MSCs with CFSE and red asterisks point out the craniotomy/wound effect.

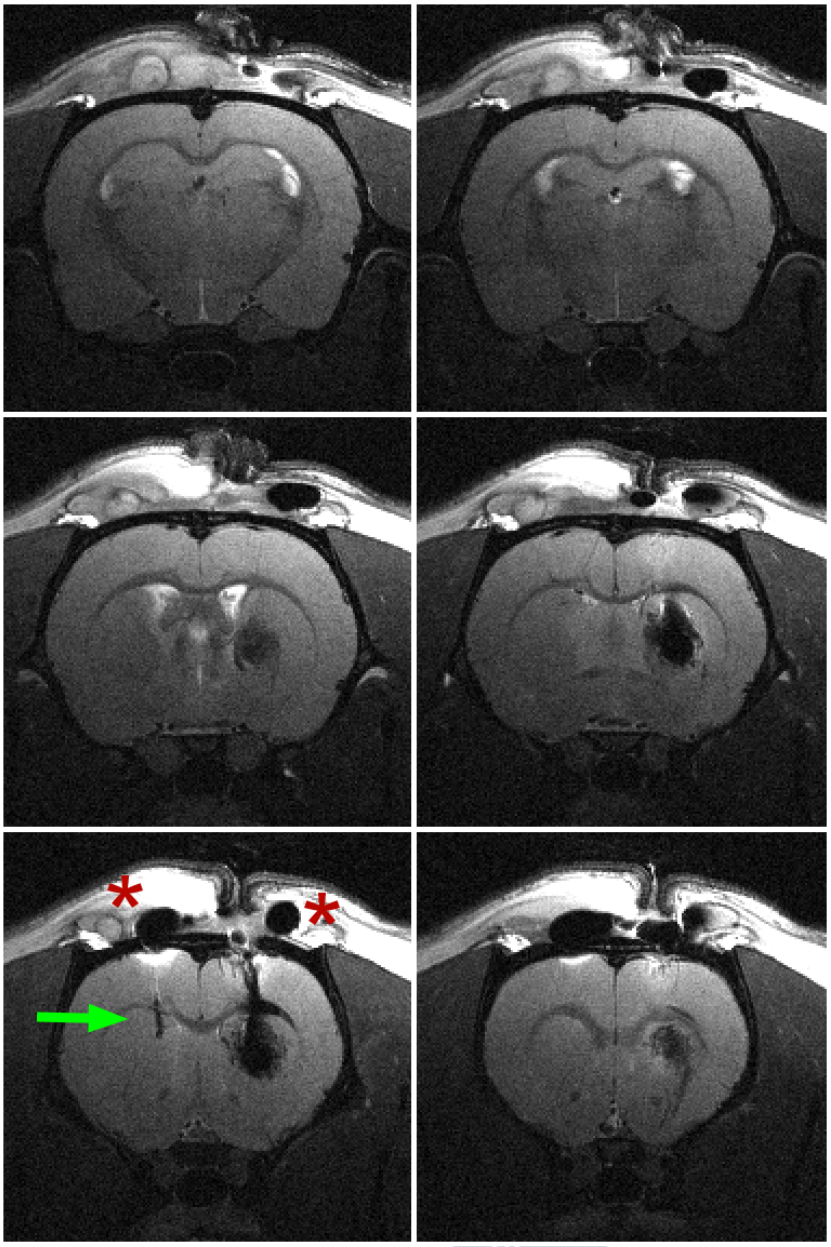

Figure 97: MR $T_2$ weighted images of an intraparenchymal injection of MSCs. Left hemisphere was injected with MSCs labeled with CFSE and right hemisphere was injected with MSCs labeled with CFSE and D-MNPs. Green arrow shows the needle trajectory for MSCs with CFSE and red asterisks point out the craniotomy/wound effect.

Immediately after MRI scanning and therefore 4h after intraparenchymal delivery, these animals were perfunded and brain tissue sections were processed and fixed in paraffin. Brain slices of 10 µm were obtained, processed for Prussian blue staining and mounted. Bright field and fluorescence optical images of left hemisphere and right hemisphere were taken to co-localize Prussian blue and CFSE. Figure 98(A) and (B) corresponds to the injection of MSCs labeled exclusively with CFSE in the left hemisphere. No staining for Prussian blue is observed in bright field microscopy (Figure 98 (A)) and CFSE labeled cells can be noted (Figure 98 (B)). This result is in accordance with MR $T_2$ and $T_2$* of left hemisphere where no cells were detected and no Prussian blue either because MSCs are exclusively labeled with CFSE. (Figure 96 and Figure 97)

On the other hand, Figure 98 from C to F corresponds to MSCs labeled with D-MNPs and CFSE. Prussian blue and CFSE staining are observed. Different region of same hemisphere is shown in Figure 98 (E) and (F) where a single cell can be examined, noting that CFSE and Prussian blue are well delimited in the cell and correspond to one single labeled cell. This result of positive staining for Prussian blue is in accordance with MR $T_2$ and $T_2$* of right hemisphere where hypointensities were detected. (Figure 96 and Figure 97)

Overall, we can conclude that for MSCs labeled with D-MNPs and CFSE, three measurable signals were detected, *in vivo* contrast in MRI, and *ex vivo* Prussian blue and CFSE staining.

So far in this part we have demonstrated that we can label MSCs with a fluorescent dye and detect those cells *ex vivo* after being injected following the intraparenchymal route. In the same way, we have observed that if the

administered cells are also labeled with D-MNPs, those nanoparticles are still in the cell at least 4h after the injection and, that the detected hypointensities in MRI would correspond with D-MNPs labeled cells and not to free D-MNPs. We have also confirmed that for non-D-MNPs labeled cells, no signal is observed in MRI and in Prussian blue either; however CFSE labeled cells can be detected by histochemistry techniques.

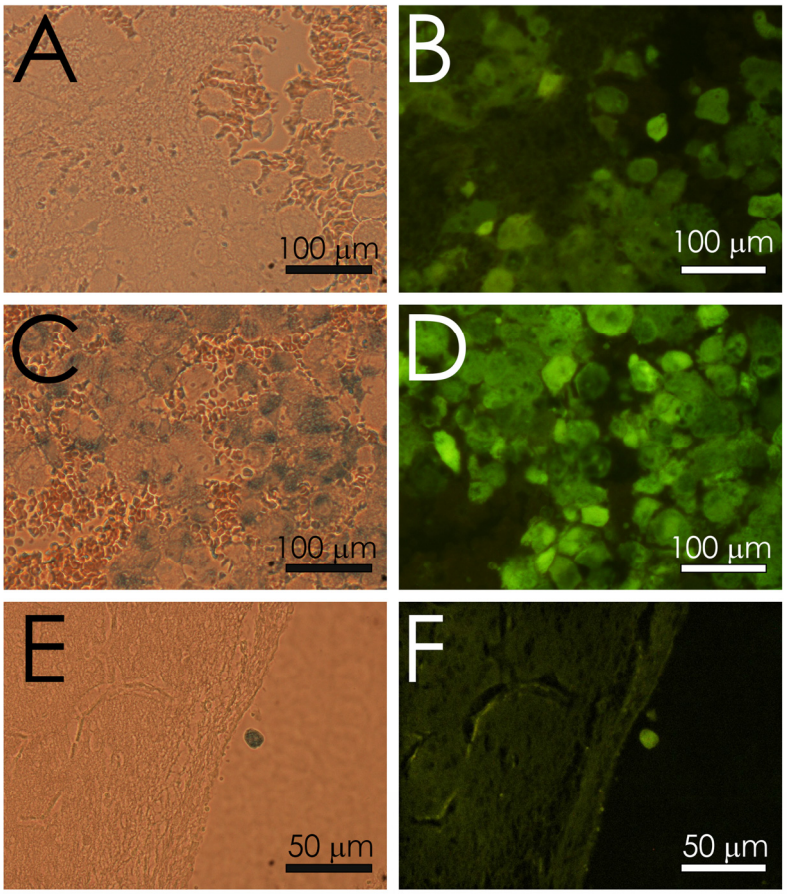


Figure 98: Intraparenchymal injection of (A) and (B) MSCs labeled exclusively with CFSE; (C), (D), (E), (F), MSCs labeled with CFSE and D-MNPs. Left column corresponds to bright field optical microscopy and right column optical fluorescence microscopy.

### 9.3.2. Intravenous and intra-arterial administration routes

We have assessed the feasibility of an intraparenchymal injection of labeled MSCs for cell detection following several techniques however, this administration route is highly invasive and in an ischemic animal multiple injections would be required to cover all ischemic regions. In order to minimize the invasiveness of the administration, the most used delivery routes for stem cell therapy are intravenous and lately, intra-arterial administration routes. Within intravenously injection several body sites have been used, tail, penile, jugular and femoral veins,[265] nevertheless most common are tail and jugular, while intra-arterial delivery is normally performed in the internal carotid through the external carotid artery.

To study intravenous and intra-arterial delivery routes, healthy animals and animals with cerebral ischemia were considered. All rats were injected with $0.5x10^6$ MSCs labeled with CFSE and D-MNPs, and one healthy animal was injected intra-arterially with MSCs labeled exclusively with CFSE to evaluate possible differences due to the D-MNPs.

#### 9.3.2.1. Intravenous administration route

Following intravenous jugular injection, no hypointensities in $T_2$* weighted images in healthy and ischemic animal brains were observed (Figure 99). Since MSCs are injected, till they could reach the brain, the organ they have to pass through is the lung. Several studies have described the lungs as the major obstacle for intravenous cell delivery and because of this, a reduced proportion of injected cells could reach the arterial circulation and therefore the brain. Cell size and receptor-mediated adhesion and/or stem cell type appear

to be crucial variables for pulmonary stem cell passage. [114,266]

Considering that MRI did not detect labeled MSCs in brain slices, animals were sacrificed and brain, heart and lungs were processed for further histological CFSE analysis. No CFSE labeled cells were detected in brain and heart using fluorescence optical microscopy; however CFSE labeled cells were observed along the lungs (Figure 100). All studied lung slices showed dispersed labeled MSCs.

Our results are in concordance with previous studies which have demonstrated that most of the mesenchymal stem cells injected intravenously get trapped inside the lungs, mostly because of the size of the cells. Histochemistry techniques are indispensable to assess lung entrapment because lung tissue appears as hypointense signal in MR images due to its weak proton density and the heterogeneity of the tissue (air-tissue interfaces), making not possible to track D-MNPs labeled cells with this technique. However, at this point it is important to mention that for tissue processing, the animal is perfused. In order to wash the blood and fix the tissues PBS and paraformaldehyde 4% are used, nevertheless lungs are difficult organs to prefund so still some blood can be observed in lungs. This is traduced in a background of blood for microscopic analysis and therefore of iron, which makes Prussian blue tissue staining non-specific of MNPs. Overall, we have observed that after a jugular administration of labeled MSCs cells are retained in the lungs and no cells were detected in the brain or heart.

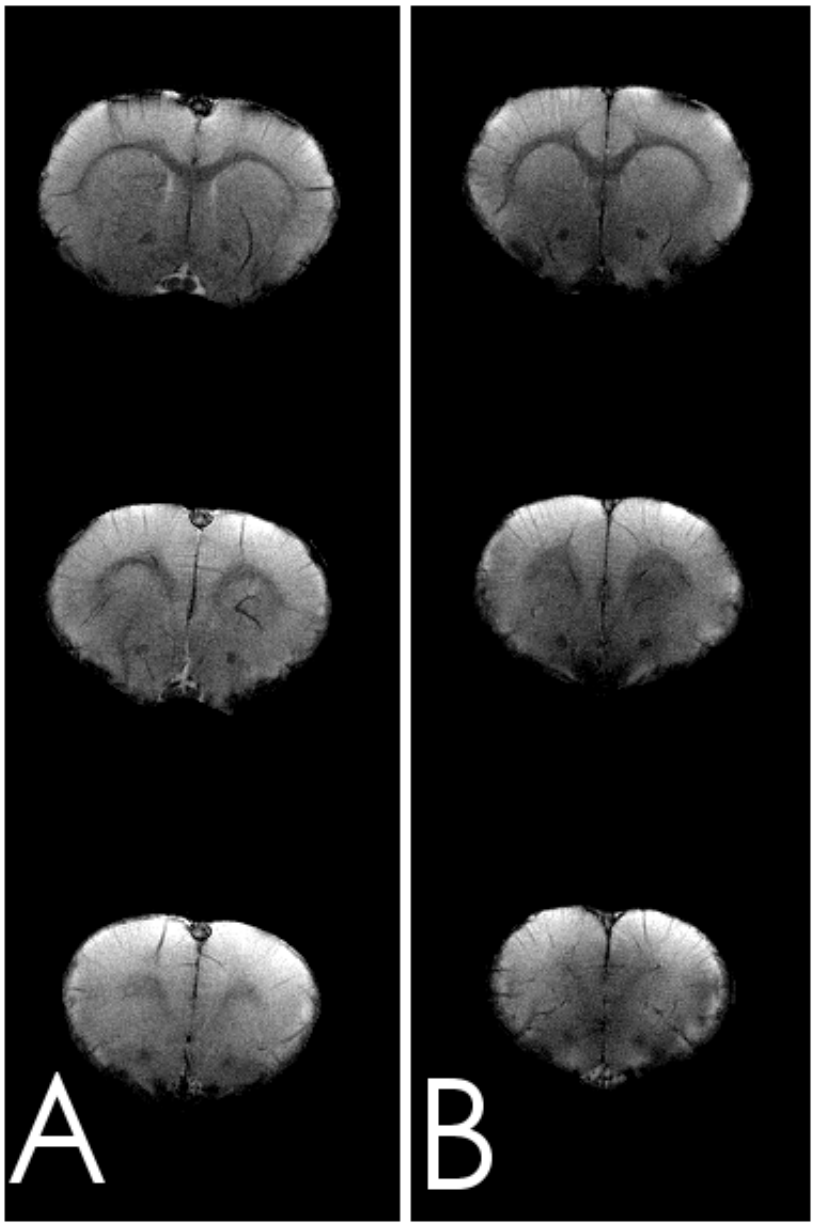


Figure 99: MR $T_2$* weighted images of 3 brain slices 4h after intravenously delivery of MSCs labeled with D-MNPs and CFSE in a (A) healthy animal and (B) in a ischemic animal.

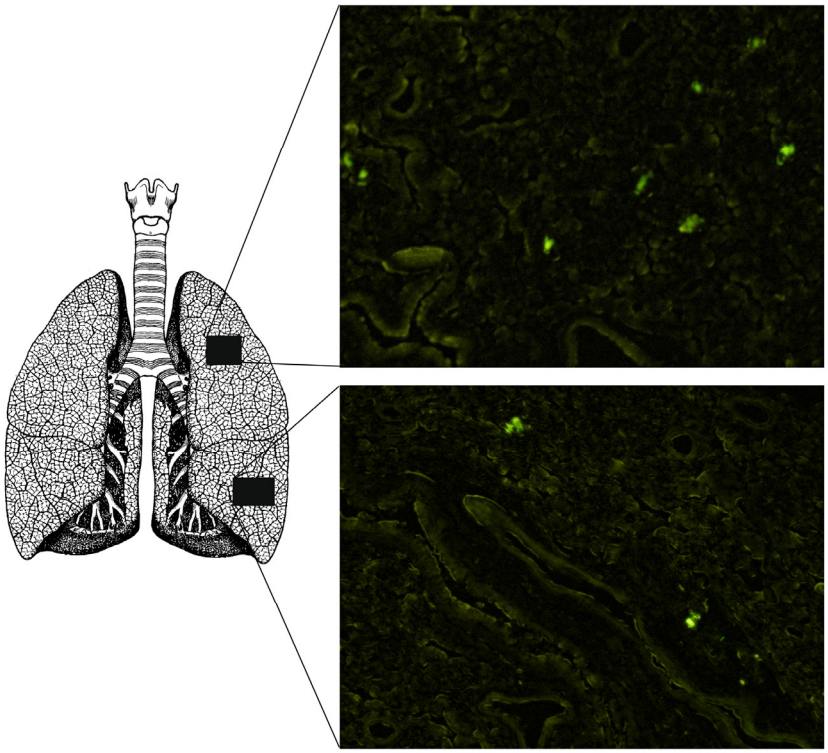

Figure 100: Representative fluorescence optical microscopy of rat lung slices where MSCs labeled with CFSE can be observed after jugular delivery.

### 9.3.2.2. Intra-arterial administration route

So far, we have studied the fate of labeled cells injected intraparenchymally and intravenously, and in this section we will track labeled cells which have been injected intra-arterially.

The timing of administration was the same as intravenously, i.e. 4h after the onset of the stroke in the case of ischemic animals, and MRI was performed 4h after the injection for ischemic and non-ischemic animals. Thus, following intra-arterial injection, Figure 101 shows MR $T_2$* weighted images 4h after intra-arterial delivery of (A) MSCs labeled

exclusively with CFSE in a healthy animal, (B) MSCs labeled with CFSE and D-MNPs in a healthy animal and (C) MSCs labeled with CFSE and D-MNPs in an animal 8h after the onset of the cerebral ischemia.

Differences between groups can be easily observed. Ischemic animal after intra-arterial delivery (C) presents more hypointensities and therefore more MSCs in the brain than the healthy animal (B) after being injected with the same number of cells. This observation could be explained by the disruption of the BBB and the tissue damage after the ischemic process, which could be retaining more cells in the brain. However, the healthy animal (B) with an intact BBB still presents labeled MSCs along the brain; the distribution pattern is more spread than ischemic brain, nevertheless cells can still be detected 4h after the injection. Figure 101 (A) does not display hypointensities, because injected cells were labeled exclusively with CFSE. Histochemistry evaluation of the tissue will elucidate MSCs distribution along these brains to compare with MRI.

After MRI scanning, animals were perfused and brain, heart and lungs were processed for further histological analysis. From one extra animal, kidneys, spleen and liver were also processed in order to evaluate cell migration towards those organs. Microscopic results revealed that no cells were found in kidneys, spleen, liver, heart and lungs, however all brain slices showed CFSE labeled cells. MSCs were found distributed mostly along the right hemisphere of the brain, in agreement with MRI $T_2$* weighted images cell distribution (Figure 102).

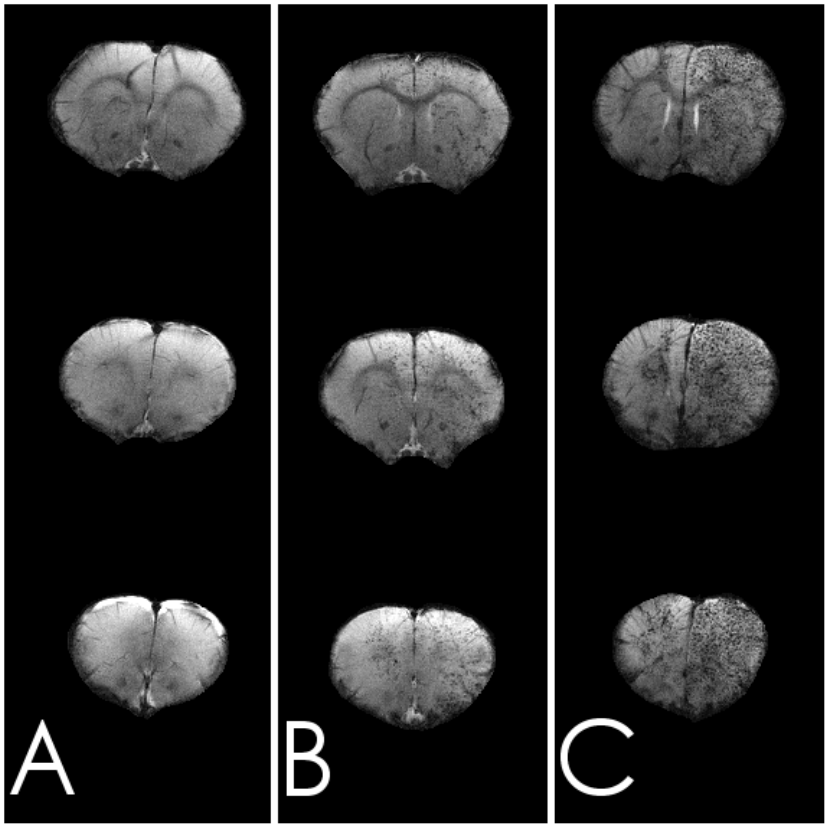


Figure 101: MR $T_2$* weighted images of 3 brain slices 4h after intra-arterial delivery of (A) MSCs labeled with CFSE in a healthy animal, (B) MSCs labeled with CFSE and D-MNPs in a healthy animal and (C) MSCs labeled with CFSE and D-MNPs in an animal 8h after the onset of the cerebral ischemia.

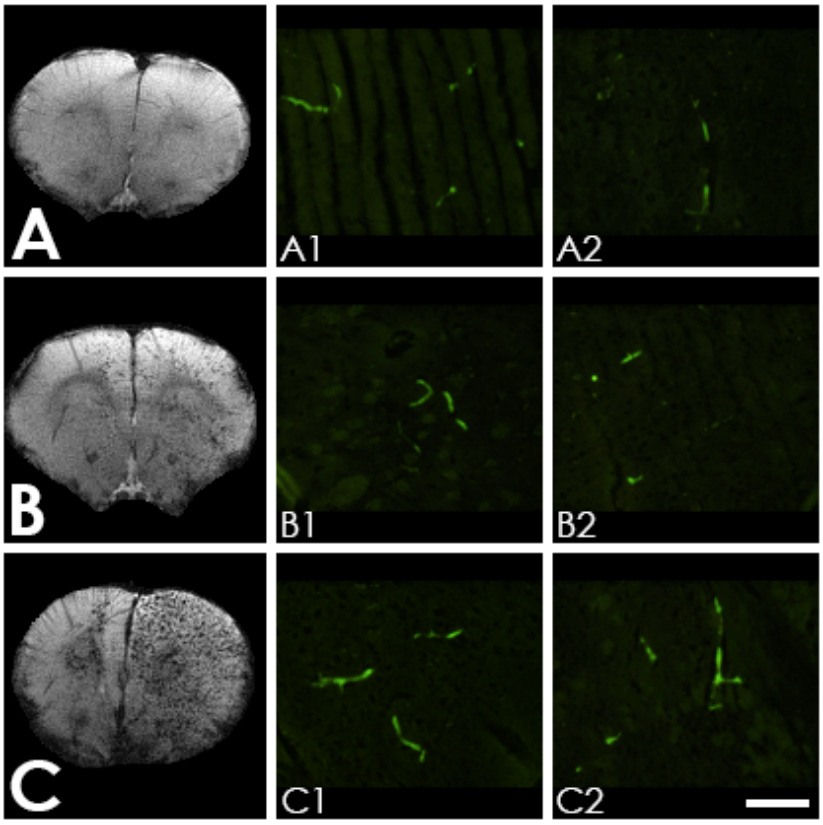


Figure 102: Fluorescence optical microscopy of brain slices after a intra-arterial delivery of MSCs (A) labeled exclusively with CFSE in a healthy animal, (B) labeled with CFSE and D-MNPs in a healthy animal and (C) labeled with CFSE and D-MNPs in a ischemic animal.

From fluorescence optical microscopy images (Figure 102) we can observe that CFSE positive cells show tubular-like configuration for all injected animals. This result together with the fact that intra-arterial delivery of MSCs provoke multifocal ischemias (see previous chapter), could mean that injected MSCs are in the vessels, adopting the tubular-like structure observed, and at the same time occluding those vessels.

In order to elucidate if the injected cells are in the vessels or they have migrated into the brain parenchyma, we investigated by immunohistochemistry techniques the expression of CD31, which is used primarily to mark endothelial cells in histological tissue sections. The combination of vessels labeled with CD31 and MSCs labeled with CFSE will let us elucidate *ex vivo* where injected cells are. Besides CD31 and CFSE, cell nucleuses were stained with Hoechst dye (Figure 104 and Figure 105).

Figure 103 is a representative brain region image of an animal injected with CFSE and D-MNPs labeled MSCs. Hoechst nucleuses and CD31 vessels staining are observed along all tissue section. After the co-localization (merge) no cells were detected out of vessels in this picture, but also in other regions of the brain. Moreover, in Figure 103, it is easy to note that the coincident vessel and CFSE labeled MSCs have a small and similar caliber. It will be interesting to observe what would happen if vessel diameter is wider than cell size to discriminate if the cells are adhered to the vessel wall or stacked there because of their similar size.

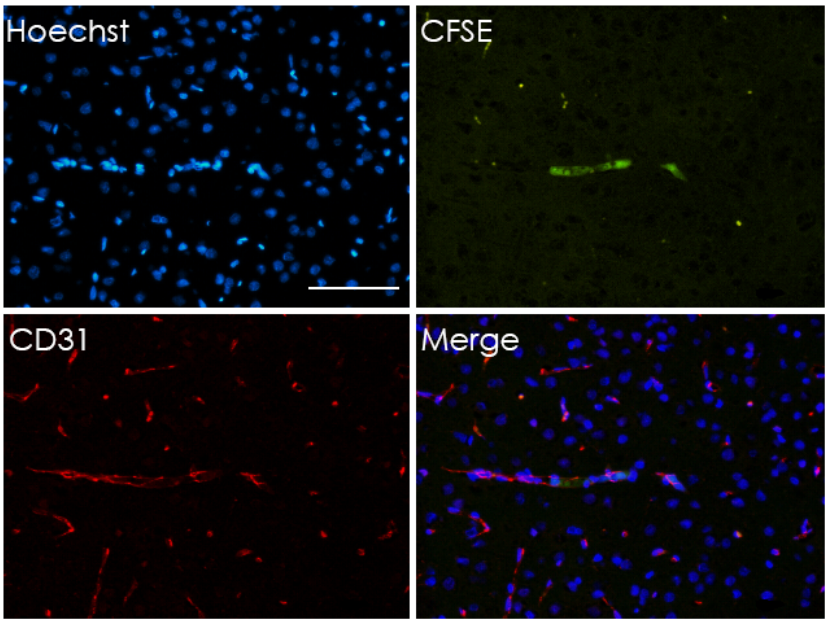


Figure 103: Injected MSCs labeled with CFSE are localized in the vessel. CFSE is co-localized with CD31 and Hoechst. (Scale bar 100µm).

In Figure 104 a representative brain region where small and big vessels can be examined is shown. We can observe that the big vessel of the image do not present CFSE positive cells, however smaller vessels do display labeled MSCs. Small vessels with positive CFSE staining are zoomed in Figure 105 and once again, the diameter of the vessel is similar to cell dimensions for both cells. Thus, in all brain slices studied, all CFSE positive cells were found in the vessels of small caliber (Figure 104 and Figure 105) and no cells were observed for wider vessels. This finding of MSCs localized in the small vessels could explain why intra-arterial injection of MSCs provokes multifocal ischemias.

However at this point we should take into account the observer effect. In science, the term "observer effect" refers to changes that the act of observation will make on a phenomenon being observed. This is often the result of

instruments that, by necessity, alter the state of what they measure in some manner. This effect in our experiments is reflected on the tissue processing protocol used for immunohistochemistry analysis. In order to eliminate the blood and therefore minimize background fluorescence, animals were perfunded with PBS and paraformaldehyde 4%. The perfusion is performed by injecting transcardially these substances, washing the animal blood. This process could alter the cell localization because the infusion parameters from the pump will be different from the heart pumping blood parameters, inducing variability on the cell positioning. However, inmunohistochemistry techniques require perfunded organs for an efficient marking and clear discrimination between structures. According to this, what we need is a technique which let us to study the distribution of the cells after being injected with the best possible resolution and without inducing changes in the tissue. The appropriate candidate to study cell positioning after injection minimizing tissue processing is the transmission electron microscopy.

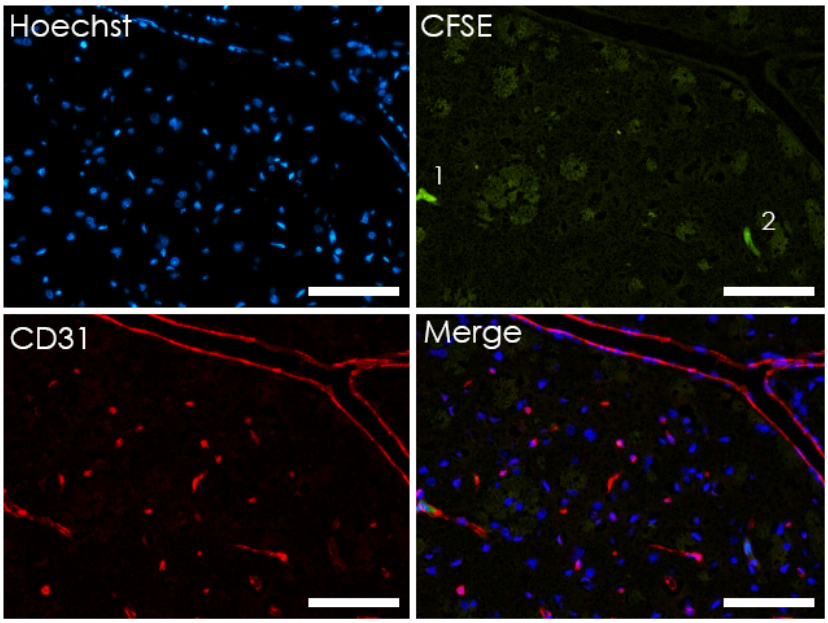


Figure 104: Injected MSCs labeled with CFSE can be found in the small vessels. CFSE is co-localizatized with CD31 and Hoechst. (Scale bar 10μm).

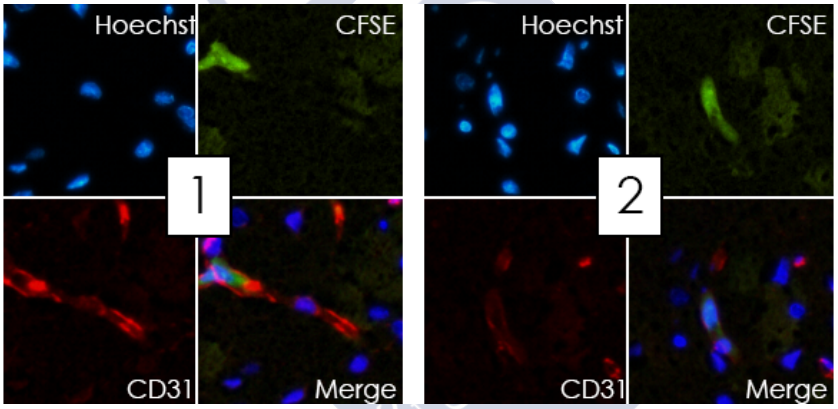


Figure 105: Magnification of Figure 39 for the two positive CFSE cells [1] and [2].

### 9.3.3. Transmission electron microscopy (TEM) of brain slices after intra-arterial delivery of D-MNPs labeled MSCs

Ultrastructural examination of tissues, cells and microorganisms plays a vital role in diagnostic pathology and biologic research. TEM is used to study the morphology of cells and their organelles,[267] which makes this technique appropriate for studying cell distribution once cells are injected.

In order to study if the injected cells are in the vessels or dispersed in the brain parenchyma, injected MSCs were labeled with D-MNPs. In Section 3 we have assessed that MSCs labeled with D-MNPs *in vitro* can be visualized by TEM, which makes possible to distinguish between non-labeled MSCs and D-MNPs labeled MSCs because of their MNPs endosomes encapsulation. This detection ability together with the fact that the TEM fixation protocol used lets us to keep the brain intact after the animal sacrifice, make this technique suitable for elucidating where the injected cells are. However, results of this section may be taken carefully because so far only one animal was used for TEM examination.

One healthy animal was selected for TEM brain examinations 4h after intra-arterial delivery of $1x10^6$ D-MNPs labeled MSCs. Administration procedure was performed as previously reported, and 4h after cell delivery, MR $T_2$* and $T_2$ weighted images were acquired to assess MRI cell distribution. In previous chapters we have shown that most of ischemic animals which have been injected with one million cells died within 24h and healthy animals presented large multifocal ischemias. However, the study of the stem cell administration in a healthy animal was more interesting

due to its undamaged vessel structure and intact blood brain barrier which could let us understand the interaction between MSCs and the brain structures under a non-pathologic condition. Besides, we have injected $1x10^6$ labeled cells to make easier the cell detection in the animal brain.

Thus 4h after the intra-arterial injection, MRI scanning was performed and $T_2$* weighted images were acquired. All right hemisphere and several regions of the left one displayed a hypointense dotted pattern as it can be observed in Figure 106. After MRI, the animal was sacrificed (not perfunded) and several sections (blue squares in Figure 106) of approximately 3 mm x 3 mm x 3 mm were extracted and immediately immersed in fresh glutaraldehyde for tissue fixation.

Electron micrographs of the cortex in a healthy rat injected with $1x10^6$ MSCs labeled with D-MNPs revealed the presence of the injected cells in the brain parenchyma, a representative cell can be observed in Figure 107. This micrograph shows one isolated MSC which had travelled from the vessels to the parenchyma and is in direct contact with the neuropil, where somas and cellular processes can be observed.[267] Not only the background color of the injected MSC is different from the surrounding, the presence of dark endosomes let us its identification as MSC (yellow arrows in Figure 107). Zoom of one endosome is shown in Figure 108, where it is possible to note the dark dotted pattern inside the wrapping endosome membrane. Distribution, size and morphology are similar to those observed *in vitro* in Chapters 5 and 6. Close to this endosome, 4 mitochondria can be also identified by their cristae, demonstrating the well-being of this mesenchymal stem cell 4h after being injected.

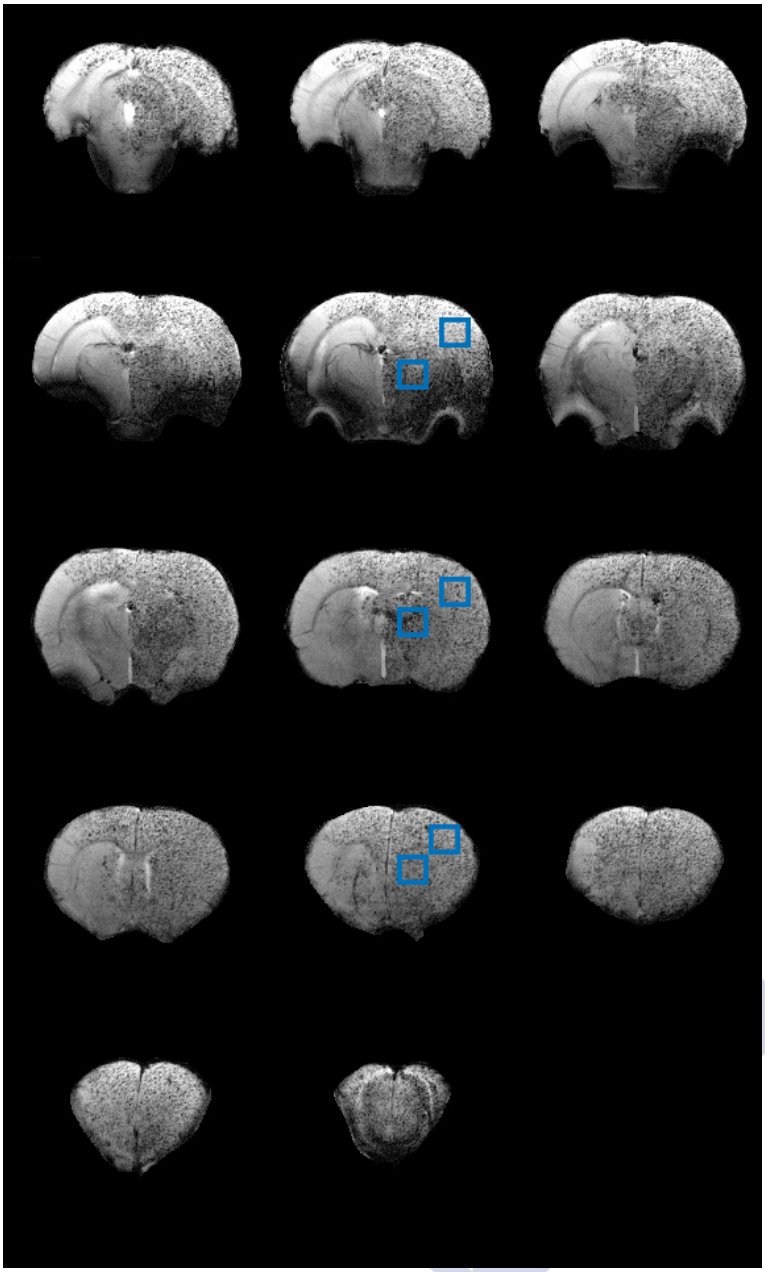

Figure 106: MR $T_2$* weighted images of the healthy rat injected with one million D-MNPs labeled MSCs. Blue squares represent the extracted sections for further TEM examination.

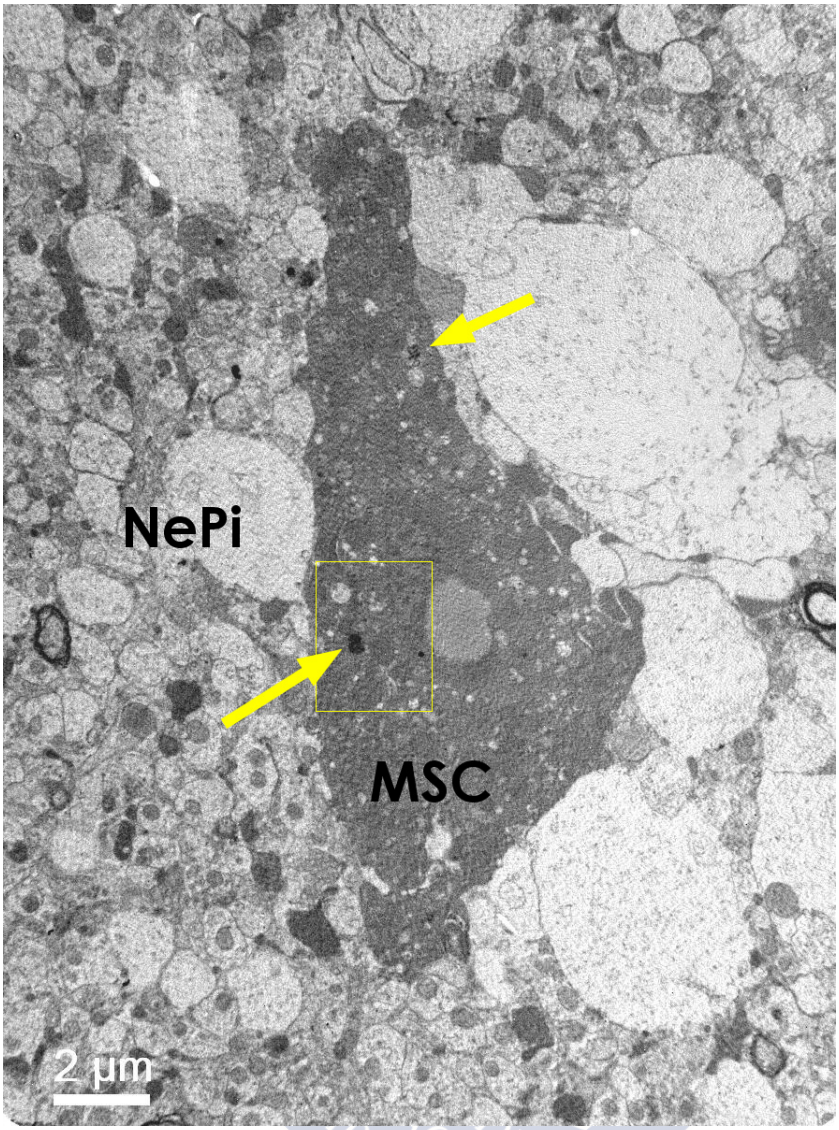


Figure 107: Electron micrograph of rat brain cortex 4h after intra-arterial delivery of D-MNPs labeled MSCs, showing one single MSC labeled with D-MNPs (yellow arrows) and surrounded by neuropil (NePi). Yellow rectangle is zoomed in next figure.

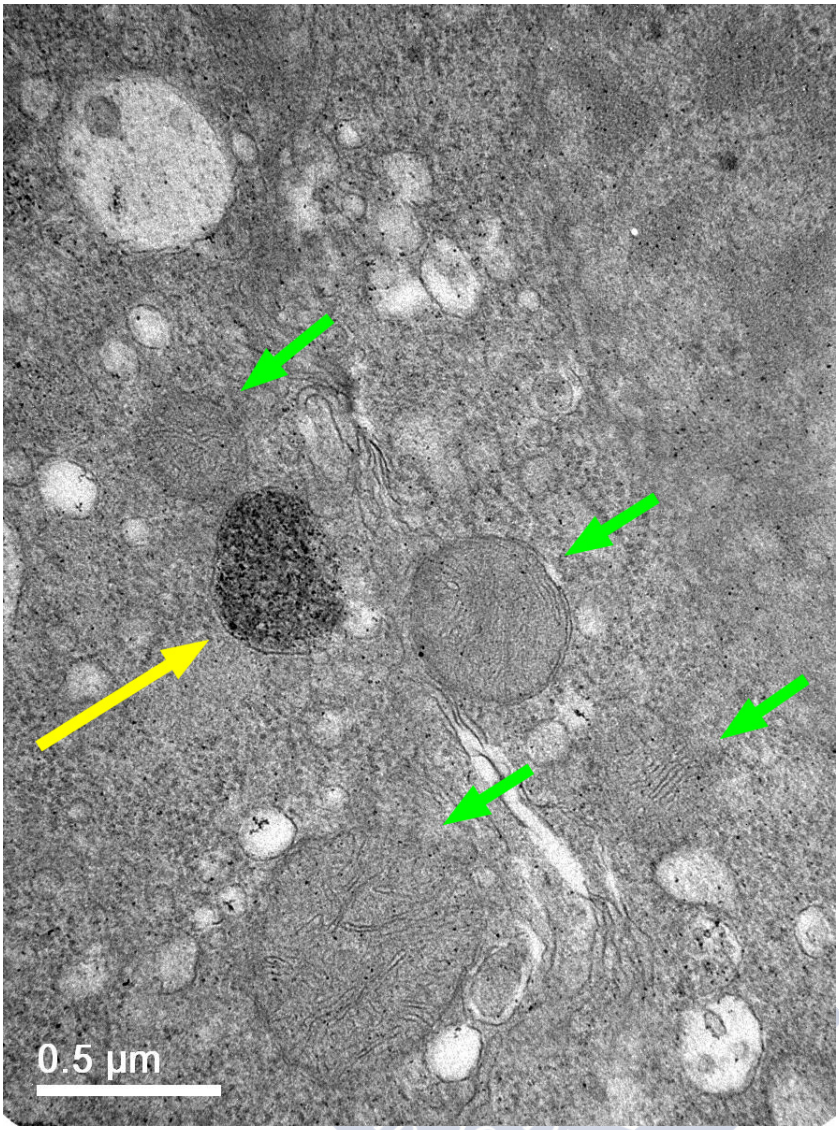


Figure 108: Electron micrograph of rat brain cortex 4h after intra-arterial delivery of D-MNPs labeled MSCs. Detail of Figure 107, showing D-MNPs contained in one endosome (yellow arrow) and several mitochondria (green arrows).

Labeled cells were found in the brain parenchyma, assessing that after an intra-arterial injection of a healthy rat MSCs can cross the BBB. However, it was also observed that some cells could be producing micro-embolus, as can be noted in Figure 109. A vessel surrounded by neuropil can be observed. Blue arrow points out the dilatation and magenta arrows denote normal vessel morphology before and after it. This vessel widening can be observed in more detail in Figure 110. Mainly 3 different cell types appeared in this expansion; red blood cells (RB), several platelets nucleus (P), one entire mesenchymal stem cell (A) and two disrupted MSCs (B and C). It is possible to note dotted hypointensities pointed with a yellow arrow in this picture; however it will be necessary to zoom in to compare them with previous *in vitro/in vivo* D-MNPs dotted patterns. In Figure 111 a magnification of these hypointensities can be observed more in detail. Magenta asterisks indicate the boundary of the cell membrane of MSC "A", in which cytoplasm some endosomes containing D-MNPs can be recognized. Close to this cell, MSC "B" has a diffuse cell membrane boundary and scattered dotted pattern is pointed out with cyan arrows. Because the spread hypointensities are not contained in an endosome but still localized in this cell, and the cell membrane boundary is not well-defined, we could think that this MSC is in apoptosis. However, our assumption is based on cell-endosome structure and membrane morphology because we do not have information about the state of its mitochondria. Apart from the well-being of these MSCs, the mechanism that is provoking this vessel broadening must be analyzed, and for this task it is necessary to examine also the morphology after/before the clot. A section of the non-expanded vessel is shown in Figure 112. Neuropil surrounds the vessel and in the inside a tubular-fiber structures can be

observed. This is fibrin, a fibrous, non-globular protein involved in the clotting of blood. It is formed by the action of the protease thrombin on fibrinogen which causes the latter to polymerize and the polymerized fibrin together with platelets forms a clot. In Figure 112 dispersed platelets nucleus and two tubular structures corresponding to fibrin fibers at the entrance of the extension can be noted. Thus gathering all electron microscopy images related to the dilatation, fibrin fibers (Figure 110 ), nucleus of the platelets (Figure 112) and MSCs, all are forming the clot, which is expanding the vessel in the scanned region.

This fibrin reaction could be the reason of the multifocal ischemias observed in MRI for healthy animals injected with MSCs. In the cannulation procedure we have followed in this work, we have always administered antiaggregants prior to cell delivery to prevent blood clotting, however Heparin concentration administered may not be enough to prevent clot formation or the injected mesenchymal stem cells may have an influence in this fibrin reaction. Moreover, in the previous chapter we have studied the influence of the heparin in the classical administration and in the magnetic vectorization in an ischemic brain; however we did not find any macroscopic difference in brain cell retention through MRI after using this antiaggregant drug.

So, attending to TEM results, most of MSCs observed in ultrathin sections are in the brain parenchyma, however it was also possible to observe one vessel occlusion where MSCs were also involved. This last fact could explain the multifocal ischemias observed in MRI after cell administration however TEM experiments were performed by injecting $1x10^6$ instead $0.25x10^6$ MSCs which was the compromise we have established between safety and efficiency for injection. In addition, it is important to take

into account that only one animal has been injected and examined through electron microscopy, and these results of parenchyma migration and vessel occlusion may be taken carefully. Further studies are needed to confirm these preliminary results.

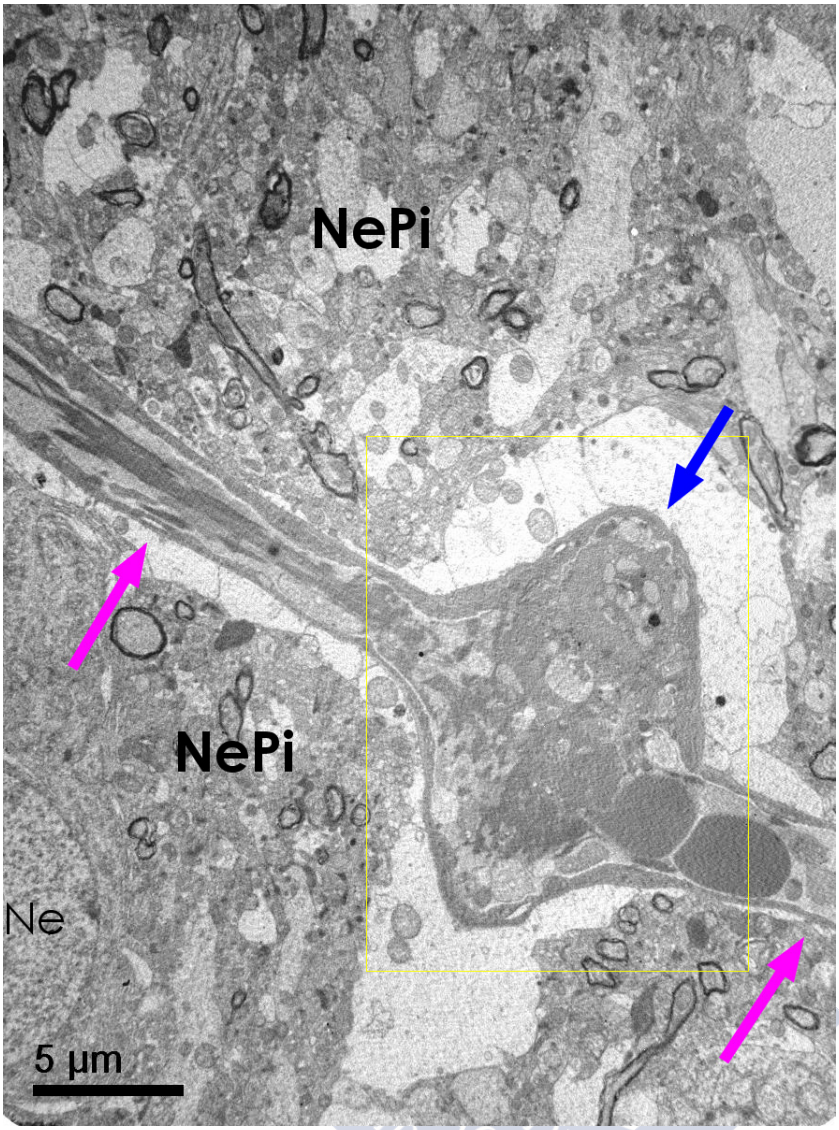


Figure 109: Electron micrograph of rat brain cortex 4h after intra-arterial delivery of D-MNPs labeled MSCs. It can be observed a neuron nucleus (Ne), surrounded by neuropil (NP). Magenta arrows point out a vessel with an expansion (blue arrow) due to MSCs presence.

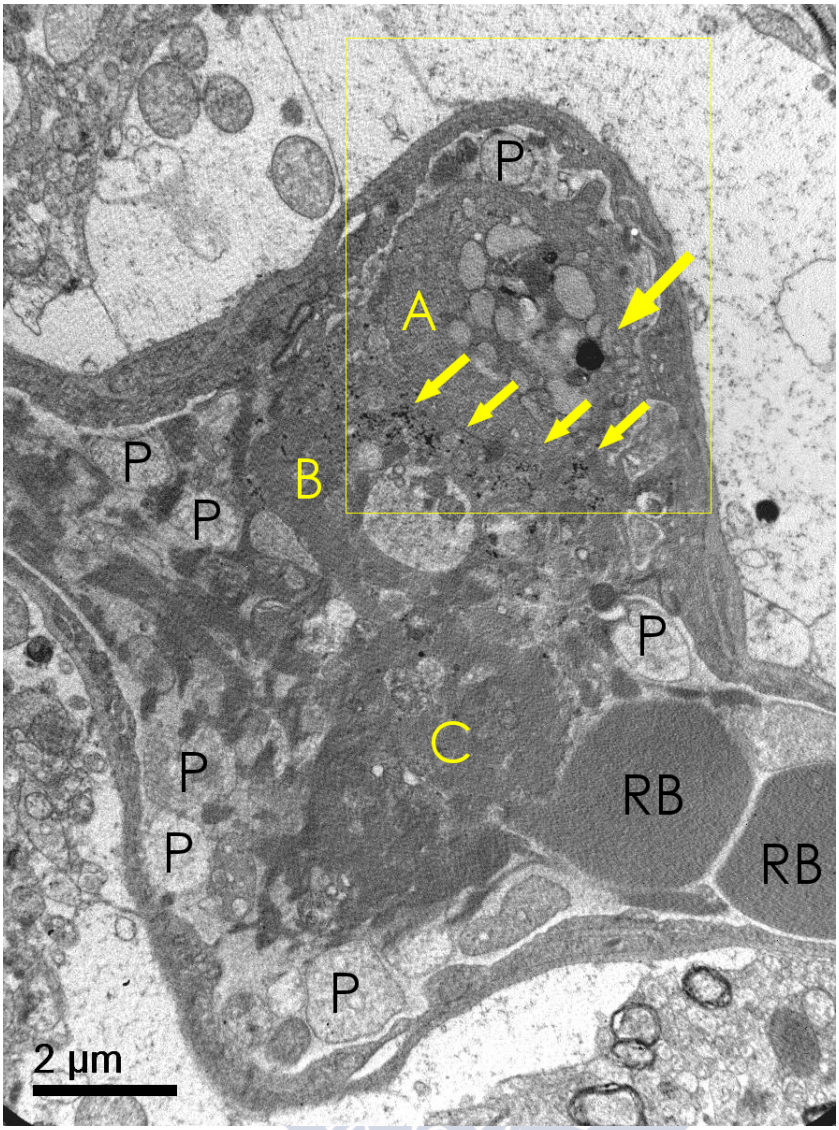


Figure 110: Electron micrograph of rat brain cortex 4h after intra-arterial delivery of D-MNPs labeled MSCs, zoom of Figure 109. Red blood corpuscles (RB), Platelets nucleus (P), mesenchymal stem cells (A, B, C) and yellow arrows point out D-MNPs.

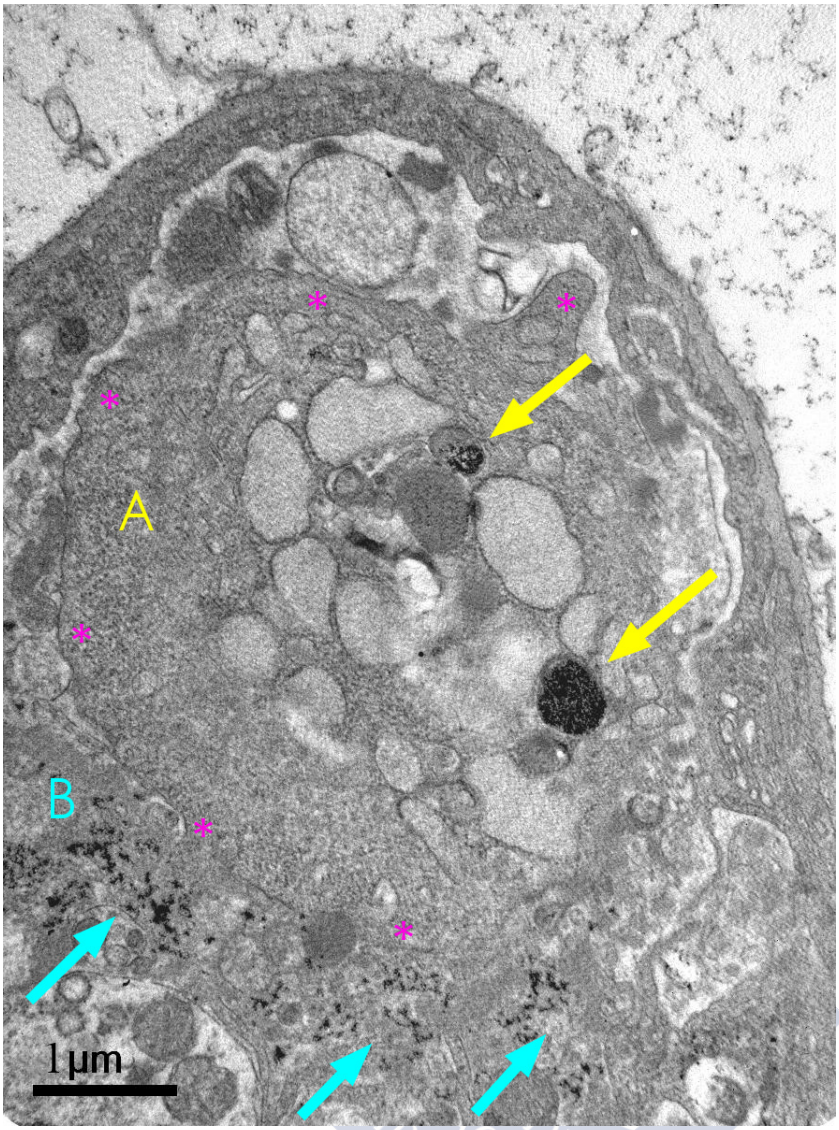


Figure 111: Electron micrograph of rat brain cortex 4h after intra-arterial delivery of D-MNPs labeled MSCs, zoom of Figure 110. Endosomes of "A" MSC containing D-MNPs (yellow arrows), boundary of cellular membrane of MSC "A" denoted with magenta asterisks, Opened endosomes of a dead MSC "B" (cyan arrows).

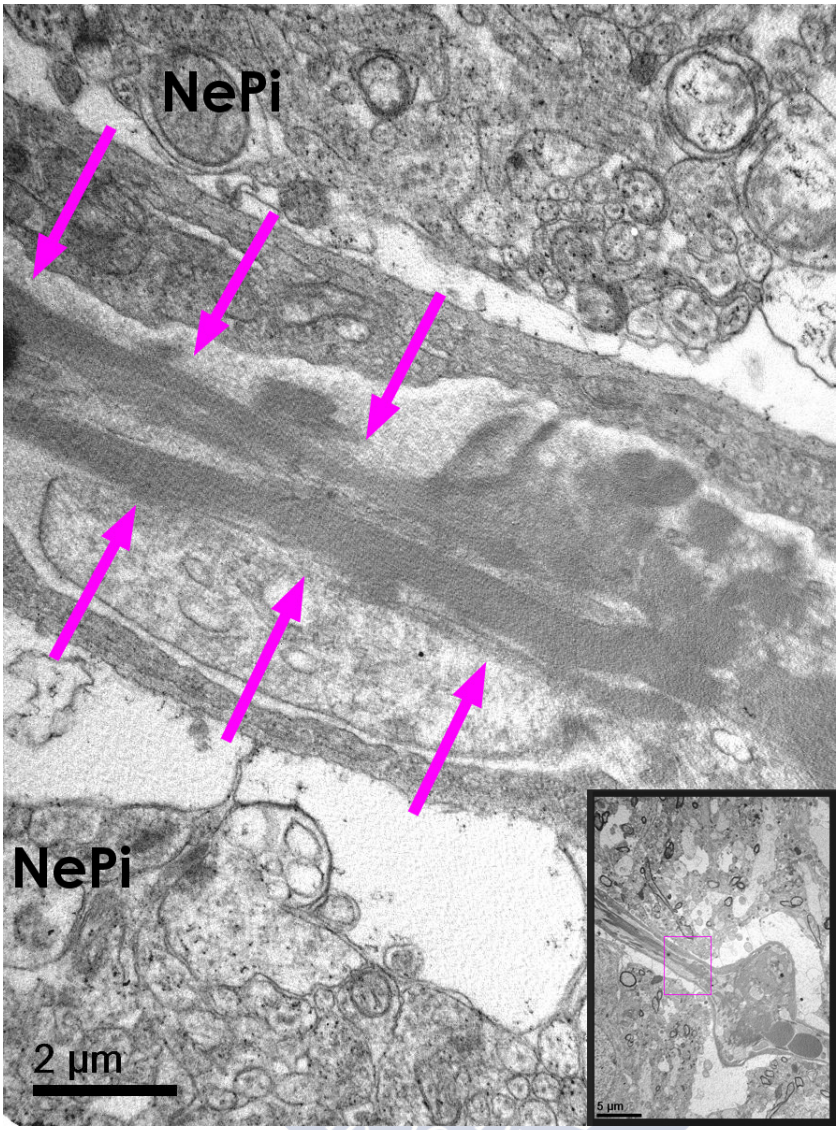


Figure 112: Electron micrograph of rat brain cortex 4h after intra-arterial delivery of D-MNPs labeled MSCs, zoom of Figure 109. A vessel surrounded by neuropil (NePi) is observed. Fibrin

## 9.4. Conclusions

Cell tracking of labeled MSCs following different administration routes is essential for a further understanding of the interaction between injected and host cells. In previous chapters, we had demonstrated the efficient labeling of MSCs with D-MNPs for *in vivo* MRI cell tracking. In this chapter we have assessed the feasibility of tagging MSCs with D-MNPs and also with CFSE, which let us not only *in vivo* cell tracking, ex vivo MSCs identification as well.

In order to assess the efficiency of this double labeling, intraparenchymal injections for MSCs delivery were performed. *Ex vivo* histology demonstrated that injected cells were still labeled with D-MNPs 4h after the injection and no particles were found out of the cells assessed by CFSE and Prussian blue staining, therefore MRI *in vivo* signal corresponds to labeled MSCs and not to free particles.

Intraparenchymal injection is a feasible administration route, however it is not the preferred for stem cell delivery due to the high invasiveness of the technique. Less invasive routes for stem cell delivery are intravenous and intra-arterial injection. We have studied the fate after the injection of labeled cells through jugular vein and through the internal carotid artery and we have found important differences between them. On one hand, we have assessed by MRI and/or histochemistry techniques that cells injected through jugular vein were found in the lungs and no cells were detected in the brain, for healthy and ischemic animals. On the other hand, following the intra-arterial route we have demonstrated that, for ischemic or non-ischemic animals, injected MSCs are found in the brain and no cells can be detected in other organs, opening a big window for further stem cell therapy administration.

Because of the blood brain barrier integrity in healthy animals and its disruption in ischemic ones, we also studied the localization of the injected cells by immunohistochemistry techniques after an intra-arterial administration. By CD31 staining and CFSE labeling it was possible to assess that injected cells are found in small vessels along the brain while large ones do not express CFSE positive cells. This selective intra-vessel localization could explain the multifocal ischemias observed in ischemic and non-ischemic intra-arterial injected rats, however because it is necessary to perfuse de animal to perform immunohistochemistry, other technique for corroborating this result was studied.

Preliminary results of electron microscopy have shown that MSCs labeled with D-MNPs are able to migrate into brain parenchyma in a healthy animal after an intra-arterial delivery of one million cells. However, TEM images of same animal also revealed vessel occlusions with MSCs and fibrin reaction associated which could explain previous results of multifocal ischemias.

In conclusion, for a non invasive brain localization of injected MSCs, intra-arterial injection is the most efficient administration route. On the other hand, MSCs delivered following intra-jugular injection results in cell entrapment in the lungs, and no cells reach the brain.

USC
UNIVERSIDADE
DE SANTIAGO
DE COMPOSTELA

# Section VI

## Neuroreparation mediated by mesenchymal stem cell therapy

USC
UNIVERSIDADE
DE SANTIAGO
DE COMPOSTELA

# 10. Neuroreparation study in an animal model of ischemic stroke using mesenchymal stem cells labeled with Dextran-coated superparamagnetic nanoparticles

## 10.1. Hypothesis

In previous chapters we have assessed the fate and the kinetics of labeled mesenchymal stem cells after an intra-arterial (ia) and intravenous (iv) administration routes. In this chapter, MSCs were ia and iv delivered during the acute phase in a cerebral ischemia model to investigate whether the cell distribution, and therefore administration route may improve the therapeutic outcome. MRI studies, behavioral tests, histological examinations and blood serum determinations were performed to evaluate the therapeutic benefits of the treatment.

# 10.2.Materials & Methods

## 10.2.1.Cell labeling preparation

### 10.2.1.1. Cell lines

All experiments were performed using Mesenchymal Stem Cells (MSCs) purchased from Cultrex, Trevigen and were cultured in IMDM (78%), Fetal bovine serum (10%), Horse serum (10%), Penicillin-Streptomycin (1%) all from Gibco Invitrogen, and Amphotericin-B (1%) from Sigma-Aldrich. Cell passage numbers between 7 and 18 were used in these experiments.

### 10.2.1.2. Dextran-coated superparamagnetic nanoparticles

Dextran coated MNPs (D-MNPs) were synthesized in the Clinical Neuroscience Research Laboratory following the *in situ* protocol described in Chapter 4.

### 10.2.1.3. Preparation of Poly-L-lysine hydrobromide-coated D-MNPs

1.5 µg/mL of Poly-L-lysine hydrobromide (PLL) (Sigma-Aldrich) was used. One hour prior to cell incubation, D-MNPs were mixed with cell medium and with 1.5 µg/mL PLL and vigorously shaken.

### 10.2.1.4. Cell labeling with PLL-coated D-MNPs

MSCs were labeled following the protocol described elsewhere[227] with slight modifications. Cells were incubated with 1.5 µg/mL PLL and 100 µg/mL of D-MNPs for 24h. The MNP containing medium was removed and the cells were 3 times washed with 1.5 mL of Phosphate

Buffered Saline (PBS without $Mg^{2+}$ and $Ca^{2+}$, Gibco Invitrogen) to remove non-attached MNPs. After washing, the cells were left overnight (12h) in 1 mL of fresh medium. Cells were washed once with 1.5 mL of PBS and 0.5 mL of EDTA-trypsin (Gibco Invitrogen) was added to detach the cells from the well. The trypsin was neutralized with fresh medium and the detached cells were collected in a Falcon tube. After a mild centrifugation, the supernatant was discarded and the cells were resuspended in PBS 1x. Cell count was performed with Trypan Blue staining and a Neubauer chamber. Samples were diluted 1:5 with PBS and 1:2 with Trypan Blue.

### 10.2.2.Animal management

In this study we have used 53 Wistar rats (Harlan) with a weight of 288±9 g. Animals were kept at controlled conditions of temperature (22±1 °C) and humidity (60±5%), with a 12/12 hours light/dark cycle, and granting free access to food (commercial chow pellets) and tap water. For surgery and MRI, rats were anesthetized with sevoflurane (3% in 70% $N_2O$ and 30% $O_2$). Rectal temperature was monitored and maintained at 37±0.5 °C with a feedback controlled heating system (1025 system, SA Instruments). At the end of the procedures animals were sacrificed under deep anesthesia (8% sevoflurane). Experimental protocols were approved by the local Animal Care Committee according to the Spanish and European Union (EU) rules (86/609/CEE, 2003/65/CE, 2010/63/EU, RD 1201/2005 and RD53/2013.

### 10.2.3.Model of focal transient ischemia in the rat

Transient focal ischemia was induced in rats by intraluminal occlusion of the middle cerebral artery (tMCAO), performed as previously described[171] with several modifications. In order to monitor the relative cerebral blood flow (CBF) during the surgery, a laser-Doppler flow probe (tip diameter 1 mm) attached to a flow meter (PeriFlux 5000; Perimed AB) was located over the thinned skull, over the middle cerebral artery territory (approximately 4 mm lateral to bregma). To perform tMCAO, both vertebral arteries and contralateral common carotid remained intact all surgical procedures.

Under a surgical microscope, common carotid, external carotid, and the internal carotid of the left side were dissected from connective tissue through a midline neck incision. Left external carotid and pterygopalatine arteries were separated and tied permanently with 6-0 silk sutures, showing a CBF reduction of 20% measured by laser Doppler. A silicon rubber-coated monofilament (403512PK5Re; Doccol Corporation) was inserted through the external carotid into the left common carotid artery and advanced into the internal carotid 17-20 mm from the bifurcation to occlude the origin of the MCA. The intraluminal filament was removed after 45 minutes of occlusion. Common carotid artery was perfunded immediately after removing the intraluminal filament.

Only animals with a CBF reduction measured by laser Doppler higher than 60% and with reperfusion after occlusion, MCA occluded on MR angiography and a infarct volume during the occlusion between 25-45% of the hemisphere measured on ADC maps were included in this study.

### 10.2.4.Administration delivery routes

Cells were administrated 4h after the perfusion of the ACM.

#### 10.2.4.1. Intra-arterial injection

Cannulation for intra-arterial delivery of labeled MSCs is performed in the left side where pterigopalatin and external carotid arteries were already sutured during tMCAO procedures.

Ipsilateral common carotid is temporally ligated to insert the cannula for the MSCs intra-arterial delivery. A 0.28 mm ID & 0.61 mm OD catheter (Smiths) connected to a 30G needle and a 1 mL syringe was inserted into the stump of ECA through an incision on the vessel under the operation microscope, and was tightened to ECA by a 6-0 silk suture. The catheter went forward into ICA till reach the branch of common and internal carotid. This tube was filled with heparinized physiological saline to prevent air bubble and coagulation. Common carotid is opened and a small blood reflux in the catheter could be observed. The syringe was filled with labeled cells in PBS and using slow hand injection over 15 minutes, $0.25x10^6$ labeled cells in 300 µL of PBS were delivered into the internal carotid. When the injection is finished, common carotid artery is temporally ligated to remove the catheter. EC is tied and common carotid artery is opened again.

#### 10.2.4.2. Intravenous injection

Intravenously administration was performed through the jugular vein. A 0.5 cm incision was made in the animal's neck just above the clavicle 1 cm to both left and right of the midline. Subcutaneous fat was cut and the jugular vein was revealed. A 30G gauge needle was used for every

injection since after withdrawal; the puncture rapidly closes preventing bleeding. . One million cells in 300 µL of PBS were administered manually in less than 1 min.

### 10.2.5. Magnetic resonance imaging

Infarct size, angiography and cell tracking were assessed by magnetic resonance imaging. Magnetic resonance imaging studies were conducted on a 9.4-T horizontal bore magnet (Bruker BioSpin, Ettligen, Germany) with 20 cm wide actively shielded gradient coils (440 mT/m). Radio-frequency transmission was achieved with a birdcage volume resonator; signal was detected using a four-element surface coil, positioned over the head of the animal, which was fixed with a teeth bar, earplugs, and adhesive tape. Transmission and reception coils were actively decoupled from each other. Gradient-echo pilot scans were performed at the beginning of each imaging session for accurate positioning of the animal inside the magnet bore.

Apparent diffusion coefficient maps were acquired using a spin-echo echo-planar imaging sequences with the following acquisition parameters: FOV 24 x 16 $mm^2$, image matrix 96 x 64 (in plane resolution 200mm/pixel x 200mm/pixel), 14 consecutive slices of 1mm thickness, repetition time 4 s, 4 averages, echo time 26.91 ms, spectral bandwidth 200.000 Hz and 7 diffusion *b* values: 0; 300; 600; 900; 1200; 1600 and 2000. Diffusion-weighted images were acquired during the ACM occlusion.

To evaluate the status of the ACM occlusion in a noninvasive manner, the TOF-MRA was performed. The MRA scan was performed with a 3D Flash sequence with the following acquisition parameters: FOV 30.72 x 30.72 x 14

$mm^3$, image matrix 256 x 256 x 58 (in plane resolution 120 mm/pixel x 120 mm/pixel x 241 mm/pixel), repetition time 15 ms, 2 averages and echo time 2.5 ms. MRA was performed during ACM occlusion and 24h, 1, 3, 7 and 14 days after the ischemia.

$T_2$-weighted images were acquired using a multislice multiecho spin-echo sequence with the following acquisition parameters: FOV 19.2 x 19.2 $mm^2$, image matrix 192 x 192 (isotropic in-plane resolution of 100 µm/pixel x 100 µm/pixel), 14 consecutive slices of 1mm thickness, repetition time of 3 s, and 16 echoes with 9 ms of echo time. $T_2$-weighted images were acquired 24h, 1, 3, 7 and 14 days after the onset of the ischemia.

$T_2$*-weighted axial images were acquired using a multi gradient echo sequence with the following acquisition parameters: FOV 19.2 x 19.2 $mm^2$, image matrix 192 x 192 (isotropic in-plane resolution of 100 µm/pixel x 100 µm/pixel), 14 consecutive slices of 1mm thickness, repetition time of 1.5 s, and 16 echoes with 2.9 ms. $T_2$*-weighted images were acquired 4h after the MSCs administration and 24h, 1, 3, 7 and 14 days after the onset of the ischemia.

Post-processing of all images was performed using ImageJ software (Rasband, W. NIH).

### 10.2.6.Functional test: Cylinder test

The Cylinder test is designed to evaluate locomotor asymmetry in rodent models of CNS disorders. As the animal moves within an open-top, clear plastic cylinder, its forelimb activity while rearing against the wall of the arena is recorded. Forelimb use is defined by the placement of the whole palm on the wall of the arena, which indicates its use

for body support. Forelimb contacts while rearing are scored with a total of 10 contacts recorded for each animal. The number of impaired and non-impaired forelimb contacts is calculated as a percentage of total contacts. Cylinder test was performed prior to tMCAO and 7 and 14 days after the ischemia.

### 10.2.7. Blood serum determinations: Vascular endothelial growth factor (VEGF) and interleunkin-6 (IL-6)

Venous blood was collected from the tail vein prior to tMCAO, 4h, 8h, 24h, 1day, 3 days, 7 days and 14 days after the onset of the ischemia. Blood serum was obtained and stored at -80ºC for further VEGF and IL-6 determinations. ELISA assays were performed using Quantikine ELISA Rat VEGF kit (R&D Systems, Inc.) and Quantikine ELISA Rat IL-6 kit (R&D Systems, Inc.) respectively.

### 10.2.8. Immunohistochemistry processing

Rats were anesthetized under sevofluorane (8%), perfused transcardiacally with 4% paraformaldehyde (PFA) in 0.1 M PBS, the brains were removed, postfixed (4% PFA, 4ºC, 24 h), cryopreserved (Sucrose 35%), included in OCT and stored at -80ºC. 15 µm thick axial sections were cut by a cryostat and dried in an oven at 38ºC for 4h. Slices were rehydrated in PBS, exposed to Citrate buffer (0.01 M, pH 6.0) (Dako) for 20 min at 99ºC and washed with PBS 1x.

#### 10.2.8.1. Immunohistochemistry processing for Ki-67 and CD31 staining dyes

Slides were incubated first with Rabbit polyclonal antibody to CD31 (Abcam) (1:25), Mouse monoclonal antibody to ki-67 (Dako) (1:30), normal horse serum (15%), normal goat serum (15%), Triton X-100 (0.2%) and PBS overnight. The slides were then incubated at room temperature for 1h with biotinylated horse anti-Mouse IgG antibody (Vector) (1:200), DyLight 488 Goat anti-Rabbit IgG antibody (Vector) (1:100), Triton (0.2%) and PBS. After 3 washes with PBST, slides were incubated with dylight 594 streptavidin (Vector) (1:500), Triton (0.2%) and PBS. Then, 10 µL of Hoechst (Invitrogen) in 60 mL of PBS 1x were added to the slides, incubated for 15 min and washed afterwards with PBS. Slides were mounted with fluorescence mounting medium. Photographs were taken using a Leica DMI 6000 B and processed using LAS AF V.1.0.0 software (Leica Microsystems).

#### 10.2.8.2. Immunohistochemistry processing for Ki-67 and doublecortin (DCX) staining dyes

Slides were incubated first with Rabbit polyclonal antibody to DCX (1:25), Mouse monoclonal antibody to ki-67 (Dako) (1:30), normal horse serum (15%), normal goat serum (15%), Triton X-100 (0.2%) and PBS overnight. The slides were then incubated at room temperature for 1h with biotinylated horse anti-Mouse IgG antibody (Vector) (1:200), DyLight 488 Goat anti-Rabbit IgG antibody (Vector) (1:100), Triton (0.2%) and PBS. After 3 washes with PBST, slides were incubated with dylight 594 streptavidin (Vector) (1:500), Triton (0.2%) and PBS. Then, 10 µL of Hoechst (Invitrogen) in 60 mL of PBS 1x were added to the slides, incubated for 15 min and washed afterwards with PBS. Slides were mounted with

fluorescence mounting medium. Photographs were taken using a Leica DMI 6000 B and processed using LAS AF V.1.0.0 software (Leica Microsystems)

### 10.2.9. Statistical analysis

The statistical analyses of the data were performed using GraphPad Prism 5.01 (GraphPad Software, Inc). For descriptive analyses, means and standard deviations were calculated for the normally distributed continuous variables. For confirmatory analyses one-way ANOVA was performed to calculate overall p-values for the comparison of the different groups for each variable. The global significance level for all statistical test procedures was chosen as $\alpha$=0.05.

### 10.2.10. Timeline of the study

In order to evaluate the therapeutic properties of different administration routes for of MSCs in an animal model of ischemic stroke, 4 groups were studied:

- Control 1 (n=6): tMCAO
- Control 2 (n=6): tMCAO which were injected i.a. with 300 µL of PBS 4h after the onset of the ischemia.
- MSCs ia (n=6): tMCAO which were injected i.a. with $0.25x10^6$ of MSCs labeled with D-MNPs dispersed in 300 µL of PBS 4h after the onset of the ischemia.
- MSCs iv (n=6): tMCAO which were injected i.v. with $1x10^6$ of MSCs labeled with D-MNPs dispersed in 300 µL of PBS 4h after the onset of the ischemia.

Experimental procedures diagram can be observed in Figure 113.

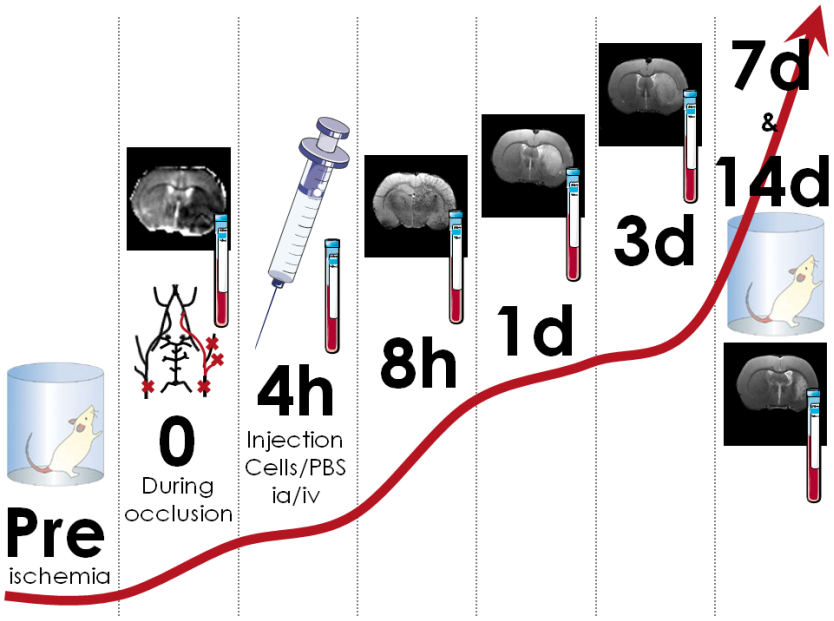


Figure 113: Timeline evaluation of the therapeutic benefits of the different routes for MSCs administration in an animal model of ischemic stroke.

Cylinder test was performed prior to tMCAO to assess the locomotor symmetry of the animals and on the days 7$^{th}$ and 14$^{th}$ to assess the symmetry/asymmetry due to the stem cell administration. The infarct size and brain edema follow-up were performed during the occlusion by a MR-DWI sequence and by a $T_2$-weighted images on the 1st, 3rd, 7th and 14th day after the ischemia induction. Moreover, $T_2$*-weighted images were acquired to track the injected cells and to evaluate hemorrhagic lesions 8h, 1 day, 3 days, 7 days and 14 days after the ischemia. We have also included MR angiography to evaluate the occlusion during the tMCAO and to study morphologic changes on the vessels during the following-up of the animals. Venous blood samples were collected during the occlusion, 4h, 8h, 1 day, 3 days, 7 days and 14 days after the onset of the

insult for further VEGF and IL-6 determinations. And finally, on the 14th day, animals were transcardiacally perfused and their brains processed as described previously for further histology analysis.

## 10.3.Results

### 10.3.1.Cell tracking after intra-arterial administration

D-MNPs labeled MSCs were easily detected by MR $T_2$* weighted images 4h, 24h and 3 days after the injection.. Next timepoint is 7 days, and it was not possible to observe labeled cells in all animals scanned (Figure 114).

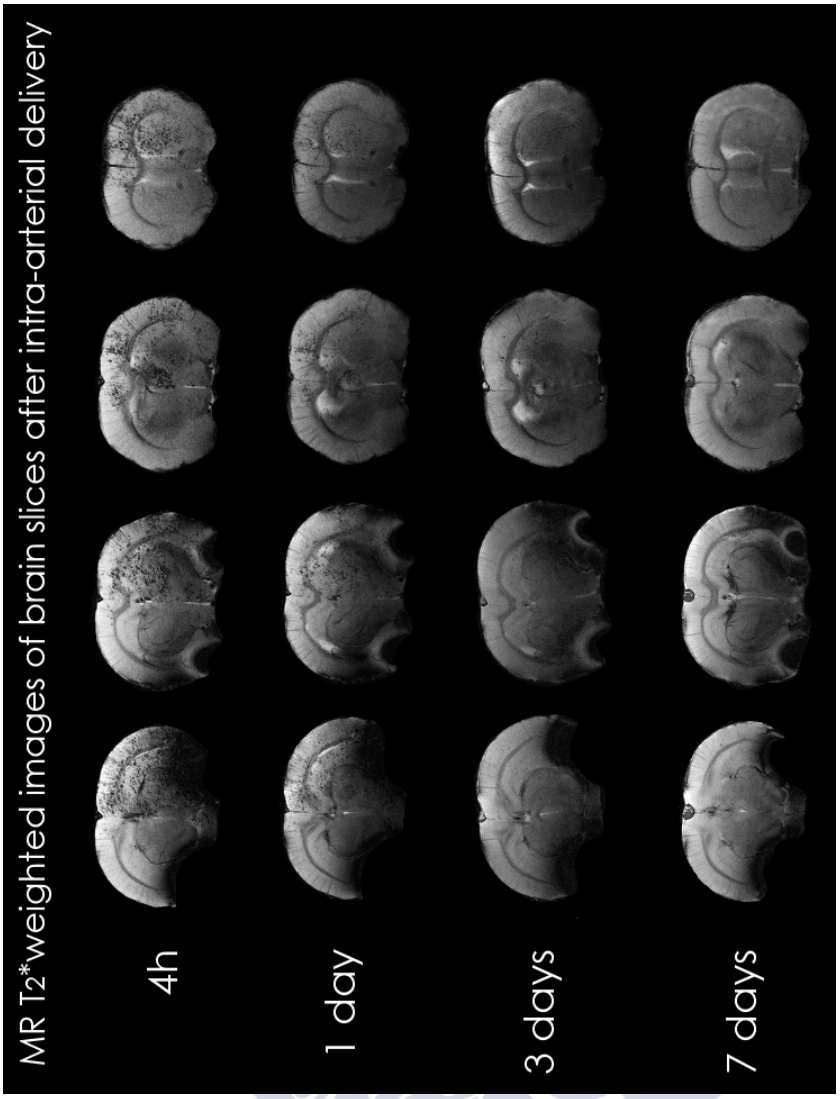


Figure 114: MR $T_2$* weighted images of one ischemic animal injected with $0.25x10^6$ D-MNPs labeled MSCs at different timepoints.

## 10.3.2.Effects on ischemic lesion volume

Infarct volume sizes were measured on ADC maps, calculated from MR DWI, acquired during the occlusion (t=0), and on $T_2$ maps, obtained from $T_2$ weighted images at days 1, 3, 7 and 14 after the induction of the ischemia. In Table 11 and Figure 115, infarct volume sizes are expressed in percentage respect the hemisphere volume corrected by edema factor.

| | **Control 1** | | **Control 2** | | **MSCs ia** | | **MSCs iv** | |
|---|---|---|---|---|---|---|---|---|
| | *Mean* | *SD* | *Mean* | *SD* | *Mean* | *SD* | *Mean* | *SD* |
| 0 (tMCAO) | 32 | 6 | 33 | 6 | 35 | 2 | 35 | 7 |
| Day 1 | 25 | 5 | 30 | 10 | 32 | 3 | 27 | 7 |
| Day 3 | 30 | 5 | 37 | 11 | 36 | 3 | 32 | 10 |
| Day 7 | 20 | 8 | 22 | 11 | 22 | 3 | 18 | 11 |
| Day 14 | 15 | 5 | 19 | 11 | 19 | 4 | 15 | 10 |

Table 11: Infarct volumes (% hemisphere) measured from MR ADC and $T_2$ maps for all groups.

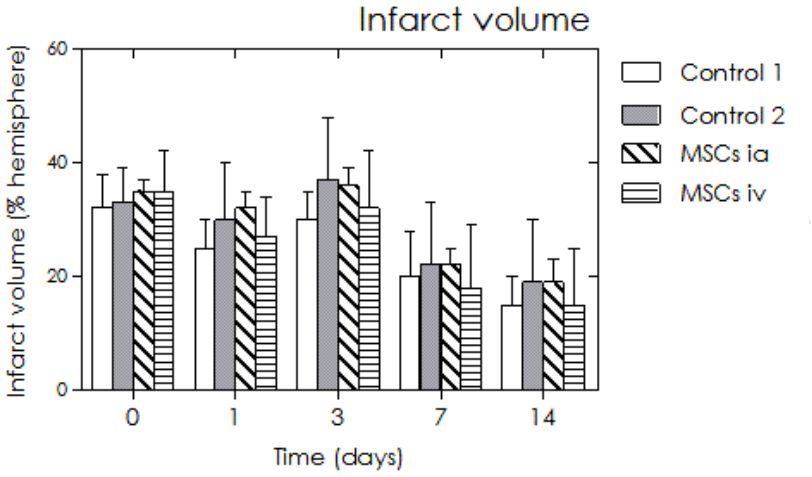


Figure 115: Infarct volumes (% hemisphere) measured from MR ADC and $T_2$ maps for all groups.

No infarct volume reduction compared to control was observed 14 days after the onset of the ischemia and mesenchymal stem cell administration in any group (Figure 116). Infarct volumes for intra-arterial administration of PBS or MSCs are slightly increased respect to control or intravenous administration of MSCs, however results are not statistically significant.

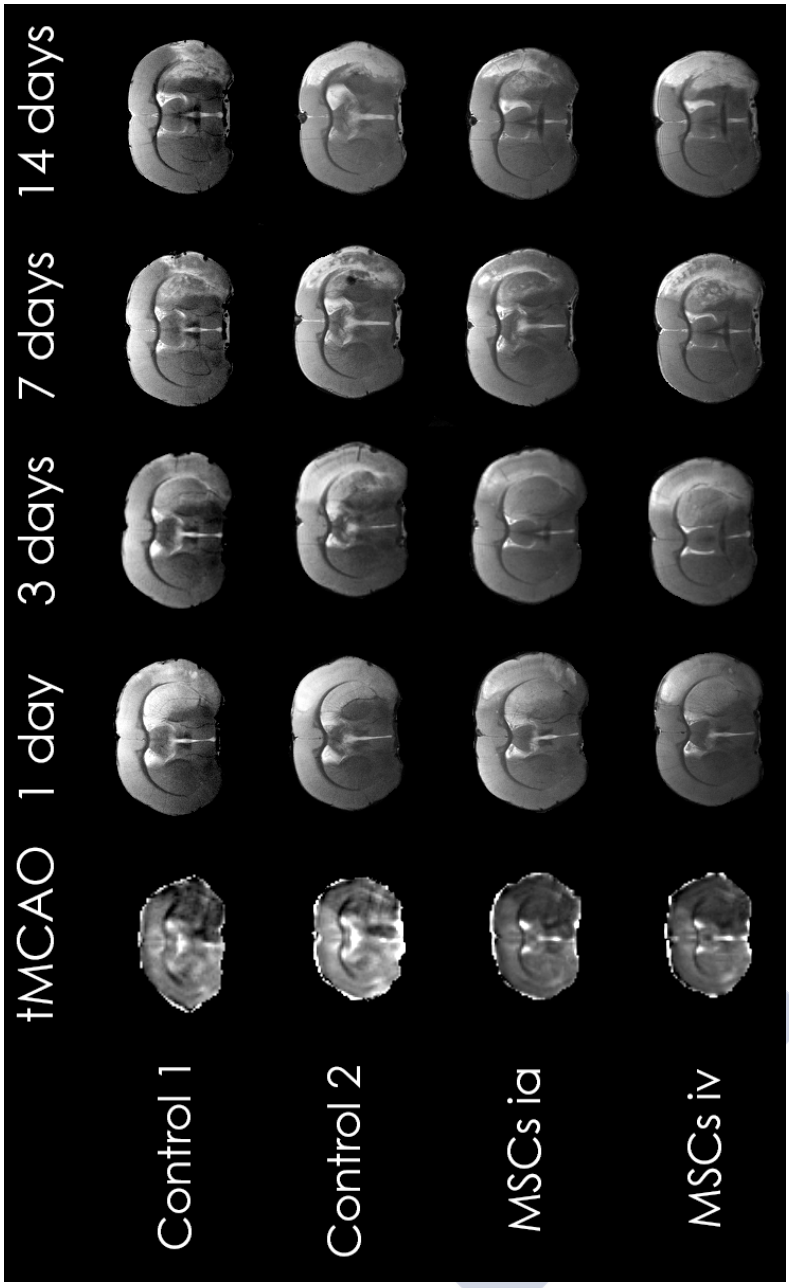


Figure 116: Representative MRI of each group at different time points. tMCAO corresponds to ADC maps and 24h, 3days, 7days and 14days to $T_2$ weighted images.

## 10.3.3.Effects on edema formation

Brain edema volume sizes were measured on $T_2$ maps, obtained from $T_2$ weighted images at days 1, 3, 7 and 14 after the induction of the ischemia. Edema volumes were calculated as the increase of ipsilateral hemispheric volume respect to contralateral hemispheric volume expressed in percentage (Table 12 and Figure 117).

| | **Control 1** | | **Control 2** | | **MSCs ia** | | **MSCs iv** | |
|---|---|---|---|---|---|---|---|---|
| | *Mean* | *SD* | *Mean* | *SD* | *Mean* | *SD* | *Mean* | *SD* |
| Day 1 | 7 | 3 | 9 | 5 | 12 | 3 | 7 | 3 |
| Day 3 | 9 | 3 | 11 | 5 | 13 | 2 | 10 | 5 |
| Day 7 | 2 | 3 | 1 | 2 | 2 | 1 | 1 | 2 |
| Day 14 | -4 | 1 | -4 | 2 | -4 | 1 | -4 | 2 |

Table 12: Edema volume formation (% of the increase of ipsilateral hemispheric volume respect to contralateral hemispheric volume).

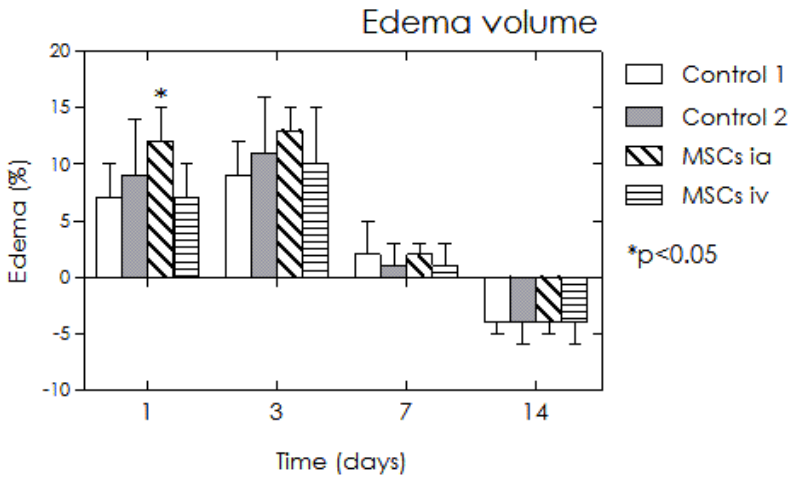


Figure 117: Edema volume (% of the increase of ipsilateral hemispheric volume respect to contralateral hemispheric volume).

No edema volume reduction was observed after MSCs intra-arterial or intravenous administration in the acute

phase of the cerebral ischemia. 24h after the ischemia and cell delivery, a significant increment of the edema volume formation following intra-arterial delivery of mesenchymal stem cells was observed (*p<0.05).

## 10.3.4.Cylinder test

Cylinder test was performed prior to tMCAO (Pre-ischemia) and 7 and 14 days after the ischemia by counting the number of forelimb contacts. The number of impaired and non-impaired forelimb contacts is calculated as a percentage of total contacts (Table 13 and Figure 118).

| | **Control 1** | | **Control 2** | | **MSCs ia** | | **MSCs iv** | |
|---|---|---|---|---|---|---|---|---|
| | *Mean* | *SD* | *Mean* | *SD* | *Mean* | *SD* | *Mean* | *SD* |
| Pre-isch | 48 | 2 | 50 | 5 | 51 | 4 | 50 | 4 |
| Day 7 | 65 | 19 | 63 | 8 | 62 | 15 | 57 | 13 |
| Day 14 | 64 | 17 | 63 | 6 | 73 | 13 | 58 | 5 |

Table 13: Edema formation (% of the increase of ipsilateral hemispheric volume respect to contralateral hemispheric volume).

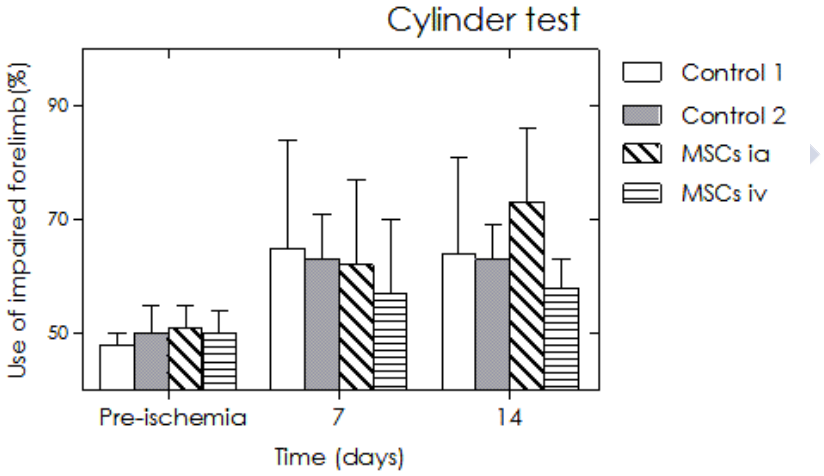


Figure 118: Use of impaired forelimb (%) in the cylinder test.

No significant differences in functional recovery determined by cylinder behavioral test were observed between groups. Attending to the obtained results, i.v. administration of MSCs shows a reduction on the use of impaired forelimb, however not statistically significant.

### 10.3.5.Blood serum determinations: VEGF and IL-6

Blood serum samples were evaluated for detectable levels of VEGF and IL-6 with its respective ELISA kit and all samples measured showed lower levels than the detectable for both assays. (31.2 pg/mL for VEGF ELISA kit and 62.5 pg/mL for IL-6 ELISA kit)

### 10.3.6.Immunohistochemistry

Subventricular region of the contralateral and ipsilateral ventricles were examined with doublecortin (DCX) and Ki-67 staining in order to evaluate the neurogenesis. In Figure 119 a representative image of each group is shown. DCX and Ki-67 co-localization seemed to be higher for the treated groups compared to control, and specially the DCX staining, marking neuronal precursor cells and immature neurons, however we did not perform a quantification. (Figure 119)

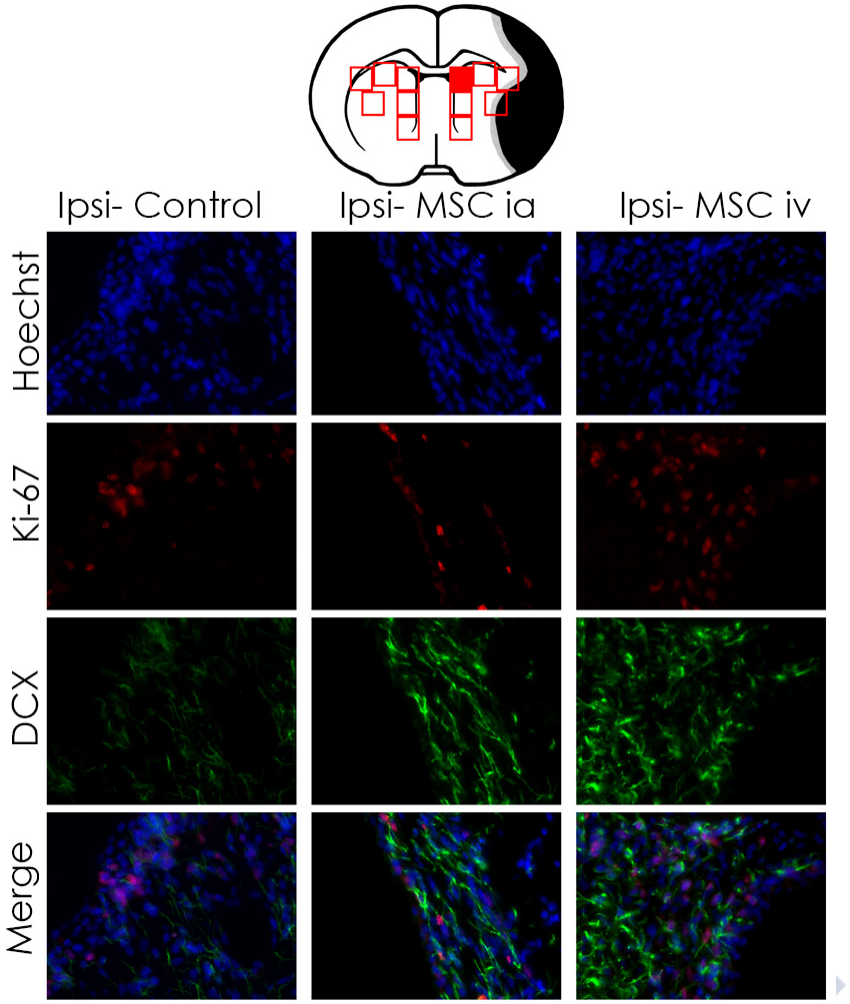


Figure 119: Immunohistochemistry of subventricular zone to evaluate the neurogenesis by using DCX and Ki-67. Representative pictures of the different groups corresponding to the red rectangle in the scheme. (Scale bar 50 µm)

Infarct and peri-infarct regions were observed for angiogenesis evaluation by studying the co-localization of CD31 and DCX. No differences in Ki-67 and CD31 were observed, therefore, no differences in angiogenesis were seen between groups. (Figure 120).

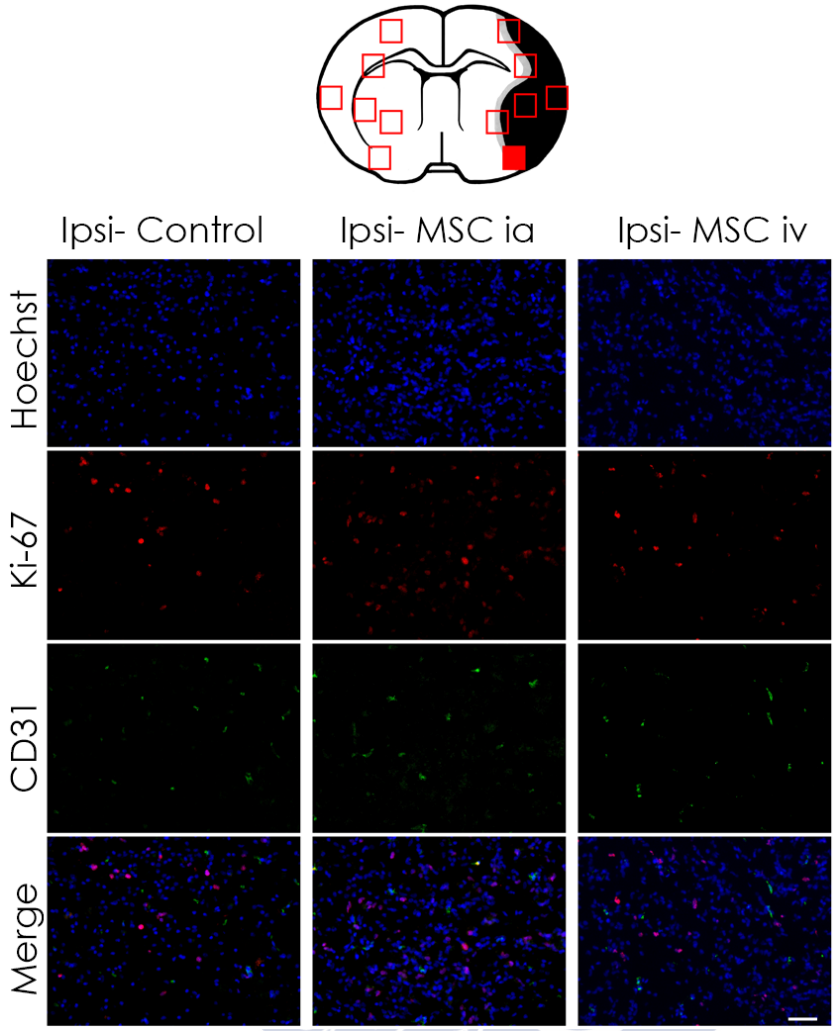


Figure 120: Immunohistochemistry of peri-infarct region to evaluate the angiogenesis by using CD31 and Ki-67. Representative pictures of the different groups corresponding to red rectangles in the scheme. (Scale bar 50 µm)

## 10.4.Discussion

Mesenchymal stem cells have received special attention last years as a therapeutic candidate for stroke due to their possible multi-mechanistic effects on the damaged brain. However, several parameters as therapeutic window, cell dosage or administration route are still under discussion. In previous chapters we have reported the relationship between safety and cell dosage for intra-arterial and intravenous delivery routes and moreover, we have studied the fate of these injected cells by using superparamagnetic nanoparticles. In this chapter, we have compared the outcome after intra-arterial and intravenous injection of labeled mesenchymal stem cells in terms of functional recovery, reduction of ischemic lesion size, edema formation and also evaluating the neurogenesis and angiogenesis 14 days after the ischemia.

Several groups have studied the therapeutic window for stem cells administration in animal models of cerebral ischemia, suggesting that an early intervention could reduce lesion size and improve functional outcome.[119,268] Considering these results we have injected D-MNPs labeled MSCs 4h after the onset of the ischemia. Cell dosage for i.a. delivery route is limited by the safety of the injection reported in the previous chapter. Thus, $0.25x10^6$ D-MNPs were i.a. injected, while we considered $1x10^6$ for iv administration.

We have assessed that after an intra-arterial injection of D-MNPs labeled MSCs it is possible to track administered cells *in vivo* with MRI. We have observed that all animals injected following intra-arterial route with labeled cells displayed brain hypointensities for the 3 days after the administration and, on the other hand, in the animals injected

intravenously it was not possible to detect labeled cells in brain. These two facts have demonstrated that the fate after delivery is determined by the injection site and also, it opened the possibility to compare ia and i.v. administration routes of MSCs for cerebral ischemia therapy.

In this chapter we have studied the neuroreparation after an ischemic event by measuring the infarct volume, edema formation and functional recovery. No significant differences in infarct volume reduction and edema formation were observed for treated and non-treated animals, although i.a. delivery has shown bigger infarct volumes and edema formation than control or i.v. administration. On the other hand, a slightly improvement in functional recovery was observed for i.v. administered cells, but not statistically significant. These results are in consonance with previous studies that have reported that stem cell therapies improved neurological function recovery without the reduction of lesion volume.[269-271] Parameters such as stem cell type, dose, therapeutic window, and administration route have shown high influence on infarct volume reduction studies however, most of them cannot be compared because the initial conditions are different.[261,268,269,272,273] But favorable effects on behavioral outcomes after an ischemic insult are normally associated with regenerative processes onto the microenvironment, as neurogenesis and angiogenesis. [62,274,275]

Thus, in our study we have assessed that treatment with MSCs significantly increased the number of Ki-67 and DCX immunoreactive area in the ipsilateral subventricular zone suggesting that MSC treatment enhanced endogenous neurogenesis, but no differences between intra-arterial and intravenous administration were found. On the contrary,

CD31 combined with Ki-67 did not show an increase in the angiogenesis process in treated animals compared to control 14 days after cerebral ischemia.

Furthermore, VEGF and IL-6 were analyzed in blood serum samples. VEGF is an angiogenic and neuroprotective factor that increase axonal outgrowth, block neuronal apoptosis and increase neurogenesis, thus promoting neuroprotection from stroke.[156] In this work we have previously demonstrated that D-MNPs labeled MSCs secrete same levels of VEGF than non-labeled cells. Thus, at this point the study of VEGF levels after MSCs administration was crucial for further understanding of the stem cells therapeutic mechanism. However, blood serum samples showed lower levels than the detectable by ELISA technique. Other studies have determined VEGF levels by measuring brain sections by ELISA instead by blood serum.[276] Besides VEGF, IL-6 was determined in blood serum samples because its demonstrated relationship with pro- and anti-immflamatory effects following focal ischemia. Serum levels measurements of IL-6 were lower than the resolution limit of the ELISA kit. As happened before with VEGF determination, brain sections would report values for measuring using ELISA assays.

Collectively, our data indicates that intravenous administration of $1x10^6$ MSCs slightly improve functional outcome after cerebral ischemia, and that the intra-arterial or intravenous delivery of mesenchymal stem cells promotes neurogenesis measured 14 days after the injection.

## 10.5.Conclusions

In this study we have compared intra-arterial and intravenous administration of MSCs for the therapy of focal cerebral ischemia. Only cells injected i.a. reached the brain and were detectable for 3 days after the delivery, guaranteeing the cellular proximity to the injury site.
Under our experimental conditions and by using dextran-coated superparamagnetic nanoparticles, we have assessed that the local effect of MSCs injected following i.a. route did not improve the outcome after a cerebral ischemia compared to a systemic administration following the i.v. route.

USC
UNIVERSIDADE
DE SANTIAGO
DE COMPOSTELA

# Section VII
# Conclusions

USC
UNIVERSIDADE
DE SANTIAGO
DE COMPOSTELA

# General conclusions

1. Three types of superparamagnetic nanoparticles coated with different polymers, dextran, pluronic F127 and tetronic 908, have been developed and characterized for further biological and biomedical applications as MRI contrast agents.
2. The optimization procedure and *in vitro* validation of our synthesized superparamagnetic nanoparticles have been performed in mesenchymal stem cells and neural stem cells assessing the biocompatibility of these nanoparticles for cell labeling.
3. We have assessed *in vitro* the feasibility of label and detect mesenchymal stem cells after proliferation when labeled with dextran- coated superparamagnetic nanoparticles without harmful effects. In addition, it is possible to vectorize these labeled cells with magnetic fields *in vitro*.
4. We have demonstrated that MSCs labeled with D-MNPs can be visualized *in vivo* by $T_2$ and $T_2$* weighted images in MRI, and the hypointensities observed correspond to labeled cells and not to free superparamagnetic nanoparticles.
5. A model of intra-arterial administration of stem cells with low associated risks and high brain delivery efficiency has been developed for further cerebral ischemia treatment studies.
6. The doses of mesenchymal stem cells for intra-arterial administration as a potential treatment for ischemic stroke are determined by the presence of multifocal ischemias, being $2.5x10^5$ cells the highest administrable dose.

7. We have assessed that the brain targeting with labeled mesenchymal stem cells has not been increased by the use of the magnetic vectorization *in vivo*.
8. We have observed that after an intravenous administration of labeled mesenchymal stem cells, no cells were found in the brain while cells were detected in the lungs.
9. Dextran-coated superparamagnetic nanoparticles labeling has also allowed the visualization of injected cells for electron microscopy *ex vivo* analysis. Our first results suggested that some labeled MSCs remained in the vessels and some crossed to the brain parenchyma 4h after an intra-arterial administration.
10. Superparamagnetic nanoparticles are a valuable tool for distinguishing the fate between injected cells following intra-arterial and intravenous administration in an animal model of stroke.
11. Under our experimental conditions, we have not observed that the intra-arterial administration of mesenchymal stem cells presents more advantages than an intravenous delivery in terms of safety and outcome after cerebral ischemia.

# Conclusiones generales

1. Hemos desarrollado y caracterizado 3 tipos de nanopartículas superparamagnéticas recubiertas de diferentes polímeros, dextran, pluronic F127 y tetronic 908 para uso biomédico como agentes de contraste de resonancia magnética nuclear.
2. Estas nanopartículas se han probado en cultivos celulares de células madre mesenquimales y de células madre neurales, demostrando su alta biocompatibilidad y sus posibles aplicaciones para seguimiento celular.
3. Las células madre mesenquimales marcadas con nanopartículas recubiertas de dextran han sido examinadas tras diversas divisiones celulares asegurando que sus propiedades no se ven afectadas por el marcaje. Además, la vectorización magnética de estas células no sólo es posible sino que no afecta a su viabilidad en estudios *in vitro*.
4. Diversos experimentos *in vivo*, han puesto de manifiesto que es posible la visualización de las células marcadas tras ser inyectadas, y que las hipointensidades observadas por resonancia magnética se corresponden a células marcadas y no a nanopartículas libres.
5. Hemos desarrollado un modelo de administración intra-arterial de células en animales con isquemia cerebral que minimiza los riesgos asociados a la inyección y que asegura la presencia de células en el cerebro.
6. Las dosis de células madre mesenquimales administradas intra-arterialmente como futura opción terapéutica en la isquemia cerebral, están limitadas por la posibilidad de inducción de isquemias

multifocales, siendo $2.5x10^5$ la dosis máxima administrable encontrada.

7. Los experimentos *in vivo* de vectorización magnética han evidenciado que no es posible incrementar el número de células madre mesenquimales marcadas por la acción de campos magnéticos bajo nuestras condiciones experimentales.
8. Las células madre mesenquimales marcadas y administradas a través de la vena yugular han sido detectadas en los pulmones, sin que se haya observado migración de las mismas al cerebro del animal.
9. El marcaje con nanopartículas superparamagnéticas recubiertas de dextran ha permitido la discriminación entre células inyectadas y células del cerebro del animal mediante técnicas de microscopía electrónica. Nuestros resultados sugieren que las células madre mesenquimales en algunos casos han permanecido en el interior de los vasos, mientras que en otros, han cruzado al parénquima cerebral de un animal sano 4h tras ser administradas.
10. Hemos demostrado que las nanopartículas superparamagnéticas desarrolladas en este trabajo son la herramienta idónea para estudiar la migración celular a nivel cerebral con células administradas tanto i.a. como i.v.
11. Bajo nuestras condiciones experimentales, no hemos observado que la administración intra-arterial suponga una mejora en términos de riesgo beneficio respecto la administración intravenosa de células madre mesenquimales.

# Section VIII
# Appendix

USC
UNIVERSIDADE
DE SANTIAGO
DE COMPOSTELA

In this section we present several moments of beauty in our day-to-day research. Maybe results of those experiments were not what we were looking for, however the images remain beautiful.

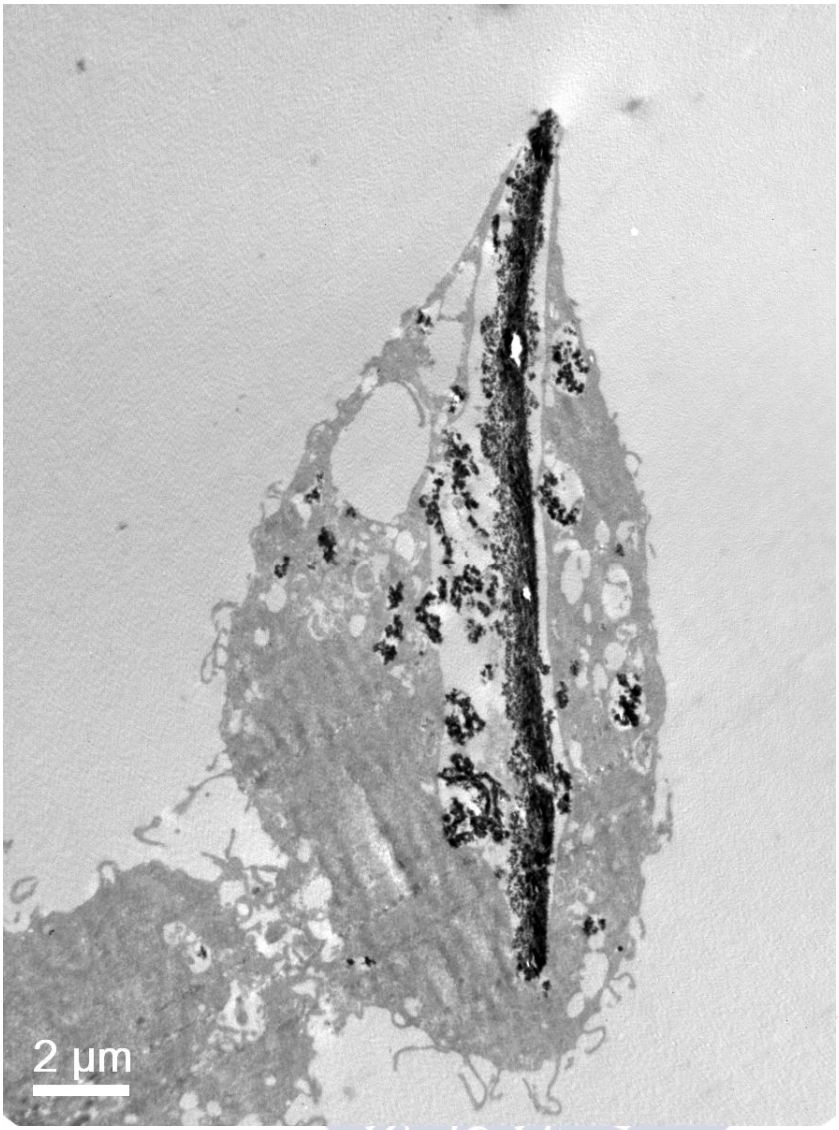


Figure 121: TEM micrograph of a mesenchymal stem cell labeled with Tetronic 908-coated superparamagnetic nanoparticles. Apart from spherical-shape particles, one fiber was wrapped with the polymer and the cell also included it.

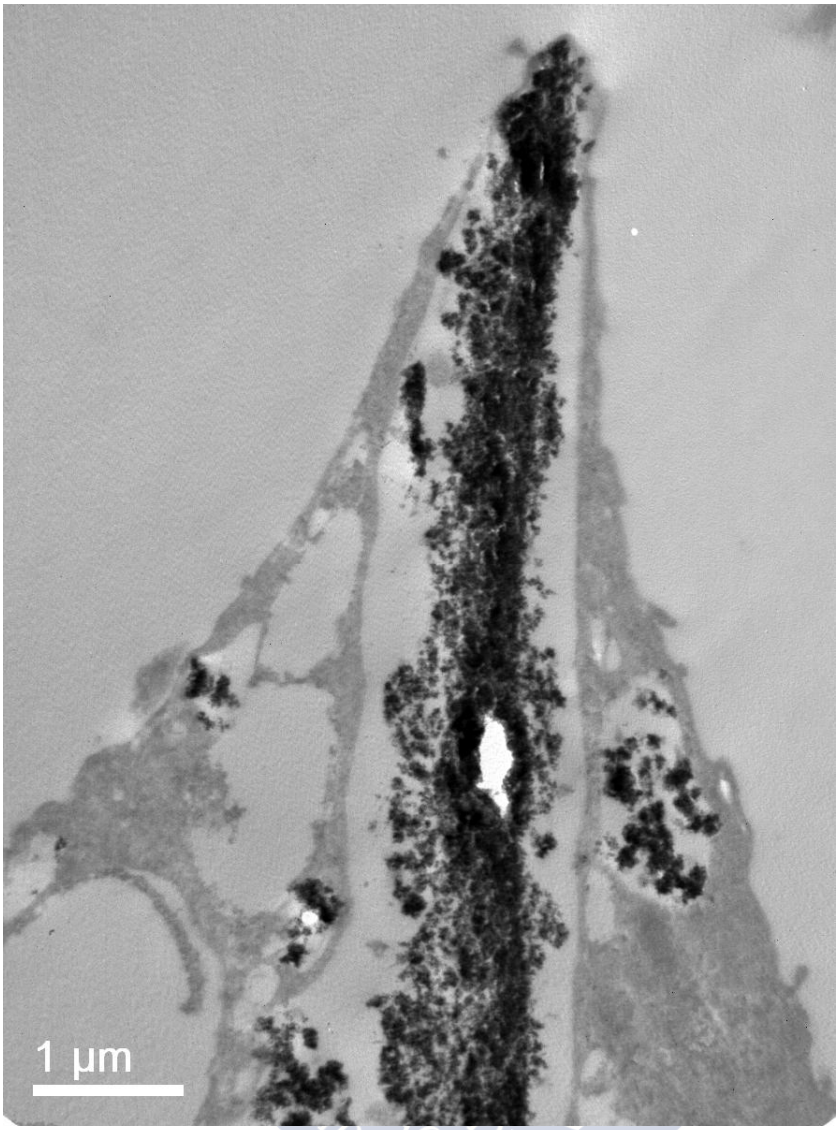


Figure 122: Magnification of Figure 121, where it is possible to observe how the Tetronic 908-wrapped fiber is fully internalized.

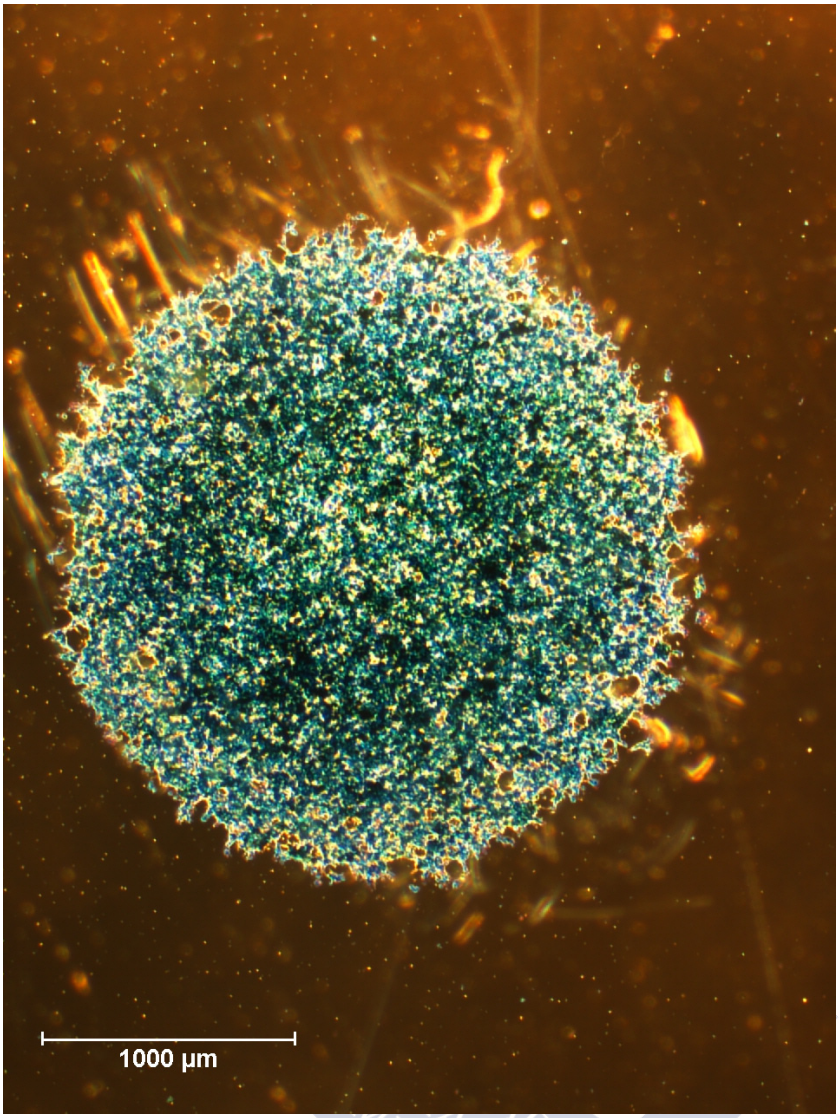


Figure 123: Optical image of dextran-labeled mesenchymal stem cells after 2D vectorization stained with Prussian Blue. One magnet was placed below the Petri-dish, cells were vectorized to that region and got attached to the surface.

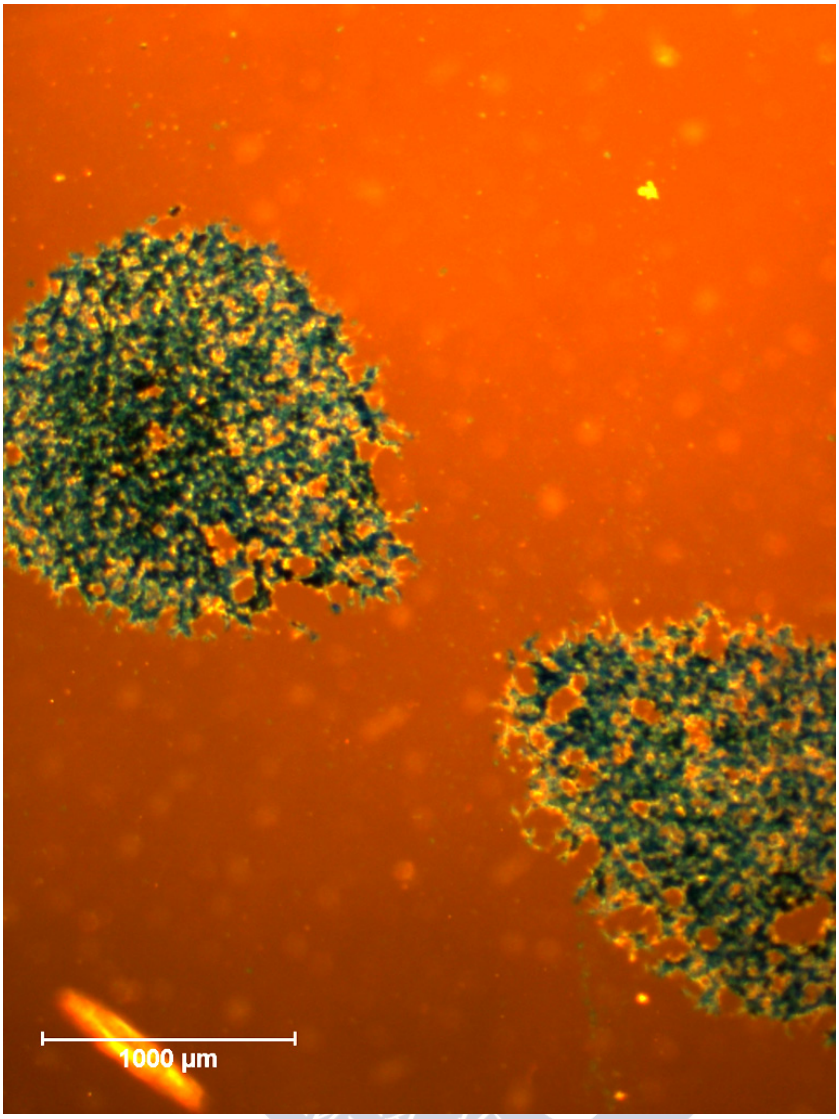


Figure 124: Optical image of dextran-labeled mesenchymal stem cells after 2D vectorization stained with Prussian Blue. Two magnets were placed below the Petri-dish close enough to observe their attraction on the distribution of the attached cells.

Figure 125: MR $T_2$ weighted image of one brain slice of a Wistar rat 7 days after the onset of the cerebral ischemia. Black and white ring inhomogeneities were observed at the last part of the internal carotid artery. $T_2$* weighted image and MR angiography of this animal is shown in Figure 126 and Figure 127 respectively.

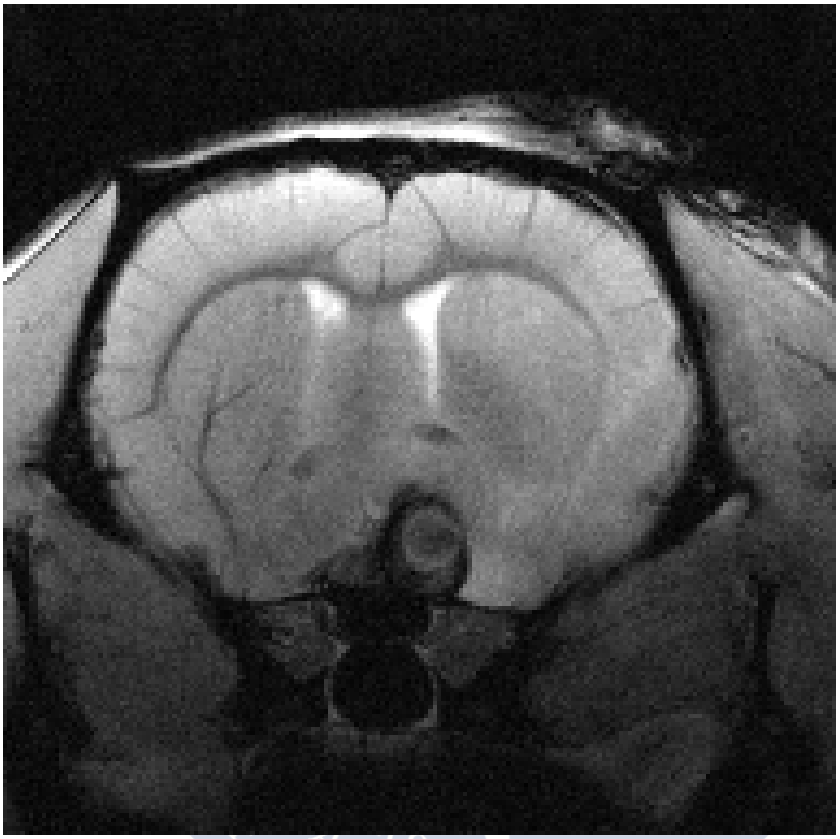

Figure 126: MR $T_2$* weighted image of one brain slice of a Wistar rat 7 days after the onset of the cerebral ischemia. White density surrounded by a black ring was observed at the last part of the internal carotid artery. Hemorrhagic event was discarded due to the white density observed. MR angiography of this animal is shown in Figure 127.

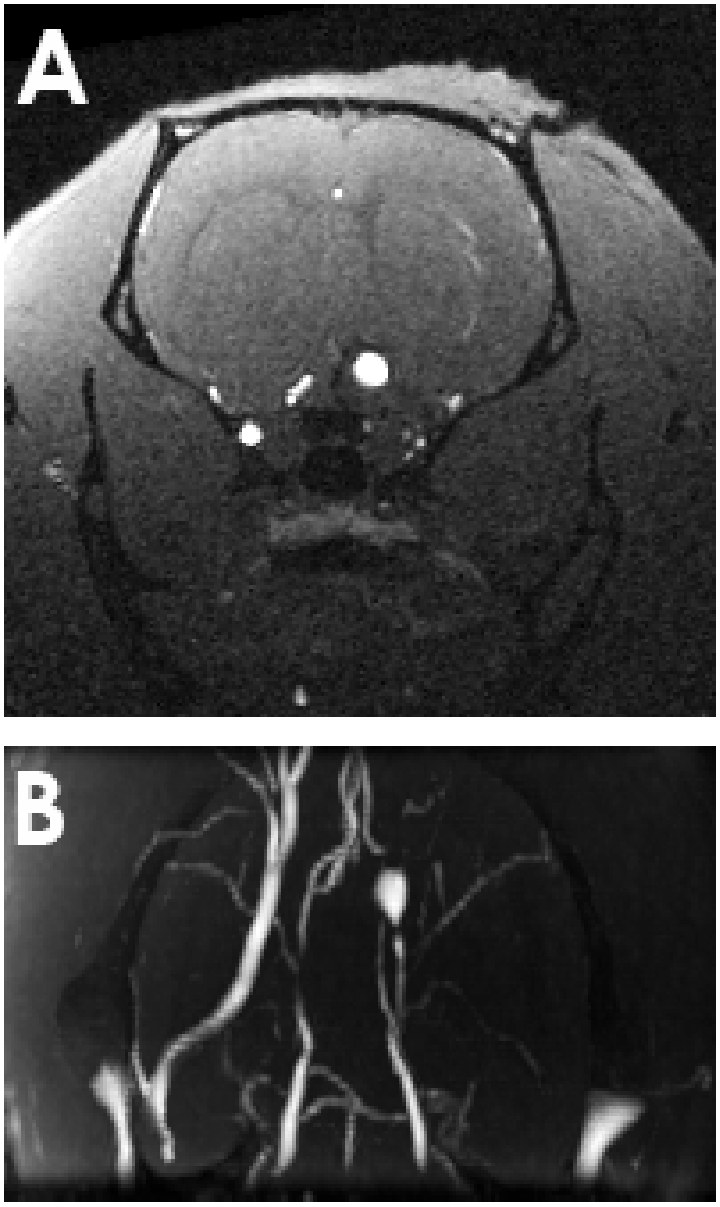


Figure 127: (A) Brain slice of MR angiography of one brain slice of a Wistar rat 7 days after the onset of the cerebral ischemia where it is possible to note that anterior cerebral artery is expanded. (B) Z-Projection of MR angiography where the aneurism can be observed.

Figure 128: MR $T_2$* weighted image of one brain slice of a Wistar rat 8h after the onset of the cerebral ischemia and 4h after the intra-arterial administration of $10^6$ Mesenchymal stem cells labeled with dextran coated superparamagnetic nanoparticles.

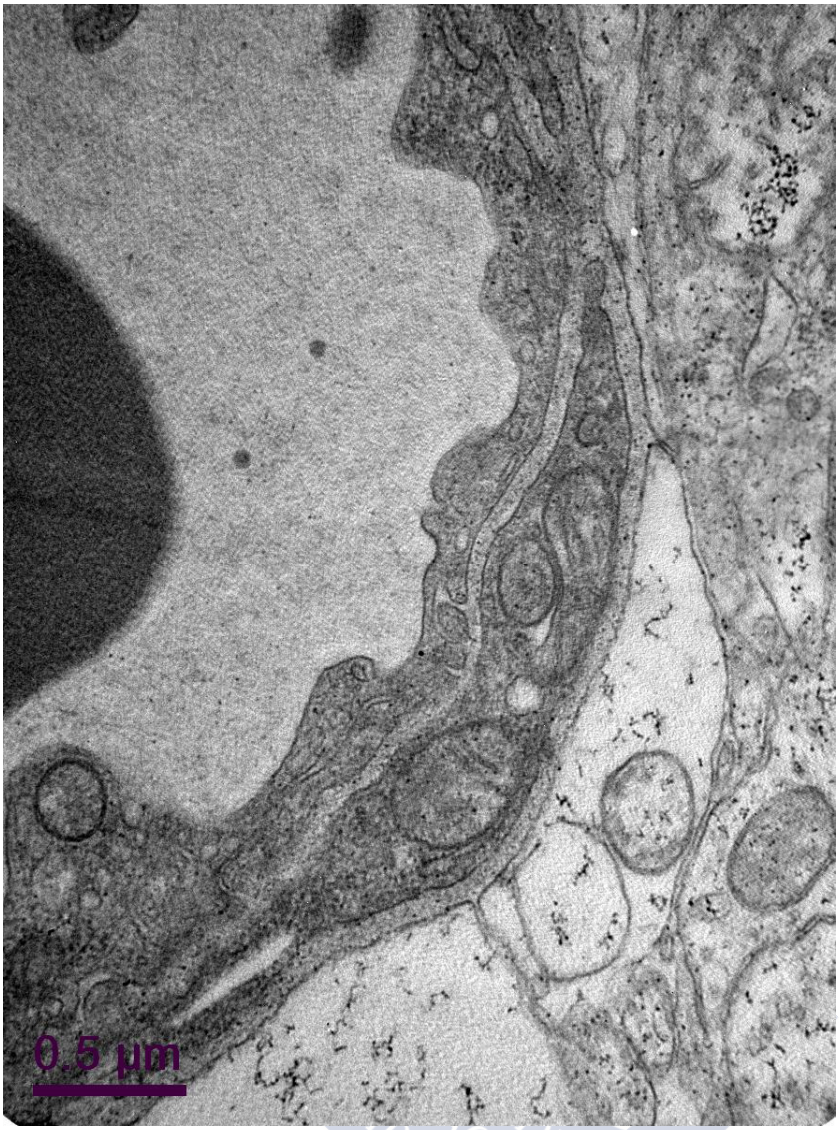


Figure 129: TEM micrograph of a brain capillary wall. (From the left to the right) Black shape corresponds to a red blood cell inside the vessel. The wall of the vessel is composed by endothelial cells, basal membrane, smooth muscle cells, basal membrane and astrocytic processes.

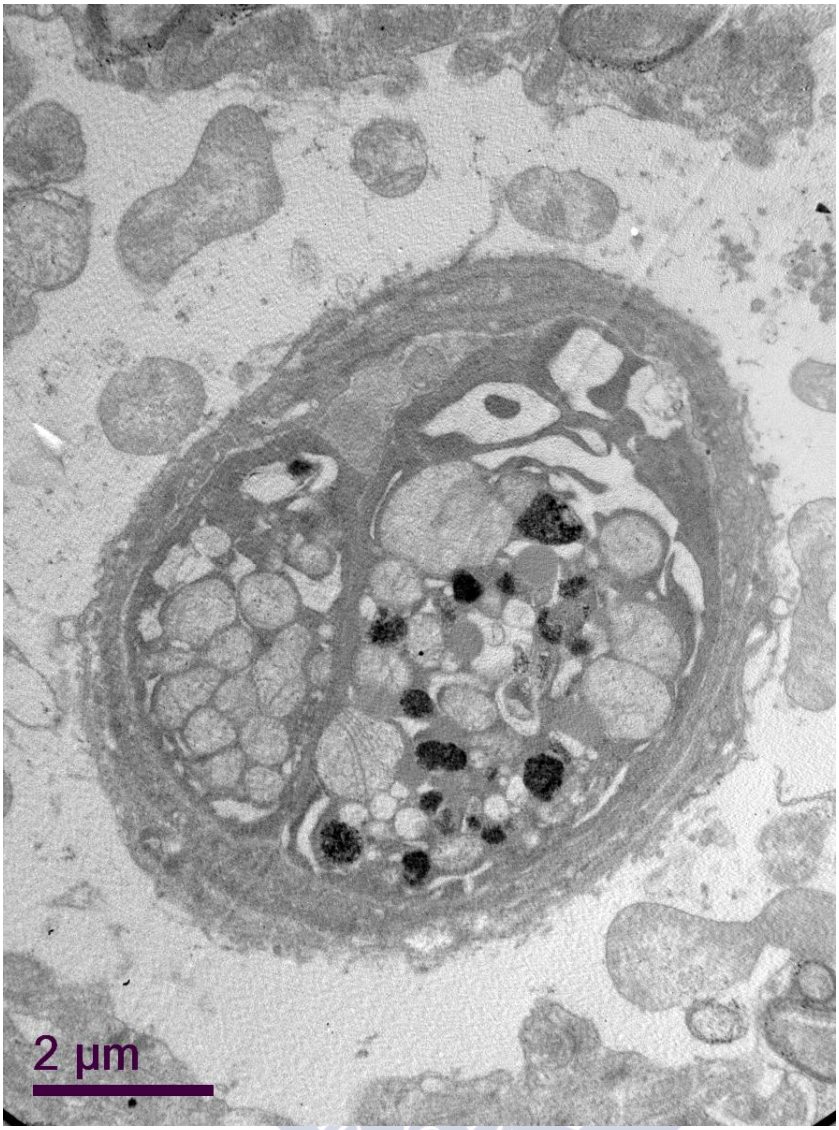


Figure 130: Two mesenchymal stem cells can be observed inside a capillary transversally observed by TEM micrograph. Their membranes allow its differentiation, and black hypointensities point out the nature of these cells.

USC
UNIVERSIDADE
DE SANTIAGO
DE COMPOSTELA

# Section IX

USC
UNIVERSIDADE
DE SANTIAGO
DE COMPOSTELA

# Summary

Cerebrovascular diseases are the second cause of death and the first cause of disability in developed countries. However, despite their social and economical importance, therapies for these diseases are quite limited. The most common etiology of stroke, ischemic stroke, consists in the reduction of blood flow in a brain area after the occlusion of a cerebral artery. This process triggers a series of events at molecular and cellular levels that leads to energy depletion in the affected area, yielding on a quick process of cell death by necrosis. This area is called the infarct core. The surrounding zone, usually called the ischemic penumbra but probably better defined as the peri-infarct area, it is constituted by hypo-perfused tissue. Here, blood flow is reduced to maintain electric activity, but cerebral tissue is still viable. This area is subjected to a wave of deleterious metabolic processes that propagate from the ischemic core to the neighboring tissue, including excitotoxicity, spreading depression, oxidative stress, and inflammatory response, all of them leading to the expansion of the ischemic core into the peri-infarct region, and subsequent worsening of the clinical outcome.

So far, pharmacological thrombolysis or mechanical reperfusion are the strategies that report higher benefits in the acute phase for the patients, in terms of neurological outcome, being the recombinant tissue plasminogen activator (rt-PA) the most common thrombolytic agent. However, only 3-7% of stroke patients are currently treated by these procedures due to the narrow therapeutic window (4.5h after the onset of the symptoms) and due to the risks associated to this pharmacological therapy. One of the most important associated risks is the high rate of

hemorrhagic events induced by the reperfusion of the arteries. The efficiency of neuropretective strategies during the acute phase of the stroke is conditioned by the maintenance of the blood brain barrier, fluid homeostasis and disabling free radicals after a reperfusion treatment. Thus, several therapies have emerged with a neuroprotective aim while others are based on their neurorepair possible approaches.

Neuroprotection is the term that includes all therapies aimed to reduce cell death after an ischemic process without influencing tissue reperfusion during the acute phase of the stroke. So far experimental studies of neuroprotective drugs have shown promising results, however they have failed once were applied in clinical trials.

On the other hand, neurorepair strategies have a wider therapeutic window than the acute phase of stroke. These strategies involve the restoration of brain function, either by regeneration of damaged cerebral tissue (neuroregeneration) or by the establishment of alternative neuronal pathways or synapses (brain plasticity). In this way, neurorepair therapies are not restricted to neurons, since the repair of the neurovascular unit includes also procedures focused in the enhancement of angiogenesis and synaptogenesis. Neurorepair treatments may include pro-neurogeinc, pro-angiogenic and pro-synaptogenic drug administration, but stem cell therapies as well.

Cell based therapies have emerged as a promissing approaches to conventional pharmacological treatments due to their multipotential action mechanisms. Integration in the host, immunomodulation processes or growth factors secretion are the possible ways of action, however

fundamental questions related to cell type, characterization and dosage, therapeutic timing versus toxicity or the relationship between biodistribution, fate and outcome must be elucidated. Several types of stem cells have demonstrated beneficial effects in preclinical studies of ischemic stroke, including Embrionic Stem cells (ESCs), Neural Stem Cells (NSCs), Induced Pluripotent Stem Cells (iPSCs) and Mesenchymal Stem Cells (MSCs) among others, and different administration time points and delivery routes have been studied.

MSCs are one of the best candidates for regenerative therapies, also in stroke, not only due to their multipotentiality, but mainly because of their ability of releasing growth factors and their immunomodulatory properties. Several mechanisms of action of these cells in the ischemic brain have been described, mechanisms like transdifferentiation into cells of neural lineage, induction of neurogenesis, angiogenesis, synaptogenesis, activation of endogenous restorative processes by producing cytokines and trophic factors, regulating the cerebral blood flow and the blood brain barrier and other neuroprotective mechanisms like the reduction of apoptosis, immflamation, demyelination and the increase of astrocyte survival. Moreover, several studies have reported functional recovery and infarct volume reduction after ischemic stroke following different administration routes of MSC delivery. A large number of preclinical and clinical trials have used systemic infusion of these cells, nevertheless it is still necessary to understand if transplanted MSCs can home to and engraft at ischemic and injured sites in the brain to exert their therapeutic effects. On one hand, brain intraparenquimal and intraventricular administration routes are invasive and it would be necessary several injection sites to cover the ischemic region. On the other hand, tail,

jugular or femoral intravenous administrations are less invasive but most of cells remain trapped in lungs, liver and spleen. In spite of this, intra-arterial administration route would be the best candidate to direct most of the injected cells to the brain, especially on the region of the ischemic injury. Some studies have shown that approximately 21% of the delivered cells after an intra-arterial injection were found in the ipsilateral hemisphere, while a recent study has reported that 24h after injection, 95% of the delivered cells were found in the spleen, however, administration procedures for intra-arterial delivery in these studies were different. Thus, due to the high variability reported in preclinical studies of stem cell therapy in animal models of ischemic stroke, the fate of the injected cells following the intra-arterial delivery route remains unknown.

Several imaging techniques combined with cellular labeling agents have been developed to monitor the fate of injected cells following different administration routes. However, for stem cell therapy the goal of imaging techniques is double. On one hand is crucial to determine where and when the cells are, but on the other hand imaging modality is also important to evaluate the pathological progress of the target organ as well. Nowadays, magnetic resonance imaging (MRI) is one of the most powerful medical diagnostic tools available due to the high resolution images, but also because of the non-invasive and no ionizing radiation nature of the technique. Moreover, MRI is the gold standard not only in the acute phase of the stroke; as well to evaluate the progression of the pathology. Nevertheless, administered cells are too small to be detectable in MRI. In order to overcome this limitation, the use of biocompatible contrast agents to label injected cells leads us to an *in vivo* real time monitoring of delivered cells without harmful side effects. Thus,

superparamagnetic nanoparticles (MNPs) are an excellent tool for stem cell labeling, not only for the high quality of the MRI image, for the low toxicity and the ease for tagging as well.

MNPs for biological applications are basically composed by a magnetic core of nanocrystalline magnetite or maghemite, which provides MRI signal, and this core is wrapped with a polymeric coating, which not only gives colloidal stability and protects the core from degradation, but will condition the future biological application as well. Particularly, MNPs for cell tracking must be specific of the studied type of cell, detectable at low concentrations, reasonable clearing period, stable and the associated toxicity must be low. In addition to these tagging properties, cells labeled with MNPs could be guided by using external magnetic fields due to the magnetic nature of the core of these contrast agents, enabling not only the detection, but the vectorization of the stem cell therapy as well.

Overall, in this work we have hypothesized that it is possible to synthesize biocompatible superparamagnetic nanoparticles for *in vivo* cell tracking. Superparamagnetic nanoparticles-tagged cells can be monitored *in vivo* by MRI and guided with magnetic fields without harmful effects, providing information of the cellular fate after different routes of administration. Moreover, the nanoparticle labeling will allow us to study therapeutic effects in an animal model of ischemic stroke based on the localization of the cells after delivery.

In order to synthesize biocompatible MNPs, coprecipitation method was used. The main advantages of coprecipitation procedure are the ease for the synthesis and the high amount of MNPs obtained. Thus three types of coated

superparamagnetic nanoparticles were synthesized and characterized in this study.

Dextran is one of the most widely polymers used as magnetic nanoparticle coating due to its reported biocompatibility. The synthesis of dextran coated MNPs (D-MNPs) was performed by following a *one step* procedure, i.e. the magnetite is formed under the presence of this polymer. The characterization of the dextran-coated superparamagnetic nanoparticles was performed attending to the magnetic core and to the coated MNP. On one hand, magnetic cores of synthesized D-MNPs have a spherical shape with a mean size of 3.7±0.8 nm measured by TEM and 4.8±0.5 nm measured with X-ray diffraction analysis (XRD), and with regard to the composition, the D-MNPs synthesized magnetic cores were found to be a combination of magnetite and maghemite as showed the lattice parameter measured by XRD (8.33±0.02 Å). The magnetic characterization of the D-MNPs reported that at 300K these MNPs exhibit superparamagnetic behavior. In addition, Fourier-transform infrared spectroscopy (FTIR) and thermal gravimetric analysis (TGA) reported the polymer absorption onto the surface of the MNPs, demonstrating that magnetic cores are wrapped by dextran coating. Moreover, the mean size of these coated MNPs measured by dynamic light scattering (DLS) was 94±3 nm and they are negatively charged -11±3 mV determined by Z-Potential. MR $T_2$-weighted images of D-MNPs phantoms were acquired, evidencing that dextran- coated superparamagnetic nanoparticles feasibility as contrast agents for MRI.

Apart from dextran, other polymers can be also used as MNPs coating. This is the case of the poloxamers and poloxamines, which their use have been approved by FDA

and EMEA for several applications in food, pharmaceutical and agricultural industries. Among all of them, Pluronic F127 and Tetronic 908 were also used in this work as MNPs coatings. The synthesis procedure for Pluronic F127- and Tetronic 908-coated superparamagnetic nanoparticles (P-MNPs and T-MNPs respectively) was a *two step* method. First, after the formation of the magnetic cores by following the coprecipitation method, a surrounding layer of oleic acid was created on the cores surface for further polymer anchoring. After this first step, magnetic core mean sizes were 8.6±1.4 nm determined by TEM, 7.7±0.8 nm measured by DLS and 7.7±0.8 nm by XRD. Moreover, XRD data have shown that magnetic cores are composed by magnetite and maghemite with an associated lattice parameter of 8.361±0.004 Å, and VSM data reported that MNPs exhibit superparamagnetic behavior at 300K. The second step for P-MNPs and T-MNPs synthesis was the polymer functionalization, FTIR and TGA data demonstrated the presence of oleic acid and polymers in each MNP formulation and P-MNPs mean size was 120±6 nm measured by DLS while T-MNPs was 154±6 nm. Both Z-Potentials were found negative, -18±3 mV for P-MNPs and -24±3 mV for T-MNPs. MR $T_2$-weighted images of P-MNPs and T-MNPs phantoms were acquired, evidencing the feasibility of Pluronic F127 and Tetronic 908- coated superparamagnetic nanoparticles as contrast agents for MRI.

Physicochemical characterization of D-MNPs, P-MNPs and T-MNPs suggested the suitability for being used as contrast agents for cell tracking in MRI. However, an *in vitro* study of cell labeling, biocompatibility and MRI signal detection was needed prior to *in vivo* cell tracking studies.

Several studies have reported the need of different techniques for an efficient cell tagging, and among all of

them transfect agents (TA) as poly-l-lysine (PLL) are the most used. Preliminary experiments using dextran-, Pluronic F127- and Tetronic 908- coated MNPs have shown that only D-MNPs needed PLL to tag cells, while P-MNPs and T-MNPs were internalized without the use of TA. Experimental data revealed that 1.5 μg/mL of PLL combined with D-MNPs ensured a full internalization of MNPs without harmful effects for the cells.

In order to study the biocompatibility and elucidate which was the best superparamagnetic nanoparticle for cell tagging, D-MNPs combined with PLL, P-MNPs and T-MNPs were evaluated *in vitro* by using rat MSCs and a mice multi-potent neural progenitor cell line C17.2. Several parameters as incubation time and MNPs concentration were also studied. The observed uptake mechanism for D-MNPs was different from P-MNPs and T-MNPs; the first one was conditioned by the concentration and incubation time, while for P-MNPs and T-MNPs the internalization depended mostly on the MNP concentration in the cell medium. MNPs influence on the cellular wellbeing depended on the internalized iron; thus proliferation and viability was reduced for those cells with more than 28 pg of iron/cell. Moreover, the combination of MRI and TEM techniques showed that MNPs were fully internalized, and MR $T_2$ and $T_2$* weighted images showed that labeled cells could be properly detected in MRI, providing promising results for further *in vivo* applications. Overall, considering the MNPs distribution in the cell, amount of internalized iron, proliferation and viability, D-MNPs were pointed as the best candidates for cell labeling.

However, the biocompatible study of D-MNPs with different types of cells was performed just after labeling. Prior to go into *in vivo* studies of cell tracking, a long term evaluation of

labeled cells and how the cellular proliferation rate influenced the MR signal was evaluated.

Because of the multi-potential abilities of MSCs and with the aim of a future stem cell therapy in an animal model of ischemic stroke, the long term biocompatibility study and the evaluation of the MRI signal clearance with the proliferation was performed in MSCs. Experimental results showed that labeled cells did not differ from control cells in terms of proliferation rate and viability after 5 days, as well as the maintenance of $CD45^-$, $CD90^+$ and $CD73^+$ cellular phenotype. Angiogenesis capacity was not altered by the presence of internalized D-MNPs, as well as vascular endothelial growth factor (VEGF) release measurements did not exhibit differences between control and labeled cells. Under the labeling conditions studied and for cell tracking applications, MRI can easily detect labeled cells in a phantom 3 days after being tagged. From then, MRI signal is affected by the clearance of the internalized D-MNPs due to proliferation, being only possible to detect MNPs loaded cells by ICP techniques.

In addition to MRI cell detection, dextran coated superparamagnetic nanoparticles could be combined with magnetic fields for enhancing targeted delivery of stem cells. In this work the *in vitro* efficacy of cellular magnetic vectorization in a liquid environment without harmful effects for future targeted delivery of stem cells has been demonstrated. However, in a non-liquid environment the use of external magnetic fields for labeled cell vectorization showed no cellular migration.

Overall, the in vitro validation of synthesized superparamagnetic nanoparticles suggest that MSCs loaded with D-MNPs were a promising tool for cell tracking

and cellular magnetic vectorization *in vivo* without cellular harmful effects.

In order to elucidate if labeled cells could be detected in vivo and to corroborate that MRI signal corresponded to labeled cells and not to free particles, the intraparenchymal injection was the best approach. Moreover, in addition to MNPs labeling, MSCs can be tagged also with CFSE, which let us not only *in vivo* cell tracking, *ex vivo* MSCs identification as well. In order to assess the efficiency of this double labeling, intraparenchymal injections for MSCs delivery were performed. Histology demonstrated that injected cells were still labeled with D-MNPs 4h after the injection and no particles were found outside of the cells assessed by CFSE and Prussian blue staining. Therefore, MRI *in vivo* signal corresponded to labeled MSCs and not to free particles.

Animal models of cerebral ischemia are designed to generate reproducible infarcts with a minimum of surgical manipulation; however therapeutic approaches have to be also optimized for each disease. Thus, optimal conditions for applying stem cell therapies for cerebral ischemia are still under discussion, fundamental questions related to cell type, characterization and dosage, administration route, therapeutic timing, toxicity, or the relationship between biodistribution, fate and outcome are still on the bench. Administration routes of labeled cells was a crucial parameter to take into account not only for cell tracking, but for stem cell therapy as well.

For intra-arterial delivery route, different combinations of animal models of ischemic stroke and intra-arterial administration routes of MSCs were studied. In order to elucidate which model was the most efficient and the

safest for an intra-arterial injection, MSCs labeled with D-MNPs were used. The optimization of the method for transient middle cerebral artery occlusion (tMCAO) and intra-arterial delivery of tagged cells was performed by using D-MNPs labeled MSCs. Thus, for an efficient intra-arterial delivery, after tMCAO surgery the common carotid artery must be perfused and also during and after the cell administration (that is performed through the external carotid artery) so the heart pumping would help on carrying the delivered cells to the brain territory.

These intra-arterial injected cells could be detected in the ischemic brain for more than 4h after injection, and their presence was not increased by the use of external magnetic fields, as magnetic vectorization. Moreover, the monitoring of cerebral blood flow (CBF) by transcranial laser Doppler was not enough to assess the safety of the intra-arterial delivery, and healthy animals injected with $2.5x10^5$ MSCs showed multifocal ischemic lesions 24h after the stem cell administration, evidencing that injected cells could be inducing focal ischemias.

Tracking of administered cells is important to understand the relationship between possible therapeutic mechanisms and cell localizations. Intraparenchymal injection is a feasible administration route, however it is not the preferred for stem cell delivery due to the high invasiveness of the technique. Less invasive routes for stem cell delivery are intravenous and intra-arterial injection. We have studied the fate after the injection of labeled cells through jugular vein and through the internal carotid artery and we have found important differences between them. On one hand, we have assessed by MRI and/or histochemistry techniques that cells injected through jugular vein were found in the lungs and no cells were detected in the brain, both in

healthy and ischemic animals. On the other hand, following the intra-arterial route we have demonstrated that, for ischemic or non-ischemic animals, injected MSCs were found in the brain and no cells can be detected in other organs, opening a big window for further stem cell therapy administration.

Because of the blood brain barrier integrity in healthy animals and its disruption in ischemic ones, we also studied the localization of the injected cells by immunohistochemistry techniques after an intra-arterial administration. By CD31 staining and CFSE labeling it was possible to assess that injected cells were found in small vessels along the brain while large ones do not express CFSE positive cells. This selective intra-vessel localization could explain the multifocal ischemias observed in ischemic and non-ischemic intra-arterial injected rats, however because it was necessary to perfuse de animal to perform immunohistochemistry, other technique for corroborating this result was studied.

Preliminary results of electron microscopy have shown that MSCs labeled with D-MNPs were able to migrate into brain parenchyma in a healthy animal after an intra-arterial delivery of one million cells. However, TEM images of same animal also revealed vessel occlusions with MSCs and fibrin reaction associated which could explain previous results of multifocal ischemias. Nevertheless, more studies of intra-arterial administration of D-MNPs labeled MSCs at different time points are needed for a better understanding of these mechanisms.

Thus, intra-arterial injection was found as the most efficient administration route for brain targeting, and also MSCs

delivered following intra-jugular injection resulted in cell entrapment in the lungs, with no cells reaching the brain.

Finally, MSCs were intra-arterially and intravenously delivered during the acute phase in a cerebral ischemia model to investigate whether the cell distribution, and therefore administration route may improve the therapeutic outcome. MRI studies, behavioral tests, histological examinations and blood serum determinations were performed to evaluate the therapeutic benefits of the treatment. Experimental results showed that only cells injected intra-arterially reached the brain and were detectable for 3 days after the delivery, guaranteeing the cellular proximity to the injury site. Under our experimental conditions and by using D-MNPs, we have assessed that the local effect of MSCs injected following intra-arterial route did not improve the outcome after a cerebral ischemia compared to a systemic administration following the intravenous route.

In summary, we have synthesized biocompatible superparamagnetic nanoparticles for *in vivo* cell tracking. Superparamagnetic nanoparticles-tagged mesenchymal stem cells can be monitored *in vivo* by MRI without harmful effects, providing information of the cellular fate after different routes of administration. Moreover, the nanoparticle labeling allowed us the study of therapeutic effects in an animal model of ischemic stroke based on the localization of the cells after delivery.

USC
UNIVERSIDADE
DE SANTIAGO
DE COMPOSTELA

# Resumen

Las enfermedades cerebrovsculares son la segunda causa de muerte y la primera de discapacidad en países desarrollados. Sin embardo, a pesar de su importancia socio-económica, las terapias disponibles son limitadas. La etiología más frecuente del ictus, el ictus isquémico, consiste en la reducción localizada del flujo cerebral tras la oclusión de una arteria cerebral. Este proceso desencadena una serie de eventos a nivel molecular y celular que culminan con un fallo energético en el área afectada, seguida de un proceso de muerte celular por necrosis. Esta área recibe el nombre de *core* isquémico. La región circundante, llamada penumbra isquémica pero normalmente definida como región peri-infarto, está constituida por tejido hipoperfundido. En esa región el flujo cerebral se encuentra reducido para mantener la actividad eléctrica, pero el tejido es todavía viable si se establece el flujo cerebral. Esta área se encuentra además sometida a una serie de procesos metabólicos que se propagan desde el core isquémico al tejido circundante, incluyendo procesos de exitotoxicidad, estrés oxidativo, respuesta inflamatoria, condicionando el pronóstico clínico.

La trombolisis farmacológica o la reperfusión mecánica son las estrategias que reportan mejores beneficios a los pacientes, en términos de pronóstico neurológico, siendo el activador tisular del plasminógeno recombinante (rt-PA) el más común de todos ellos. Sin embargo, solo entre el 3 y el 7% de los pacientes con un ictus pueden beneficiarse de esta terapia debido principalmente la estrecha ventana terapéutica de aplicación (4.5h tras el comienzo de los síntomas) y también debido a los riesgos asociados a esta

terapia farmacológica. Uno de los riesgos más relevantes es el alto grado de transformación hemorrágica inducida por la reperfusión de las arterias. Así, el mantenimiento de la barrera hematoencefálica, la homeostasis de los fluidos, y el bloqueo de los radicales libres tras el tratamiento de reperfusión constituyen algunas de las principales estrategias neuroprotectoras durante la fase aguda del ictus.

La neuroprotección es un término que incluye a todas las terapias dirigidas a reducir la muerte celular tras un proceso isquémico sin ejercer ningún tipo de influencia en la reperfusión del tejido durante la fase aguda del ictus. Hasta ahora, algunos fármacos han mostrado resultados prometedores en estudios experimentales, pero una vez trasladados a ensayos clínicos no han demostrado su eficacia.

Por otro lado, las estrategias neurorreparadoras cuentan con una ventana terapéutica mayor que la fase aguda del ictus. Estas estrategias incluyen la restauración de la función cerebral, ya sea bien por regeneración del tejido cerebral dañado (neurorregeneración) o bien por la creación de nuevas conexiones neuronales o sinapsis (plasticidad cerebral). De esta forma, las terapias de neurorreparación no están exclusivamente dirigidas a neuronas, ya que la restauración de la unidad neurovascular incluye también procedimientos enfocados a la potenciación del a angiogénesis y sinaptogénesis. Los tratamientos neurorreparativos incluyen pues la formación de nuevas neuronas, sinapsis, y vasos, ya sea por la aplicación de nuevas terapias farmacológicas o bien por tratamiento con células madre.

La terapia celular ha surgido como una estrategia prometedora frente a tratamientos farmacológicos convencionales debido a sus múltiples y potenciales mecanismos de acción, entre los cuales se han destacado la integración de las células administradas en los tejidos, procesos de inmunomodulación o secreción de factores de crecimiento. Sin embargo, otros aspectos como el tipo celular, dosis, ventana terapéutica, toxicidad o la relación entre biodistribución y pronóstico deben ser todavía estudiadas en profundidad. En cuanto a la estirpe celular, varios tipos celulares han demostrado efectos beneficiosos en estudios preclínicos de isquemia cerebral, incluyendo células madre embrionarias, células madre neurales, células madre pluripotentes inducidas y células madre mesenquimales (MSCs) entre otras. En numerosos estudios también se han evaluado diferentes tiempos y rutas de administración con prometedores resultados.

Las MSCs han sido descritas como son unas de las candidatas favoritas para terapias regenerativas no sólo en el campo de la isquemia cerebral. Esto se debe no sólo a que son multipotentes, sino también a sus capacidades inmunomoduladoras y de secreción de factores de crecimiento. En los últimos años se han descrito varios mecanismos de acción de esas células en el cerebro isquémico, como su diferenciación a células de estirpe neural, inducción de la neurogénesis, angiogénesis, sinaptogénesis, activación de procesos endógenos, regulación del flujo sanguíneo cerebral, y otros mecanismos neuroprotectores como la reducción de la apoptosis, de la inflamación o incremento de la supervivencia astrocitaria, entre otros. Además, algunos estudios preclínicos en roedores han encontrado recuperación funcional y reducción del volumen de infarto siguiendo diversas rutas de administración de éstas células.

Aunque la administración sistémica es la preferida para la mayoría de estos ensayos *in vivo* con células madre hasta el momento, no está claro todavía si las células administradas van a ejercer su efecto terapéutico desde el cerebro o desde otra parte del cuerpo.

Las inyecciones intraparenquimal e intraventricular aseguran una localización cerebral de las células inyectadas, pero esta técnica es altamente invasiva y requeriría de múltiples inyecciones para abarcar la lesión isquémica. Siguiendo rutas de administración sistémicas y por tanto menos invasivas, en diversos estudios se ha observado que la mayoría de las células administradas intravenosas en cola, yugular o vena femoral se han encontrado en pulmones, hígado o bazo, y muy pocos estudios apuntan a una migración cerebral. Por otro lado, la inyección intra-arterial está descrita como la mejor vía para dirigir células al cerebro, especialmente a la región isquémica. Algunos trabajos han demostrado que aproximadamente un 21% de las células administradas intra-arterialmente fueron halladas en el hemisferio ipsilateral, mientras que un estudio más reciente ha observado que 24h tras la administración, el 95% de las células inyectadas se encontraban en el bazo; esta variedad de resultados podría residir en que los procedimientos de administración celular intra-arterial son diferentes entre estudios. Así, todavía se necesitan más trabajos de seguimiento tras la administración intra-arterial de células madre en modelos animales de ictus isquémico.

Para estudiar la biodistribución, se han desarrollado varias técnicas de imagen combinadas con marcajes celulares específicos siguiendo distintas rutas de administración. Estas técnicas aplicadas a terapia celular tienen un papel doble; el de seguimiento celular tras la inyección en tiempo real, y

el de evaluación de la progresión de la patología. Hoy en día, la resonancia magnética nuclear (RMN) es una de las mejores herramientas de diagnóstico disponibles, no solo por la alta resolución de sus imágenes, sino también por su carácter no invasivo y radiación no ionizante. Además, la RMN es el *gold standard* no sólo en la fase aguda del ictus, sino también como herramienta para evaluar la progresión de la enfermedad. Sin embargo, las células inyectadas son demasiado pequeñas para poder ser visualizadas por RMN. Para su detección y estudio es necesario el uso de agentes de contraste que marquen esas células y que permitan una monitorización en tiempo real de las células administradas sin efectos colaterales, tanto para las células como para el paciente. En esta línea, las nanopartículas superparamagnéticas (MNPs) son una herramienta idónea para marcaje celular, no sólo por el alto contraste que generan en RMN, sino también por la reducida toxicidad y sencillez en el proceso de marcaje.

Las MNPs para aplicaciones biológicas están compuestas básicamente por un núcleo de magnetita o maghemita, que proporciona la señal en RMN, el cual está rodeado por una cubierta normalmente polimérica, que no sólo proporciona estabilidad coloidal, sino que también lo protege de la degradación y condiciona las futuras aplicaciones biomédicas. Las nanopartículas destinadas al seguimiento celular por RMN han de tener ciertas características especiales, como ser específicas para cada tipo celular, detectables a concentraciones bajas, estables y de toxicidad reducida. Además de esas propiedades de seguimiento, las células marcadas con MNPs poseen también propiedades de vectorización magnética, es decir, pueden ser guiadas mediante campos magnéticos externos debido a la naturaleza magnética del núcleo de

las MNPs, posibilitando no sólo la detección celular por RMN sino también la vectorización de la terapia celular.

Así, la hipótesis de este trabajo se basó en la síntesis de nanopartículas superparamagnéticas biocompatibles para seguimiento celular *in vivo*. Las células marcadas con estas nanopartículas superparamagnéticas pueden ser monitorizadas *in vivo* por técnicas de RMN y guiadas mediante campos magnéticos externos sin dañar a las células y proporcionando información de la biodistribución celular siguiendo distintas rutas de administración. Además, este marcaje nos permitirá el estudio de los efectos terapéuticos en un modelo animal de isquemia cerebral dependiendo de la localización de las células tras la administración.

La síntesis de MNPs biocompatibles se llevó a cabo mediante el procedimiento de coprecipitación química. Es un método simple que proporciona gran cantidad de nanopartículas en pocos pasos. En este trabajo se sintetizaron 3 tipos de nanopartículas con distintos recubrimientos poliméricos.

El dextrano es uno de los polímeros más utilizados como recubrimiento de nanopartículas debido a su alta biocompatibilidad. La síntesis de nanopartículas recubiertas de dextrano (D-MNPs) se llevó a cabo mediante un procedimiento de un solo paso (*one step)*, donde la magnetita se forma en presencia del polímero. Según la técnica empleada, ha sido posible la caracterización independiente de los núcleos y del conjunto núcleo y recubrimiento. Por un lado, los núcleos presentaron una morfología esférica con un tamaño medio de 3.7±0.8 nm medido mediante TEM y 4.8±0.5 nm medido por X-ray diffraction analysis (XRD). La composición de los núcleos

fue una mezcla de magnetita y maghemita, como muestra el *lattice parameter* medido por XRD (8.33±0.02 Å). La caracterización magnética de las D-MNPs ha puesto de manifiesto que a 300K el comportamiento es superparamagnetico. Además, los resultados obtenidos por Fourier-transform infrared spectroscopy (FTIR) y thermal gravimetric analysis (TGA) han mostrado que el polímero se encuentra en la superficie de las MNPs, demostrando que los núcleos están envueltos por una cubierta de dextrano. Los tamaños medios de las nanopartículas recubiertas medidos por dynamic light scattering (DLS) fueron 94±3 nm and y estaban cargadas negativamente (-11±3) mV. Y en último lugar, las imágenes de RMN con peso $T_2$ de los phantoms de D-MNPs demostraron que estas nanopartículas podían ser usadas como agentes de contraste de resonancia magnética nuclear.

Además del dextrano, otros polímeros pueden ser usados como recubrimiento de MNPs. Es el caso de los poloxamers y poloxamines, cuyo uso ha sido aprobado por la FDA y EMEA para diversas aplicaciones en comida, e industrias farmacéutica y agrícola. Entre todos ellos, el Pluronic F127 y el Tetronic 908 fueron los elegidos como cubiertas poliméricas en este trabajo. El procedimiento de síntesis para Pluronic F127 y Tetronic 908 (P-MNPs and T-MNPs respectivamente) es un método de dos etapas *(two step)*. Primero, y tras la formación de los núcleos magnéticos siguiendo el proceso de coprecipitación química, se creó una capa de ácido oleico en la superficie del núcleo que fué posteriormente utilizada para anclaje polimérico. Tras este primer paso, el tamaño medio de los núcleos recubiertos de ácido oleico fue 8.6±1.4 nm determinado mediante TEM, 7.7±0.8 nm determinado mediante DLS y 7.7±0.8 nm medido por XRD. Además, los núcleos están compuestos por una mezcla de magnetita/maghemita tal

como muestra el *lattice parameter*, 8.361±0.004 Å, y los resultados de VSM muestran que el comportamiento de estas nanopartículas a 300K es superparamagnético. El segundo paso en la síntesis de estas nanopartículas fue la funcionalización de su superficie con una cubierta polimérica de Pluronic F127 y Tetronic 908. Los resultados experimentales de FTIR and TGA demostraron la presencia de ácido oleico y polímero en cada formulación de MNPs, y que el tamaño medio de P-MNPs fue 120±6 nm determinado por DLS mientras que para T-MNPs fue 154±6 nm. Ambos potenciales Z fueron negativos y de valor medio -18±3 mV para P-MNPs y -24±3 mV para T-MNPs, y las imágenes de resonancia con peso $T_2$ de ambos tipos de nanopartículas corroboraron su futura aplicación como agentes de contraste para RMN.

La caracterización fisicoquímica de las D-MNPs, P-MNPs y T-MNPs han puesto de manifiesto las grandes capacidades de estas nanopartículas como agentes de contraste para seguimiento celular por RMN. Sin embargo, fue necesario el estudio *in vitro* de biocompatibilidad, marcaje celular y detección por RMN antes de pasar a estudios de seguimiento *in vivo*.

Para mejorar la eficiencia de transfección con nanopartículas, diversos estudios han publicado la necesidad de diferentes técnicas, y entre todos ellos el uso de agentes transfectantes como la poly-L-lysine (PLL) son los más utilizados. Experimentos preliminares en cultivos celulares con D-MNPs, P-MNPs y T-MNPs han puesto de manifiesto que sólo fue necesario el uso de PLL para el marcaje con D-MNPs, mientras que las células incubadas con P-MNPs y T-MNPs internalizaron directamente estas nanopartículas. Así, es necesaria la utilización de 1.5 µg/mL PLL para una internalización completa de D-MNPS.

Con el fin de estudiar la biocompatibilidad y verificar cuál es la nanopartículas superparamagnética más idónea para marcaje celular, se llevaron a cabo experimentos de marcaje con dos tipos celulares, MSCs de rata y multi-potent neural progenitor cell line C17.2 de ratón y con los 3 tipos de MNPs, D-MNPs combinadas con PLL, P-MNPs y T-MNPs. También se estudiaron varios parámetros como el tiempo de incubación y la concentración de nanopartículas en el medio. El mecanismo de inclusión observado para las D-MNPs fue diferente del de P-MNPs y T-MNPs; en el primero la captación de MNPs está mayormente condicionada por la concentración y el tiempo de incubación, mientras que para P-MNPs y T-MNPs la internalización depende en mayor medida de la concentración de nanopartículas en el medio. En cualquier caso, solo aquellas células que internalizaron más de 28 pg de hierro/célula expresaron proliferación y viabilidad reducidas. La combinación de imágenes de TEM y RMN ha verificado que todas las nanopartículas están internalizadas en el citoplasma celular, y que por tanto, la señal observada por RMN se corresponde con MNPs intracelulares. Además, las imágenes de RMN con peso $T_2$ y $T_2$* mostraron que las células marcadas pueden ser detectadas fácilmente por RMN, proporcionando resultados prometedores para futuros experimentos preclínicos. Así, a la vista de estos resultados de distribución de MNPs en las células, proliferación y viabilidad, las D-MNPs fueron seleccionadas como las mejores candidatas para marcaje celular.

Sin embargo, la evaluación de la biocompatibilidad de D-MNPs con distintos tipos de células ha sido llevada a cabo inmediatamente tras el marcaje celular. Así, y antes de aplicar su uso *in vivo* fue necesario un estudio a más largo plazo que asegure la viabilidad celular y que además

proporcione información de la evolución de la señal de RMN con la proliferación celular.

Considerando una futura terapia celular en un modelo animal de isquemia cerebral, y debido a sus múltiples capacidades regenerativas, el estudio *in vitro* de biocompatibilidad celular y de evolución de señal de RMN a largo plazo se llevó a cabo en MSCs. Su seguimiento a largo plazo (5 días tras la internalización de las MNPs) fue condicionado por la señal en RMN ya que el fin último de las D-MNPs es seguimiento celular por RMN.

Los resultados experimentales mostraron iguales valores de proliferación y viabilidad de las células marcadas con D-MNPs y las no marcadas tras 5 días de seguimiento, al igual que se mantuvo inalterada la expresión de marcadores de MSCs como $CD45^-$, $CD90^+$ and $CD73^+$. La capacidad angiogénica no se encontró alterada en aquellas células que estaban marcadas, al igual que la secreción de *vascular endothelial growth factor (VEGF)*. Considerando las condiciones de marcaje estudiadas y para aplicaciones de seguimiento celular, fue posible detectar por RMN en un phantom células que han sido marcadas hasta 3 días tras el marcaje. A partir del tercer día no fue posible detectar por RMN estas células ya que la cantidad de MNPs/célula se ha reducido debido a la proliferación celular, aunque los valores de ICP demostraron que todavía había nanopartículas internalizadas.

Además de la detección por RMN, las D-MNPs combinadas con campos magnéticos externos podrían incrementar la presencia de MSCs en ciertas regiones de interés, como podría ser el cerebro en patología isquémica cerebral. Dos aproximaciones de vectorización magnética de MSCs marcadas con D-MNPs fueron estudiadas en este trabajo;

por un lado se estudió la vectorización en un entorno líquido, demostrando que esta aproximación es no sólo posible sino que no afecta a la viabilidad celular, y por otro lado, la vectorización magnética fue también evaluada en un entorno tridimensional, usando Matrigel como soporte. En este último caso no se observó migración celular.

En general, la validación in vitro llevada a cabo sugirió que las MSCs marcadas con D-MNPs son una herramienta prometedora en el campo del seguimiento celular por RMN y para la vectorización magnética *in vivo* sin daños asociados a las células marcadas.

Para corroborar que las células administradas pueden ser detectadas *in vivo,* y que la señal de RMN se corresponde a células marcadas y no a nanopartículas libres, se llevaron a cabo inyecciones intraparenquimales en rata sana. Las células administradas se marcaron con D-MNPs y también con CFSE, una sonda fluorescente que permitirá la identificación histológica de las células inyectadas. Así, los estudios histológicos con tinción de Prussian Blue y CFSE demostraron que las nanopartículas seguían internalizadas en las células, y que no se observaron nanopartículas libres, con lo que la señal de RMN observada *in vivo* se correspondió exclusivamente a células marcadas.

Para llevar a cabo estudios fiables preclínicos de ictus isquémico se necesita un modelo animal de isquemia cerebral que proporcione lesiones isquémicas reproducibles y cuya cirugía sea mínimamente invasiva. Sin embargo también es necesaria la optimización de las estrategias terapéuticas para cada patología. Así, las condiciones óptimas para terapia celular en la isquemia cerebral todavía no han sido establecidas. La ruta de administración es un parámetro crucial, no sólo para

estudiar la biodistribución celular, sino también para el estudio de los mecanismos involucrados en la terapia celular.

La administración intra-arterial está íntimamente relacionada con el modelo animal de ictus isquémico. La optimización del modelo de isquemia cerebral y de inyección celular se llevó a cabo atendiendo a la seguridad y a la eficiencia de la administración y mediante el uso de MSCs marcadas con D-MNPs. Así, y tras varias configuraciones de las cirugías se observó que tras la oclusión transitoria de la arteria cerebral media (tMCAO), es necesario reperfundir la arteria común carótida, y que ésta también ha de permanecer abierta durante la administración de las MSCs (que se hace a través de la arteria carótida externa), para que la sangre procedente del corazón colabore en el transporte estas células al cerebro. Las células administradas intra-arterialmente pudieron ser detectadas en el cerebro isquémico durante más de 4h tras la inyección.

Además, la vectorización magnetica llevada a cabo con un imán de 1T demostró no incrementar la presencia de MSCs marcadas con D-MNPs en el cerebro, desde el punto de vista macroscópico de imagen por RMN. Lo que sí se observó fue que la administración intra-arterial de $2.5x10^5$ MSCs en animales sanos cuyo flujo cerebral fue monitorizado con laser doppler transcraneal produjo isquemias multifocales 24h tras la administración, evidenciando que las mediciones por laser Doppler no son suficientes para asegurar el mantenimiento del flujo cerebral.

El seguimiento celular es crucial para estudiar la relación entre localización celular y posibles mecanismos

terapéuticos. Las inyecciones intraparenquimales han sido utilizadas al comienzo de la aplicación de la terapia celular, sin embargo su carácter altamente invasivo hace que poco a poco haya caído en desuso. La administración intra-arterial e intravenosa son técnicas menos invasivas y por tanto más atractivas para terapia celular, y en este trabajo se ha estudiado la biodistribución de MSCs marcadas con D-MNPs siguiendo estas vías por RMN y/o técnicas histoquímicas. Así, se observó que las células administradas en animales sanos e isquémicos a través de la vena yugular se encontraban en los pulmones y no en el cerebro, mientras que tras una administración intra-arterial sólo se detectaron células en el cerebro y no en otros órganos. Estos resultados han abierto una vía de estudio que relacione la función terapéutica frente a localización de las células madre administradas.

Además, se ha estudiado histológicamente mediante el marcaje de vasos con CD31 y el marcaje de CFSE de las MSCs administradas, la localización de las células inyectadas intra-arterialmente debido a las diferencias en integridad de la barrera hematoencefálica de animales sanos e isquémicos. Estos estudios mostraron que las células administradas se encontraban en pequeños vasos, mientras que vasos de mayor calibre no mostraron células. Esta presencia selectiva de pequeños vasos podría explicar las isquemias multifocales observadas en animales sanos e isquémicos tras la administración celular, sin embargo dado que para llevar a cabo estos estudios histológicos fue preciso perfundir el animal, sería adecuado utilizar otra técnica que confirmase estos resultados.

Los primeros resultados de microscopía electrónica muestran que las MSCs marcadas con D-MNPs pueden migrar al parénquima cerebral en un animal sano tras una

administración intra-arterial de $10^6$ de células. Sin embargo, imágenes de TEM del mismo animal en otra región cerebral evidenciaron una oclusión en un capilar producida por las MSCs administradas y donde también se observó una reacción de fibrina, lo cual explicaría así las isquemias multifocales observadas en este trabajo con otras técnicas. Estos resultados de TEM no son concluyentes, pues se necesitaría evaluar la migración en más animales y estudiar el perfil temporal de migración y/o oclusión tras la administración.

Finalmente, se estudió las capacidades terapéuticas de las MSCs administradas intravenosas e intra-arteriales, y por tanto, la influencia de la distribución celular en la mejora tras la isquemia cerebral en un modelo animal. Para determinar los efectos beneficiosos de esta terapia se llevaron a cabo estudios de RMN, test de comportamiento, análisis histológico, y determinaciones en suero sanguíneo. Los resultados experimentales de seguimiento celular mostraron que sólo las células inyectadas intra-arterialmente fueron detectadas en el cerebro del animal durante los 3 días siguientes a su administración. Además, bajo las condiciones experimentales utilizadas en este estudio y mediante el marcaje con D-MNPs, los animales tratados con MSCs administradas intra-arterialmente no mejoraron significativamente respecto de los tratados con MSCs administradas intravenosamente.

En resumen, hemos sintetizado nanopartículas superparamagneticas biocompatibles para seguimiento celular *in vivo*. Las células madre mesenquimales marcadas con estas nanopartículas superparamagneticas pueden ser monitorizadas in vivo por resonancia magnética nuclear sin afectar a su viabilidad, proporcionando información de la biodistribución celular tras ser administradas siguiendo

distintas vías de administración. Además, el marcaje celular nos ha permitido el estudio de los efectos terapéuticos en un modelo animal de ictus isquémico basándonos en la localización de las células tras la administración.

USC
UNIVERSIDADE
DE SANTIAGO
DE COMPOSTELA

# Section X
# Bibliography

1. (1988) The World Health Organization MONICA Project (monitoring trends and determinants in cardiovascular disease): a major international collaboration. WHO MONICA Project Principal Investigators. J Clin Epidemiol 41: 105-114.

2. Rodríguez-Yáñez M, Fernández Maiztegui C, Pérez-Concha T, Castillo J, Zarranz J (2008) Enfermedades vasculares cerebrales. Neurología. Cuarta Edición ed. Madrid, España: Elsevier España. pp. 337-411.

3. Arboix A, Díaz J, Pérez-Sempere A, Álvarez-Sabín J (2002) Ictus: Tipos etiológicos y criterios diagnósticos. Rev Neurol 17: 3-12.

4. Arias-Rivas S, Vivancos-Mora J, Castillo J (2012) Epidemiología de los subtipos de ictus en pacientes hospitalizados atendidos por neurólogos: resultados del registro EPICES (I). Rev Neurol 54: 385-393.

5. Del Zoppo GJ, Saver JL, Jauch EC, Adams HP, Jr., American Heart Association Stroke C (2009) Expansion of the time window for treatment of acute ischemic stroke with intravenous tissue plasminogen activator: a science advisory from the American Heart Association/American Stroke Association. Stroke 40: 2945-2948.

6. Adams HP, Jr., Bendixen BH, Kappelle LJ, Biller J, Love BB, et al. (1993) Classification of subtype of acute ischemic stroke. Definitions for use in a multicenter clinical trial. TOAST. Trial of Org 10172 in Acute Stroke Treatment. Stroke 24: 35-41.

7. Feinberg WM, Albers GW, Barnett HJ, Biller J, Caplan LR, et al. (1994) Guidelines for the management of transient ischemic attacks. From the Ad Hoc Committee on Guidelines for the Management of Transient Ischemic Attacks of the Stroke Council of the American Heart Association. Circulation 89: 2950-2965.

8. Castillo J (2000) Fisiopatología de la isquemia cerebral. Rev Neurol 30: 459-464.

9. Back T (1998) Pathophysiology of the ischemic penumbra--revision of a concept. Cell Mol Neurobiol 18: 621-638.

10. Astrup J, Symon L, Branston NM, Lassen NA (1977) Cortical evoked potential and extracellular K+ and H+ at critical levels of brain ischemia. Stroke 8: 51-57.

11. Hansen AJ (1985) Effect of anoxia on ion distribution in the brain. Physiol Rev 65: 101-148.

12. Blank WF, Jr., Kirshner HS (1977) The kinetics of extracellular potassium changes during hypoxia and anoxia in the cat cerebral cortex. Brain Res 123: 113-124.

13. Choi DW (1987) Ionic dependence of glutamate neurotoxicity. J Neurosci 7: 369-379.

14. Choi DW, Rothman SM (1990) The role of glutamate neurotoxicity in hypoxic-ischemic neuronal death. Annu Rev Neurosci 13: 171-182.

15. White BC, Sullivan JM, DeGracia DJ, O'Neil BJ, Neumar RW, et al. (2000) Brain ischemia and reperfusion: molecular mechanisms of neuronal injury. J Neurol Sci 179: 1-33.

16. Choi DW (1992) Excitotoxic cell death. J Neurobiol 23: 1261-1276.

17. Schiene K, Bruehl C, Zilles K, Qu M, Hagemann G, et al. (1996) Neuronal hyperexcitability and reduction of GABAA-receptor expression in the surround of cerebral photothrombosis. J Cereb Blood Flow Metab 16: 906-914.

18. Banasiak KJ, Xia Y, Haddad GG (2000) Mechanisms underlying hypoxia-induced neuronal apoptosis. Prog Neurobiol 62: 215-249.

19. Grandati M, Verrecchia C, Revaud ML, Allix M, Boulu RG, et al. (1997) Calcium-independent NO-synthase activity and nitrites/nitrates production in transient focal cerebral ischaemia in mice. Br J Pharmacol 122: 625-630.

20. Nogawa S, Zhang F, Ross ME, Iadecola C (1997) Cyclo-oxygenase-2 gene expression in neurons contributes to ischemic brain damage. J Neurosci 17: 2746-2755.

21. Akins PT, Liu PK, Hsu CY (1996) Immediate early gene expression in response to cerebral ischemia. Friend or foe? Stroke 27: 1682-1687.

22. Massa SM, Swanson RA, Sharp FR (1996) The stress gene response in brain. Cerebrovasc Brain Metab Rev 8: 95-158.

23. Koistinaho J, Hokfelt T (1997) Altered gene expression in brain ischemia. Neuroreport 8: i-viii.

24. Kovacs Z, Ikezaki K, Samoto K, Inamura T, Fukui M (1996) VEGF and flt. Expression time kinetics in rat brain infarct. Stroke 27: 1865-1872; discussion 1872-1863.

25. McDonald ES, Windebank AJ (2000) Mechanisms of neurotoxic injury and cell death. Neurol Clin 18: 525-540.

26. Jander S, Kraemer M, Schroeter M, Witte OW, Stoll G (1995) Lymphocytic infiltration and expression of intercellular adhesion molecule-1 in photochemically induced ischemia of the rat cortex. J Cereb Blood Flow Metab 15: 42-51.

27. Rami A, Agarwal R, Botez G, Winckler J (2000) mu-Calpain activation, DNA fragmentation, and synergistic effects of caspase and calpain inhibitors in protecting hippocampal neurons from ischemic damage. Brain Res 866: 299-312.

28. Hossmann KA (1994) Viability thresholds and the penumbra of focal ischemia. Ann Neurol 36: 557-565.

29. Hossmann KA (2008) Cerebral ischemia: models, methods and outcomes. Neuropharmacology 55: 257-270.

30. Ramos-Cabrer P, Campos F, Sobrino T, Castillo J (2011) Targeting the ischemic penumbra. Stroke 42: S7-11.

31. Lo EH (2008) A new penumbra: transitioning from injury into repair after stroke. Nat Med 14: 497-500.

32. Adams HP, Jr., del Zoppo G, Alberts MJ, Bhatt DL, Brass L, et al. (2007) Guidelines for the early management of adults with ischemic stroke: a guideline from the American Heart Association/American Stroke Association Stroke Council, Clinical Cardiology Council, Cardiovascular Radiology and Intervention Council, and the Atherosclerotic Peripheral Vascular Disease and Quality of Care Outcomes in Research Interdisciplinary Working Groups: The American Academy of Neurology affirms the value of this guideline as an educational tool for neurologists. Circulation 115: e478-534.

33. Dirks M, Niessen LW, van Wijngaarden JD, Koudstaal PJ, Franke CL, et al. (2011) Promoting thrombolysis in acute ischemic stroke. Stroke 42: 1325-1330.

34. Donnan GA, Davis SM, Parsons MW, Ma H, Dewey HM, et al. (2011) How to make better use of thrombolytic therapy in acute ischemic stroke. Nat Rev Neurol 7: 400-409.

35. Lees KR, Bluhmki E, von Kummer R, Brott TG, Toni D, et al. (2010) Time to treatment with intravenous alteplase and outcome in stroke: an updated pooled analysis of ECASS, ATLANTIS, NINDS, and EPITHET trials. Lancet 375: 1695-1703.

36. Wahlgren N, Ahmed N, Davalos A, Ford GA, Grond M, et al. (2007) Thrombolysis with alteplase for acute ischaemic stroke in the Safe Implementation of Thrombolysis in Stroke-Monitoring Study (SITS-MOST): an observational study. Lancet 369: 275-282.

37. Rodriguez-Yáñez M, Sobrino T, Arias S, Vazquez-Herrero F, Brea D, et al. (2011) Early biomarkers of clinical-diffusion mismatch in acute ischemic stroke. Stroke 42: 2813-2818.

38. Ginsberg MD (2009) Current status of neuroprotection for cerebral ischemia: synoptic overview. Stroke 40: S111-114.

39. Chen F, Qi Z, Luo Y, Hinchliffe T, Ding G, et al. (2014) Non-pharmaceutical therapies for stroke: Mechanisms and clinical implications. Prog Neurobiol.

40. Castillo J, Álvarez-Sabín J, Dávalos A, Díez-Tejedor E, Lizasoain I, et al. (2003) Neuroprotección farmacológica en la isquemia cerebral: ¿es todavía una opción terapéutica? Rev Neurol 18: 368-384.

41. Donnan GA, Davis SM (2008) Neuroprotection: still achievable in humans. Stroke 39: 525.

42. Hazell AS (2007) Excitotoxic mechanisms in stroke: an update of concepts and treatment strategies. Neurochem Int 50: 941-953.

43. Horn J, de Haan RJ, Vermeulen M, Limburg M (2001) Very Early Nimodipine Use in Stroke (VENUS): a randomized, double-blind, placebo-controlled trial. Stroke 32: 461-465.

44. Brea D, Castillo J (2010) El ictus isquémico en Atención Primaria: Profármaco. In: Martinez-Vila E, editor. Neuroprotección y neurorrestauración.

45. Warach S, Kaufman D, Chiu D, Devlin T, Luby M, et al. (2006) Effect of the Glycine Antagonist Gavestinel on cerebral infarcts in acute stroke patients, a randomized placebo-controlled trial: The GAIN MRI Substudy. Cerebrovasc Dis 21: 106-111.

46. Davis SM, Lees KR, Albers GW, Diener HC, Markabi S, et al. (2000) Selfotel in acute ischemic stroke : possible

neurotoxic effects of an NMDA antagonist. Stroke 31: 347-354.

47. Muir KW, Lees KR, Ford I, Davis S, Intravenous Magnesium Efficacy in Stroke Study I (2004) Magnesium for acute stroke (Intravenous Magnesium Efficacy in Stroke trial): randomised controlled trial. Lancet 363: 439-445.

48. Ginsberg MD (2008) Neuroprotection for ischemic stroke: past, present and future. Neuropharmacology 55: 363-389.

49. Campos F, Sobrino T, Ramos-Cabrer P, Argibay B, Agulla J, et al. (2011) Neuroprotection by glutamate oxaloacetate transaminase in ischemic stroke: an experimental study. J Cereb Blood Flow Metab 31: 1378-1386.

50. Perez-Mato M, Ramos-Cabrer P, Sobrino T, Blanco M, Ruban A, et al. (2014) Human recombinant glutamate oxaloacetate transaminase 1 (GOT1) supplemented with oxaloacetate induces a protective effect after cerebral ischemia. Cell Death Dis 5: e992.

51. Teichberg VI (2011) GOT to rid the body of excess glutamate. J Cereb Blood Flow Metab 31: 1376-1377.

52. Teichberg VI, Cohen-Kashi-Malina K, Cooper I, Zlotnik A (2009) Homeostasis of glutamate in brain fluids: an accelerated brain-to-blood efflux of excess glutamate is produced by blood glutamate scavenging and offers protection from neuropathologies. Neuroscience 158: 301-308.

53. Koziol JA (2006) NXY-059 for acute ischemic stroke. N Engl J Med 354: 2075-2076; author reply 2075-2076.

54. Savitz SI, Fisher M (2007) Future of neuroprotection for acute stroke: in the aftermath of the SAINT trials. Ann Neurol 61: 396-402.

55. Serebruany V (2006) NXY-059 for acute ischemic stroke. N Engl J Med 354: 2075-2076; author reply 2075-2076.

56. Secades JJ, Frontera G (1995) CDP-choline: pharmacological and clinical review. Methods Find Exp Clin Pharmacol 17 Suppl B: 1-54.

57. Hurtado O, Cardenas A, Pradillo JM, Morales JR, Ortego F, et al. (2007) A chronic treatment with CDP-choline improves functional recovery and increases neuronal plasticity after experimental stroke. Neurobiol Dis 26: 105-111.

58. Adibhatla RM, Hatcher JF, Larsen EC, Chen X, Sun D, et al. (2006) CDP-choline significantly restores phosphatidylcholine levels by differentially affecting phospholipase A2 and CTP: phosphocholine cytidylyltransferase after stroke. J Biol Chem 281: 6718-6725.

59. Ferro JM, Davalos A (2006) Other neuroprotective therapies on trial in acute stroke. Cerebrovasc Dis 21 Suppl 2: 127-130.

60. Hurtado O, Pradillo JM, Fernandez-Lopez D, Morales JR, Sobrino T, et al. (2008) Delayed post-ischemic administration of CDP-choline increases EAAT2 association to lipid rafts and affords neuroprotection in experimental stroke. Neurobiol Dis 29: 123-131.

61. Alvarez-Buylla A, Garcia-Verdugo JM (2002) Neurogenesis in adult subventricular zone. J Neurosci 22: 629-634.

62. Zhang ZG, Chopp M (2009) Neurorestorative therapies for stroke: underlying mechanisms and translation to the clinic. Lancet Neurol 8: 491-500.

63. Marti-Fabregas J, Romaguera-Ros M, Gomez-Pinedo U, Martinez-Ramirez S, Jimenez-Xarrie E, et al. (2010)

Proliferation in the human ipsilateral subventricular zone after ischemic stroke. Neurology 74: 357-365.

64. Le Belle JE, Orozco NM, Paucar AA, Saxe JP, Mottahedeh J, et al. (2011) Proliferative neural stem cells have high endogenous ROS levels that regulate self-renewal and neurogenesis in a PI3K/Akt-dependant manner. Cell Stem Cell 8: 59-71.

65. Arenillas JF, Sobrino T, Castillo J, Davalos A (2007) The role of angiogenesis in damage and recovery from ischemic stroke. Curr Treat Options Cardiovasc Med 9: 205-212.

66. Brea D, Sobrino T, Ramos-Cabrer P, Castillo J (2009) Reorganización de la vasculatura cerebral tras la isquemia. Rev Neurol 49: 645-654.

67. Seevinck PR, Deddens LH, Dijkhuizen RM (2010) Magnetic resonance imaging of brain angiogenesis after stroke. Angiogenesis 13: 101-111.

68. Sobrino T, Hurtado O, Moro MA, Rodriguez-Yanez M, Castellanos M, et al. (2007) The increase of circulating endothelial progenitor cells after acute ischemic stroke is associated with good outcome. Stroke 38: 2759-2764.

69. Zacharek A, Chen J, Cui X, Li A, Li Y, et al. (2007) Angiopoietin1/Tie2 and VEGF/Flk1 induced by MSC treatment amplifies angiogenesis and vascular stabilization after stroke. J Cereb Blood Flow Metab 27: 1684-1691.

70. Font MA, Arboix A, Krupinski J (2010) Angiogenesis, neurogenesis and neuroplasticity in ischemic stroke. Curr Cardiol Rev 6: 238-244.

71. Liu XS, Chopp M, Zhang RL, Hozeska-Solgot A, Gregg SC, et al. (2009) Angiopoietin 2 mediates the differentiation and migration of neural progenitor cells in the subventricular zone after stroke. J Biol Chem 284: 22680-22689.

72. Teng H, Zhang ZG, Wang L, Zhang RL, Zhang L, et al. (2008) Coupling of angiogenesis and neurogenesis in cultured endothelial cells and neural progenitor cells after stroke. J Cereb Blood Flow Metab 28: 764-771.

73. Chopp M, Zhang ZG, Jiang Q (2007) Neurogenesis, angiogenesis, and MRI indices of functional recovery from stroke. Stroke 38: 827-831.

74. Jiang Q, Zhang ZG, Ding GL, Zhang L, Ewing JR, et al. (2005) Investigation of neural progenitor cell induced angiogenesis after embolic stroke in rat using MRI. Neuroimage 28: 698-707.

75. Parr AM, Tator CH, Keating A (2007) Bone marrow-derived mesenchymal stromal cells for the repair of central nervous system injury. Bone Marrow Transplant 40: 609-619.

76. Hurty A (2009) The other brain cells. In: Spector R, editor. Stanford Medicine Magazine.

77. Gage FH, Ray J, Fisher LJ (1995) Isolation, characterization, and use of stem cells from the CNS. Annu Rev Neurosci 18: 159-192.

78. Sobrino T, Campos F, Castillo J (2015) The Role of Endothelial Progenitor Cells in Stroke. In: Zhao L-R, Zhang JH, editors. Cellular Therapy for Stroke and CNS Injuries: Springer International Publishing. pp. 109-123.

79. Takagi Y, Nishimura M, Morizane A, Takahashi J, Nozaki K, et al. (2005) Survival and differentiation of neural progenitor cells derived from embryonic stem cells and transplanted into ischemic brain. J Neurosurg 103: 304-310.

80. Buhnemann C, Scholz A, Bernreuther C, Malik CY, Braun H, et al. (2006) Neuronal differentiation of transplanted embryonic stem cell-derived precursors in stroke lesions of adult rats. Brain 129: 3238-3248.

81. Shen LH, Li Y, Chen J, Cui Y, Zhang C, et al. (2007) One-year follow-up after bone marrow stromal cell treatment in middle-aged female rats with stroke. Stroke 38: 2150-2156.

82. Chen J, Li Y, Wang L, Zhang Z, Lu D, et al. (2001) Therapeutic benefit of intravenous administration of bone marrow stromal cells after cerebral ischemia in rats. Stroke 32: 1005-1011.

83. Mehler MF, Rozental R, Dougherty M, Spray DC, Kessler JA (1993) Cytokine regulation of neuronal differentiation of hippocampal progenitor cells. Nature 362: 62-65.

84. Wei X, Du Z, Zhao L, Feng D, Wei G, et al. (2009) IFATS collection: The conditioned media of adipose stromal cells protect against hypoxia-ischemia-induced brain damage in neonatal rats. Stem Cells 27: 478-488.

85. Borlongan CV, Kaneko Y, Maki M, Yu SJ, Ali M, et al. (2010) Menstrual blood cells display stem cell-like phenotypic markers and exert neuroprotection following transplantation in experimental stroke. Stem Cells Dev 19: 439-452.

86. Martino G, Pluchino S (2006) The therapeutic potential of neural stem cells. Nat Rev Neurosci 7: 395-406.

87. Sheikh AM, Nagai A, Wakabayashi K, Narantuya D, Kobayashi S, et al. (2011) Mesenchymal stem cell transplantation modulates neuroinflammation in focal cerebral ischemia: contribution of fractalkine and IL-5. Neurobiol Dis 41: 717-724.

88. Bacigaluppi M, Pluchino S, Peruzzotti-Jametti L, Kilic E, Kilic U, et al. (2009) Delayed post-ischaemic neuroprotection following systemic neural stem cell transplantation involves multiple mechanisms. Brain 132: 2239-2251.

89. Hirko AC, Dallasen R, Jomura S, Xu Y (2008) Modulation of inflammatory responses after global ischemia by transplanted umbilical cord matrix stem cells. Stem Cells 26: 2893-2901.

90. Arvidsson A, Collin T, Kirik D, Kokaia Z, Lindvall O (2002) Neuronal replacement from endogenous precursors in the adult brain after stroke. Nat Med 8: 963-970.

91. Mine Y, Tatarishvili J, Oki K, Monni E, Kokaia Z, et al. (2013) Grafted human neural stem cells enhance several steps of endogenous neurogenesis and improve behavioral recovery after middle cerebral artery occlusion in rats. Neurobiol Dis 52: 191-203.

92. Goldman SA, Chen Z (2011) Perivascular instruction of cell genesis and fate in the adult brain. Nat Neurosci 14: 1382-1389.

93. Chopp M, Li Y, Zhang ZG (2009) Mechanisms underlying improved recovery of neurological function after stroke in the rodent after treatment with neurorestorative cell-based therapies. Stroke 40: S143-145.

94. Lee SH, Lumelsky N, Studer L, Auerbach JM, McKay RD (2000) Efficient generation of midbrain and hindbrain neurons from mouse embryonic stem cells. Nat Biotechnol 18: 675-679.

95. Nagai N, Kawao N, Okada K, Okumoto K, Teramura T, et al. (2010) Systemic transplantation of embryonic stem cells accelerates brain lesion decrease and angiogenesis. Neuroreport 21: 575-579.

96. Tae-Hoon L, Yoon-Seok L (2012) Transplantation of mouse embryonic stem cell after middle cerebral artery occlusion. Acta Cir Bras 27: 333-339.

97. Seyed Jafari SS, Ali Aghaei A, Asadi-Shekaari M, Nematollahi-Mahani SN, Sheibani V (2011) Investigating the

effects of adult neural stem cell transplantation by lumbar puncture in transient cerebral ischemia. Neurosci Lett 495: 1-5.

98. Guzman R, De Los Angeles A, Cheshier S, Choi R, Hoang S, et al. (2008) Intracarotid injection of fluorescence activated cell-sorted CD49d-positive neural stem cells improves targeted cell delivery and behavior after stroke in a mouse stroke model. Stroke 39: 1300-1306.

99. Chen SJ, Chang CM, Tsai SK, Chang YL, Chou SJ, et al. (2010) Functional improvement of focal cerebral ischemia injury by subdural transplantation of induced pluripotent stem cells with fibrin glue. Stem Cells Dev 19: 1757-1767.

100. Wang J, Chao F, Han F, Zhang G, Xi Q, et al. (2013) PET demonstrates functional recovery after transplantation of induced pluripotent stem cells in a rat model of cerebral ischemic injury. J Nucl Med 54: 785-792.

101. Chen J, Sanberg PR, Li Y, Wang L, Lu M, et al. (2001) Intravenous administration of human umbilical cord blood reduces behavioral deficits after stroke in rats. Stroke 32: 2682-2688.

102. Kozlowska H, Jablonka J, Janowski M, Jurga M, Kossut M, et al. (2007) Transplantation of a novel human cord blood-derived neural-like stem cell line in a rat model of cortical infarct. Stem Cells Dev 16: 481-488.

103. Li Y, Chen J, Wang L, Lu M, Chopp M (2001) Treatment of stroke in rat with intracarotid administration of marrow stromal cells. Neurology 56: 1666-1672.

104. Kurozumi K, Nakamura K, Tamiya T, Kawano Y, Ishii K, et al. (2005) Mesenchymal stem cells that produce neurotrophic factors reduce ischemic damage in the rat middle cerebral artery occlusion model. Mol Ther 11: 96-104.

105. Oki K, Tatarishvili J, Wood J, Koch P, Wattananit S, et al. (2012) Human-induced pluripotent stem cells form functional neurons and improve recovery after grafting in stroke-damaged brain. Stem Cells 30: 1120-1133.

106. Robinton DA, Daley GQ (2012) The promise of induced pluripotent stem cells in research and therapy. Nature 481: 295-305.

107. Shinozuka K, Dailey T, Tajiri N, Ishikawa H, Kaneko Y, et al. (2013) Stem Cell Transplantation for Neuroprotection in Stroke. Brain Sci 3: 239-261.

108. Lee JM, Jung J, Lee HJ, Jeong SJ, Cho KJ, et al. (2012) Comparison of immunomodulatory effects of placenta mesenchymal stem cells with bone marrow and adipose mesenchymal stem cells. Int Immunopharmacol 13: 219-224.

109. Liu R, Yuan H, Yuan F, Yang SH (2012) Neuroprotection targeting ischemic penumbra and beyond for the treatment of ischemic stroke. Neurol Res 34: 331-337.

110. Fazekasova H, Lechler R, Langford K, Lombardi G (2011) Placenta-derived MSCs are partially immunogenic and less immunomodulatory than bone marrow-derived MSCs. J Tissue Eng Regen Med 5: 684-694.

111. Netto CA, Hodges H, Sinden JD, Le Peillet E, Kershaw T, et al. (1993) Effects of fetal hippocampal field grafts on ischaemic-induced deficits in spatial navigation in the water maze. Neuroscience 54: 69-92.

112. Darsalia V, Kallur T, Kokaia Z (2007) Survival, migration and neuronal differentiation of human fetal striatal and cortical neural stem cells grafted in stroke-damaged rat striatum. Eur J Neurosci 26: 605-614.

113. Hoehn M, Kustermann E, Blunk J, Wiedermann D, Trapp T, et al. (2002) Monitoring of implanted stem cell migration in vivo: a highly resolved in vivo magnetic resonance

imaging investigation of experimental stroke in rat. Proc Natl Acad Sci U S A 99: 16267-16272.

114. Fischer UM, Harting MT, Jimenez F, Monzon-Posadas WO, Xue H, et al. (2009) Pulmonary passage is a major obstacle for intravenous stem cell delivery: the pulmonary first-pass effect. Stem Cells Dev 18: 683-692.

115. Lee ST, Chu K, Jung KH, Kim SJ, Kim DH, et al. (2008) Anti-inflammatory mechanism of intravascular neural stem cell transplantation in haemorrhagic stroke. Brain 131: 616-629.

116. Li L, Jiang Q, Ding G, Zhang L, Zhang ZG, et al. (2010) Effects of administration route on migration and distribution of neural progenitor cells transplanted into rats with focal cerebral ischemia, an MRI study. J Cereb Blood Flow Metab 30: 653-662.

117. Guo L, Ge J, Wang S, Zhou Y, Wang X, et al. (2013) A novel method for efficient delivery of stem cells to the ischemic brain. Stem Cell Res Ther 4: 116.

118. Keimpema E, Fokkens MR, Nagy Z, Agoston V, Luiten PG, et al. (2009) Early transient presence of implanted bone marrow stem cells reduces lesion size after cerebral ischaemia in adult rats. Neuropathol Appl Neurobiol 35: 89-102.

119. Gutierrez-Fernandez M, Rodriguez-Frutos B, Alvarez-Grech J, Vallejo-Cremades MT, Exposito-Alcaide M, et al. (2011) Functional recovery after hematic administration of allogenic mesenchymal stem cells in acute ischemic stroke in rats. Neuroscience 175: 394-405.

120. Gorelik M, Orukari I, Wang J, Galpoththawela S, Kim H, et al. (2012) Use of MR cell tracking to evaluate targeting of glial precursor cells to inflammatory tissue by exploiting the very late antigen-4 docking receptor. Radiology 265: 175-185.

121. Suarez-Monteagudo C, Hernandez-Ramirez P, Alvarez-Gonzalez L, Garcia-Maeso I, de la Cuetara-Bernal K, et al. (2009) Autologous bone marrow stem cell neurotransplantation in stroke patients. An open study. Restor Neurol Neurosci 27: 151-161.

122. Savitz SI, Dinsmore J, Wu J, Henderson GV, Stieg P, et al. (2005) Neurotransplantation of fetal porcine cells in patients with basal ganglia infarcts: a preliminary safety and feasibility study. Cerebrovasc Dis 20: 101-107.

123. Li WY, Choi YJ, Lee PH, Huh K, Kang YM, et al. (2008) Mesenchymal stem cells for ischemic stroke: changes in effects after ex vivo culturing. Cell Transplant 17: 1045-1059.

124. Savitz SI, Misra V, Kasam M, Juneja H, Cox CS, Jr., et al. (2011) Intravenous autologous bone marrow mononuclear cells for ischemic stroke. Ann Neurol 70: 59-69.

125. Honmou O, Houkin K, Matsunaga T, Niitsu Y, Ishiai S, et al. (2011) Intravenous administration of auto serum-expanded autologous mesenchymal stem cells in stroke. Brain 134: 1790-1807.

126. Bhasin A, Srivastava MV, Kumaran SS, Mohanty S, Bhatia R, et al. (2011) Autologous mesenchymal stem cells in chronic stroke. Cerebrovasc Dis Extra 1: 93-104.

127. Moniche F, Montaner J, Gonzalez-Marcos JR, Carmona M, Pinero P, et al. (2014) Intra-arterial bone marrow mononuclear cell (BM-MNC) transplantation correlates with GM-CSF, PDGF-BB and MMP-2 serum levels in stroke patients: Results from a clinical trial. Cell Transplant.

128. Friedrich MA, Martins MP, Araujo MD, Klamt C, Vedolin L, et al. (2012) Intra-arterial infusion of autologous bone marrow mononuclear cells in patients with moderate to severe middle cerebral artery acute ischemic stroke. Cell Transplant 21 Suppl 1: S13-21.

129. Battistella V, de Freitas GR, da Fonseca LM, Mercante D, Gutfilen B, et al. (2011) Safety of autologous bone marrow mononuclear cell transplantation in patients with nonacute ischemic stroke. Regen Med 6: 45-52.

130. Liu X, Ye R, Yan T, Yu SP, Wei L, et al. (2014) Cell based therapies for ischemic stroke: from basic science to bedside. Prog Neurobiol 115: 92-115.

131. Paul G, Anisimov SV (2013) The secretome of mesenchymal stem cells: potential implications for neuroregeneration. Biochimie 95: 2246-2256.

132. Boxall SA, Jones E (2012) Markers for characterization of bone marrow multipotential stromal cells. Stem Cells Int 2012: 975871.

133. Chamberlain G, Fox J, Ashton B, Middleton J (2007) Concise review: mesenchymal stem cells: their phenotype, differentiation capacity, immunological features, and potential for homing. Stem Cells 25: 2739-2749.

134. Pittenger MF, Mackay AM, Beck SC, Jaiswal RK, Douglas R, et al. (1999) Multilineage potential of adult human mesenchymal stem cells. Science 284: 143-147.

135. Makino S, Fukuda K, Miyoshi S, Konishi F, Kodama H, et al. (1999) Cardiomyocytes can be generated from marrow stromal cells in vitro. J Clin Invest 103: 697-705.

136. Chung DJ, Choi CB, Lee SH, Kang EH, Lee JH, et al. (2009) Intraarterially delivered human umbilical cord blood-derived mesenchymal stem cells in canine cerebral ischemia. J Neurosci Res 87: 3554-3567.

137. Koh SH, Kim KS, Choi MR, Jung KH, Park KS, et al. (2008) Implantation of human umbilical cord-derived mesenchymal stem cells as a neuroprotective therapy for ischemic stroke in rats. Brain Res 1229: 233-248.

138. Wislet-Gendebien S, Hans G, Leprince P, Rigo JM, Moonen G, et al. (2005) Plasticity of cultured mesenchymal stem cells: switch from nestin-positive to excitable neuron-like phenotype. Stem Cells 23: 392-402.

139. Brazelton TR, Rossi FM, Keshet GI, Blau HM (2000) From marrow to brain: expression of neuronal phenotypes in adult mice. Science 290: 1775-1779.

140. Kopen GC, Prockop DJ, Phinney DG (1999) Marrow stromal cells migrate throughout forebrain and cerebellum, and they differentiate into astrocytes after injection into neonatal mouse brains. Proc Natl Acad Sci U S A 96: 10711-10716.

141. Mezey E, Chandross KJ, Harta G, Maki RA, McKercher SR (2000) Turning blood into brain: cells bearing neuronal antigens generated in vivo from bone marrow. Science 290: 1779-1782.

142. Chen J, Li Y, Katakowski M, Chen X, Wang L, et al. (2003) Intravenous bone marrow stromal cell therapy reduces apoptosis and promotes endogenous cell proliferation after stroke in female rat. J Neurosci Res 73: 778-786.

143. Li Y, Chen J, Chen XG, Wang L, Gautam SC, et al. (2002) Human marrow stromal cell therapy for stroke in rat: neurotrophins and functional recovery. Neurology 59: 514-523.

144. Li Y, Chopp M, Chen J, Wang L, Gautam SC, et al. (2000) Intrastriatal transplantation of bone marrow nonhematopoietic cells improves functional recovery after stroke in adult mice. J Cereb Blood Flow Metab 20: 1311-1319.

145. Shen LH, Li Y, Chen J, Zhang J, Vanguri P, et al. (2006) Intracarotid transplantation of bone marrow stromal cells

increases axon-myelin remodeling after stroke. Neuroscience 137: 393-399.

146. Borlongan CV, Lind JG, Dillon-Carter O, Yu G, Hadman M, et al. (2004) Bone marrow grafts restore cerebral blood flow and blood brain barrier in stroke rats. Brain Res 1010: 108-116.

147. Chen J, Li Y, Wang L, Lu M, Chopp M (2002) Caspase inhibition by Z-VAD increases the survival of grafted bone marrow cells and improves functional outcome after MCAo in rats. J Neurol Sci 199: 17-24.

148. Chopp M, Li Y (2002) Treatment of neural injury with marrow stromal cells. Lancet Neurol 1: 92-100.

149. Li X, Zuo P (2005) Effects of Abeta25-35 on neurogenesis in the adult mouse subventricular zone and dentate gyrus. Neurol Res 27: 218-222.

150. Wang C, Liu F, Liu YY, Zhao CH, You Y, et al. (2011) Identification and characterization of neuroblasts in the subventricular zone and rostral migratory stream of the adult human brain. Cell Res 21: 1534-1550.

151. Curtis MA, Kam M, Nannmark U, Anderson MF, Axell MZ, et al. (2007) Human neuroblasts migrate to the olfactory bulb via a lateral ventricular extension. Science 315: 1243-1249.

152. Hou SW, Wang YQ, Xu M, Shen DH, Wang JJ, et al. (2008) Functional integration of newly generated neurons into striatum after cerebral ischemia in the adult rat brain. Stroke 39: 2837-2844.

153. Yamashita T, Ninomiya M, Hernandez Acosta P, Garcia-Verdugo JM, Sunabori T, et al. (2006) Subventricular zone-derived neuroblasts migrate and differentiate into mature neurons in the post-stroke adult striatum. J Neurosci 26: 6627-6636.

154. Shin YJ, Choi JS, Choi JY, Cha JH, Chun MH, et al. (2010) Enhanced expression of vascular endothelial growth factor receptor-3 in the subventricular zone of stroke-lesioned rats. Neurosci Lett 469: 194-198.

155. Wittko IM, Schanzer A, Kuzmichev A, Schneider FT, Shibuya M, et al. (2009) VEGFR-1 regulates adult olfactory bulb neurogenesis and migration of neural progenitors in the rostral migratory stream in vivo. J Neurosci 29: 8704-8714.

156. Jin KL, Mao XO, Greenberg DA (2000) Vascular endothelial growth factor: direct neuroprotective effect in in vitro ischemia. Proc Natl Acad Sci U S A 97: 10242-10247.

157. Craig CG, Tropepe V, Morshead CM, Reynolds BA, Weiss S, et al. (1996) In vivo growth factor expansion of endogenous subependymal neural precursor cell populations in the adult mouse brain. J Neurosci 16: 2649-2658.

158. Wang Y, Cooke MJ, Morshead CM, Shoichet MS (2012) Hydrogel delivery of erythropoietin to the brain for endogenous stem cell stimulation after stroke injury. Biomaterials 33: 2681-2692.

159. Li J, Feng L, Fan L, Zha Y, Guo L, et al. (2011) Targeting the brain with PEG-PLGA nanoparticles modified with phage-displayed peptides. Biomaterials 32: 4943-4950.

160. de Boer AG, Gaillard PJ (2007) Strategies to improve drug delivery across the blood-brain barrier. Clin Pharmacokinet 46: 553-576.

161. Justicia C, Martin A, Rojas S, Gironella M, Cervera A, et al. (2006) Anti-VCAM-1 antibodies did not protect against ischemic damage either in rats or in mice. J Cereb Blood Flow Metab 26: 421-432.

162. Wiebers DO, Adams HP, Jr., Whisnant JP (1990) Animal models of stroke: are they relevant to human disease? Stroke 21: 1-3.

163. Agulla J, Argibay B, Perez-Mato M, Brea D, Ramos-Cabrer P, et al. (2011) Comparison of the lesion produced by permanent focal cerebral ischaemia in three animal models using magnetic resonance imaging. Rev Neurol 53: 265-274.

164. Fisher M, Stroke Therapy Academic Industry R (2003) Recommendations for advancing development of acute stroke therapies: Stroke Therapy Academic Industry Roundtable 3. Stroke 34: 1539-1546.

165. Casals JB, Pieri NC, Feitosa ML, Ercolin AC, Roballo KC, et al. (2011) The use of animal models for stroke research: a review. Comp Med 61: 305-313.

166. Traystman RJ (2003) Animal models of focal and global cerebral ischemia. ILAR J 44: 85-95.

167. Ricardo P, Yanlin W-F, Lee K (2008) Anatomy and Cerebral Circulation of the Rat. Manual of Stroke Models in Rats: CRC Press. pp. 13-23.

168. Esteves A FA, Rossi-Junior WC and Fernandez GJM. (2013) Anatomical arrangement and distribution of the cerebral arterial circle in rats J Morphol Sci 30: 132-139.

169. Kandel E SJaJT (2001) Principios de Neurociencia: Madrid: McGraw-Hill/Interamericana.

170. Yanlin W-F, Lee K (2008) Which Model to Use? Manual of Stroke Models in Rats: CRC Press. pp. 31-36.

171. Longa EZ, Weinstein PR, Carlson S, Cummins R (1989) Reversible middle cerebral artery occlusion without craniectomy in rats. Stroke 20: 84-91.

172. Abe K, Yamashita T, Takizawa S, Kuroda S, Kinouchi H, et al. (2012) Stem cell therapy for cerebral ischemia: from basic science to clinical applications. J Cereb Blood Flow Metab 32: 1317-1331.

173. Purves D AG, Fitzpatrick D, et al. (2001) The Blood Supply of the Brain and Spinal Cord. In: Associates NSMS, editor. 2nd ed.

174. Ballabh P, Braun A, Nedergaard M (2004) The blood-brain barrier: an overview: structure, regulation, and clinical implications. Neurobiol Dis 16: 1-13.

175. Engelhardt B (2006) Molecular mechanisms involved in T cell migration across the blood-brain barrier. J Neural Transm 113: 477-485.

176. Strbian D, Durukan A, Pitkonen M, Marinkovic I, Tatlisumak E, et al. (2008) The blood-brain barrier is continuously open for several weeks following transient focal cerebral ischemia. Neuroscience 153: 175-181.

177. Belayev L, Busto R, Zhao W, Ginsberg MD (1996) Quantitative evaluation of blood-brain barrier permeability following middle cerebral artery occlusion in rats. Brain Res 739: 88-96.

178. Liu L, Eckert MA, Riazifar H, Kang DK, Agalliu D, et al. (2013) From blood to the brain: can systemically transplanted mesenchymal stem cells cross the blood-brain barrier? Stem Cells Int 2013: 435093.

179. Nakano-Doi A, Nakagomi T, Fujikawa M, Nakagomi N, Kubo S, et al. (2010) Bone marrow mononuclear cells promote proliferation of endogenous neural stem cells through vascular niches after cerebral infarction. Stem Cells 28: 1292-1302.

180. Giraldi-Guimardes A, Rezende-Lima M, Bruno FP, Mendez-Otero R (2009) Treatment with bone marrow

mononuclear cells induces functional recovery and decreases neurodegeneration after sensorimotor cortical ischemia in rats. Brain Res 1266: 108-120.

181. de Vasconcelos Dos Santos A, da Costa Reis J, Diaz Paredes B, Moraes L, Jasmin, et al. (2010) Therapeutic window for treatment of cortical ischemia with bone marrow-derived cells in rats. Brain Res 1306: 149-158.

182. Brenneman M, Sharma S, Harting M, Strong R, Cox CS, Jr., et al. (2010) Autologous bone marrow mononuclear cells enhance recovery after acute ischemic stroke in young and middle-aged rats. J Cereb Blood Flow Metab 30: 140-149.

183. Jolkkonen J, Walczak P (2013) Cell-Based Therapies in Stroke: Springer.

184. Walczak P, Zhang J, Gilad AA, Kedziorek DA, Ruiz-Cabello J, et al. (2008) Dual-modality monitoring of targeted intraarterial delivery of mesenchymal stem cells after transient ischemia. Stroke 39: 1569-1574.

185. Latchaw RE, Alberts MJ, Lev MH, Connors JJ, Harbaugh RE, et al. (2009) Recommendations for imaging of acute ischemic stroke: a scientific statement from the American Heart Association. Stroke 40: 3646-3678.

186. Pankhurst QA, Connolly J, Jones SK, Dobson J (2003) Applications of magnetic nanoparticles in biomedicine. Journal of Physics D: Applied Physics 36: R167.

187. Putnis A (1992) An Introduction to Mineral Sciences: Cambridge University Press.

188. Panagiotis V, Matthieu F, Antoine F, Constantinos M (2010) MRI-Guided Nanorobotic Systems for Drug Delivery. Handbook of Nanophysics: CRC Press. pp. 1-33.

189. Varadan VK, Chen L, Xie J (2008) Physical Background for the Biomedical Applications of Functional Magnetic Nanomaterials. Nanomedicine: John Wiley & Sons, Ltd. pp. 37-83.

190. Salata O (2004) Applications of nanoparticles in biology and medicine. J Nanobiotechnology 2: 3.

191. Mody VV, Siwale R, Singh A, Mody HR (2010) Introduction to metallic nanoparticles. J Pharm Bioallied Sci 2: 282-289.

192. Appenzeller T (1991) The man who dared to think small. Science 254: 1300.

193. Sun C, Lee JS, Zhang M (2008) Magnetic nanoparticles in MR imaging and drug delivery. Adv Drug Deliv Rev 60: 1252-1265.

194. Blakemore R (1975) Magnetotactic bacteria. Science 190: 377-379.

195. L. Villaraza AJ, Bumb A, Brechbiel MW (2010) Macromolecules, Dendrimers, and Nanomaterials in Magnetic Resonance Imaging: The Interplay between Size, Function, and Pharmacokinetics. Chemical Reviews 110: 2921-2959.

196. Laurent S, Forge D, Port M, Roch A, Robic C, et al. (2008) Magnetic Iron Oxide Nanoparticles: Synthesis, Stabilization, Vectorization, Physicochemical Characterizations, and Biological Applications. Chemical Reviews 108: 2064-2110.

197. Swami A, Kumar A, Sastry M (2003) Formation of Water-Dispersible Gold Nanoparticles Using a Technique Based on Surface-Bound Interdigitated Bilayers. Langmuir 19: 1168-1172.

198. Liu X, Ye R, Yan T, Yu SP, Wei L, et al. (2013) Cell based therapies for ischemic stroke: From basic science to bedside. Prog Neurobiol.

199. Easo SL, Mohanan PV (2013) Dextran stabilized iron oxide nanoparticles: synthesis, characterization and in vitro studies. Carbohydr Polym 92: 726-732.

200. Molday RS, Mackenzie D (1982) Immunospecific ferromagnetic iron-dextran reagents for the labeling and magnetic separation of cells. Journal of Immunological Methods 52: 353-367.

201. Albukhaty S, Naderi-Manesh H, Tiraihi T (2013) In vitro labeling of neural stem cells with poly-L-lysine coated super paramagnetic nanoparticles for green fluorescent protein transfection. Iran Biomed J 17: 71-76.

202. Wang L, Wang Z, Frank TG, Brown SI, Chudek SA, et al. (2009) Rapid and efficient cell labeling with a MRI contrast agent by electroporation in the presence of protamine sulfate. Nanomedicine (Lond) 4: 305-315.

203. Liu G, Yang H, Zhang XM, Shao Y, Jiang H (2010) MR imaging for the longevity of mesenchymal stem cells labeled with poly-L-lysine-Resovist complexes. Contrast Media Mol Imaging 5: 53-58.

204. Sibov TT, Miyaki LA, Mamani JB, Marti LC, Sardinha LR, et al. (2012) Evaluation of umbilical cord mesenchymal stem cell labeling with superparamagnetic iron oxide nanoparticles coated with dextran and complexed with Poly-L-lysine. Einstein (Sao Paulo) 10: 180-188.

205. Jain TK, Morales MA, Sahoo SK, Leslie-Pelecky DL, Labhasetwar V (2005) Iron oxide nanoparticles for sustained delivery of anticancer agents. Mol Pharm 2: 194-205.

206. Moghimi SM, Hunter AC (2000) Poloxamers and poloxamines in nanoparticle engineering and experimental medicine. Trends Biotechnol 18: 412-420.

207. Jain TK, Foy SP, Erokwu B, Dimitrijevic S, Flask CA, et al. (2009) Magnetic resonance imaging of multifunctional pluronic stabilized iron-oxide nanoparticles in tumor-bearing mice. Biomaterials 30: 6748-6756.

208. Alvarez-Lorenzo C, Sosnik A, Concheiro A (2011) PEO-PPO block copolymers for passive micellar targeting and overcoming multidrug resistance in cancer therapy. Curr Drug Targets 12: 1112-1130.

209. Bae KH, Ha YJ, Kim C, Lee KR, Park TG (2008) Pluronic/chitosan shell cross-linked nanocapsules encapsulating magnetic nanoparticles. J Biomater Sci Polym Ed 19: 1571-1583.

210. Soenen SJ, De Smedt SC, Braeckmans K (2012) Limitations and caveats of magnetic cell labeling using transfection agent complexed iron oxide nanoparticles. Contrast Media Mol Imaging 7: 140-152.

211. Soenen SJ, Nuytten N, De Meyer SF, De Smedt SC, De Cuyper M (2010) High intracellular iron oxide nanoparticle concentrations affect cellular cytoskeleton and focal adhesion kinase-mediated signaling. Small 6: 832-842.

212. Crabbe A, Vandeputte C, Dresselaers T, Sacido AA, Verdugo JM, et al. (2010) Effects of MRI contrast agents on the stem cell phenotype. Cell Transplant 19: 919-936.

213. Soenen SJ, De Cuyper M (2010) Assessing iron oxide nanoparticle toxicity in vitro: current status and future prospects. Nanomedicine (Lond) 5: 1261-1275.

214. Soenen SJ, Himmelreich U, Nuytten N, De Cuyper M (2011) Cytotoxic effects of iron oxide nanoparticles and

implications for safety in cell labelling. Biomaterials 32: 195-205.

215. Soenen SJ, Himmelreich U, Nuytten N, Pisanic TR, 2nd, Ferrari A, et al. (2010) Intracellular nanoparticle coating stability determines nanoparticle diagnostics efficacy and cell functionality. Small 6: 2136-2145.

216. Arbab AS, Yocum GT, Wilson LB, Parwana A, Jordan EK, et al. (2004) Comparison of transfection agents in forming complexes with ferumoxides, cell labeling efficiency, and cellular viability. Mol Imaging 3: 24-32.

217. Kalish H, Arbab AS, Miller BR, Lewis BK, Zywicke HA, et al. (2003) Combination of transfection agents and magnetic resonance contrast agents for cellular imaging: relationship between relaxivities, electrostatic forces, and chemical composition. Magn Reson Med 50: 275-282.

218. Son KK, Patel DH, Tkach D, Park A (2000) Cationic liposome and plasmid DNA complexes formed in serum-free medium under optimum transfection condition are negatively charged. Biochim Biophys Acta 1466: 11-15.

219. Wang S, Fang J, Zhang T, Wang B, Chen J, et al. (2011) Magnetic resonance imaging targeting of intracranial glioma xenografts by Resovist-labeled endothelial progenitor cells. J Neurooncol 105: 67-75.

220. Jasmin, Torres AL, Nunes HM, Passipieri JA, Jelicks LA, et al. (2011) Optimized labeling of bone marrow mesenchymal cells with superparamagnetic iron oxide nanoparticles and in vivo visualization by magnetic resonance imaging. J Nanobiotechnology 9: 4.

221. Riggio C, Calatayud MP, Hoskins C, Pinkernelle J, Sanz B, et al. (2012) Poly-l-lysine-coated magnetic nanoparticles as intracellular actuators for neural guidance. Int J Nanomedicine 7: 3155-3166.

222. Smirnov P, Gazeau F, Beloeil JC, Doan BT, Wilhelm C, et al. (2006) Single-cell detection by gradient echo 9.4 T MRI: a parametric study. Contrast Media Mol Imaging 1: 165-174.

223. Carenza E, Barcelo V, Morancho A, Levander L, Boada C, et al. (2013) In vitro angiogenic performance and in vivo brain targeting of magnetized endothelial progenitor cells for neurorepair therapies. Nanomedicine.

224. Nishida K, Tanaka N, Nakanishi K, Kamei N, Hamasaki T, et al. (2006) Magnetic targeting of bone marrow stromal cells into spinal cord: through cerebrospinal fluid. Neuroreport 17: 1269-1272.

225. Kyrtatos PG, Lehtolainen P, Junemann-Ramirez M, Garcia-Prieto A, Price AN, et al. (2009) Magnetic tagging increases delivery of circulating progenitors in vascular injury. JACC Cardiovasc Interv 2: 794-802.

226. Pardoe H, Chua-anusorn W, St. Pierre TG, Dobson J (2001) Structural and magnetic properties of nanoscale iron oxide particles synthesized in the presence of dextran or polyvinyl alcohol. Journal of Magnetism and Magnetic Materials 225: 41-46.

227. Trekker J, Leten C, Struys T, Lazenka VV, Argibay B, et al. (2014) Sensitive in vivo cell detection using size-optimized superparamagnetic nanoparticles. Biomaterials 35: 1627-1635.

228. Petcharoen K, Sirivat A (2012) Synthesis and characterization of magnetite nanoparticles via the chemical co-precipitation method. Materials Science and Engineering: B 177: 421-427.

229. Kim W, Suh CY, Cho SW, Roh KM, Kwon H, et al. (2012) A new method for the identification and quantification of magnetite-maghemite mixture using conventional X-ray diffraction technique. Talanta 94: 348-352.

230. Wang YX (2011) Superparamagnetic iron oxide based MRI contrast agents: Current status of clinical application. Quant Imaging Med Surg 1: 35-40.

231. Park JH, von Maltzahn G, Zhang L, Schwartz MP, Ruoslahti E, et al. (2008) Magnetic Iron Oxide Nanoworms for Tumor Targeting and Imaging. Adv Mater 20: 1630-1635.

232. Simberg D, Park JH, Karmali PP, Zhang WM, Merkulov S, et al. (2009) Differential proteomics analysis of the surface heterogeneity of dextran iron oxide nanoparticles and the implications for their in vivo clearance. Biomaterials 30: 3926-3933.

233. Carmen Bautista M, Bomati-Miguel O, del Puerto Morales M, Serna CJ, Veintemillas-Verdaguer S (2005) Surface characterisation of dextran-coated iron oxide nanoparticles prepared by laser pyrolysis and coprecipitation. Journal of Magnetism and Magnetic Materials 293: 20-27.

234. Mahdavi M, Ahmad MB, Haron MJ, Namvar F, Nadi B, et al. (2013) Synthesis, surface modification and characterisation of biocompatible magnetic iron oxide nanoparticles for biomedical applications. Molecules 18: 7533-7548.

235. Gao Q, Liang Q, Yu F, Xu J, Zhao Q, et al. (2011) Synthesis and characterization of novel amphiphilic copolymer stearic acid-coupled F127 nanoparticles for nano-technology based drug delivery system. Colloids Surf B Biointerfaces 88: 741-748.

236. Kassis I, Vaknin-Dembinsky A, Bulte J, Karussis D (2010) Effects of supermagnetic iron oxide labeling on the major functional properties of human mesenchymal stem cells from multiple sclerosis patients. Int J Stem Cells 3: 144-153.

237. Yu MX, Chen WL, Zhou Q, Gao P (2010) Study on ASTC-a-1 cells labeled with superparamagnetic iron oxide and its

magnetic resonance imaging. Exp Biol Med (Maywood) 235: 1053-1061.

238. Roeder E, Henrionnet C, Goebel JC, Gambier N, Beuf O, et al. (2014) Dose-response of superparamagnetic iron oxide labeling on mesenchymal stem cells chondrogenic differentiation: a multi-scale in vitro study. PLoS One 9: e98451.

239. Struys T, Ketkar-Atre A, Gervois P, Leten C, Hilkens P, et al. (2013) Magnetic resonance imaging of human dental pulp stem cells in vitro and in vivo. Cell Transplant 22: 1813-1829.

240. Nohroudi K, Arnhold S, Berhorn T, Addicks K, Hoehn M, et al. (2010) In vivo MRI stem cell tracking requires balancing of detection limit and cell viability. Cell Transplant 19: 431-441.

241. Soenen SJ, Brisson AR, Jonckheere E, Nuytten N, Tan S, et al. (2011) The labeling of cationic iron oxide nanoparticle-resistant hepatocellular carcinoma cells using targeted magnetoliposomes. Biomaterials 32: 1748-1758.

242. Kroll A, Pillukat MH, Hahn D, Schnekenburger J (2012) Interference of engineered nanoparticles with in vitro toxicity assays. Arch Toxicol 86: 1123-1136.

243. Holder AL, Goth-Goldstein R, Lucas D, Koshland CP (2012) Particle-induced artifacts in the MTT and LDH viability assays. Chem Res Toxicol 25: 1885-1892.

244. Schmidtke-Schrezenmeier G, Urban M, Musyanovych A, Mailander V, Rojewski M, et al. (2011) Labeling of mesenchymal stromal cells with iron oxide-poly(L-lactide) nanoparticles for magnetic resonance imaging: uptake, persistence, effects on cellular function and magnetic resonance imaging properties. Cytotherapy 13: 962-975.

245. Bradford MM (1976) A rapid and sensitive method for the quantitation of microgram quantities of protein utilizing the principle of protein-dye binding. Anal Biochem 72: 248-254.

246. Jones E, McGonagle D (2008) Human bone marrow mesenchymal stem cells in vivo. Rheumatology 47: 126-131.

247. Ma S, Xie N, Li W, Yuan B, Shi Y, et al. (2014) Immunobiology of mesenchymal stem cells. Cell Death Differ 21: 216-225.

248. Song M, Kim YJ, Kim YH, Roh J, Kim SU, et al. (2010) Using a neodymium magnet to target delivery of ferumoxide-labeled human neural stem cells in a rat model of focal cerebral ischemia. Hum Gene Ther 21: 603-610.

249. Vanecek V, Zablotskii V, Forostyak S, Ruzicka J, Herynek V, et al. (2012) Highly efficient magnetic targeting of mesenchymal stem cells in spinal cord injury. Int J Nanomedicine 7: 3719-3730.

250. Mikhaylova M, Mori N, Wildes FB, Walczak P, Gimi B, et al. (2008) Hypoxia increases breast cancer cell-induced lymphatic endothelial cell migration. Neoplasia 10: 380-389.

251. Gelosa P, Ballerio R, Banfi C, Nobili E, Gianella A, et al. (2010) Terutroban, a thromboxane/prostaglandin endoperoxide receptor antagonist, increases survival in stroke-prone rats by preventing systemic inflammation and endothelial dysfunction: comparison with aspirin and rosuvastatin. J Pharmacol Exp Ther 334: 199-205.

252. Yukawa H, Noguchi H, Oishi K, Takagi S, Hamaguchi M, et al. (2009) Cell transplantation of adipose tissue-derived stem cells in combination with heparin attenuated acute liver failure in mice. Cell Transplant 18: 611-618.

253. Yukawa H, Watanabe M, Kaji N, Okamoto Y, Tokeshi M, et al. (2012) Monitoring transplanted adipose tissue-derived

stem cells combined with heparin in the liver by fluorescence imaging using quantum dots. Biomaterials 33: 2177-2186.

254. Stroke Therapy Academic Industry R (1999) Recommendations for standards regarding preclinical neuroprotective and restorative drug development. Stroke 30: 2752-2758.

255. Wang-Fischer Y (2008) Manual of Stroke Models in Rats: Taylor & Francis.

256. Devault K, Gremaud PA, Novak V, Olufsen MS, Vernieres G, et al. (2008) Blood Flow in the Circle of Willis: Modeling and Calibration. Multiscale Model Simul 7: 888-909.

257. Coyle P, Jokelainen PT (1982) Dorsal cerebral arterial collaterals of the rat. Anat Rec 203: 397-404.

258. van Everdingen KJ, van der Grond J, Kappelle LJ, Ramos LM, Mali WP (1998) Diffusion-weighted magnetic resonance imaging in acute stroke. Stroke 29: 1783-1790.

259. Yavagal DR, Lin B, Raval AP, Garza PS, Dong C, et al. (2014) Efficacy and dose-dependent safety of intra-arterial delivery of mesenchymal stem cells in a rodent stroke model. PLoS One 9: e93735.

260. Karlupia N, Manley NC, Prasad K, Schafer R, Steinberg GK (2014) Intraarterial transplantation of human umbilical cord blood mononuclear cells is more efficacious and safer compared with umbilical cord mesenchymal stromal cells in a rodent stroke model. Stem Cell Res Ther 5: 45.

261. Vasconcelos-dos-Santos A, Rosado-de-Castro PH, Lopes de Souza SA, da Costa Silva J, Ramos AB, et al. (2012) Intravenous and intra-arterial administration of bone marrow mononuclear cells after focal cerebral ischemia: Is

there a difference in biodistribution and efficacy? Stem Cell Res 9: 1-8.

262. Fagan SC, Lapchak PA, Liebeskind DS, Ishrat T, Ergul A (2013) Recommendations for preclinical research in hemorrhagic transformation. Transl Stroke Res 4: 322-327.

263. Wang L, Menendez P, Shojaei F, Li L, Mazurier F, et al. (2005) Generation of hematopoietic repopulating cells from human embryonic stem cells independent of ectopic HOXB4 expression. J Exp Med 201: 1603-1614.

264. Finley RB (1953) A New Subspecies of Wood Rat (Neotoma mexicana) from Colorado: University of Kansas Publications Museum of Natural History. 527-534 p.

265. Willing AE, Garbuzova-Davis S, Sanberg PR, Saporta S (2002) Routes of stem cell administration in the adult rodent. Methods Mol Biol 198: 357-374.

266. Schrepfer S, Deuse T, Reichenspurner H, Fischbein MP, Robbins RC, et al. (2007) Stem cell transplantation: the lung barrier. Transplant Proc 39: 573-576.

267. Villalobos V, Bonilla E, Castellano A, Novo E, Caspersen R, et al. (2009) Ultrastructural changes of the olfactory bulb in manganese-treated mice. Biocell 33: 187-197.

268. Iihoshi S, Honmou O, Houkin K, Hashi K, Kocsis JD (2004) A therapeutic window for intravenous administration of autologous bone marrow after cerebral ischemia in adult rats. Brain Res 1007: 1-9.

269. Zhang L, Li Y, Zhang C, Chopp M, Gosiewska A, et al. (2011) Delayed administration of human umbilical tissue-derived cells improved neurological functional recovery in a rodent model of focal ischemia. Stroke 42: 1437-1444.

270. Zhang L, Yi L, Chopp M, Kramer BC, Romanko M, et al. (2012) Intravenous administration of human umbilical tissue-

derived cells improves neurological function in aged rats after embolic stroke. Cell Transplant.

271. Ramos-Cabrer P, Justicia C, Wiedermann D, Hoehn M (2010) Stem cell mediation of functional recovery after stroke in the rat. PLoS One 5: e12779.

272. Vu Q, Xie K, Eckert M, Zhao W, Cramer SC (2014) Meta-analysis of preclinical studies of mesenchymal stromal cells for ischemic stroke. Neurology 82: 1277-1286.

273. Suzuki J, Sasaki M, Harada K, Bando M, Kataoka Y, et al. (2013) Bilateral cortical hyperactivity detected by fMRI associates with improved motor function following intravenous infusion of mesenchymal stem cells in a rat stroke model. Brain Res 1497: 15-22.

274. Chopp M, Li Y (2008) Treatment of stroke and intracerebral hemorrhage with cellular and pharmacological restorative therapies. Acta Neurochir Suppl 105: 79-83.

275. Zhang ZG, Zhang L, Jiang Q, Zhang R, Davies K, et al. (2000) VEGF enhances angiogenesis and promotes blood-brain barrier leakage in the ischemic brain. J Clin Invest 106: 829-838.

276. Chen J, Shehadah A, Pal A, Zacharek A, Cui X, et al. (2013) Neuroprotective effect of human placenta-derived cell treatment of stroke in rats. Cell Transplant 22: 871-879.